Development of Novel Tools for Assisted Reproductive Technologies based on Electrically Switchable Surfaces

by

Bárbara Micaela Santos Gomes

A thesis submitted to the University of Birmingham
for the degree of DOCTOR OF PHILOSOPHY

UNIVERSITY OF BIRMINGHAM

School of Chemical Engineering
College of Engineering and Physical Sciences
University of Birmingham
United Kingdom
September 2018

Abstract

A variety of stimuli have been explored in the last few decades to develop dynamic interfaces with biotechnological and biomedical applications, such as biosensors, point of care devices, cell behaviour control and tissue engineering. In this work, the use of an electrical stimulus was explored for the development of a smart switchable surface with the ability to, in an on-demand fashion, expose and conceal progesterone - an ovarian steroid hormone which plays a crucial role as a modulator of sperm function. In this system, an electric potential drives a conformational change in the surface bound peptide moiety with fast response time. Focus was given to the design of a device that could be used in assisted reproductive treatments and grown into a commercially marketable product. Whilst being developed for assessment of sperm quality and fertilizing potential, the application of this system can be widely extended as this approach can be applied to other relevant antigen-antibody systems, which have so far only been evaluated in static conditions. Fabrication of a micropatterned surface was performed and a novel method for orthogonal functionalisation of gold and glass developed, where gold was functionalised with a polyethylene glycol thiol self-assembled monolayer (SAM) and glass was functionalised with a covalently bound poly-d-lysine layer for sperm cell attachment. In addition to the investigations on SAMs and mixed SAMs formed on gold, silicon and glass substrates, studies with fluospheres were also undertaken. These tools are aimed to be used for further studies with cells, namely the investigation of their response in terms of Ca^{2+} signalling, a key player in the regulation of sperm function.

Acknowledgements

I would like to thank my supervisor, Professor Paula Mendes, for guidance, support and trust.

Thank you to my colleagues and friends at the University of Birmingham and all the wonderful people I met there, including my ex-flatmates Alex and Rosi. Thank you to all the PhD students I've shared the lab with, who made my time there more enjoyable and offered me valuable feedback about my work: Alice, Bárbara, Eleonora, Fatima, Giuseppe, James, Josh, Kam, Simone, Yazmin, and Zarrar. Thank you to the postdocs in the lab for guidance and support: Aaron, Eduardo, Josh, Lewis, Marcos and Stefano. A special thanks to Pippa Mitchell and Monika Köpf, who were there for the whole journey of my PhD, including the best and the hardest moments, and whose friendship I am very grateful for. And a special thanks to Francia for reading my thesis and providing me valuable feedback. And thank you to the great people I've shared the office with: Ana, João, Konstantina, Lais and Stella. Thank you to Dr. Sarah Costello and Professor Stephen Publicover, Dr. Jackson Kirkman-Brown and Dr. Joao Correia, for receiving me in their lab and for offering me technical support and guidance in the work with cells. Thank you to Dr. James Bowen for the fruitful discussions about ellipsometry. Thank you to Neal Fairley and Dr. David Morgan for sharing their knowledge about XPS data fitting and clarifying my doubts. Thank you to Dr James McGettrick in Swansea University, for training me on the XPS system.

Thank you to my friends outside the University who were there for me along the PhD journey.

Thank you to my close family for the support and apologies for not going home more often, particularly in the most difficult times.

Thank you to Jon, who accompanied me on this journey, providing love, valuable knowledge and support.

Table of Contents

List of Figures

List of Tables

List of Abbreviations and Acronyms

2MET	2-mercaptoethanol
3GPS	(3-glycidyloxypropyl)trimethoxy silane
AAO	anodized aluminum oxide
Ab	antibody
ABBA	diboronic acid
ABHD2	serine hydrolase
AFM	atomic force microscope
AMAS	N-α-maleimidoacet-oxysuccinimide ester
anti-Pg MAb	progesterone-3 anti-mouse monoclonal antibody
ART	assisted reproductive technologies
ATP	adenosine triphosphate
ATR-FTIR	attenuated total reflectance - fourier transform infrared spectroscopy
BC	binding capacity
BCML	block copolymer micelle lithography
BE	binding energy
BTB	1,3,5-tris(4-carboxyphenyl)benzene
C11EG6	hexaethylene glycol-terminated thiol
CatSper	cationic channel of the sperm flagellum
CCD	charge-coupled device
CD	cyclodextrin
cDNA	complementary DNA
Con A	concanavalin A
cTnT	cardiac troponin T
CV	cyclic voltammetry
DC	direct current
DLS	dynamic light scattering
DMF	dimethylformamide
DMSO	dimethyl sulfoxide
DTSP	dithiobis(succinimidyl propionate)
ECM	extracellular matrix

EDX	energy-dispersive x-ray spectroscopy
EG3SH	tri(ethylene glycol) thiol
EIS	electrochemical impedance spectroscopy
E-QCM-D	electrochemical quartz crystal microbalance with dissipation
ESCA	electron apectroscopy for chemical analysis
eSPR	electrochemical surface plasmon resonance
FWCNTs	few-walled carbon nanotubes
GOx	glucose oxidase
HEMA	2-hydroxyethyl methacrylate
HOEGMA	hydroxyl-terminated oligo(ethylene glycol) methacrylate
HOPG	highly oriented pyrolytic graphite
ICSI	intracytoplasmic sperm injection
IDPs	intrinsically disordered proteins
IL	interferometric lithography
IMFP	ineslastic mean free path
ITO	indium tin oxide
IVF	in vitro fertilization
KE	kinetic energy
LBL	layer-by-layer
LCST	lower critical solution temperature
LV	liquid-vapour
MEO_2MA	2-(2-methoxyethoxy)ethyl methacrylate
MET	mercaptoethanol
MHA	16-mercapto)hexadecanoic acid
MIP	molecular imprinted polymers
MUA	11-mercaptoundecanoic-acid
nCP	nanocontact printing
NG	nanographene
NHS	N-hydroxysuccinimide
NIR	near-infrared
NMR	nuclear magnetic resonance
nps	nanoparticles
OC	open circuit

OEG	oligo ethylene glycol
OEGMA	oligo(ethylene glycol) methacrylate
P(AAc-co-AAM)	poly(acrylamide-co-acrylic acid)
P4VP	poly(4-vinyl pyridine)
PAA	polyacrylic acid
PANI	polyaniline
PBA	phenylboronicacid
PBS	phosphate buffer solution
PCS	photon correlation spectroscopy
PDEAEMA	poly(2-diethylaminoethyl methacrylate)
PDL	poly-d-lysine
PDMAEMA	poly(2-(dimethylamino)ethyl methacrylate)
PEDOT	poly(3,4-ethylenedioxythiophene)
PEEs	poly(phenylene ethynylenes)
PEG	polyethylene glycol
PMAA	poly(methyl methacrylate
PNIPAM	poly(N-isopropylacrylamide)
polyAAPBA	poly(acrylamidophenylboronic acid)
PPy	polypyrrole
PR	photoresist
PSS	poly(styrenesulfonate)
PTh	polythiophene
PVD	physical vapor deposition
QAS	quaternary ammonium salt
QCM	quartz crystal microbalance
RF	radio frequency
RGD	arginylglycylaspartic acid
RGDS	L-arginylglycyl-L-α-aspartyl-L-serine
ROS	reactive oxygen species
RU	response units
SAM	self-assembled monolayer
SD	standard deviation
SDBS	sodium dodecylbenzenesulfonate

SE	switching efficiency
SEM	scanning electron microscope
SH-OEG	2-(2-(1-mercaptoundec-11-yloxy)-ethoxy)-ethanol
SiN	silicon nanowire
SL	solid-liquid
SPR	surface plasmon resonance
Sulfo-GMBS	N-(γ-Maleimidobutyryloxy) sulfosuccinimide ester
SV	solid-vapour
TEA	triethylamine
TEGT	3-mercaptopropyl)tri(ethylene glycol)
TEM	transmission electron microscope
TIR	total internal reflection
TOF-SIMS	time of flight secondary ion mass spectrometry
UV	ultraviolet
UVO	ultraviolet-ozone
XPS	x-ray photoelectron spectroscopy
β-CD	*β*-cyclodextrin

1 Introduction

1.1 PhD Aim and Objectives

The work herein described, aims to address issues associated with assisted reproductive technologies, by developing novel tools based on electrically switchable surfaces. The lack of a tool for quick and efficient selection of high-quality sperm cells for use in intracytoplasmic sperm injection (ICSI), motivated the development of a smart device which could increase the success rate of this treatment.

In order to achieve this aim, the following objectives were delineated, which are fundamental for further studies with cells and the monitoring of cell responses in real time:

- Development of a smart electrically switchable surface, able to expose and conceal progesterone on-demand;
- Design and fabrication of a micropatterned device where a group of cells can be attached, each cell being isolated from the others and in contact with the electrically switchable surface which is able to expose progesterone in a controlled manner;
- Development of a method for the orthogonal functionalisation of the fabricated micropatterned device;
- Development of a method for the functionalisation of fluorescent spheres with a low density of progesterone oligopeptide.

Whilst being developed for assessment of sperm quality and fertilizing potential, the application of these tools can be widely extended, and the strategies herein described can be applied for the development of a variety of systems incorporating other biomolecules of interest.

1.2 Thesis outline

This thesis consists of the chapters describe below.

- Chapter 2 presents a review of the literature on stimuli-responsive nanostructured surfaces for biomedical applications.
- Chapter 3 outlines the techniques used in this work, mostly surface characterisation techniques.
- Chapter 4 starts with a brief introduction to biosensing platforms based on antibody-antigen interactions, followed by introducing stimuli responsive surfaces as the foundation for the development of novel tools for assisted reproductive technologies. A summary of preliminary studies performed on the development of a sensing platform that allows for controlled and specific capture of antibodies is also included. Investigations on the development of an ON-OFF switchable system are then presented, as well as preliminary studies on an OFF-ON alternative switchable system.
- Chapter 5 begins with a short introduction to photolithography techniques and orthogonal functionalisation. This chapter then describes the design and fabrication of a micropatterned device composed of gold and glass, followed by the development of a method for chemical functionalisation of the fabricated device.
- Chapter 6 starts with a brief introduction to the functionalisation of nanoparticles. The development of a method for bi-functionalisation of fluorescent spheres with a low density of progesterone peptide is then presented.
- Chapter 7 describes the chemicals, materials and protocols related to the studies described in chapters 4-6.
- Chapter 8 outlines conclusions drawn from this work and suggests future investigations.

2 Literature Review

Stimuli-Responsive Nanostructured Surfaces for Biomedical Applications

This chapter presents a review on stimuli-responsive nanostructured surfaces for biomedical applications, starting with a brief introduction to assembly strategies for precise control over thin film architecture on surfaces and lithographic processes to define surface structures with nanometer resolution. The following four sections are organized according to the type of external stimuli that triggers surface responsiveness, either chemical (pH, salinity and biochemical) or energy-based, namely electrical, photo and thermal stimuli. The chapter concludes by highlighting the key progress in the field and future prospects. This text is reproduced from a book chapter written by the author of this dissertation:

Gomes, B. S.; Mendes, P. M., Stimuli-Responsive Nanostructured Surfaces for Biomedical Applications. In *Functional Organic and Hybrid Nanostructured Materials: Fabrication, Properties, and Applications*, Li, Q., Ed. Wiley-VCH: 2018; pp 203-246.

2.1 Introduction

Nanotechnology is revolutionizing various disciplines of science and technology. Prominent among these are biology and medicine. Nanotechnology is providing the means to develop *in vitro* models which capture more of the relevant complexity that entails the native extracellular matrix in structure and function. These advances are creating unprecedented opportunities not only to study cell behaviour, but to control it, with a large impact in the fields of tissue engineering and regenerative medicine. Biofouling is a major challenge for several industries, including the biomedical industry. Biofilm formation and persistence on medical devices, such as catheters or wound dressings, can be a prelude to infection which accounts for high medical costs and an increasing number of deaths in

hospitals. Nanotechnology tools are persistently being applied to develop new and more-efficient anti-biofouling strategies. Researchers have also been exploiting the unique properties of nanostructured systems for early diagnosis, for efficient treatments with reduced invasiveness and for treating diseases at the genetic level. The route to nanomedicine products is long but a wide range of innovative and exciting solutions are currently undergoing clinical trials, promising a sudden and dramatic change in the whole healthcare scene.

Overcoming the barrier of biocompatibility, nanocarriers are being developed with high blood circulation stability, able to respond to tumor stimuli (variation of environmental pH) by switching to a positive surface charge, thus enhancing cellular internalization, and finally delivering drug molecules with high precision inside the human body [1]. Photo-switchable drugs for cancer treatment or vision restoration therapy are being tested [2]. Graphene-based devices able to measure glucose levels from human sweat and to release treatment via thermo-responsive drug loaded microneedles promise a non-invasive solution for diabetic patients [3].

The developed capability of nanostructured materials to undergo changes in properties under the influence of an external stimulus has resulted in many of the recent nanotechnological medical and biological advances. The nanostructured materials are controlled by a chemical or energy-based external stimuli (such as pH, light or temperature, as in the aforementioned examples) and the response may consist of spatial concealment or exposure of molecules, volume swell or shrinkage, change of transparency, wettability, shape or charge.

In nature, one of the characteristics of living systems (at all scales) is the ability to respond to stimuli in the surrounding environment, being fundamental to human and nature existence. From the *Mimosa pudica* whose leaves collapse suddenly when touched, to

human beings whose body core temperature is raised through fever to fight off invading bacteria or viruses, all living organisms have evolved a variety of responsive mechanisms to sustain their integrity or well-being. Biological systems are able to convert a diversity of stimuli, including temperature, pH, chemicals, pressure, magnetic and electric fields, into a wide range of fine-tuned responses. While the stimuli-triggered responses of natural systems can be observed at micro- or macroscopic scale, these events are based on molecular level processes [4-6].

Thus, inspired by nature and with the advent of nanotechnology and our increased capability of controlling matter at both the nanoscale and molecular level [7-9], we are now equipped for the construction of materials and surfaces with specific chemical and physical properties that change in response to different stimuli. In this context, self-assembly strategies and lithographic techniques are being widely explored and successfully applied to design and fabricate nanostructured surface materials with stimuli-responsive properties for a wide range of biomedical applications [10-13].

2.1.1 Thin Film Formation by Assembly on Surfaces

Self-assembly, which is prominent in biological systems, involves non-covalent interactions (*i.e.* hydrogen bonding, van der Waals, electrostatic, π-π interactions, hydrophilic-hydrophilic and hydrophobic-hydrophobic interactions) of subunits (molecules or meso-scale objects) that spontaneously organize into stable and well-defined structures close to or at thermodynamic equilibrium [14]. Self-assembly provides a simple, cheap and reproducible method of obtaining nanoscale films with a wide variety of functional groups, which can be chemically manipulated on conducting, semiconducting and insulating surface materials [15-19]. Self-assembled monolayers (SAMs) are an example of these structures [14,20]

and they have been widely used on the fabrication of responsive surfaces. SAMs are formed when organic molecular structures spontaneously adsorb onto a substrate, resulting in a highly ordered and packed layer with a thickness no bigger than the length of a single molecule. The molecular structure of SAMs comprises three main features (Figure 2.1A): i) the headgroup, which has a strong affinity to the substrate and anchors the molecule to it; ii) the backbone group, which takes a major role in the molecular ordering and iii) the terminal functional group, which determines the surface functionality. SAMs derived from the adsorption of thiol headgroup derivatives on gold and silane headgroup derivatives on silicon dioxide have been extensively studied for the modification of surface properties of metallic and inorganic substrates [12]. The strength of thiol-gold interactions and ease of preparation for this family of SAMs [21] make it a popular choice. Furthermore, gold is particularly useful for applications in biology due to its compatibility with cells and suitability for analytical techniques such as surface plasmon resonance spectroscopy (SPR), quartz crystal microbalances (QCM) and ellipsometry [14]. Silane-silicon dioxide SAMs are thermally more stable than thiol-Au SAMs. However, silane-silicon dioxide SAMs are inherently associated with reproducibility issues due to the sensitivity of the silanes to moisture [22].

SAMs very often undergo further functionalization, for example, for the immobilisation of macromolecules. Ideally, the order and stability of the underlying monolayer is not affected and this new molecule being introduced into the layer does not need to be compatible with the head group attached to the substrate. The strategy of modifying the SAM, in contrast with creating the SAM with a pre-synthesized molecule, can be advantageous since it requires fewer amounts of reagents and avoids complex synthesis processes [14]. A wide variety of strategies, covalent or noncovalent, has been applied for SAM surface modification. Amongst these strategies is "click" chemistry, which

provides selective and efficient chemical modification with low by-product formation and easy surface characterization [23].

The versatility of SAMs can be extended to the formation of low-density monolayers (Figure 2.1B) and mixed or multi-component SAMs, which comprises a well-defined mixture of molecular structures (Figure 2.1C). This latter methodology allows the creation of compositional gradients of functional groups and/or the incorporation of molecular species which, on their own, would not form a SAM due to its physical dimensions [24]. Another possible strategy is the use of orthogonal self-assembly in a multi-component surface material (*e.g.* surface comprising gold and silica regions) (Figure 2.1D). In this scenario, molecular structures with different affinities to the different substrates, lead to the formation of distinct SAMs in defined structured areas of the surface.

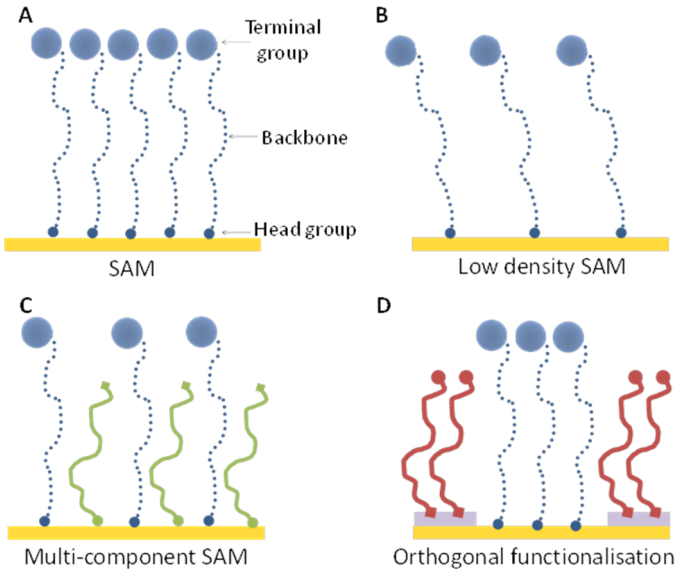

Figure 2.1 A) Cartoon representation of the molecular structure of a SAM and their representation B) in a low density SAM, C) multi-component SAM and D) when employed for orthogonal functionalization of a substrate exposing two different materials at its surface.

Layer-by-*layer (LBL) assembly* is another approach to develop ultrathin films. LBL allows for thin film formation on a broad range of topologies and surface materials by alternating its exposure to solutions containing chemical entities (e.g. polymers, proteins, lipids, nucleic acids and nanoparticles) of complementary affinities [25-27]. While electrostatic interactions are widely explored to prepare the multilayer assemblies, other molecular interactions, such as charge-transfer and host-guest interactions, covalent and hydrogen bonding, are also used to grow LBL films. The stability and robustness of the molecularly layered films are affected by the strength of such interactions. The LBL cyclical process can be achieved mainly *via* five assembly approaches, such as immersive, spin, spray, electromagnetic, and fluidic assembly [25] (Figure 2.2). They differ in terms of their ease of use, time and equipment required, material consumption and suitability of the substrate in terms of its size or shape. The assembly process selected strongly influences the physicochemical properties of the multilayer assemblies, in particular layer stratification and density, packing order, thickness and roughness. For instance, spin assembly generates more thin, organized and stratified films than immersive assembly, but its use is limited to small planar substrates. Spray assembly produces similar film characteristics to spin assembly, but with the added advantage of allowing faster LBL formation and coating of large and nonplanar substrates. Electromagnetic assembly, which uses either electric or magnetic fields, facilitates the formation of thick and densely packed films, whilst fluidic assembly allows formation of thin films on surfaces not easily accessible to other assembly approaches, such as inside capillaries. These two more recent approaches – electromagnetic assembly and fluidic assembly – involve specialized equipment and expertise.

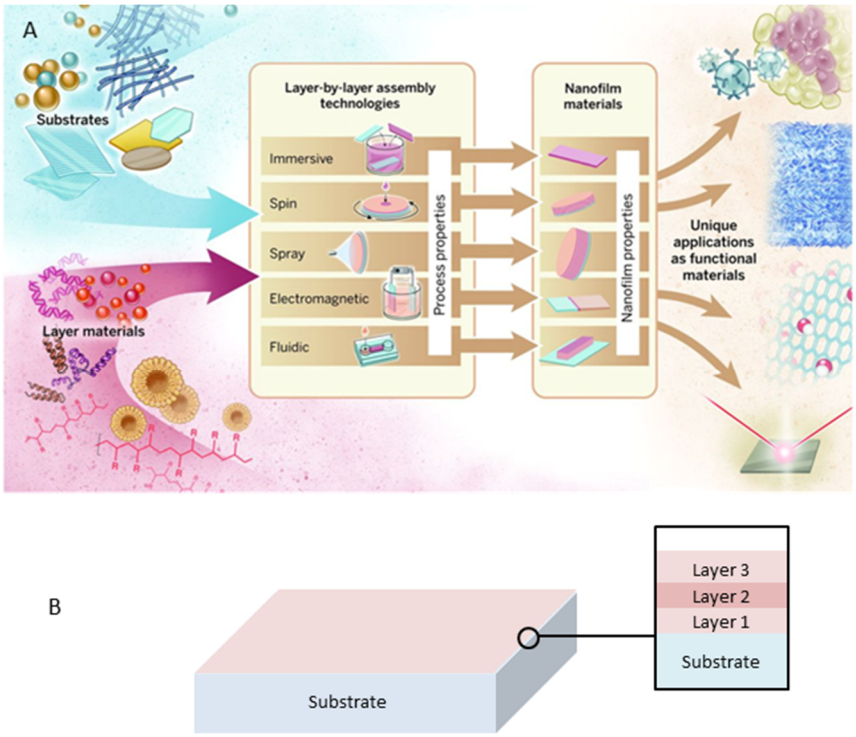

Figure 2.2 A) Layer-by-layer assembly of thin films using different assembly approaches. From [25]. Reprinted with permission from AAAS. B) Schematic representation of multilayer nanofilm created by Layer-by-layer assembly.

2.1.2 Lithographic Techniques

Novel lithographic methods for the fabrication of nanostructured surfaces are continuously being developed, aiming for cost reduction, smaller feature size or improved flexibility in terms of substrate or function. Herein, we focus the discussion on the lithographic methods that have been associated with the development of stimuli-responsive nanostructured surfaces (Figure 2.3). Currently a number of methodologies are available for generating nanoscale features on material surfaces by using conventional lithographic techniques, such as photolithography and electron-beam (e-beam) lithography. Photolithography uses light and a photomask to generate a pattern of photosensitive resist layer deposited on a surface material that in turn is used to control the spatial distribution of other materials. In the e-beam lithography, an electron beam source is used instead of

light to generate nanopatterns. Even though these lithographic techniques have proven to be useful in patterning a variety of materials, their use is restricted due to the high cost of equipment and non-applicability to a variety of substrate topologies and materials to be patterned (*e.g.* biological entities). These limitations have motivated the development of alternative lithographic techniques.

Soft-lithography, which involves a patterned elastomer as a mold, stamp, or mask to generate or transfer patterns with nanometer resolution, meets some of these needs, since it is considered a simple and low-cost patterning technology with high versatility [28]. Microcontact printing (μCP) is a form of soft lithography wherein a microstructured elastomer stamp is coated with a solution that contains the chemical species to be patterned, and applied to a substrate of choice to create a microstructured surface [29]. Microcontact printing has been extended to nanoscale dimensions, a process also known as nanocontact printing (nCP) [30]. This technique allows the patterning of various chemical species over macroscopic areas.

Interferometric lithography (IL) is another technique that allows the fabrication of large-area, nanometer-scale patterned surfaces [31]. IL involves the maskless exposure of a photoresist layer with two or more coherent light beams, leading to the production of periodic and quasi-periodic nanostructures. IL is a facile and inexpensive lithography technique but has a major limitation in the restriction of the classes of patterns that can be produced.

Block copolymer micelle lithography (BCML) is another technique that provides large area nanopatterning capability at low cost [32,33]. BCML encompasses the use of amphiphilic block copolymer micelles, which in a non-polar solvent form a hydrophilic core and a hydrophobic shell. By incorporating salt precursors for the synthesis of nanoparticles into the micellar core, periodically ordered nanoparticles with even size distribution can be

produced on surfaces. The micelles are able to self-assemble into a hexagonally, close packed configuration on the substrate surface, which upon nanoparticle formation can be removed by exposing the surface to hydrogen, oxygen or argon plasma treatment. Interparticle spacing can be tuned by varying the molecular weight of the block copolymers.

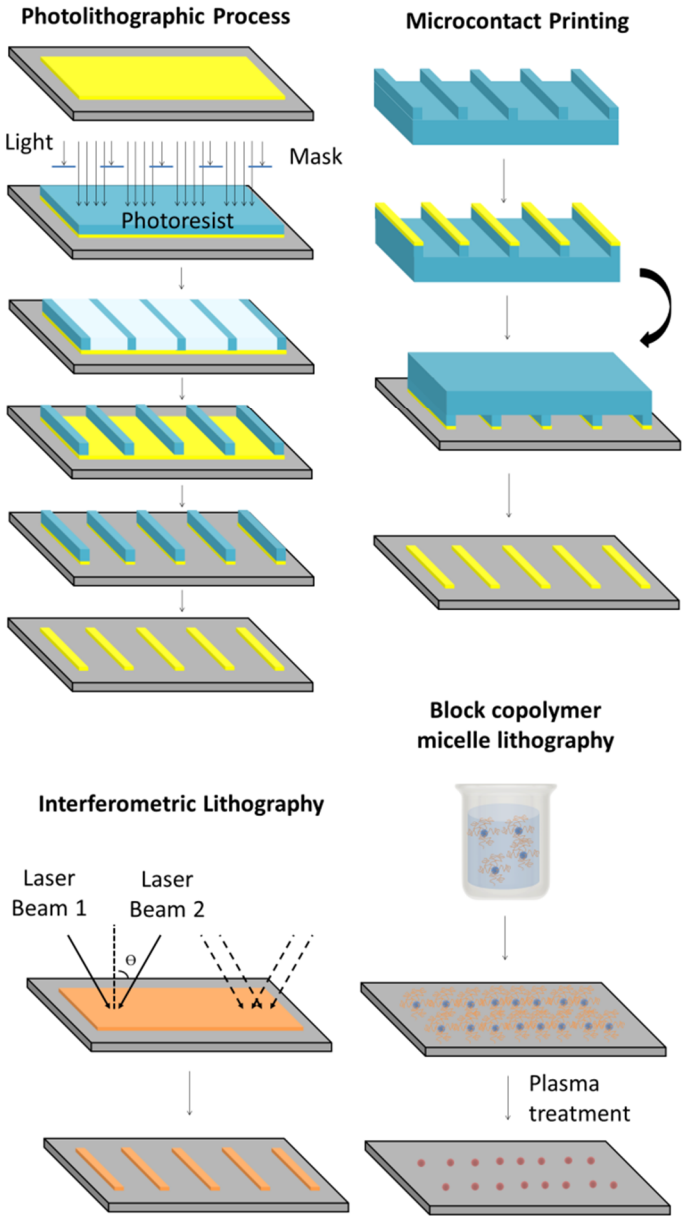

Figure 2.3 Scheme representing the main lithographic techniques used to create stimuli-responsive nanostructured surfaces.

2.2 Electrically-driven Nanostructured Responsive Surfaces

Most of the electrically-driven surfaces developed for biomedical applications are based on SAMs which incorporate redox active systems or charged groups that induce a change in the surface properties when electrical potentials are applied to the conductive substrate [12,13,34]. Electroactive end groups (e.g. nitro and hydroquinone moieties) within SAMs have been shown to undergo oxidation or reduction upon application of an electrical potential and be responsible for control over the immobilisation of different biological entities, including peptides [35-40], DNA [41-43], proteins [44] and cells [35-39] on surfaces. An approach developed by us [44] applied the capability of nitro (NO_2) moieties to be electrochemically reduced to amino (NH_2) groups to selectively immobilize proteins on certain regions of a surface. In other studies, redox active hydroquinone groups have been exploited for controlling, in real time, the immobilisation of ligands, proteins or cells on a surface [35-40]. These studies have begun to address the need for more sophisticated surfaces to understand and control cell behaviour.

The highly complex process that commands cell interaction with the extracellular environment in a tissue is still not completely understood and this topic has been a major subject of interest in biology. Efforts have been made to develop synthetic extracellular matrices (ECMs) that more closely mimic tissue microenvironments as they can be powerful tools for fundamental studies on cell behaviour [45]. Successful design and fabrication of dynamic platforms with precise control of physical microenvironments can provide fundamental knowledge on cellular behaviour (e.g. adhesion, migration, growth, differentiation) and open new routes for tissue engineering and regenerative medicine. In addition, studies on cellular behaviour in tumour microenvironments are of major importance for the development of cancer treatment.

In order to realize such dynamic control, electroactive functionalized surfaces based on the hydroquinone–quinone redox couple have been developed to regulate arginylglycylaspartic acid (RGD) immobilisation and promote cell attachment or detachment [36]. RGD is the most studied ECM ligand and is known to play a key role in integrin-mediated adhesion. Conversion of a hydroquinone monolayer to the corresponding reactive quinone is obtained upon a mild electrochemical pulse that is compatible with and non-invasive to the cell. In response to an applied electrical stimulus, precise densities of RGD peptides can be selectively attached to or released from the surface, therefore allowing controlled selective adhesion or release of cells. A related strategy was used to design substrates with two distinct electroactive groups, quinone ester and O-silyl hydroquinone, for selective release of cells adhered to RGD ligands [37]. One of the electroactive groups would respond to positive potentials while the other would respond to negative potentials.

Yousaf and co-workers [46] have also taken advantage of the hydroquinone–quinone redox couple for conducting real-time cell mobility studies. The gold surface was patterned by microcontact printing and cells were confined to precisely defined areas functionalized with fibronectin (an ECM protein known to play a key role in cell adhesion, growth, migration and differentiation) and fibroblasts. Rapid and highly selective immobilisation of RGD peptides onto the SAM was performed *via* activation of the quinones by applying an oxidative potential to the monolayer. The density of the immobilized peptide was characterized *in situ* by cyclic voltammetry. The switch from an inert to an adhesive surface (with RGD ligands) was monitored in real time and initiated cell migration, demonstrating communication between the cell integrin receptors and the RGD ligands. This dynamic surface was used for studies comprising the role of cell population, pattern shape, integrin

composition and memory mechanisms on cell migration and a novel behaviour of cell migration memory was detected.

Electrochemical active coatings based on thiol chemistry have also been used for cell manipulation. By taking advantage of the fact that thiol SAMs can be detached from gold surfaces via electrochemical reduction, alkanethiol SAMs with covalently bound RGD peptides have been employed to promote cell attachment and then release by the application of a negative electrical potential. This strategy was used for obtaining two-dimensional (2D) cell sheets and for harvesting spheroids formed on microcontact printed structures [47]. Following the same principle, detachment of single cells from microarrayed indium tin oxide (ITO) electrodes (fabricated via photolithography) was achieved by electrochemical desorption of alkanethiol SAMs [48] (Figure 2.4).

Electrically-switchable surfaces have also been designed and created to respond to electrical potentials with altered conformations and therefore exhibiting different, reversible, surface properties. In 2003, Langer and co-workers demonstrated the reversible switch of a carboxylic acid-terminated alkyl ((16-mercapto)hexadecanoic acid -MHA) SAM from hydrophilic to hydrophobic in response to an applied electric field [49]. The MHA SAM underwent conformational changes upon attraction of the carboxylic acid charged end group to the substrate surface by an applied electric field. In order to achieve conformational changes between i) straight chains with carboxylate anions exposed at the surface (hydrophilic) and ii) bent chains with alkyl chains exposed at the surface, a low packing density monolayer was created. This was achieved by creating a SAM derivative of MHA with a bulky, globular end group ((2-chlorophenyl)diphenylmethyl ester), which was subsequently cleaved to produce the less densely packed layer.

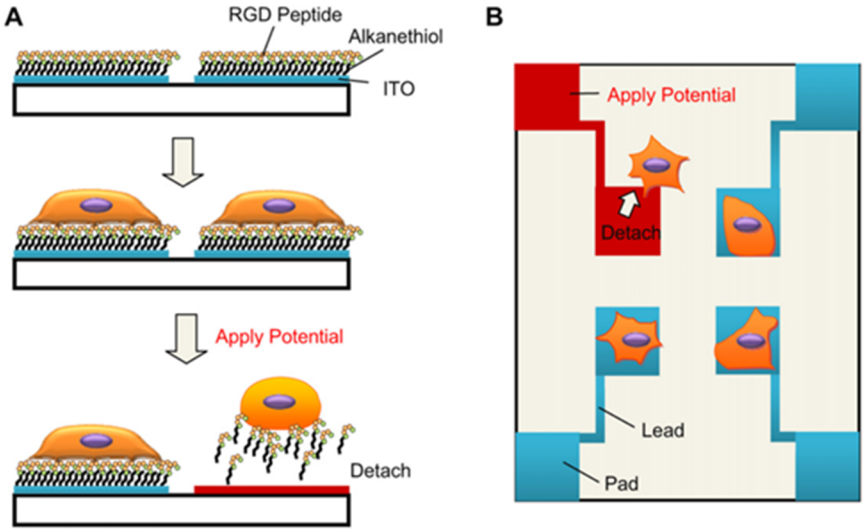

Figure 2.4 Scheme representing micropatterned surface for controlling cell detachment. A) Cross-sectional view of the ITO electrodes functionalized with RGD peptide, showing cell detachment from one of the electrodes upon applying a negative potential. B) Top view of the ITO electrodes, showing contact pads for potentiostat connection. Adapted from [48], with permission from Elsevier.

An alternative method for preparing loosely packed carboxylic acid-terminated and amino-terminated alkyl monolayers was later reported [50,51], which made use of a pre-formed inclusion complex – a cyclodextrin (CD)-wrapped alkanethiolate – to create SAMs on gold. By releasing the CD space-filling group from the anchored pseudorotaxane, SAMs with a low packing density were formed that were shown to undergo conformational changes and control the adsorption of proteins under an applied electrical potential.

Following a different approach, we devised a well-defined two-component SAM of 11-mercaptoundecanoic-acid (MUA) and mercaptoethanol (MET) on gold that could expose either negatively charged or hydrophobic moieties in response to an applied electrical potential [52]. The spacer component – MET - was incorporated into the monolayer to prevent non-specific binding and ensure sufficient spatial freedom for synergistic molecular reorientation of the surface-bound MUA. These switchable surfaces were able to control the early stages of bacterial cell adhesion by switching between an attractive and a

repellent state, followed in real time by electrochemical SPR. This dynamic surface platform can be a valuable tool in medical diagnosis and for understanding fouling mechanisms.

Apart from controlling non-specific interactions, electrically switchable surfaces have also been developed to control specific biomolecular interactions. For instance, we have constructed [53] an electro-switchable surface based on the response of a charged molecular backbone on the structure of a mixed SAM that dramatically altered the binding activity of a ligand (biotin) to a protein (neutravidin). The switchable mixed SAM comprised two molecular components: (i) a positively charged 4-mer of lysine (K) that was functionalized at one end with the bioactive moiety biotin that recognizes the neutravidin protein, and at the other end with a cysteine (C) for gold surface binding (biotin-4KC), and (ii) an ethylene glycol-terminated thiol (*i.e.* (3-mercaptopropyl)tri(ethylene glycol) - TEGT) that acts as spacer for the biotin-4KC peptides and also prevents non-specific binding. Upon application of a positive potential (+0.3 V), high neutravidin protein binding was detected, while the application of a negative potential (–0.4V) resulted in minimal protein binding. Open circuit (OC) conditions afforded intermediated protein binding capability. The bio-inactive state induced more than 90% reduction in protein binding. The biomolecular interactions were controlled by conformational changes between fully extended (ON state) and collapsed (OFF state) oligopeptide conformer structures. In the fully extended conformation, the biotin linked to the oligopeptide is largely free from steric factors allowing it to efficiently bind to the neutravidin from solution. By contrast, under a collapsed conformation, the ligand presented at the surface is partially embedded in the second component of the mixed SAM, and thus sterically shielded and inaccessible for neutravidin binding. This switching mechanism was later employed to modulate cell adhesion (Figure 2.5A) [54]. In this case, application of an electrical potential induced small

changes in the conformation/orientation of the RGD peptide on the surface, modulating the availability of cell surface receptors.

Instead of changing the conformation of the RGD peptide, Gooding and co-workers [55] used neighbour molecules with terminated charged groups to control the RGD accessibility to the cells (Figure 2.5B). The SAMs formed on silicon contained two components: i) an ethylene glycol chain with either a sulfonate (anionic) distal moiety or an ammonium (cationic) distal moiety and ii) a RGD peptide. By applying a potential of the same polarity as the charged moiety, the ethylene glycol molecules stretched out from the surface and concealed the RGD peptides from the cells, preventing cell adhesion. On the other hand, an applied potential of opposite polarity induced the ethylene glycol molecules to bend towards the surface, exposing the RGD peptides and promoting cell adhesion.

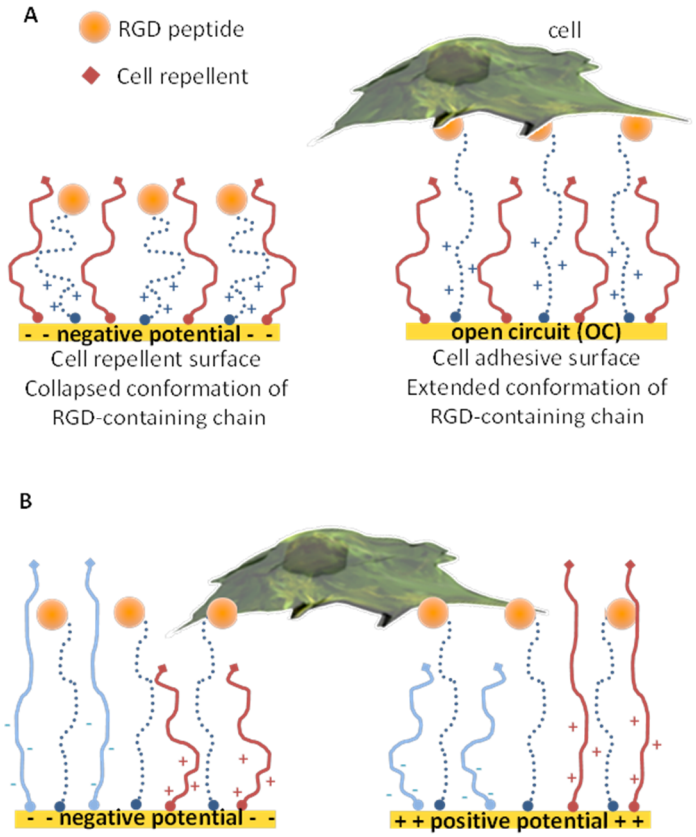

Figure 2.5 Scheme illustrating two different approaches, using either A) a charged backbone [54] or B) charged neighbour molecules, to electrically control the exposure and concealment of RGD, and thus promote or inhibit cell adhesion [55].

Electrically responsive surfaces that take advantage of the negative electrical charges exhibited in DNA molecules for inducing conformational changes have also been developed [56]. DNA-based SAMs have been demonstrated to be a suitable molecular platform for cell culture, with cell adhesion modulation being dependent on the DNA orientation on gold [57]. These molecules exhibit distinct mechanical properties when in single or double strand forms, being extremely flexible in single form and exhibiting a rigid duplex conformation. DNA nanodevices are based on this principle, going from an OFF state (single random coil conformation) to an activated ON state (rigid double strand conformation) when exposed to complementary DNA, and a variety of them have been designed for biomedical applications [11]. The next generation of smart DNA nanodevices is envisioned to incorporate custom-designed host immune responses [58].

Electro-active polymer films have also been explored for biomedical applications, namely tissue engineering, drug delivery and biosensing. Electrically responsive polymers are a class of polymers with conductive behaviour, which is tunable via doping processes. The most widely studied electro-active polymers are aromatic polymers and include polypyrrole (PPy), polyaniline (PANI), polythiophene (PTh) and its derivatives such as poly(3,4-ethylenedioxythiophene) (PEDOT). These polymers present a unique ability to intrinsically transfer electrical signals to cells [59] and their efficacy in stimulating a multitude of cellular functions, such as cell proliferation and differentiation, has been reported [12,60,61]. However, their inherent inability to degrade is a limiting factor. Attempts to improve their biodegradability have been made, namely by coupling electrically responsive polymers with biodegradable polymers [61]. Furthermore, their biocompatibility has also been improved through the incorporation of cell-adhesive peptides [62] or other ECM-derived biomolecules [63].

Electro-responsive polymers have been key components in the development of systems with controlled release capabilities. An example of a system for precise release of chemical entities on demand includes a thin film on a gold substrate that was formed by immersive LBL assembly [64] (Figure 2.6). The film comprised four components: (i) complementary DNA (cDNA), (ii) poly(β-amino ester), to help cDNA release from the film, (iii) conductive polymers (PEDOT:PSS) and (iv) reduced graphene oxide. The multilayer film had a thickness of 25 nm and showed a quick response to reductive potentials. This responsive platform allowed controlled release of complementary DNA and therefore controlled activation of a DNA nanodevice (Figure 2.6B).

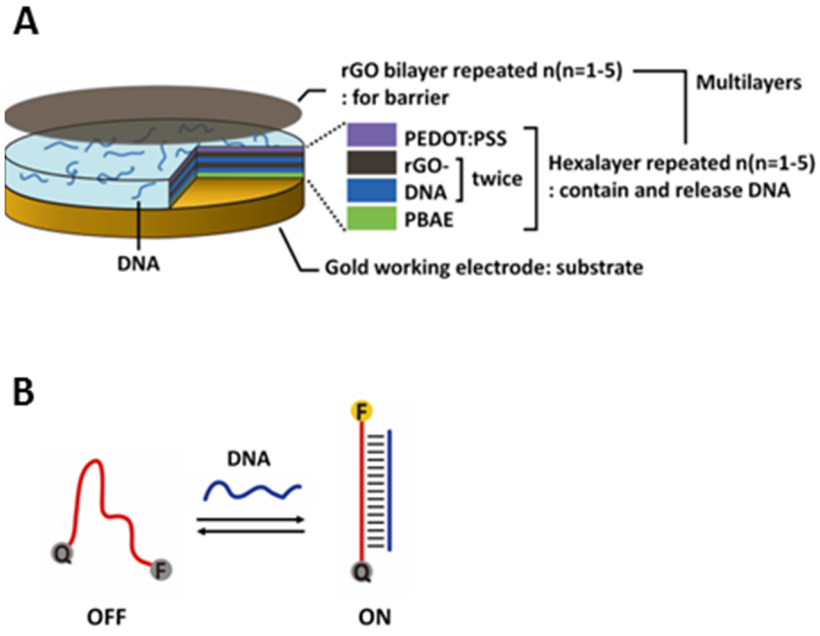

Figure 2.6 A) Schematic illustration of a multilayer film on a gold electrode. B) Schematic diagram of a DNA nanodevice, where the OFF state reversibly changes to the ON state in the presence of complementary DNA, resulting in the generation of fluorescence (F representing a fluorophore and Q representing a quencher). From [64]. Adapted with permission from Wiley-VCH.

A novel approach for membrane biofouling release has been proposed based on a redox-responsive supramolecular polymer system [65]. A PTFE membrane was prepared

using a cross-linked polymer structure incorporating the *β*-cyclodextrin (*β*-CD) and ferrocene (Fc) complex, which can then be dissociated by electrical stimulation. After promotion of protein adsorption, the modified membrane is cleaned by the electrically induced dissociation of the Fc-*β*-CD inclusion complex. Moreover, the membrane can possibly be regenerated by re-formation of the Fc-*β*-CD complex into the PTFE membrane.

The combination of responsive polymers with molecular imprinting technique, a versatile technique for incorporation of molecular recognition sites, is another possible approach for developing responsive surfaces for biomedical applications [66]. The strategy of using molecular imprinted polymers (MIPs) in biosensors replaces the conventional immobilisation of biomolecular probes by molecular recognition sites [67]. A molecularly imprinted glutamate-doped-polypyrrole polymer film was electrochemically deposited on a conductive surface, attracting or repelling glutamate molecules from the liquid surface in response to an applied voltage [68]. The neurotransmitter glutamate is known to play a central role in cell metabolism and function and some responsive surfaces have emerged that are able to regulate interactions with this biomolecule. Another glutamate-MIP-based surface demonstrated selective binding of glutamate in the absence of an applied electrical potential and then glutamate release under low negative potential [69].

Recent studies have been also focused on the development of three–dimensional (3D) electro-responsive scaffolds in order to increase drug loading for on-demand delivery and more closely recreate the *in vivo* cellular environment. With this proviso in mind, Gourdon and co-workers [70] created 3D macroporous architectures using PEDOT doped with poly(styrenesulfonate) (PSS) for precise control over ECM protein (i.e. fibronectin) conformation. The 3D scaffolds were fabricated *via* ice-templating, which is based on ice crystal nucleation and growth along a temperature gradient to yield a porous structure

when the crystals are removed from the solute [71]. The macroporous architecture exhibited low impedance and tunable electrochemical properties by changing its redox state. Cell studies were performed and distinct secretion levels of vascular endothelial growth factor were observed in reduced and oxidised scaffolds, enhancing the trend previously observed in 2D polymer systems. This platform can be useful not only for tissue engineering and regenerative medicine but also for its inclusion in bioelectronics systems.

In addition to ice templating, another method for the fabrication of 3D structures based on crystals is the colloidal crystal template method. This method uses close-packed colloid crystal spheres as templates for the fabrication of 3D structured materials with ordered pores ranging from the nano- and microscopic to the macroscopic level [72]. Electrically-responsive macroporous PPy inverse opal thin films have been devised that allowed higher electrical responsiveness and superior drug release than non-porous PPy films [73]. The active release of corticosteroid hormone, incorporated in the polymer, was electrically triggered and occurred due to a change in volume caused by the movement of ions into and out of the polymer.

Electro-responsive 3D structures have also been constructed with nanoscale pore size. Kon and co-workers employed anodized aluminum oxide (AAO) membranes, which exhibit high density arrays of uniform and parallel nanopores, coated with conductive polymers for on demand electrically actuatable pulsative drug release [74]. PPy doped with the dodecylbenzenesulfonate anions (PPy/DBS) was electropolymerized onto the top and upper side wall of the AAO membrane. The pore size of the membrane changed with the electrochemical state as a result of a volume change, being therefore actuatable by electrical signal (Figure 2.7).

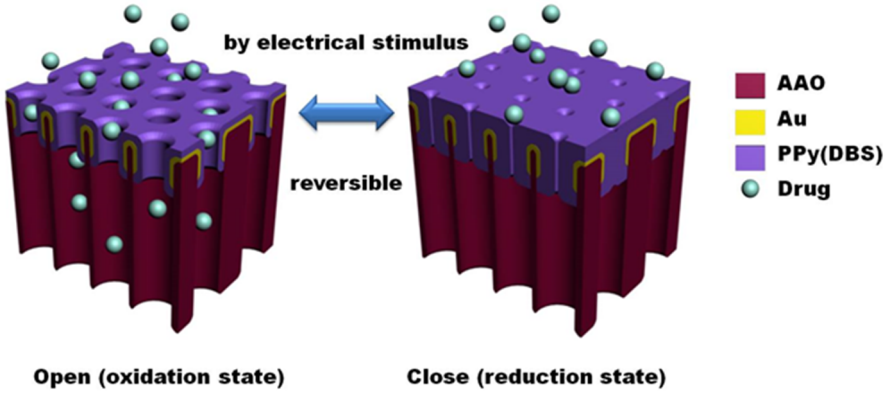

Figure 2.7 Schematic representation of reversible change of pore size and drug release rate in an electrically-responsive nanoporous membrane. Reprinted with permission from [74]. Copyright 2016 American Chemical Society.

2.3 Photo-driven Nanostructured Responsive Surfaces

The abundance of light and its minimal invasiveness make it a stimulus of interest for biological applications [75]. Photocleavage, photo-triggered reversible isomerization and ring opening/closing reactions are useful photoreactions that have been exploited to change surface properties. However, some limitations such as slow reaction kinetics, low photochemical efficiency and the need for UV-light (which can induce severe cell and tissue damage) still need to be overcome [76]. A key consideration and major challenge when developing photo-responsive surfaces for biomedical applications is obtaining a quick response to benign wavelengths and low intensities of irradiated light, the so called "biologically friendly window" [77].

The incorporation of functional molecules into SAMs that can be cleaved on demand upon light irradiation, e.g. nitrobenzyl groups, has been widely exploited for the immobilisation and release of bioactive molecules, such as proteins and cells [76-78]. Recently, a more generalized nitrobenzyl linker was synthesized for patterning a wide variety of

bioactive molecules *via* click-chemistry to also enable the controlled release of proteins upon photo-cleavage [76] (Figure 2.8).

A method for analysing the impact of cellular micro- and nano-environments on collective cell migration based on a photoactivatable and well-defined nanopatterned substrate has been recently developed [79]. In this approach, ECM ligands (RGD peptide) were exposed to cells when photocleavable polyethylene glycol (PEG) containing 2-nitrobenzyl ester was released upon light irradiation. Gold nanoparticles (10 nm) were arrayed on a glass substrate in a well-defined quasi-hexagonal geometry, using block copolymer micelle nanolithography, and functionalized with photocleavable PEG and a cyclic RGD ligand. The surrounding glass was passivated with PEG-silanes for minimizing non-specific interactions. Cells were confined within defined micro-regions, where the exposure to RGD was precisely tuned. Due to its small size comparing to PEG, the cyclic RGD ligand only became accessible when PEG was photocleaved. This study demonstrated the loss of collective migration characteristics in HeLa cells migrating on nanopatterned surfaces and highlights the importance of the contribution of cell-ECM interactions on the regulation of migration collectivity.

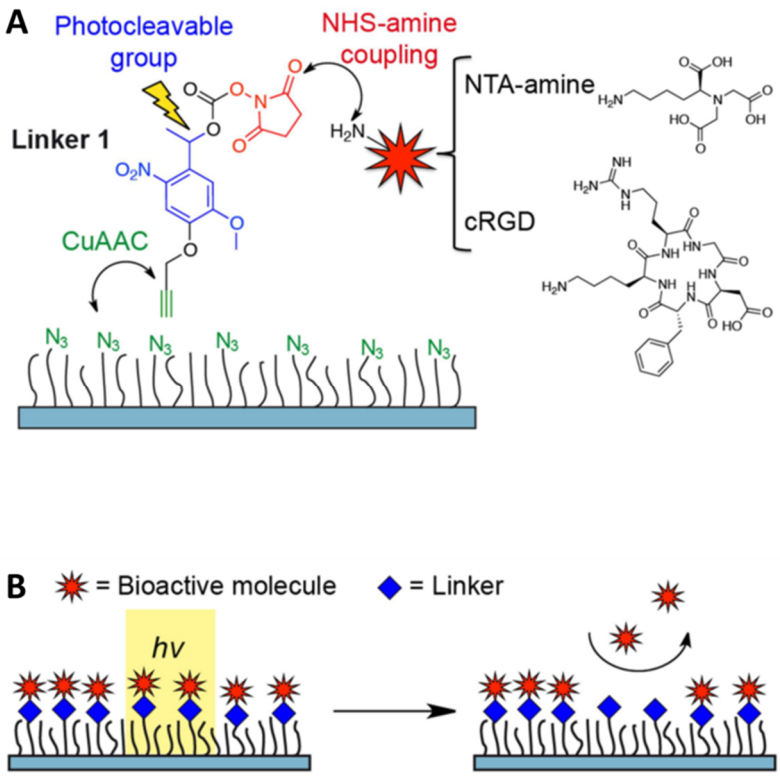

Figure 2.8 A) Schematic representation of a photo-responsive surface, showing an azide-terminated SAM that allows covalent immobilisation, via click chemistry, of a linker containing a photocleavable nitrobenzyl group and additional immobilisation of a bioactive molecule exhibiting an amide group. B) Schematic representation of selective detachment of bioactive molecules by localized exposure to light. Adapted from [76] with permission from Nature.

Cell adhesion properties can also be changed by photodriven motions involving *cis-trans* isomerization of the azobenzene. The azobenzene molecular dimensions, which are decreased by approximately 3.4 Å upon isomerization from the *trans* to *cis* conformation, have been shown to change the orientation of attached RGD peptides and its distance to the substrate[80,81]. In a recent study, mixed monolayers of PEG and azobenzene derivatized with an RGD-containing peptide were formed on glass and used for cell adhesion switching, triggered by UV irradiation [82] (Figure 2.9). In contrast with previous studies, this reported photo-switchable SAM system allowed control over cell adhesion using significant shorter UV irradiation times of only a few tens of seconds.

A similar case using light triggered transitions between *trans* and *cis* configurations of an azobenzene for controlled cell adhesion with reversible regeneration, was based on SAMs formed on quartz substrates containing *a*-cyclodextrin (α-CD)-terminated alkanesilane complexed with azobenzene-GRGDS. It is well known that the host-guest interaction between azobenzene and *a*-CD or *β*-CD can be controlled through the photoisomerization of azobenzene. In this study, this principle was applied to promote cell detachment by irradiation of azobenzene that led to the breaking of the supramolecular complex and subsequent release of the cells [83] (Figure 2.10).

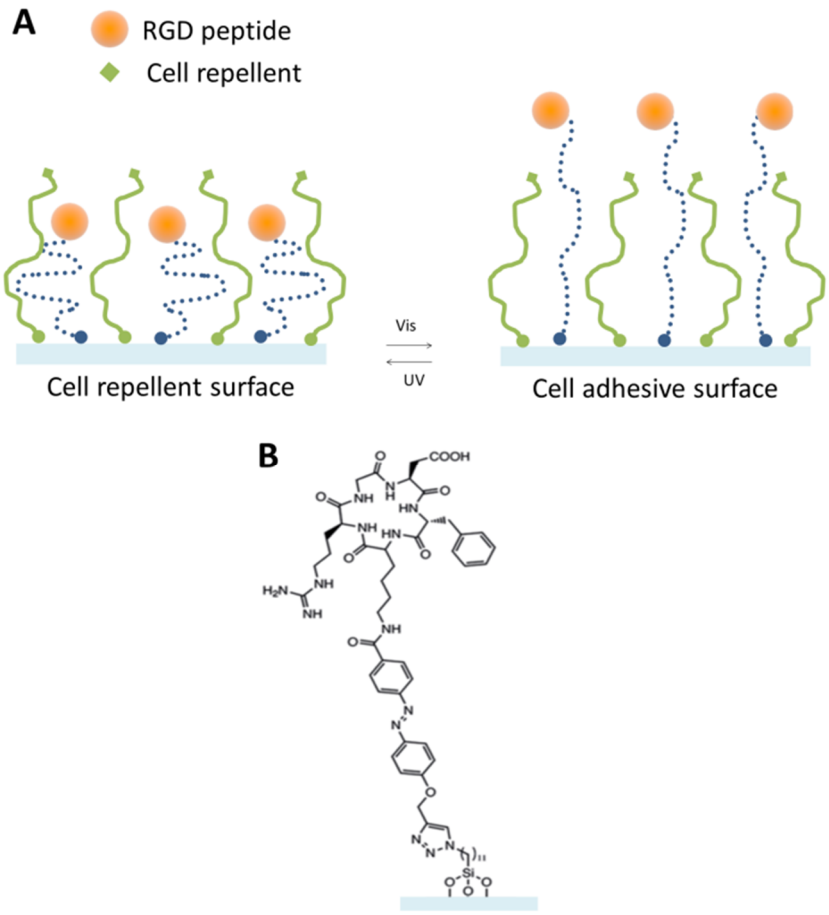

Figure 2.9 A) Schematic representation of photo-responsive surface formed of mixed monolayers of PEG and c(RGDfK)-azobenzene [82]. B) Structure of c(RGDfK)-azobenzene immobilized on glass substrate.

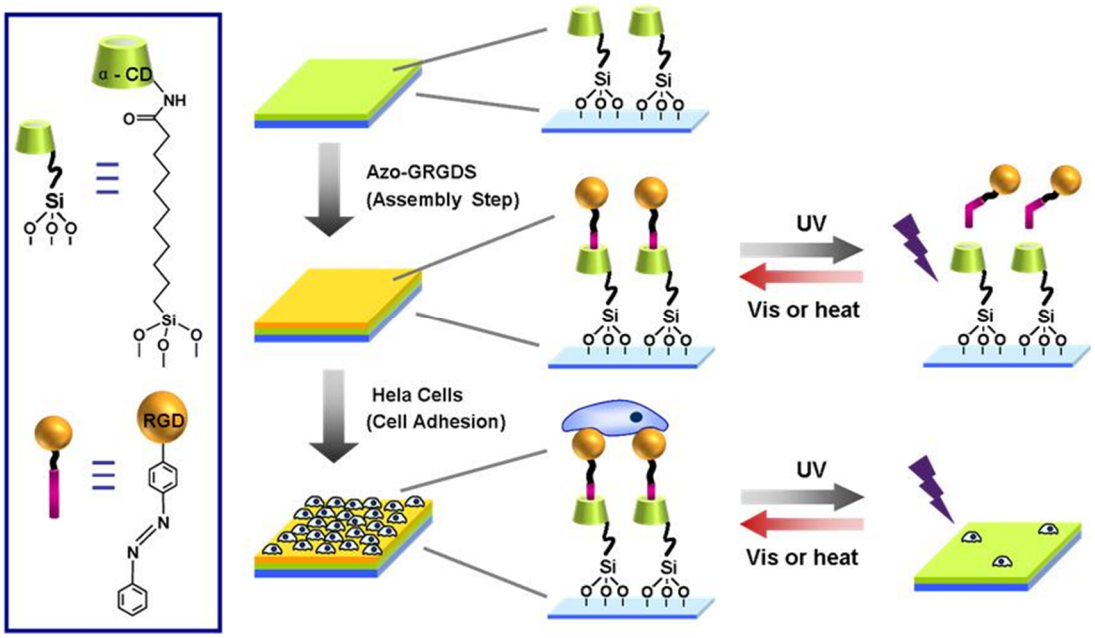

Figure 2.10 Schematic representation of a reversible light-responsive surface, which employs host-guest chemistry to promote the release of cells. Hela cells cultured on the substrate are detached when trans-azobenzene is transformed to cis-azobenzene upon UV irradiation. Reprinted with permission from [83]. Copyright 2016 American Chemical Society.

Another example combining host-guest chemistry and light induced isomerization of azobenzene units was reported which demonstrated the capture and release of functional guest species, i.e. copper phthalocyanine [84]. In this case, host-guest chemistry was combined with surface-confined synthesis of photosensitive covalent frameworks (COF) based on the polycondensation of diboronic acid (ABBA) to create single-layer photo-responsive surfaces (Figure 2.11). Upon UV irradiation, the guest molecules are released and the photo-responsive surfaces can then be recovered by annealing.

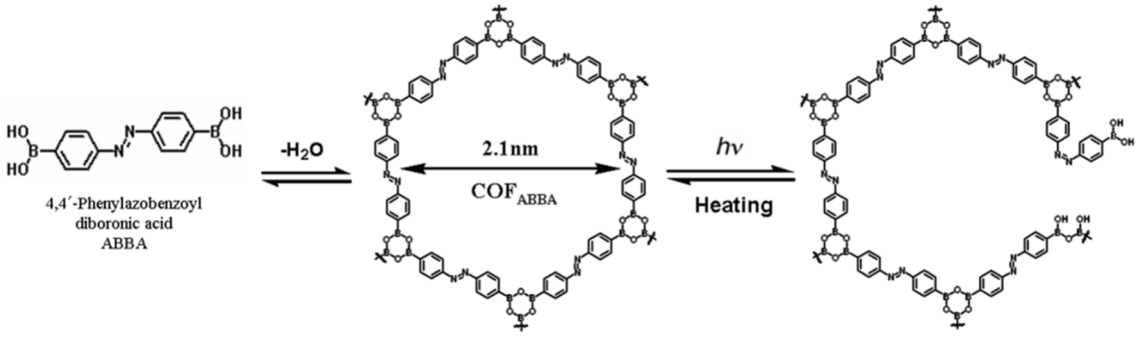

Figure 2.11 Schematic representation of reversible photo-isomerization of covalent frameworks (COF), based on polycondensation of diboronic acid (ABBA). From [84]. Reprinted with permission from Wiley-VCH.

Photo-switchable surfaces with the ability to release other molecules, such as cytotoxic reactive oxygen species (ROS), have also been developed for the regulation of cell apoptosis [85] and inhibition of bacterial growth [86,87]. These surfaces can be constructed using polymers containing photosensitizers, such as porphyrins [88,89]. In this context, a photodynamic surface based on porphyrin-layered double hydroxide (LDH)-polyurethane composites has been shown to exhibit photo-stability and photo-bactericidal properties [89]. The LDH host (in this case, Zn_2Al) was able to prevent the aggregation of porphyrins and improve the structural stability of the guest (in this case, the (Pd(II)-5,10,15,20-tetrakis(4-carboxyphenyl) porphyrin (PdTPPC) photosensitizer) as well as increase the resistance of PdTPPC to light degradation (photobleaching). The films were analysed by Attenuated Total Reflectance - Fourier Transform Infrared Spectroscopy (ATR-FTIR) after light-triggered oxygen production and no damage was observed.

Photo-responsive polymers are also providing new opportunities for manipulating cells on surfaces. Azobenzene, spiropyran and nitrobenzyl groups are light sensitive chromophores commonly incorporated in photo-responsive polymers [90]. Light-triggered manipulation of RGD exposure has been achieved using azobenzene moieties incorporated into polyelectrolyte layers. A variety of surfaces with different thickness and stiffness were

fabricated for the identification of the best conditions for cell culture [91]. Azobenzene-containing polymers based on a flexible polysiloxane matrix have also been used for developing photoactive surfaces that can be finely tuned through optical excitation for cell growth and cellular behaviour studies [92].

New biocompatible polymers that incorporate photo-switching molecules are emerging for surface nanopatterning and for controlling surface topography. Surface topography is known to play an important role in cellular responses. Nanoridge/groove structures were built into a thin film of a polymer containing bio-azobenzene using a single beam laser. Using this technique, the pattern was easily prepared, erased and re-written. The adhesion and growth of PC12 cells to these submicron patterns was then investigated and it was shown that the topographies provided directional cues to guide cell alignment and orientation [93].

Near-infrared (NIR)-responsive nanocomposites, embedded with light absorbing nanoparticles, are emerging as an alternative to UV-responsive polymers with promising applications in biomaterials. An advantage of NIR light over UV-Vis is that NIR light is highly transmissive to tissue without damaging it [94] whilst not inducing photomodification of biomolecules. An actuator with a soft photo-responsive bilayer structure has been developed, where one layer was formed of pristine polydimethylsiloxane (PDMS) and the other incorporated both PDMS and graphene-nanoplatelets. This actuator exhibited controllable and reversible mechanical bending response to NIR light irradiation due to the temperature change attributed to the photothermal effect of graphene [95].

An alternative NIR-triggered system has been developed for non-invasive cell harvesting. This system was based on a nanoscale film of a conductive polymer, i.e. PEDOT, prepared by simple solution-casting polymerization. Stem cells were controllably detached from the surface upon NIR light exposure. The integrity of the detached cells was

then investigated by live/dead staining, proliferation and differentiation assays, western blot analysis and immunophenotyping, and it was shown that the cells preserved their intrinsic characteristics. The absorbance of NIR light is dependent on the doping state of the conductive polymer, which is controlled electrochemically, and the detachment is a result of the photothermal effect on the PEDOT film exposed area [94]. Controlled release of cells from surfaces is of major importance in biomedical research and there is a need for methods that allow controlled and non-invasive detachment of cells, preserving cellular integrity.

Another route has been proposed for NIR-triggered cell detachment based on nanoplasmonic surfaces. The plasmonic substrates were fabricated by BCML, leading to the formation of dense arrays of branched gold nanostructures (branch diameter being about 30 nm and interparticle distance below 10 nm), which were functionalized with thiolated c-RGD peptide. The detachment of cells occurred upon irradiation with a 980 nm NIR laser, mainly due to photo-thermal effects. Cell viability upon detachment with NIR laser was investigated by MTT assay (colorimetric assay for accessing cell metabolic activity) and it was shown that the well-known formation of small pores caused by NIR laser irradiation was not cytotoxic for cells, as they still maintained an active metabolism [96]. In a different approach, a surface was designed and fabricated for the transmission of spatio-temporally controlled mechanical forces into cells in response to NIR light exposure, again with no sign of cell viability damage. This system was based on a bilayer nanocomposite substrate, where the bottom layer consisted of a PNIPAM film covalently connected to uniformly distributed few-walled carbon nanotubes (FWCNTs) and the top layer of a PNIPAM film functionalized with collagen for cell seeding. Due to the presence of FWCNTs, which can absorb NIR light and convert it into localized heat, a mechano-

response of the thermo-responsive PNIPAM matrix is achieved when a point laser source is applied [97].

2.4 Thermo-driven Nanostructured Responsive Surfaces

Physisorbed self-assembled networks, SAMs and polymers have been harnessed for the creation of thermo-responsive surfaces. To gage the effects of reversible transitions in physisorbed multicomponent supramolecular networks, host-guest chemistry has been investigated for controlled guest release [98]. Hydrogen-bonded 1,3,5-tris(4-carboxyphenyl)benzene (BTB) supramolecular networks were adsorbed on a highly oriented pyrolytic graphite (HOPG) surface and a fast increase in temperature induced the switching between low and high density packing of the porous network. Reversible phase transformation occurred upon surface cooling. Release of the guest molecule, in this case nanographene (NG), was caused by compression of the host, BTB, network (Figure 2.12). The transition was also observed when an electrical field, instead of a thermal stimulus, was applied to the system.

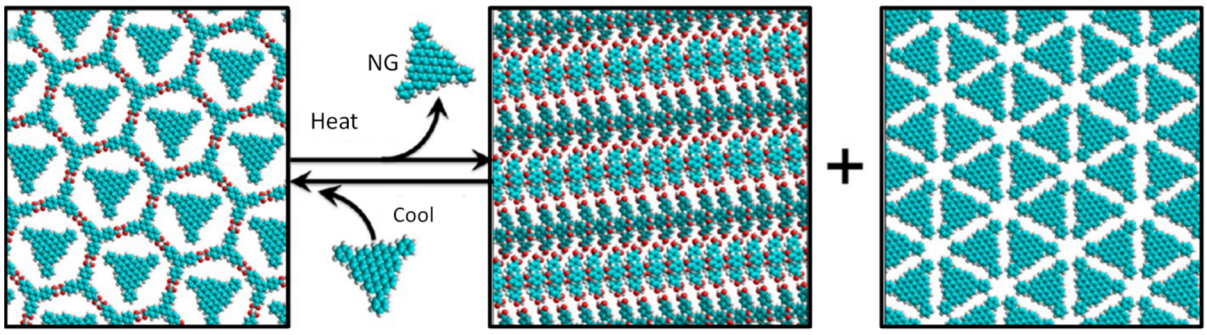

Figure 2.12 Schematic representation of reversible guest release in the BTB-NG host-guest system, triggered by a thermal stimulus. NG, the guest specie, is released when BTB switches from a compact (closed) structure to a low density (open) structure at the HOPG interface. Adapted with permission from [98]. Copyright 2016 American Chemical Society.

Temperature-responsive SAMs based on oligo ethylene glycol (OEG)-derivatives have been used for reversible wettability switch of a surface and furthermore for controlling the interaction between immobilized proteins and ligands [99]. However, the use of thermo-responsive polymers films, instead of physisorbed self-assembled networks or SAMs, has been a more popular choice for creating thermo-responsive surfaces. Thermo-responsive polymers exhibit a volume phase transition in response to temperature change and have been subject of extensive studies for biomedical applications, particularly for controlled drug delivery, gene delivery, antifouling, cell culture and tissue engineering [100,101]. Among the different thermo-responsive polymers, poly(N-isopropylacrylamide) (PNIPAM) is the most studied and it has been extensively exploited for controlled drug release and tissue engineering [102].

Formation of polymer brushes has been one of the routes chosen for coating substrates with thermo-responsive polymers. Polymer brushes are defined as long chain polymer molecules that are attached with one or with a few anchor sites to a surface. The tethering of polymer to the surface should be sufficiently dense in order to allow the polymer chains to adopt a stretched chain conformation, which significantly differs from the random-walk conformation of free polymer chains in solution, or in conventional solution casted polymer coatings. In more recent times, nanopatterned polymer brushes have emerged as powerful tools for biointerfaces engineering. By taking advantage of such developments, Lopez and co-workers [103] have reported temperature-responsive switchable surfaces for controlled display of immobilized biomolecules, based on nanopatterned PNIPAM brushes synthesized by the combination of surface initiated polymerization and UV interferometric lithography. Reversible conformational changes (swelling and collapse) of nanopatterned PNIPAM brush architectures triggered by a temperature change were shown to influence the adsorption of biomolecules. Active biomolecules attached to

polymer free confined areas, surrounded by the polymer brushes, were exposed and hidden in response to the hydration of the polymer brushes upon temperature change above and below the Lower Critical Solution Temperature (LCST), *i.e.* 32°C (Figure 2.13). The system was demonstrated for the biotin-streptavidin system. Controlled detachment of fibroblast cells from the same dynamic surface was also demonstrated, with further studies showing detachment of endothelial cells in mild conditions [104]. Polymer free areas were functionalized with fibronectin for enhancing cellular attachment. This strategy overcame the barrier of critical PNIPAM thickness reported in previous studies when using unpatterned PNIPAM films for cells harvesting. In a different approach, the use of terminal carboxylation of PNIPAM brushes was previously reported as a solution for this thickness limitation [105]. In fact, Okano and coworkers reported the use of PNIPAM for cultured cells recovery for the first time more than 20 years ago [106].

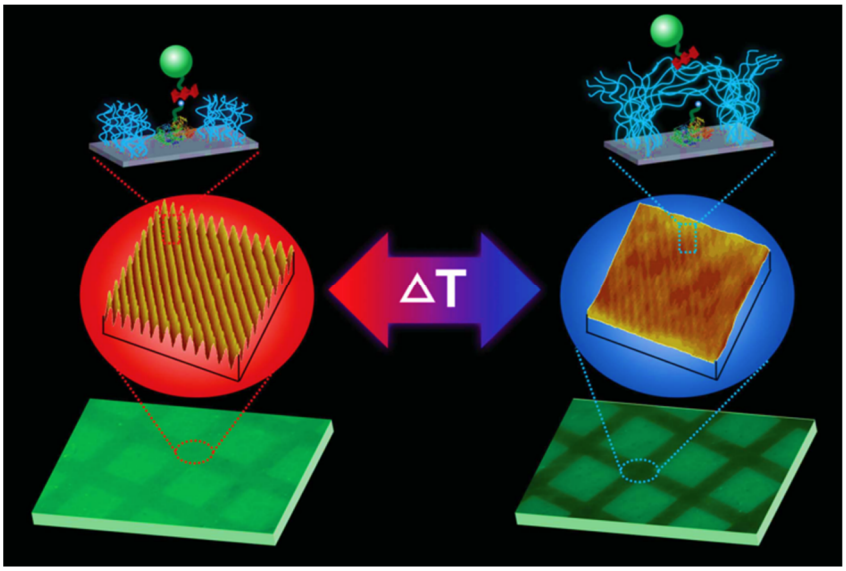

Figure 2.13 Illustration of a nanopatterned PNIPAM surface, which switches from a state where a biomolecule attached to the surface is exposed to a state where the biomolecule is hidden. It occurs due to changes in temperature that induces conformational changes of the PNIPAM brushes. Reproduced from [103] with permission of The Royal Society of Chemistry.

The harvesting of cell sheets has been also accomplished using molecular imprinting with thermo-responsive specific recognition sites. Using L-arginylglycyl-L-α-aspartyl-L-serine (RGDS) peptide as the selected active biomolecule, specific recognition sites for this peptide were molecularly imprinted on PNIPAM by redox-initiated polymerization. The non-covalent RGDS peptide system demonstrated efficacy for both cell adhesion and cell detachment upon temperature change [107]. Cell capture and release has also been demonstrated by harnessing hydrophobic interactions and thermo-responsive nanostructured surfaces. In this regard, PNIPAM-coated silicon nanopillar arrays were shown to reversibly capture and release targeted cancer cells [108].

In addition to being applied for cell capture and release, thermo-responsive polymers have also been explored to control bacterial adhesion. Nanopatterned PNIPAM brushes have been shown to control the attachment, killing and release of bacteria in response to changes in temperature [109]. Firstly, the bacteria attached to the responsive surface were exposed to immobilized biocidal molecules. Then, a change in temperature triggered conformational changes of the nanopatterned polymer brushes and, as a result, the killed bacteria were released (Figure 2.14). The biocidal efficacy of a quaternary ammonium salt (QAS) was tested for *E. Coli* K12. This same principle was later applied with the more environmentally friendly antimicrobial enzyme lysozyme, instead of the QAS [110].

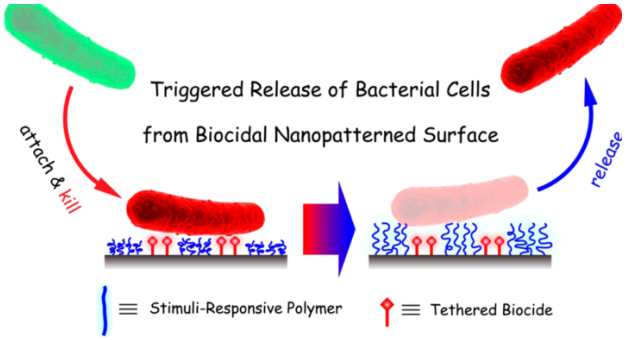

Figure 2.14 Schematic representation of a thermo-responsive surface, showing attachment of bacteria followed by biocidal exposure and further release of killed bacteria from the surface. Reprinted with permission from [109]. Copyright 2016 American Chemical Society.

Another route has been proposed, whereby biocidal activity was based on cationic and anionic poly(phenylene ethynylenes) (PEEs) [111]. In this case, the biocidal mechanism was suggested to be related to the ionic disruption of the bacterial cell envelope. PEEs were deposited by LBL assembly onto the voids in between nanopatterned PNIPAM brushes. These surfaces were also shown to be reusable.

The use of thermoresponsive polymers brushes on designing platforms that switch from bactericidal to cell-repellent has been extended to other polymers, such as hydroxyl-terminated oligo(ethylene glycol) methacrylate (HOEGMA) and 2-hydroxyethyl methacrylate (HEMA), modified with antimicrobial peptides [112]. Temperature-responsive comb-like copolymers have also been adopted to control the accessibility of ligands on surfaces, and thus holding the promise to manipulate processes such as bacterial attachment [113].

Thermoresponsive polymer platforms using alternative polymers to PNIPAM have also been reported for cell engineering. For instance, 2-(2-methoxyethoxy)ethyl methacrylate (MEO_2MA) brushes have been fabricated by surface initiated polymerization and afterwards functionalized with cell-adhesive peptides, which were reversibly masked upon temperature changes [114] (Figure 2.15). Fibroblast cells were successfully attached at

37°C and detached at 23°C, and more importantly in serum-free cell culture conditions. This feature is an advantage over other strategies used for cell sheet engineering that use serum-containing media for cell attachment facilitation. The presence of serum raises concerns regarding toxicity in the final cell sheets, and can prevent the growth of specific cell types and make the process of controlling the stimulation and differentiation of cells more difficult [115,116].

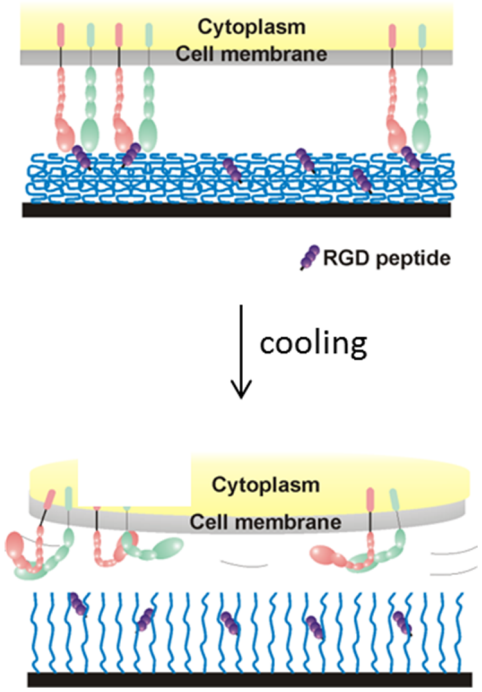

Figure 2.15 Illustration of a thermo-responsive surface containing RGD cell adhesive peptides for interaction with cells. Reprinted with permission from [114]. Copyright 2016 American Chemical Society.

Thermo-responsible polymers have been the basis for the development of reusable sensors. An immunosensor for cardiac troponin T (cTnT) has been constructed based on PNIPAM conjugated with anti-cTnT deposited on gold [117]. The system was characterized by electrochemistry techniques, namely cyclic voltammetry (CV) and electrochemical impedance spectroscopy (EIS). Structural changes occurred in response to temperature as the polymer switched between collapsed and extended states and so the binding of cTnT

was switched ON and OFF (Figure 2.16). Furthermore, the system was regenerated when the temperature was decreased below the LCST, resulting in cTnT being pushed away from the anti-cTnT surface.

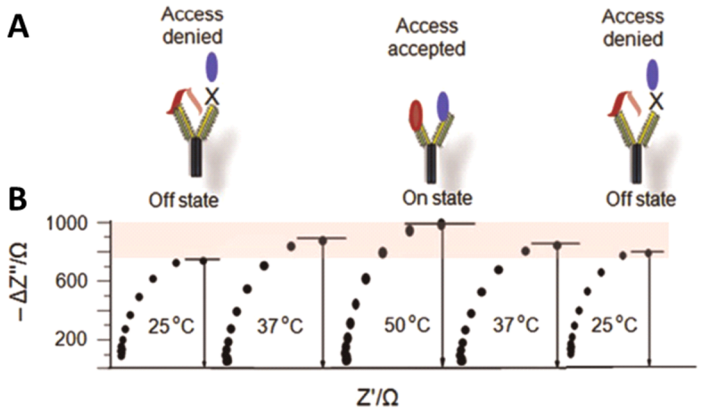

Figure 2.16 A) Schematic representation of the interaction between an antibody and an antigen on a thermo-responsive bioelectrode. The system switches reversibly in response to temperature changes from an OFF state, where access of the antigen to the immobilized antibody is denied, to an ON state, where access is accepted. B) Impedance values at distinct temperatures. Reprinted from [117], with permission from Elsevier.

Thermo-responsive polymers have also been studied to create sensors with switchable readouts. A methodology has been reported for the surface modification of gold substrates with thermo-responsive polymers, wherein a reversible switching between swollen and collapsed states, in response to temperature change around the LCST, led to a large change of charge transfer resistance (86%). Therefore, a strong barrier effect was produced with these responsive polymer films [118]. Gold substrates were first functionalized with a disulphide (dithiobis(succinimidyl propionate) (DTSP)-SAM, followed by covalent coupling of a polyamine layer. Afterwards, a polyelectrolyte multilayer was formed by LBL technique and a macroinitiator was adsorbed on the top of it for surface initiated polymerization. The thermo-responsive brushes were then constructed from the co-polymers of MEO_2MA and oligo(ethylene glycol) methacrylate (OEGMA).

Electrochemical quartz crystal microbalance with dissipation (E-QCM-D) was the method chosen for monitoring surface modifications and investigating the system's ability to undergo phase transition in response to temperature changes.

The thermo-responsiveness of polymers and electrochemistry have also been merged to develop ON/OFF-switchable platforms and modulate bioelectrocatalysis. One notable work was reported by Tiwari and co-workers, where the interface for electrochemical bioreactions was developed based on functionalized graphene [119]. A zipper nanostructured interface was constructed combining (i) graphene nanosheets, (ii) a negatively charged surfactant, sodium dodecylbenzenesulfonate (SDBS), (iii) thermo-responsive polymer PNIPAM, (iv) gold nanoparticles and (v) cholesterol oxidase. SDBS allowed stabilization of the surface and directed the self-assembly of the enzyme and the gold nanoparticles. Gold nanoparticles prevented thermal aggregation of the enzyme and catalysed the electrochemical reactions. Interaction between the donor-graphene and the receptor-polymer was controlled by temperature. At low temperatures, donor-acceptor interactions, *i.e.* hydrogen bonding, were active, impeding the access of the enzyme to its substrate. Above the LCST of PNIPAM, the interactions were broken, allowing the bioelectrocatalytic reactions to occur. This platform has promising applications in bioelectronics and biocatalysis

2.5 Chemically-controlled Nanostructured Surfaces

Chemical stimuli have been used for a variety of applications in biology and medicine. One example is the control of cell adhesion. A DNA aptamer-based mixed SAM responsive to adenosine triphosphate (ATP) - the energy currency of cells - was developed for regulating cell adhesion without cell-specific ligands. SAMs were created on gold from thiolated DNA strands and then co-assembled with the hydrophilic synthetic polymer 2-(2-(1-

mercaptoundec-11-yloxy)-ethoxy)-ethanol (SH-OEG). The presence of ATP regulated the ATP's aptamer conformation between an extended state, with good cell adhesion properties, and a folded state, with unfavourable cell adhesion [57].

Different strategies have been explored for controlling exposure of RGD ligands and, therefore, manipulating cell adhesion, in response to surface exposure to chemical/biochemical entities. For instance, surfaces have been functionalized with RGD peptides containing blocking groups that are then cleaved upon exposure to enzymes [120]. One other strategy is based on the use of a pair of complementary leucine zipper-molecules for reversible conversion of the accessibility of an RGD peptide immobilized on the surface [121]. RGD peptide was fused to a leucine zipper domain A and immobilized on the surface, being easily accessed by cells. When PEG fused to a leucine zipper domain B (PEG-B) was added to the surface, heterodimerization between leucine zipper domain A and B occurred, allowing co-immobilisation of PEG-B on the surface (Figure 2.17). After this co-immobilisation, the RDG peptide is no longer exposed on the surface and therefore the cells have no easy access to it. The surface can be switched again by addition, in excess, of unconjugated polypeptide A, which binds to PEG-B and then induces release of PEG-B from the surface.

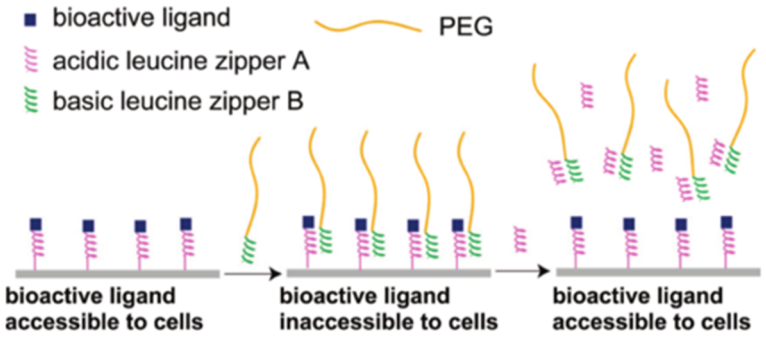

Figure 2.17 Illustration of a reversible switchable surface, in which immobilized bioactive ligands are accessible or not to cells due to the interaction of complementary zipper-molecules. Reprinted with permission from [121]. Copyright 2016 American Chemical Society.

A methodology for the reversible control of cell adhesion based on multi-covalent immobilisation of a modified RGD peptide has been recently reported [122]. Biomolecule-triggered release of RGD, and therefore cell release from the surface, was achieved by taking advantage of interactions between phenylboronicacid (PBA) groups in grafted polymer brushes and cis-diol groups in glycopolymer chains (Figure 2.18). A specific molecule-exchange process is triggered by glucose or fructose, mimicking natural biomolecular feedback systems. The multiple strong interactions in PBA/cis-diol polymeric complexes can be further explored for dynamic immobilisation of other biomacromolecules with potential applications in diagnostics and regenerative medicine.

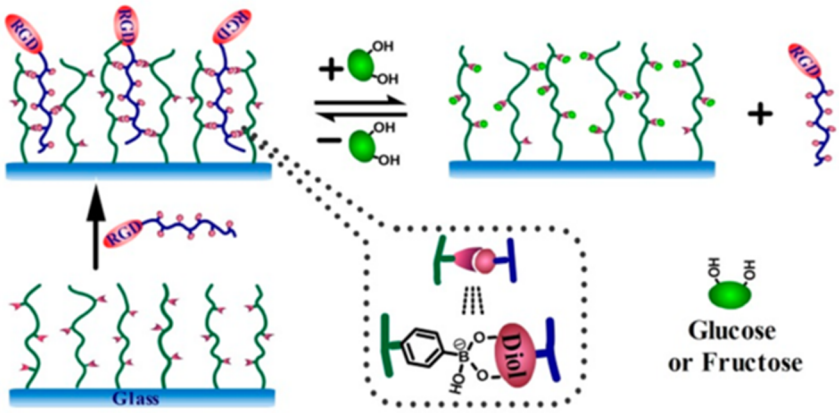

Figure 2.18 Schematic representation of a surface functionalization strategy, starting from PHEMA-graft-PBA, followed by introduction of RGD-PGAPMA, which in turn is reversibly removed from the matrix when glucose or fructose are added due to a specific molecule-exchange process. This functionalized surface then allows reversible cell adhesion, triggered by addition of glucose or fructose. Reprinted with permission from [122]. Copyright 2016 American Chemical Society.

PBA groups have also been combined with vertical nanowire arrays for the rapid and efficient capture and release of breast cancer cells [123]. In this case, vertical silicon nanowire arrays with poly(acrylamidophenylboronic acid) (polyAAPBA)-polymer brushes acted as a pH and glucose dual-responsive surface (Figure 2.19). The surface switched between cell capture, at pH 6.8 and in the absence of glucose, and cell release, at pH 7.8 with 70 mM glucose (Figure 2.19B). Moreover, the surface was shown to maintain switchability for at least 5 cycles and the cells maintained their viability after capture and release. The mechanism behind this reversible switching was the formation of stable complexes at low pH between PBA and sialic acid, which is present in the cell membrane. By increasing the pH, the polymer changed into a tetrahedral anionic form, which in turn formed stable complexes with glucose, replacing the polyAAPBA/sialic complex and thus releasing the cells.

pH-driven nanostructured responsive surfaces have also been developed by incorporating pH-responsive polymers and hydrogels. pH-responsive polymers undergo an abrupt phase transition caused by electrostatic repulsions of charges generated by ionization of weak acid or basic moieties attached to a hydrophobic backbone [90]. Polyacrylic acid (PAA), poly(methyl methacrylate (PMAA), poly(2-diethylaminoethyl methacrylate) (PDEAEMA), chitosan and albumin are examples of pH-responsive polymers that have been exploited for biomedical applications, namely for the control of protein and cell adhesion [124,125], antifouling [126], redox activity for bioelectronics applications [127] and drug release [128].

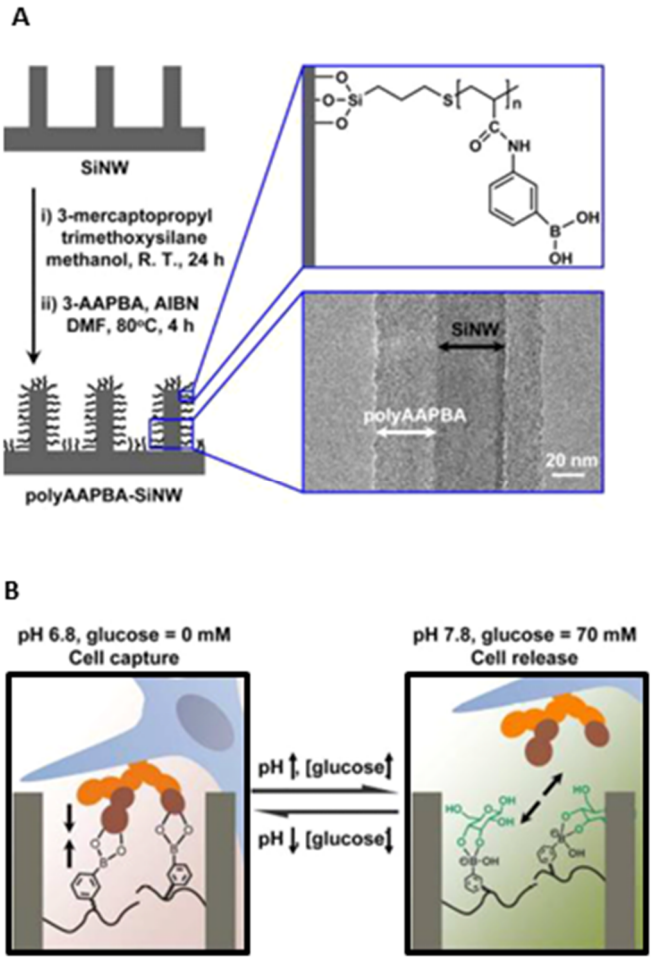

Figure 2.19 Illustration of A) a responsive surface composed of SiN arrays coated with polyAAPBA and Transmission Electron Microscopy image showing the thickness of polyAAPBA and SiN; B) reversible switching between cell capture and release upon changes in pH and glucose concentration, on the same surface. Reprinted with permission from [123]. Copyright 2016 American Chemical Society.

Hydrogels are polymer networks that become extensively swollen in aqueous media [129] and have been widely used in biomedical applications, for instance as coatings for implantable sensors [130], as base for microchannels used to engineer tissue microvasculature [131], as wound healing dressings [88] or as base for controlled cell staining [124]. A methodology for preparing surfaces with reversible wettability has been proposed by Soh and co-workers [132] that involved the use of superhydrophobic silanized micrometer sized glass particles

embedded into responsive superhydrophilic hydrogels. In response to different external stimuli (pH, temperature, stress), selected according to the hydrogel in use, the hydrogel can change its size and the surface wettability can be switched between hydrophobic and hydrophilic states.

Another example of an interesting pH-responsive switchable surface incorporating a pH-responsive hydrogel, i.e. poly(acrylamide-co-acrylic acid) (P(AAc-co-AAM), has been recently reported that was inspired by the ability of vesicle-carrying kinesins and dyneins to shuttle different biomolecule cargos along the microtubule network [133]. A microfluidic system was designed to provide two parallel fluid streams undergoing laminar flow. Furthermore, it incorporated flexible polymeric microscopic fins functionalized with aptamers that were embedded in P(AAc-co-AAM) for the modulation of biomolecular capture and transport into a distinct compartment (Figure 2.20). At pH 7.2, aptamers were exposed on the top fluidic layer, allowing binding of target biomolecules in solution. In acidic conditions, the hydrogel contracted (Figure 2.20B), inducing the fins to bend. The pH change also induced aptamer denaturation (Figure 2.20A), resulting in the release of captured molecules onto the bottom fluidic layer. This system was tested for the separation of thrombin and computer simulations were performed for system optimization. This is a platform with potential application on clinical technologies that focus on diagnostics and purification.

Following a different route, host-guest chemistry has been combined with a pH-responsive block copolymer and an azobenzene-based SAM for the creation of a system that reversibly adsorbed and released the protein cytochrome c [134]. pH-responsive block copolymer was first prepared by grafting β-CD moieties to PEG-block-PAA, which were then assembled on the azobenzene mixed SAM by host-guest interactions between azobenzene and CD. PAA exhibits pH sensitivity and can be switched from an

electronegative state with an extended structure at pH 7 to an electroneutral relaxed state at pH 4. These changes between extended and relaxed states allowed controlled adsorption and release of the positively charged cytochrome c (Figure 2.21). Due to its protein-resistance properties, PEG played a key role in the system.

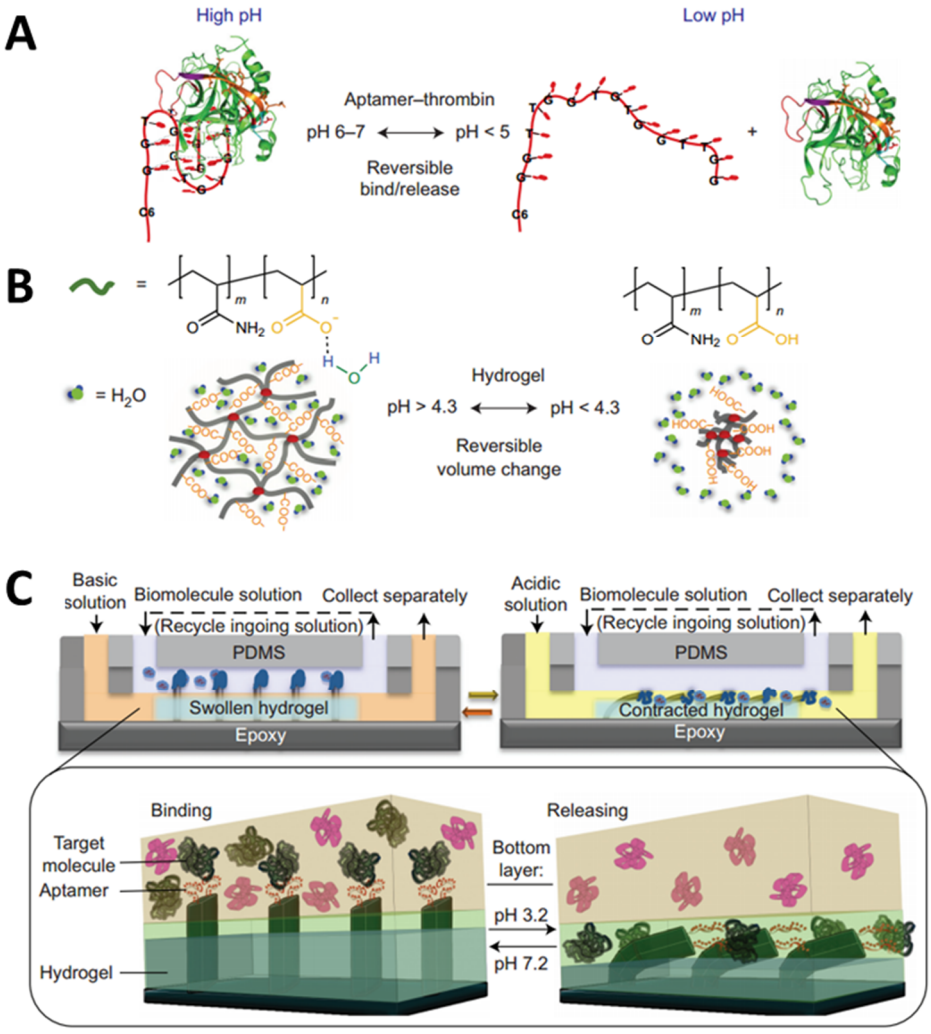

Figure 2.20 Illustration of A) reversible binding between aptamer and thrombin in response to a change in pH and B) reversible volume change in pH-responsive hydrogel P(AAc-co-AAM); C) capture and release system in biphasic microfluidic chamber, showing binding of target molecules to the aptamers attached to polymeric fins at pH 7.2 and release of target molecules to the bottom layer upon pH change to 3.2. Reprinted from [133] with permission from Nature.

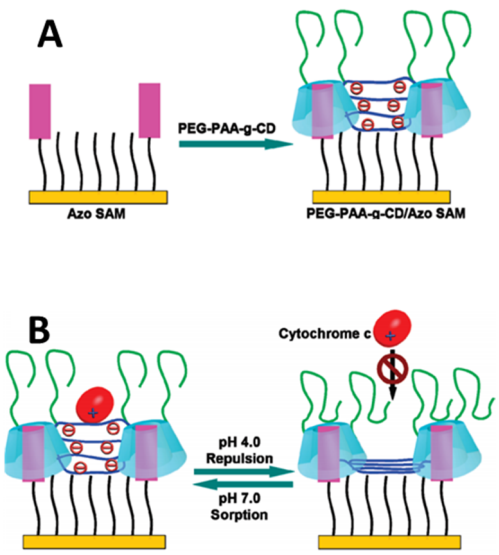

Figure 2.21 Illustration of A) pH-responsive polymer PEG-PAA-g-CD assembly on azobenzene-based SAM via host-guest interactions between azobenzenes and cyclodextrins; B) reversible surface switching from a state where adsorption of protein Cyt c occurs to a state where the protein is released in response to structural changes of PAA chains induced by pH variation. Reprinted with permission from [134]. Copyright 2016 American Chemical Society.

pH-responsive polymers have been investigated to develop anti-bacterial surfaces. Chen and co-workers [135] used a pH-responsive polymer, *i.e.* PMAA, with anti-microbial lysosymes, in combination with vertical silicon nanowire (SiN) arrays, to efficiently kill and release bacteria. A chemical etching method was employed for the fabrication of the nanowire (100 nm diameter) arrays on silicon, followed by surface-initiated polymerization. Finally, lysosyme was adsorbed under acidic conditions on the SiN-PMAA surfaces. At low pH, PMAA chains were in collapsed state, allowing infiltration of lysosymes into the interstices of the SiN arrays. When environmental pH was increased to neutral conditions, some extension of the polymer chains occurred, allowing lysosymes to actuate and kill bacteria. Lastly, when the pH was increased to basic conditions, the polymer chains were in

a fully extended state, promoting the release of the dead bacteria (Figure 2.22). Moreover, this self-cleaning platform was stable over several kill-release cycles, with fresh lysozyme being loaded into the system after each cycle. This new strategy for surface engineering is not restricted to antimicrobial and antifouling, having potential application in diverse biomedical fields once new materials and bioactive molecules are exploited in replacement to the ones used here for proof-of-concept. Using a different polymer, poly(2-(dimethylamino)ethyl methacrylate) (PDMAEMA), grafted onto SiN arrays, reversible switching of wettability, triggered by environmental pH and ionic strength variations, has been previously demonstrated [136].

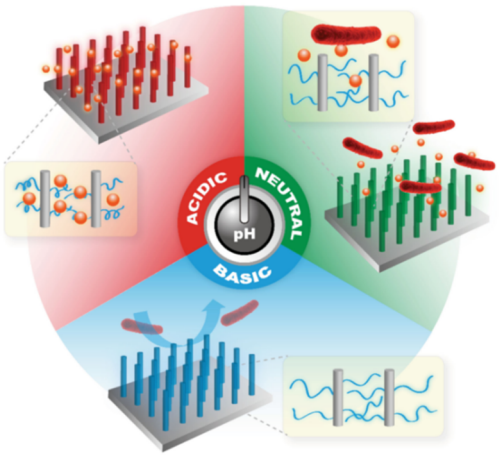

Figure 2.22 Illustration of a pH-responsive surface based on SiN arrays and PMAA polymer. It shows infiltration of lysosymes at acidic pH, attachment of bacteria at neutral pH and release of killed bacteria at basic pH, when the polymer chains are in fully extended state. From [135]. Reprinted with permission from Wiley-VCH.

Peptide-based switchable surfaces are expected to have better biocompatibility over artificial polymer-based surfaces. Thus, research on the development of responsive peptide surfaces has emerged that rely either on the use of naturally inspired peptides or designed

artificial peptides [137]. For example, pH-responsive peptide-functionalized gold surfaces, which reversibly switch between assembled coiled coil conformation and disassembled structure in response to a pH change, due to conformation dependence on the charge of ionisable amino acid residues, have been designed for reversible molecular binding [138]. A pH-responsive interface based on a protein has been also reported [139]. Protein rec1-resilin was tethered to the substrate and its conformation change was investigated by QCM-D and SPR at different pH values. The studies demonstrated reversible and fast switch between compact globular conformation and coil conformation.

Moreover, intrinsically disordered proteins (IDPs) have been proposed as a new class of smart biomaterial building blocks for the fabrication of stimuli-responsive brushes [140]. The engineered protein, rNHF-SA, was assembled into a protein-based polymer brush, which switched between collapsed and swollen conformations in response to changes in pH and ionic strength. The dynamic range in brush thickness is comparable to existing synthetic polymer brush systems. Reduction of the height of the brush by *in situ* protease digestion was also demonstrated.

pH-responsive nanostructured surfaces can also be found in electrochemical biosensors, where electrocatalysis is switched ON and OFF in response to pH changes. Electrochemical devices currently dominate the market of biosensors, a classic example being blood glucose sensors for diabetes [141]. A new version of electrochemical glucose biosensors has recently been reported [142], incorporating LBL assembled films with immobilized enzymes that respond to pH change and switch ON and OFF the electrocatalytic oxidation of glucose. The novelty of the system relies on the use of lectin concanavalin A (Con A) and glycoenzyme glucose oxidase (GOx) as building blocks. Due to their recognized biospecific affinity, Con A and GOx can be assembled into LBL films, whose net charge can be easily modulated by pH variation without disintegration.

Electrocatalysis of glucose catalysed by GOx was shown to be active at pH 4 and inactive at pH 8. The switching behaviour of the system was ascribed to the different electrostatic interaction between the electroactive probe in solution and the assembled films. Electrostatic interactions have also been the driving force for the development of other pH-responsive biocatalytic interfaces. Graphene oxide in combination with the pH-responsive poly(4-vinyl pyridine) (P4VP) and GOx was shown to modulate the biocatalytic interactions at the interface [143]. At pH 4, graphene oxide and GOx exhibited opposite charges and assembled in an ordered structured, allowing the substrate (i.e. glucose) to easily access the GOx enzyme. On the other hand, at high pH (6-10), GOx and P4VP acquired opposite charges, reducing the accessibility of GOx at the interface.

2.6 Concluding Remarks and Perspectives

A broad range of nanostructured surfaces have been developed that respond to light, temperature, electrical and chemical stimuli. These surfaces have been developed mainly by combination of lithographic techniques with SAMs or polymeric systems, and have demonstrated the ability to influence cell behaviour, provide new opportunities to capture and release molecules on demand, switch the activation or regeneration of biosensors and control bacterial adhesion - one of the major challenges in biomedical applications. Progress in the field has been remarkable and its impact in a number of different biomedical applications is and will continue to be an important driver for further innovation. While most of the stimuli-responsive surfaces for biomedical applications are based on the aforementioned stimuli, other stimuli such as magnetic [144,145] and mechanical [81,146] have been sporadically reported and open the door to very interesting capabilities. Polymeric nanoassembled surfaces have been designed that enable the induction of

biochemical reactions by the application of a mechanical stress [81]. Micro-wrinkling surfaces have also been developed that respond to mechanical strain to reduce and control biofilm attachment [146]. These examples demonstrate how one could leverage on exploring alternative stimuli to provide surface materials with unprecedented responsive properties. Moreover, nanostructured surfaces that respond to not only one but multi-stimuli [147-149] have started to emerge. The ability of combining a variety of switchable functionalities onto one surface in response to a range of distinct stimuli is of major interest. For example, it can be used to mimic complex natural systems interacting with variable physiological environments. With nature as a source of inspiration, the opportunities for new developments in stimuli-responsive nanostructured surfaces are vast and exciting. One can envision surface systems with superior reversibility characteristics and intricate mechanisms to quickly adapt to different stimuli. Development of platforms that can be easily adjusted in terms of their responsiveness and without the need for specialized chemistry [113], extending the range of users of these surfaces to multidisciplinary fields, is also highly desirable.

2.7 List of References

1. Wang, S., Huang, P. and Chen, X., Stimuli-Responsive Programmed Specific Targeting in Nanomedicine. *ACS Nano* **2016**, 10, 2991-2994.
2. Tochitsky, I., Polosukhina, A., Degtyar, V., Gallerani, N., Smith, C., Friedman, A., Van Gelder, R., Trauner, D., Kaufer, D. and Kramer, R., Restoring Visual Function to Blind Mice with a Photoswitch that Exploits Electrophysiological Remodeling of Retinal Ganglion Cells. *Neuron* **2014**, 81, 800-813.
3. Lee, H., Choi, T., Lee, Y., Cho, H., Ghaffari, R., Wang, L., Choi, H., Chung, T., Lu, N., Hyeon, T., Choi, S. and Kim, D., A graphene-based electrochemical device with thermoresponsive microneedles for diabetes monitoring and therapy. *Nat. Nanotechnol.* **2016**, 11, 566-572.
4. Alberts, B., Johnson, A., Lewis, J., Raff, M., Roberts, K. and Walter, P., *Molecular biology of the cell*, Garland Science, New York, **2008**.
5. Spiro, S. and Dixon, R., *Sensory Mechanisms in Bacteria: Molecular Aspects of Signal Recognition*, Caister Academic Press, Norfolk, **2010**.
6. Nick, P., *Plant Microtubules: Development and Flexibility*, Springer, Berlin, **2008**.
7. Xia, F. and Jiang, L., Bio-inspired, smart, multiscale interfacial materials. *Adv. Mater.* **2008**, 20, 2842-2858.
8. Iqbal, P., Preece, J. and Mendes, P., *Supramolecular Chemistry: From Molecules to Nanomaterials*, J. Steed and P. Gale (eds.), John Wiley & Sons Ltd, Chichester, **2012**.
9. Narita, A., Wang, X., Feng, X. and Mullen, K., New advances in nanographene chemistry. *Chem. Soc. Rev.* **2015**, 44, 6616-6643.
10. Guo, F. and Guo, Z., Inspired smart materials with external stimuli responsive wettability: a review. *RSC Adv.* **2016**, 6, 36623-36641.
11. Preece, J. and Stoddart, J., Concept transfer from biology to materials. *Nanobiology* **1994**, 3, 149-166.
12. Mendes, P. Stimuli-responsive surfaces for bio-applications. *Chem. Soc. Rev.* **2008**, 37, 2512-2529.
13. Mendes, P. Cellular nanotechnology: making biological interfaces smarter. *Chem. Soc. Rev.* **2013**, 42(24), 9207-9218.
14. Love, J., Estroff, L., Kriebel, J., Nuzzo, R. and Whitesides, G. Self-Assembled Monolayers of Thiolates on Metals as a Form of Nanotechnology. *Chem. Rev.* **2005**,

105, 1103.

15. Liu, W., Karpov, E., Zhang, S. and Park, H. An introduction to computational nanomechanics and materials. *Comput. Meth. Appl. Mech. Eng.* **2004**, 193, 1529-1578.
16. Mendes, P., Jacke, S., Critchley, K., Plaza, J., Chen, Y., Nikitin, K., Palmer, R., Preece, J., Evans, S. and Filtzmaurice, D. Gold Nanoparticle Patterning of Silicon Wafers Using Chemical e-Beam Lithography. *Langmuir* **2004**, 20, 3766.
17. Smith, R., Lewis, P. and Weiss, P. Patterning self-assembled monolayers. *Prog. Surf. Sci.* **2004**, 75, 1.
18. Imahori, H., Arimura, M., Hanada, T., Nishimura, Y., Yamazaki, I., Sakata, Y. and Fukuzumi, S. Photoactive Three-Dimensional Monolayers: Porphyrin−Alkanethiolate-Stabilized Gold Clusters. *J. Am. Chem. Soc.* **2001**, 123, 335.
19. Roth, K., Lindsey, J., Bocian, D. and Kuhr, W. Characterization of charge ctorage in redox-active self-assembled monolayers. *Langmuir* **2002**, 18, 4030.
20. Ulman, A. Formation and Structure of Self-Assembled Monolayers. *Chem. Rev.* **1996**, 96, 1533.
21. Xue, Y., Li, X., Li, H. and Zhang, W. Quantifying thiol-gold interactions towards the efficient strength control. *Nat. Commun.* **2014**, 5, 4348.
22. Dugas, V., Demesmay, C., Chevolot, Y. and Souteyrand, E., *Use of Organosilanes in Biosensors*, Nova Science Publishers Inc, France, 210.
23. Nicosia, C. and Huskens, J. Reactive self-assembled monolayers: from surface functionalization to gradient formation. *Mater. Horiz.* **2014**, 1, 32-45.
24. Lipomi, D., Martinez, R., Cademartiri, L. and Whitesides, G., *Polymer Science: A Comprehensive Reference*, **2012**.
25. Richardson, J., Bjornmalm, M. and Caruso, F. Technology-driven layer-by-layer assembly of nanofilms. *Science* **2015**, 348(6233).
26. Decher, G. and Schlenoff, J., *Multilayer Thin Films: Sequential Assembly of Nanocomposite Materials*, Wiley-VCH, **2003**.
27. Xiao, F., Pagliaro, M., Xu, Y. and Liu, B. Layer-by-layer assembly of versatile nanoarchitectures with diverse dimensionality: a new perspective for rational construction of multilayer assemblies. *Chem. Soc. Rev.* **2016**, 45, 3088-3121.
28. Whitesides, G., Ostuni, E., Takayama, S., Jiang, X. and Ingber, D. Soft lithography in biology and biochemistry. *Annu. Rev. Biomed. Eng.* **2001**, 3, 335-373.

29. Kumar, A. and Whitesides, G. Features of gold having micrometer to centimeter dimensions can be formed through a combination of stamping with an elastomeric stamp and an alkanethiol "ink" followed by chemical etching. *Appl. Phys. Lett.* **1993**, 63, 2002-2004.
30. Odom, T., Love, J., Wolfe, D., Paul, K. and Whitesides, G. Improved pattern transfer in soft lithography using composite stamps. *Langmuir* **2002**, 18, 5314-5320.
31. Xia, D., Ku, Z., Lee, S. and Brueck, S. Nanostructures and Functional Materials Fabricated by Interferometric Lithography. *Adv. Mater.* **2011**, 23, 147-179.
32. Glass, R., Moller, M. and Spatz, J. Block copolymer micelle nanolithography. *Nanotechnology* **2003**, 14, 1153-1160.
33. Lohmuller, T., Aydin, D., Schwieder, M., Morhard, C., Louban, I., Pacholski, C. and Spatz, J. Nanopatterning by block copolymer micelle nanolithography and bioinspired applications. *Biointerphases* **2011**, 6, MR1-MR12.
34. Cantini, E., Wang, X., Koelsch, P., Preece, J., Ma, J. and Mendes, P. Electrically responsive surfaces: experimental and theoretical investigations. *Acc. Chem. Res.* **2016**, 49, 1223-1231.
35. Yeo, W., Hodneland, C. and Mrksich, M. Electroactive monolayer substrates that selectively release adherent cells. *ChemBioChem* **2001**, 2, 590-593.
36. Yeo, W., Yousaf, M. and Mrksich, M. Dynamic interfaces between cells and surfaces: electroactive substrates that sequentially release and attach cells. *J. Am. Chem. Soc.* **2003**, 125, 14994-14995.
37. Yeo, W. and Mrksich, M. Electroactive self-assembled monolayers that permit orthogonal control over the adhesion of cells to patterned substrates. *Langmuir* **2006**, 22, 10816-10820.
38. Yousaf, M., Houseman, B. and Mrksich, M. Turning on cell migration with electroactive substrates. *Angew. Chem. Int. Ed.* **2001**, 40, 1093-1096.
39. Yousaf, M., Houseman, B. and Mrksich, M. Using electroactive substrates to pattern the attachment of two different cell populations. *Proc. Natl. Acad. Sci. U. S. A.* **2001**, 98, 5992-5996.
40. Chan, E. and Yousaf, M. Immobilization of ligands with precise control of density to electroactive surfaces. *J. Am. Chem. Soc.* **2006**, 128, 15542-15546.
41. Lee, C., Baker, S., Marcus, M., Yang, W., Eriksson, M. and Hamers, R. Electrically addressable biomolecular functionalization of carbon nanotube and carbon

nanofiber electrodes. *Nano Lett.* **2004**, 4, 1713-1716.

42. Curreli, M., Li, C., Sun, Y., Lei, B., Gundersen, M., Thompson, M. and Zhou, C. Selective functionalization of In2O3 nanowire mat devices for biosensing applications. *J. Am. Chem. Soc.* **2005**, 127, 6922-6923.
43. Yang, W., Baker, S., Butler, J., Lee, C., Russell, J., Shang, L., Sun, B. and Hamers, R. Electrically addressable biomolecular functionalization of conductive nanocrystalline diamond thin films. *Chem. Mat.* **2005**, 17, 938-940.
44. Mendes, P., Christman, K., Parthasarathy, P., Schopf, E., Ouyang, J., Yang, Y., Preece, J., Maynard, H., Chen, Y. and Stoddart, J. Electrochemically Controllable Conjugation of Proteins on Surfaces. *Bioconj. Chem.* **2007**, 18, 1919-1923.
45. Dhowre, H., Rajput, S., Russell, N. and Zelzer, M. Responsive cell–material interfaces. *Nanomedicine (Lond)* **2015***,* 10, 849-871.
46. Lee, E., Luo, W., Chan, E. and Yousaf, M. A molecular smart surface for spatio-temporal studies of cell mobility. *PLos One* **2015**, 10, e0118126.
47. Inaba, R., Khademhosseini, A., Suzuki, H. and Fukuda, J. Electrochemical desorption of self-assembled monolayers for engineering cellular tissues. *Biomaterials* **2009**, 30, 3573-3579.
48. Fukuda, J., Kameoka, Y. and Suzuki, H. Spatio-temporal detachment of single cells using microarrayed transparent electrodes. *Biomaterials* **2011**, 32, 6663-6669.
49. Lahann, J., Mitragotri, S., Tran, T., Kaido, H., Sundaram, J., Choi, I., Hoffer, S., Somorjai, G. and Langer, R. A reversibly switching surface. *Science* **2003**, 299, 371-374.
50. Liu, Y., Mu, L., Liu, B., Zhang, S., Yang, P. and Kong, J. Controlled protein assembly on a switchable surface. *Chem. Commun.***2004**, 1194-1195.
51. Mu, L., Liu, Y., Cai, S. and Kong, J. A Smart Surface in a Microfluidic Chip for Controlled Protein Separation. *Chem. Eur. J.* **2007**, 13, 5113-5120.
52. Pranzetti, A., Mieszkin, S., Iqbal, P., Rawson, F., Callow, M., Callow, J., Koelsch, P., Preece, J. and Mendes, P. An electrically reversible switchable surface to control and study early bacterial adhesion dynamics in real-time. *Adv. Mater.* **2013**, 25, 2181-2185.
53. Yeung, C., Iqbal, P., Allan, M., Lashkor, M., Preece, J. and Mendes, P. Tuning Specific Biomolecular Interactions Using Electro-Switchable Oligopeptide Surfaces. *Adv. Funct. Mater.* **2010**, 20, 2657-2663.

54. Lashkor, M., Rawson, F., Stephenson-Brown, A., Preece, J. and Mendes, P. Electrically-driven modulation of surface-grafted RGD Peptides for manipulation of cell adhesion. *Chem. Commun.* **2014**, 50, 15589-15592.

55. Ng, C., Magenau, A., Ngalim, S., Ciampi, S., Chockalingham, M., Harper, J., Gaus, K. and Gooding, J. Using an Electrical Potential to Reversibly Switch Surfaces between Two States for Dynamically Controlling Cell Adhesion. *Angew. Chem. Int. Ed.* **2012**, 51, 1-6.

56. Pranzetti, A., Preece, J. and Mendes, P., *Intelligent Stimuli-Responsive Materials: From Well-Defined Nanostructures to Applications*, Q. Li (ed.), John Wiley & Sons, **2013**.

57. Wang, S., Cai, X., Wang, L., Li, J., Li, Q., Zuo, X., Shi, J., Huang, Q. and Fan, C. DNA orientation - specific adhesion and patterning of living mammalian cells on self-assembled DNA monolayers. *Chem. Sci.* **2016**, 7, 2722-2727.

58. Surana, S., Shenoy, A. and Krishnan, Y. Designing DNA nanodevices for compatibility with the immune system of higher organisms. *Nat. Nanotechnol.* **2015**, 10, 741-747.

59. Borriello, A., Guarino, V., Alvarez-Perez, M., Schiavo, L. and Ambrosio, L. Optimizing PANi doped electroactive substrates as patches for the regeneration of cardiac muscle. *J. Mater. Sci. Mater. M.* **2011**, 22, 1053–1062.

60. Sirivisoot, S., Pareta, R. and Harrison, B. Protocol and cell responses in three-dimensional conductive collagen gel scaffolds with conductive polymer nanofibres for tissue regeneration. *Interf. Foc.* **2014**, 4(20130050).

61. Guarino, V., Zuppolini, S., Borriello, A. and Ambrosio, L. Electro-active polymers (EAPs): a promising route to design bio-organic/bioinspired platforms with on demand functionalities. *Polymers* **2016**, 8, 185.

62. Cen, L., Neoh, K., Li, Y. and Kang, E. Assessment of in vitro bioactivity of hyaluronic acid and sulfated hyaluronic acid functionalized electroactive polymer. *Biomacromolecules* **2004,** 5, 2238-2346.

63. Liu, X., Yue, Z., Higgins, M. and Wallace, G. Conducting polymers with immobilised fibrillar collagen for enhanced neural interfacing. *Biomaterials* **2011**, 32, 7309-7317.

64. Jeong, H., Ranallo, S., Rossetti, M., Heo, J., Shin, J., Park, K., Ricci, F. and Hong, J. Electronic Activation of a DNA Nanodevice Using a Multilayer Nanofilm. *Small*, **2016**.

65. Chuo, T., Wei, T., Chang, Y. and Liu, Y. Electrically driven biofouling release of a poly(tetrafluoroethylene) membrane modified with an electrically induced reversibly crosslinked polymer. *ACS Appl. Mater. Interfaces* **2013**, 5, 9918-9925.
66. Chen, W., Ma, Y., Pan, J., Meng, Z., Pan, G. and Sellergren, B. Molecularly Imprinted Polymers with Stimuli-Responsive Affinity: Progress and Perspectives. *Polymers* **2015**, 7, 1689-1715.
67. Dmitrienko, E., Pyshnaya, I., Martyanov, O. and Pyshnyi, D. Molecularly imprinted polymers for biomedical and biotechnological applications. *Russ. Chem. Rev.* **2016**, 85, 513-536.
68. Paul, N., Muller, M., Paul, A., Guenther, E., Lauermann, I., Muller-Buschbaum, P. and M., L.-S. (2012) Molecularly imprinted conductive polymers for controlled trafficking of neurotransmitters at solid–liquid interfaces. *Soft Matter* **2012**.
69. Chernov, I., Grebb, H., Janssen-Bienholdb, U., Parisia, J., Weilerb, R. and von Hauff, E. Binding and potential-triggered release of l-glutamate with molecularly imprinted polypyrrole in neutral pH solutions. *Sensor. Actuat. B Chem.* **2014**, 203, 327-332.
70. Wan, A., Inal, S., Williams, T., Wang, K., Leleux, P., Estevez, L., Giannelis, E., Fischbach, C., Malliaras, G. and Gourdon, D. 3D conducting polymer platforms for electrical control of protein conformation and cellular functions. *J. Mater. Chem. B.* **2015**.
71. Su, B., Sanchez, C. and Yang, X., *Hierarchically Structured Porous Materials: From Nanoscience to Catalysis, Separation, Optics, Energy, and Life Science*, Wiley-VCH, **2011**.
72. Velev, O. and Kaler, E. Structured porous materials via colloidal crystal templating: from inorganic oxides to metals *Adv. Mater.* **2000**, 12.
73. Seyfoddin, A., Chan, A., Chen, W. T., Rupenthal, I., Waterhouse, G. and Svirskis, D. Electro-responsive macroporous polypyrrole scaffolds for triggered dexamethasone delivery. *Eur. J. Pharm. Biopharm.* **2015**, 94, 419-426.
74. Jeon, G., Yang, S., Byun, J. and Kim, J. Electrically actuatable smart nanoporous membrane for pulsatile drug release. *Nano Lett.* **2011**, 11, 1284-1288.
75. Goulet-Hanssens, A. and Barrett, C. Photo-Control of Biological Systems with Azobenzene Polymers. *J. Polym. Sci. Part A* **2013**, 51, 3058-3070.
76. Wegner, S., Sentürk, O. and Spatz, J. Photocleavable linker for the patterning of bioactive molecules. *Sci. Rep.* **2015**, 5(18309), 1-7.

77. Zhu, C., Ninh, C. and Bettinger, C. Photoreconfigurable Polymers for Biomedical Applications: Chemistry and Macromolecular Engineering. *Biomacromolecules* **2015**, 15, 3474-3494.

78. Dillmore, W., Yousaf, M. and Mrksich, M. A Photochemical Method for Patterning the Immobilization of Ligands and Cells to Self-Assembled Monolayers. *Langmuir* **2004**, 20, 7223-7231.

79. Shimizu, Y., Boehm, H., Yamaguchi, K., Spatz, J. and Nakanishi, J. A photoactivatable nanopatterned substrate for analyzing collective cell migration with precisely tuned cell-extracellular matrix ligand interactions. *PLos One* **2014**, 9, e91875.

80. Auernheimer, J., Dahmen, C., Hersel, U., Bausch, A. and Kessler, H. Photoswitched Cell Adhesion on Surfaces with RGD Peptides. *J. Am. Chem. Soc.* **2005**, 127, 16107-16110.

81. Mertz, D., Vogt, C., Hemmerle, J., Mutterer, J., Ball, V., Voegel, J., Schaaf, P. and Lavalle, P. Mechanotransductive surfaces for reversible biocatalysis activation. *Nat. Mater.* **2009**, 8, 731-735.

82. Kadem, L., Holz, M., Suana, K., Li, Q., Lamprecht, C., Herges, R. and Selhuber-Unkel, C. Rapid Reversible Photoswitching of Integrin-Mediated Adhesion at the Single-Cell Level. *Adv. Mater.* **2016**, 28, 1799-1802.

83. Gong, Y., Li, C., Yang, J., Wang, H., Zhuo, R. and Zhang, X. Photoresponsive "Smart Template" via Host Guest Interaction for Reversible Cell Adhesion. *Macromolecules* **2011**, 44, 7499-7502.

84. Liu, C., Zhang, W., Zeng, Q. and Lei, S. A Photoresponsive Surface CovalentOrganic Framework: Surface-Confined Synthesis, Isomerization,and Controlled Guest Capture and Release. *Chem. Eur. J.* **2016**, 22, 6768-6773.

85. Xing, R., Jiao, T., Ma, K., Ma, G., Mohwald, H. and Yan, X. Regulating Cell Apoptosis on Layer-by-Layer Assembled Multilayers of Photosensitizer-Coupled Polypeptides and Gold Nanoparticles. *Sci. Rep.* **2016**, 6, 9.

86. Mosinger, J., Lang, K. and Kubat, P. Photoactivatable Nanostructured Surfaces for Biomedical Applications. *Top. Curr. Chem.* **2016**, 370, 135-168.

87. Gabriel, D., Monteiro, I., Huang, D., Langer, R. and Kohane, D. A photo-triggered layered surface coating producing reactive oxygen species. *Biomaterials* **2013**, 34, 9763-9769.

88. Wang, D., Green, M. D., Chen, K., Daengngam, C. and Kotsuchibashi, Y. Stimuli-Responsive Polymers: Design, Synthesis, Characterization, and Applications. *Int. J. Polym. Sci.* **2016**, 1-2.

89. Merchan, M., Ouk, T., Kubat, P., Lang, K., Coelho, C., Verney, V., Commereuc, S., Leroux, F., Sol, V. and Taviot-Gheho, C. Photostability and photobactericidal properties of porphyrin-layered double hydroxide–polyurethane composite films. *J. Mater. Chem. B* **2013**, 1, 2139-2146.

90. Cabane, E., Zhang, X., Palivan, C., Langowska, K. and Meier, W. Stimuli-Responsive Polymers and Their Applications in Nanomedicine. *Biointerphases* **2012**, 7, 1-27.

91. Goulet-Hanssens, A., Sun, K., Kennedy, T. and Barrett, C. Photoreversible Surfaces to Regulate Cell Adhesion. *Biomacromolecules* **2012**, 13, 2958-2963.

92. Rocha, L., C., P., Luca-Raicu, A., Resmerita, E., Rusu, A., Moleavin, I., Hamel, M., Branza-Nichita, N. and Hurduc, N. Azobenzene based polymers as photoactive supports and micellar structures for applications in biology. *J. Photoc. Photobio. A* **2014**, 291, 16-25.

93. Barillé, R., Janik, R., Kucharski, S., Eyer, J. and Letournel, F. Photo-responsive polymer with erasable and reconfigurable micro- and nano-patterns: An in vitro study for neuron guidance. *Colloid. Surface. B* **2011**, 88, 63-71.

94. You, J., Heo, J., Choi, Y., Kim, H. , Kim, J., Park, T., Kim, B., Kim, H. and Kim, E. Noninvasive Photodetachment of Stem Cells on Tunable Conductive Polymer Nano Thin Films: Selective Harvesting and Preserved Differentiation Capacity. *ACS Nano* **2013**, 7, 4119-4128.

95. Niu, D., Jiang, W., Liu, H., Zhao, T., Lei, B., Li, Y., Yin, L., Shi, Y., Chen, B. and Lu, B. Reversible Bending Behaviors of Photomechanical Soft Actuators Based on Graphene Nanocomposites. *Sci. Rep.* **2016**, 6(27366).

96. Giner-Casares, J., Henriksen-Lacey, M., Garcia, I. and Liz-Marzan, L. Plasmonic Surfaces for Cell Growth and RetrievalTriggered by Near-Infrared Light. *Angew. Chem. Int. Ed.* **2016**, 55, 974-978.

97. Zeng, Y. and Lu, J. Optothermally Responsive Nanocomposite Generating Mechanical Forces for Cells Enabled by Few-Walled Carbon Nanotubes. *ACS Nano* **2014**, 8, 11695-11706.

98. Lee, S., Fang, Y., Velpula, G., Cometto, F., Lingenfelder, M., Mullen, K., Mali, K.

and De Feyter, S. Reversible Local and Global Switching in Multicomponent Supramolecular Networks: Controlled Guest Release and Capture at the Solution/Solid Interface. *ACS Nano* **2015**, 9, 11608-11617.

99. Zareie, H., Boyer, C., Bulmus, V., Nateghi, E. and Davis, T. Temperature-Responsive Self-Assembled Monolayers of Oligo(ethylene glycol): Control of Biomolecular Recognition. *ACS Nano* **2008**, 2, 757-765.
100. Katz, E. Modified Electrodes and Electrochemical Systems Switchable by Temperature Changes. *Electroanal.* **2016**, 28, 1916-1929.
101. Gandhi, A., Paul, A., Sen, S. and Sen, K. Studies on thermoresponsive polymers: Phase behaviour, drug delivery and biomedical applications. *Asian. J. Pharm. Sci.* **2015**, 10, 99-107.
102. Guragain, S., Bastakoti, B., Malgras, V., Nakashima, K. and Yamauchi, Y. Multi-Stimuli-Responsive Polymeric Materials. *Chemistry* **2015**, 21, 13164-13174.
103. Yu, Q., Shivapooja, P., Johnson, L., Tizazu, G., Leggettd, G. and Lopez, G. P. Nanopatterned polymer brushes as switchable bioactive interfaces. *Nanoscale* **2013**, 5, 3632-3637.
104. Yu, Q., Johnson , L. and Lopez, G. Nanopatterned Polymer Brushes for Triggered Detachment of Anchorage-Dependent Cells *Adv. Funct. Mater.* **2014**, 24, 3751-3759.
105. Takahashi, H., Matsuzaka, N., Nakayama, M., Kikuchi, A., Yamato, M. and Okano, T. Terminally Functionalized Thermoresponsive Polymer Brushes for Simultaneously Promoting Cell Adhesion and Cell Sheet Harvest. *Biomacromolecules* **2012**, 13, 253-260.
106. Okano, T., Yamada, N., Sakai, H. and Sakurai, Y. A novel recovery svstern for cultured cells using plasrna-trGatid polystyrene dishes grafted with poly(N4sopropylacrylarnide) *J. Biomed. Mater. Res. A* **1993**, 27, 1243-1251.
107. Pan, G., Guo, Q., Ma, Y., Yang, H. and Li, B. Thermo-Responsive Hydrogel Layers Imprinted with RGDS Peptide: A System for Harvesting Cell Sheets. *Angew. Chem. Int. Ed.* **2013**, 52, 1-6.
108. Liu, H., Liu, X., Meng, J., Zhang, P., Yang, G., Su, B., Sun, K., Chen, L., Han, D., Wang, S. and Jiang, L. Hydrophobic Interaction-Mediated Capture and Release of Cancer Cells on Thermoresponsive Nanostructured Surfaces. *Adv. Mater.* **2013**, 25, 922-927.
109. Yu, Q., Cho, J., Shivapooja, P., Ista, L. and Lopez, G. Nanopatterned smart polymer

surfaces for controlled attachment, killing, and release of bacteria. *ACS Appl. Mater. Interfaces* **2013**, 5, 9295-9304.

110. Yu, Q., Ista, L. and Lopez, G. Nanopatterned antimicrobial enzymatic surfaces combining biocidal and fouling release properties. *Nanoscale* **2014**, 6, 4750-4757.
111. Ista, L., Yu, Q., Parthasarathy, A., Schanze, K. and Lopez, G. Reusable nanoengineered surfaces for bacterial recruitment and decontamination. *Biointerphases* **2016**, 11, 1-10.
112. Laloyaux, X., Fautré, E., Blin, T., Purohit , V., Leprince , J., Jouenne, T., Jonas , A. and Glinel, K. Temperature-Responsive Polymer Brushes Switching from Bactericidal to Cell-Repellent *Adv. Mater.* **2010**, 22, 5024-5028.
113. Dalier, F., Eghiaian, F., Scheuring, S., Marie, E. and Tribet, C. Temperature-Switchable Control of Ligand Display on Adlayers of Mixed Poly(lysine)-g-(PEO) and Poly(lysine)-g-(ligand-modified poly-N-isopropylacrylamide). *Biomacromolecules* **2016**, 17, 1727-1736.
114. Desseaux, S. and Klok, H. Temperature-Controlled Masking/Unmasking of Cell-Adhesive Cues with Poly(ethylene glycol) Methacrylate Based Brushes. *Biomacromolecules* **2014**, 15, 3859-3865.
115. Gstraunthaler, G. Alternatives to the use of fetal bovine serum: serum-free cell culture. *Altex* **2003**, 20(4/03), 275-281.
116. Mannello, F. and Tonti, G. Concise review: no breakthroughs for human mesenchymal and embryonic stem cell culture. *Stem Cells* **2007**, 25, 1603-1609.
117. Ashaduzzaman, M., Antony, A., Murugan, N., Deshpande, S., Turner, A. and Tiwari, A. Studies on an on/off-switchable immunosensor for troponin T. *Biosens. Bioelectron.* **2015**, 73, 100-107.
118. Comminges, C., Frasca, S., Sütterlin, M., Wischerhoff, E., Laschewsky, A. and Wollenberger, U. Surface modification with thermoresponsive polymer brushes for a switchable electrochemical sensor. *RSC Adv.* **2014**, 4, 43092-43097.
119. Parlak, O., Turner, A. and Tiwari, A. On/Off-Switchable Zipper-Like Bioelectronics on a Graphene Interface *Adv. Mater.* **2014**, 26, 482-486.
120. Todd, S., Scurr, D., Gough, J., Alexander, M. and Ulijn, R. Enzyme-Activated RGD Ligands on Functionalized Poly(ethylene glycol) Monolayers: Surface Analysis and Cellular Response. *Langmuir* **2009**, 25(13), 7533-7539.
121. Liu, B., Liu, Y., Riesberg, J. and Shen, W. Dynamic presentation of immobilized

ligands regulated through biomolecular recognition. *J. Am. Chem. Soc.* **2010**, 132, 13630-13632.

122. Pan, G., Guo, B., Ma, Y., Cui, W., He, F., Li, B., Yang, H. and Shea, K. Dynamic introduction of cell adhesive factor via reversible multicovalent phenylboronic acid/cis-diol polymeric complexes. *J. Am. Chem. Soc.* **2014**, 136, 6203-6206.
123. Liu, H., Li, Y., Sun, K., Fan, J., Zhang, P., Meng, J., Wang, S. and Jiang, L. Dual-responsive surfaces modified with phenylboronic acid-containing polymer brush to reversibly capture and release cancer cells. *J. Am. Chem. Soc.* **2013**, 135, 7603-7609.
124. Argentiere, S., Blasi, L., Ciccarella, G., Cazzato, A., Barbarella, G., Cingolania, R. and Gigli, G. Smart surfaces for pH controlled cell staining. *Soft Matter* **2009**, 5, 4101-4103.
125. Su, Y. and Li, C. The reorientation of poly(2-dimethylamino ethyl methacrylate) after environment stimuli improves hydrophilicity and resistance of protein adsorption. *J. Colloid. Interface Sci.* **2007**, 316, 344-349.
126. Cao, Z., Mi, L., Mendiola, J., Ella-Menye, J., Zhang, L., Xue, H. and Jiang, S. Reversibly Switching the Function of a Surface between Attacking and Defending against Bacteria. *Angew. Chem. Int. Ed.* **2012**, 51, 2602-2605.
127. Tam, T. K., Ornatska, M., Pita, M., Minko, S. and Katz, E. Polymer Brush-Modified Electrode with Switchable and Tunable Redox Activity for Bioelectronic Applications. *J. Phys. Chem. B* **2008**, 112, 8438-8445.
128. Tan, H., Xue, Y., Luana, Q. and Yao, X. Evaluation of glycol chitosan-graft-carboxymethyl b-cyclodextrin as potential pH-sensitive anticancer drug carrier by surface plasmon resonance. *Anal. Methods* **2012**, 4, 2784.
129. Ahmed, E. Hydrogel: Preparation, characterization, and applications: A review. *J. Adv. Res.* **2015**, 6, 105-121.
130. Wang, C., Yu, B., Knudsen, B., Moussy, Y., Harmon, J. and Moussy, F. Synthesis and Performance of Novel Hydrogels Coatings for Implantable Glucose Sensors. *Biomacromolecules* **2008**, 9(561-567).
131. Khademhosseinia, A. and Langer, R. Microengineered hydrogels for tissue engineering. *Biomaterials* **2007**, 28, 5087-5092.
132. Huang, X., Sun, Y. and Soh, S. Stimuli-Responsive Surfaces for Tunable and Reversible Control of Wettability. *Adv. Mater.* **2015**, 27, 4062-4068.
133. Shastri, A., McGregor, L., Liu, Y., Harris, V., Nan, H., Mujica, M., Vasquez, Y.,

Bhattacharya, A., Ma, Y., Aizenberg, M., Kuksenok, O., Balazs, A. C., Aizenberg, J. and He, X. An aptamer-functionalized chemomechanically modulated biomolecule catch-and-release system. *Nat. Chem.* **2015**, 7, 447-454.

134. Wan, P., Chen, Y., Xing, Y., Chi, L. and Zhang, X. Combining host-guest systems with nonfouling material for the fabrication of a biosurface: toward nearly complete and reversible resistance of cytochrome c. *Langmuir* **2010**, 26(15), 12515-12517.
135. Wei, T., Yu, Q., Zhan, W. and Chen, H. A Smart Antibacterial Surface for the On-Demand Killing and Releasing of Bacteria. *Adv. Healthc. Mater.* **2016**, 5(4), 449-456.
136. Wang, L., Wang, H., Yuan, L., Yang, W., Wu, Z. and Chen, H. Step-wise control of protein adsorption and bacterial attachment on a nanowire array surface: tuning surface wettability by salt concentration. *J. Mater. Chem. B* **2011**, 21, 13920-13925.
137. Zelzer, M., *Switchable and Responsive Surfaces and Materials for Biomedical Applications,* J. Zhang (ed.), Elsevier, **2015**.
138. Minelli, C., Liew, J., Muthub, M. and Andresen, H. Coiled coil peptide-functionalized surfaces for reversible molecular binding. *Soft Matter* **2013**, 9, 5119-5124.
139. Truong, M., Dutta, N., Choudhurya, N., Kimb, M., Elvin, C., Hill, A., Thierry, B. and Vasilev, K. A pH-responsive interface derived from resilin-mimetic protein Rec1-resilin. *Biomaterials* **2010**, 31, 4434-4446.
140. Srinivasan, N., Bhagawati, M., Ananthanarayanan, B. and Kumar, S. Stimuli-sensitive intrinsically disordered protein brushes. *Nat. Commun.* **2014**, 5(5145), 1-8.
141. Turner, A. Biosensors: sense and sensibility. *Chem. Soc. Rev.* **2013**.
142. Yao, H., Gan, Q., Peng, J., Huang, S., Zhu, M. and Shi, K. A Stimuli-Responsive Biosensor of Glucose on Layer-by-Layer Films Assembled through Specific Lectin-Glycoenzyme Recognition. *Sensors* **2016**, 16(4).
143. Parlak, O., Turner, A. and Tiwari, A. pH-induced on/off-switchable graphene bioelectronics. *J. Mater. Chem. B* **2015**, 3, 7434-7439.
144. Pivetal, J., Royet, D., Ciuta, G., Frenea-Robin, M., Haddour, N., Dempsey, N., Dumas-Bouchiat, F. and Simonet, P. Micro-magnet arrays for specific single bacterial cell positioning. *J. Magn. Magn. Mater.* **2015**, 380, 72-77.
145. Polte, T., Shen, M., Karavitis, J., Montoya, M., Pendse, J., Xia, S., Mazur, E. and Ingber, D. Nanostructured magnetizable materials that switch cells between life and

death. *Biomaterials* **2007**, 28, 2783-2790.

146. Epstein, A., Hong, D., Kim, P. and Aizenberg, J. Biofilm attachment reduction on bioinspired, dynamic, micro-wrinkling surfaces. *New J. Phys.* **2013**, 15, 13.
147. Osypova, A., Magnin, D., Sibret, P., Aqil, A., Jerome, C., Dupont-Gillain, C., Pradier, C., Demoustier-Champagne, S. and Landoulsi, J. Dual stimuli-responsive coating designed through layer-by-layer assembly of PAA-b-PNIPAM block copolymers for the control of protein adsorption. *Soft Matter* **2015**, 11, 8154-8164.
148. Kaniewska, K., Karbarz, M. and Stojek, Z. Electrochemical attachment of thermo- and pH sensitive interpenetrating-polymers-network hydrogel to conducting surface. *Electrochim. Acta* **2015**, 179, 372-378.
149. Parlak, O., Beyazit, S., Tse-Sum-Bui, B., Haupt, K., Turnera, A. and Tiwari, A. Programmable bioelectronics in a stimuli-encoded 3D graphene interface. *Nanoscale* **2016**, 8, 9976-9981.

3 Experimental Techniques

This section briefly describes the principles behind the techniques used throughout the work presented in this dissertation, most of them being surface characterisation techniques based on spectroscopy or microscopy. Ellipsometry, X-ray photoelectron spectroscopy (XPS), energy-dispersive X-ray spectroscopy (EDX), surface plasmon resonance spectroscopy (SPR), dynamic light scattering (DLS) and nuclear magnetic resonance spectroscopy (NMR) were the spectroscopy-based techniques explored in this work. Concerning microscopy, several instruments were used, from a simple optical microscope to more complex systems such as a scanning electron microscope (SEM), a transmission electron microscope (TEM) and an atomic force microscope (AFM). Always more than one technique was used when characterising a surface. More detail is given to the techniques that were most frequently used.

3.1 Contact Angle

Contact angle measurements are used to investigate the wettability of surfaces and are based on the properties of a liquid drop placed on the plane solid surface being analysed. Three interfaces are interacting in this system: solid-vapour (SV), solid-liquid (SL) and liquid-vapour (LV) interface. The so-called thermodynamic contact angle (θ) is defined as the angle that the tangent to the liquid surface makes with the sample surface at the three interfaces line (Figure 3.23) and, at equilibrium, this angle is a function of surface energies or interfacial tensions (γ) according to the Young Equation (Equation 3.1). Contact angle measurements are therefore often used for calculation of the solid surface free energy. However, in real samples, the ideal conditions proposed in Young's equation are not met. A few modifications to Young's equation have been proposed, which take into consideration the sample surface roughness and heterogeneity. [1]

Equation 3.1 $$\cos\theta = \frac{\gamma_{SV} - \gamma_{SL}}{\gamma_{LV}}$$

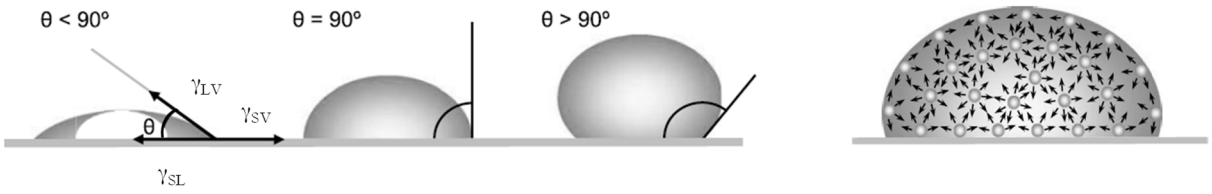

Figure 3.23 – Left: Schematic representation of contact angle measurements, showing the contact point of the three phases (solid-vapour (SV), solid-liquid (SL) and liquid-vapour (LV)). Right: schematic representation of molecules in the liquid drop causing surface tension as a result of unbalanced cohesive forces.

In order to calculate liquid surface tension values, contact angle measurements using a variety of liquids with different polarities are commonly used.[2]

Typical contact angle measurements consist of a) placing a fixed-volume drop (a few μl) of a liquid on the surface of the sample positioned on a horizontal stage, b) taking a high-resolution photo of the sessile drop profile and then 3) measuring the tangent angle at the three-phase contact point (using either left of right side of the profile). An example of an optical tensiometer is shown below (Figure 3.24).

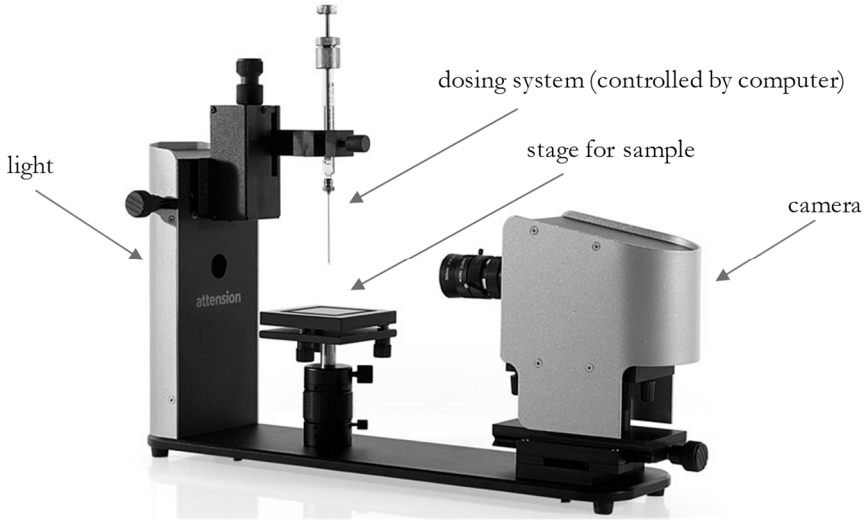

Figure 3.24 – Photo of *Biolin Scientific* optical tensiometer similar to the one used for the studies described in this dissertation.

The higher the water contact angle, the more hydrophobic, or the less hydrophilic, the surface is. Static or advanced contact angles can be measured. Dynamic contact angle is measured during wetting (advancing contact angle) and de-wetting (receding contact angle) of the surface, while static contact angle is measured after the drop has formed and rests on the surface. The difference between advancing and receding contact angle is called contact angle hysteresis and this value can bring additional information about the surface, such as the level of organization and homogeneity of the film[1].

When characterising a mixed SAM surface, the mole fraction of each component in the mixed SAM (q1 and q2, the sum of both being equal to 1) can possibly be estimated from the contact angle values of the pure SAM of each component ($\theta 1$ and $\theta 2$) and the contact angle value for the mixed SAM ($\theta 12$), following Cassie's law (Equation 3.2) described below.

Equation 3.2 $$\cos \theta_{12} = q_1 \cos \theta_1 + q_2 \cos \theta_2$$

3.2 Spectroscopic Ellipsometry

Spectroscopic ellipsometry is a non-destructive optical technique based on the analysis of the reflection of electromagnetic radiation from the surface of a solid sample of interest. The parameters measured through this technique, properties of the probing beam, allow the calculation of some properties of the materials composing the sample, such as thickness of thin films (ranging from nanometer to micrometer scale) and optical constants, for example the refractive index of the film. These calculations are based on assumed models making use of equations that describe the interaction of light with materials and therefore, if an improper model is used, the calculated values are meaningless, even if they are based on exact and reproducible measurements.[3]

The main components of an ellipsometer, shown below (Figure 3.25) are a light source, a polarizer (to convert unpolarized light to linearly polarized light), a compensator (to convert linearly polarized light into elliptically polarized light), an analyser (to determine the state of polarization of the resultant light beam) and a detector (to measure the light intensity). Different types of ellipsometers are available, mainly differing in the polarizer and analyser systems, some of which use linearly polarized incident light, others use an elliptically polarized incident light.

In a linearly polarized light source, all photons have the electric field oriented in one direction. When combining two linearly polarized light beams, polarized in different planes (parallel and perpendicular) and equal in amplitude, the resultant wave is elliptically polarized if the two components are out of phase (Figure 3.26). If they are in phase, the resultant wave is still linearly polarized. When a two-component polarized light beam reaches the surface of the sample and is reflected off the surface, a phase shift and an amplitude attenuation of either or both components might occur. In a spectroscopic

ellipsometry experiment we measure the changes in the ellipsometric parameters, Del (the relative phase change) and Psi (the relative amplitude change), over a specific wavelength range.

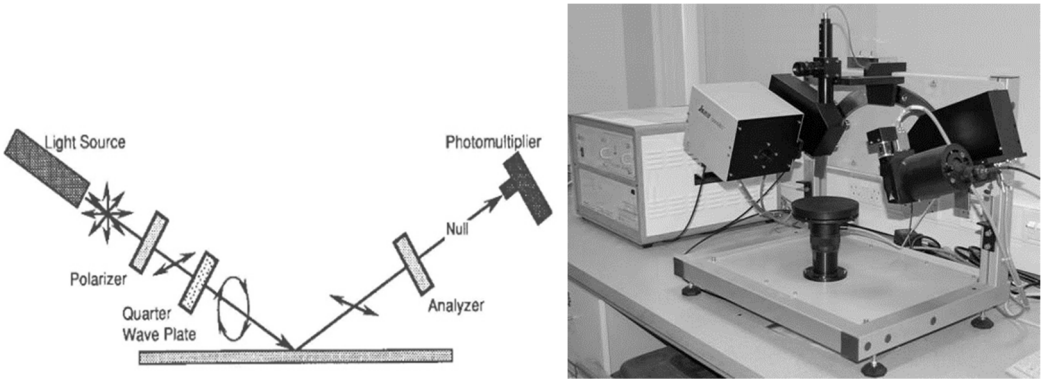

Figure 3.25 – Left: Schematic representation of one of the various possible ellipsometer setups. Right: Photo of *Horiba Scientific* ellipsometer instrument used for the studies described in this dissertation.

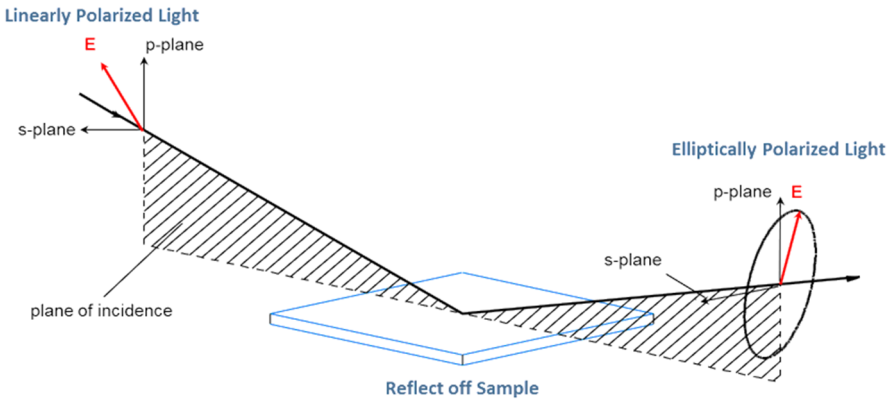

Figure 3.26 – Schematic representation of different planes in linearly polarized and elliptically polarized light.

When the thickness of the film is increased, a phase delay is observed as the separation between the light reflected from the surface and the light that travels through the film also increases (Figure 3.27). Films with different optical properties will also cause phase shifts

and/or amplitude attenuation. Reflection and refraction of light when it moves between films with different refractive indexes are described by the Fresnel equations[3].

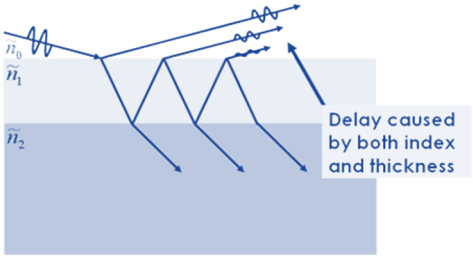

Figure 3.27 – Schematic representation of films with different optical properties and thickness, showing the light reflected from the surface and traveling through the film.

The film being studied should have enough transparency that the light will penetrate to the underlying layer, which might be another film or the substrate. It is important to know the substrate optical properties for the subsequent model analysis and even if theoretical values are available in the literature for standard materials, the substrate materials should, whenever possible, be analysed for the particular samples being studied, as the optical constants depend on several factors such as grain size, roughness, crystallinity, etc. The use of measured optical constants for the substrate, rather than handbook values, is particularly important if presence of roughness is to be ignored - it is in fact a common practice when building the models, to assume the growth of a thin film with plane parallel interfaces.[3]

Regarding the work presented in this thesis, this technique was used for calculating the thickness of organic films (SAMs and mixed-component SAMs) on gold and on silica. These films are very thin (with expected thickness lower than 5 nm) and therefore one must look at the calculated values for thickness with caution, and always in complement to other surface characterisation techniques. This approach is recommended because at this low film thickness, spectroscopic ellipsometry is very sensitive in terms of phase change

but not as much in terms of the film refractive index. Therefore, a nominal value for the refractive index must be assumed, rather than calculated, and the value of thickness is then calculated based on this assumption.

3.3 X-ray Photoelectron Spectroscopy (XPS)

X-ray Photoelectron Spectroscopy (XPS), also known as Electron Spectroscopy for Chemical Analysis (ESCA), involves irradiation with a beam of soft X-rays and detection of the photoelectrons emitted from the sample surface (Figure 3.28). By accessing the kinetic energy (KE) of the emitted photoelectrons, which is a function of the energy of the X-ray photons and the electrons binding energy (BE), elemental composition of the sample can be obtained (excluding the elements He and H [4]). Since the emitted photoelectrons will carry a different kinetic energy depending on the atom environment, it is also possible to detect the presence of different chemical/oxidation states of an element. This technique is sensitive to the top layer of the surface (up to 10 nm depth) and is commonly performed under ultra-high vacuum conditions.

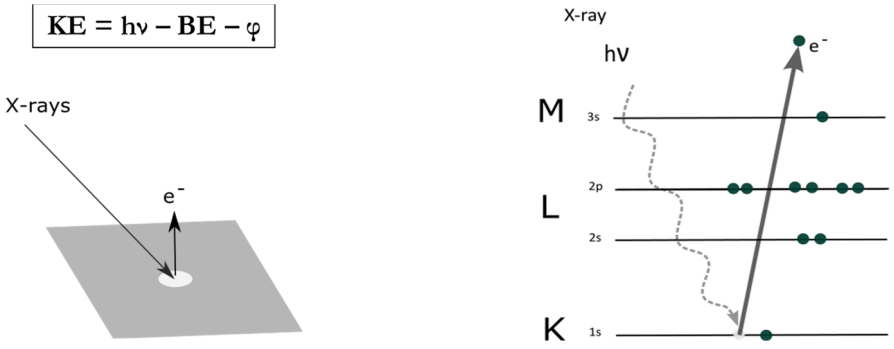

Figure 3.28 – Left: XPS principles: photoelectrons are emitted from the surface as a result of surface irradiation with a beam of X-rays. The photoelectron kinetic energy (KE) is a function of the electron binding energy (BE) and the energy of the X-ray photons (hν). Right: Representation of electron energy levels.

The main components of an XPS instrument, shown below (Figure 3.29), are an ultra-high vacuum system, an X-ray source, an electron gun, electron collection lens, an electron energy analyser and an electron detector. The X-ray source, commonly aluminium or magnesium Kα, can be used in achromatic or monochromatic mode, the latter providing overall improved resolution.

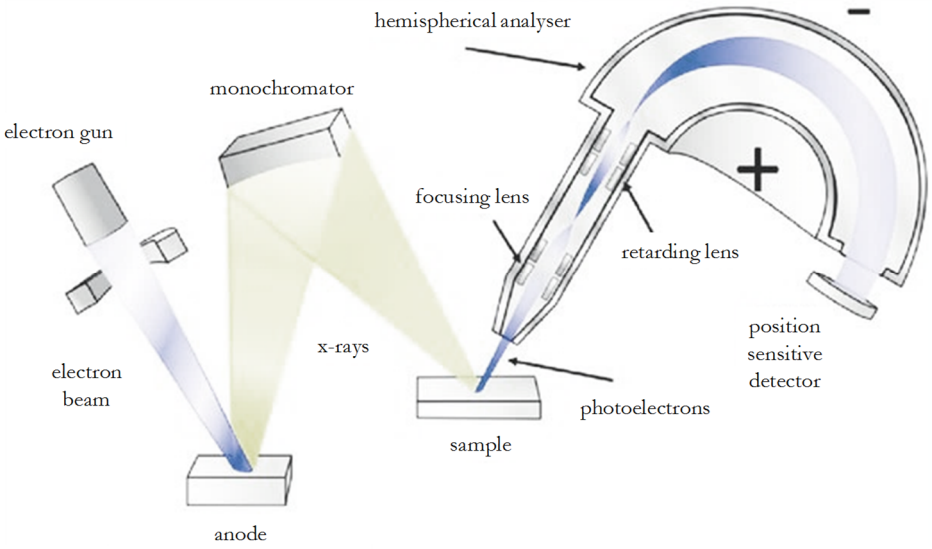

Figure 3.29 – Schematic representation of an XPS instrument setup. Adapted from [5].

The number of electrons recorded for a defined energy is proportional to the number of atoms at the surface. In fact the X-rays penetrate deeper in the sample. However, due to scattering, electrons can only travel a limited distance through a material and only the ones emitted from the top surface are likely to reach the detector without energy loss, resulting in specific peaks of the spectrum. Inelastic electron scattering also occurs to electrons emitted from the surface and this results in the signal background that constitutes the XPS spectra. The XPS signal is a function of the inelastic mean free path (IMFP) of the photoelectron, an index of how far an electron on average travels through a solid without suffering inelastic scattering. According to the exponential attenuation model, and

neglecting elastic scattering effects, the majority of the XPS signal originates from a depth of 3 x IMFP.

Quantitative surface chemical composition analysis based on XPS spectra is possible through peak modelling and background removal. An analytical sensitivity of 0.1 – 1 atomic % is achievable depending on which elements are being analysed and the nature of the sample, including composition and matrix effects.[6]

Transitions from different electronic states from the same element (for example, O 1s and O 2s for oxygen) are detected at different energies. For quantification purpose, only one transition per element is commonly required and the one selected is usually the transition that gives the most intense peaks without the presence of interfering peaks from other elements. All photoelectron peak areas are normalised by Relative Sensitivity Factors and instrument Transmission Function. For comparison of samples, relative atomic percentages are used instead of direct comparison of peak areas as these are dependent on experimental conditions. These atomic percentages take into consideration the ratio of the intensity to the total intensity of electrons in the measurement. CasaXPS software is a commonly used software for processing XPS data. Peak intensities and peak positions are of major importance, but other parameters are also considered when doing quantification, such as the shape of the peak and the full width at half maximum. The background signal is approximated by algorithms, which will then allow measurement of peak areas with subtracted background. Peak-fitting data might be complex and involve additional parameter constrains. Overlapping transitions are one of the main challenges when analysing XPS data.

A few other challenges to be considered when using this technique are mentioned below.

Contamination of samples upon storage or during transport will have an effect on XPS results. Special care should be taken in sample handling. Carbon and oxygen are the most abundant contaminants of air-exposed surfaces and therefore adventitious contamination is expected to be present in all the samples[7].

When analysing electrically insulating samples (materials that present high resistivity, which results in absence or very little electrical conduction) by XPS it is essential to use a charge compensation system. This system will compensate the loss of electrons from the surface by replenishing electrons from an external source and therefore prevent positive charge accumulation at the surface and consequent distortion of the XPS spectra. During the data acquisition, one must ensure that the charge compensation system is ON and the instrumental set-up is optimised, being vigilant for the eventual appearance of peak broadening due to surface charging.

Finally, irradiation and vacuum may cause sample degradation[8]. Radiation damage might occur when long exposure times are used, and therefore exposure times should be optimised. Damage can be checked by running repeated scan and comparing them - scans should be similar if no damage occurred. Volatile contaminants from other samples loaded at the same time or vacuum residues from previous measurements can also cause changes in the spectra.

3.4 Energy-dispersive X-ray Spectroscopy (EDX or EDS)

Energy-dispersive X-ray spectroscopy makes use of high energy particles, commonly electrons, to promote emission of characteristic X-rays from a sample. The energy of the electrons bombarding the sample as well as the mass and atomic distribution of the sample dictate the electron interaction volume. This volume is also limited by inelastic energy

losses and backscattering of incident electrons. Like XPS, this technique provides information about the elemental composition of the sample, however the information is coming from a greater depth in the sample (up to a few μm), while XPS is more surface sensitive. EDX is limited to the elemental composition of the sample, not allowing differentiation between different chemical states of an element as XPS can provide.

3.5 Surface Plasmon Resonance (SPR) Spectroscopy

Surface Plasmon Resonance (SPR) spectroscopy is an optical technique based on the analysis of the reflection of a light beam after hitting a metal surface under total internal reflection (TIR) conditions provided by a prism with high refractive index.

The typical SPR sample consists of a glass slide covered with a thin layer of metal functionalised with a film of interest, which incorporates a ligand that will interact with an analyte present in the injected solution. The metal must have conduction band electrons capable of resonating with the incoming light at the relevant wavelength, with gold being the most commonly used due to its resistance to oxidation.

The main components of a SPR piece of equipment are a light source, a coupling element (normally a prism, to provide the evanescent field which couples to surface plasmons), a photodetector and a sample cell (Figure 3.30). A drop of oil with the same refractive index as the glass substrate coated with gold is used to promote the contact between the prism surface and the sample. A microfluidic system is incorporated in this piece of equipment allowing the usage of small volumes of reagents interacting with the sample.

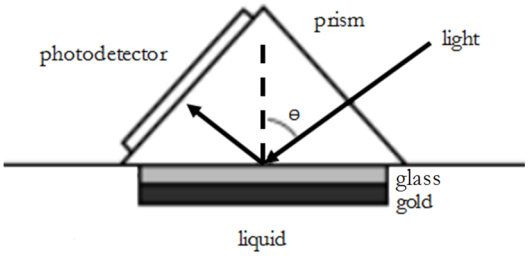

Figure 3.30 - Schematic representation of an SPR setup.

During a SPR experiment, the film surface is always in contact with a flowing solution and molecular interactions are monitored in real time as the properties of the reflected light change when molecules bind or dissociate from the metal surface. The incident light photons are absorbed by the gold and the energy is transferred to the electrons in the gold surface. This energy is then converted into surface plasmons with a distinctive momentum, which is related to the properties of the film and the medium surrounding the film. When the momentum of incoming light matches the momentum of the plasmons, resonance occurs, and an evanescent wave is created within a distance of approx. 300 nm from the interface. The coupling of the evanescent wave to the surface plasmons is monitored. The change of the angle of incident light at which resonance occurs, at a specific wavelength, gives important information about the change in the composition of the medium. This angle is proportional to the amount of analyte that binds to the ligand on the sample surface as it creates a change in the refractive index. The temperature affects the measurements as it affects the refractive index, and therefore it needs to be controlled. Also, if there is a difference in the refractive index of the injected solution and the running buffer, there will be a background response and therefore a control experiment is usually run where the ligand is not present, so that the background response can be subtracted. To minimize this effect, the analyte solution is prepared in the buffer solution[9].

3.5.1 Electrochemical SPR (eSPR)

SPR can be combined with electrochemistry, using a setup consisting of a 3-electrode electrochemistry flowcell connected to a potentiostat (Figure 3.31), which allows simultaneous investigation of both optical and electrochemical properties of the sensor surface. In this electrochemical system, the current travels between the working electrode (Au surface) and the counter electrode (Pt wire). The potential difference between the working electrode and the counter electrode is measured and controlled by the potentiostat, which comprises an electric circuit. By using a feedback mechanism, the current supplied to the counter electrode is adjusted and the potential of the working electrode is controlled with respect to the reference electrode (Ag/AgCl electrode), in accordance with the value specified by the user. The following reversible redox reaction occurs in the Ag/AgCl electrode electrode, providing a stable and reproducible potential:

$$AgCl + e^- \leftrightharpoons Ag + Cl^-$$

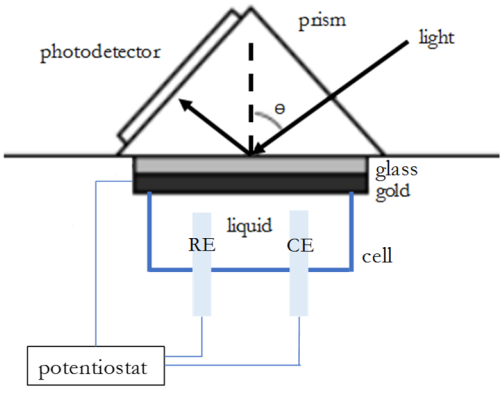

Figure 3.31 - Schematic representation of an SPR combined with an electrochemical system - potentiostat, reference electrode (RE), counter electrode (CE) and working electrode (gold surface).

3.6 Dynamic Light Scattering (DLS) also known as Photon Correlation Spectroscopy (PCS)

Dynamic Light Scattering (DLS) technique is based on the observation of random changes in the intensity of scattered light when a laser light source is directed onto particles in motion. These fluctuations as a function of time are a result of the random position change of the particles in suspension due to collisions with solvent molecules, known as the Brownian motion, which can be modelled by the Stokes-Einstein equation (Equation 3.3). Dh is the hydrodynamic diameter which is defined as the diameter of a hard sphere that diffuses at the same speed as the particle or molecule under observation. This parameter will depend on the dispersant in which the particles are suspended and the surface structure, being a function of the translational diffusion coefficient (Dt), temperature (T), dynamic viscosity (η) and the Boltzmann's constant (k_B).

Equation 3.3 $$D_h = \frac{k_B T}{3\pi\eta D_t}$$

The collected data is analysed in terms of a correlation function and suitable algorithms are used to calculate the particle size. The temperature of the sample must be controlled, and the viscosity and refractive index of the dispersant should be known with accuracy.

The main components of a DLS system (Figure 3.32) are a laser light source, a sample cell, a detector, an attenuator and a correlator (for comparison of the scattering intensity).

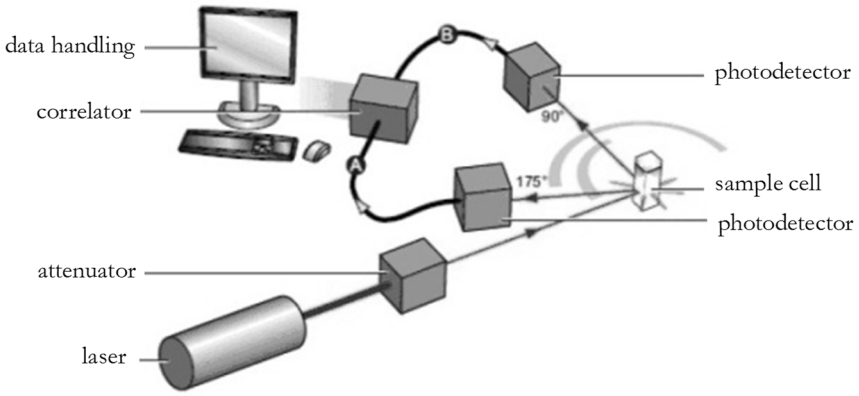

Figure 3.32 - Schematic representation of a DLS system showing detectors placed at 90° (traditional setup) and at 175°.

3.7 Nuclear magnetic resonance (NMR) spectroscopy

NMR is a spectroscopy technique that makes use of a magnetic field, generated by superconducting magnets, to detect nuclear spins. Atoms with odd numbers of protons and neutrons have a spin and a magnetic moment with unique properties. Most of the elements have at least one isotope which possesses a magnetic moment, ^{1}H and ^{13}C being the most common isotopes used for NMR signals detection. When the sample is placed in a magnetic field (Figure 3.33) at a suitable frequency, transitions occur between different energy levels and protons resonate. Different proton environments will resonate at different frequencies, which makes this technique suitable to determine the precise chemical structure of a molecule. The output of an NMR experiment is a spectrum presenting a set of peaks, also called resonances, and the area under each peak is proportional to the number of nuclei in that chemical environment.

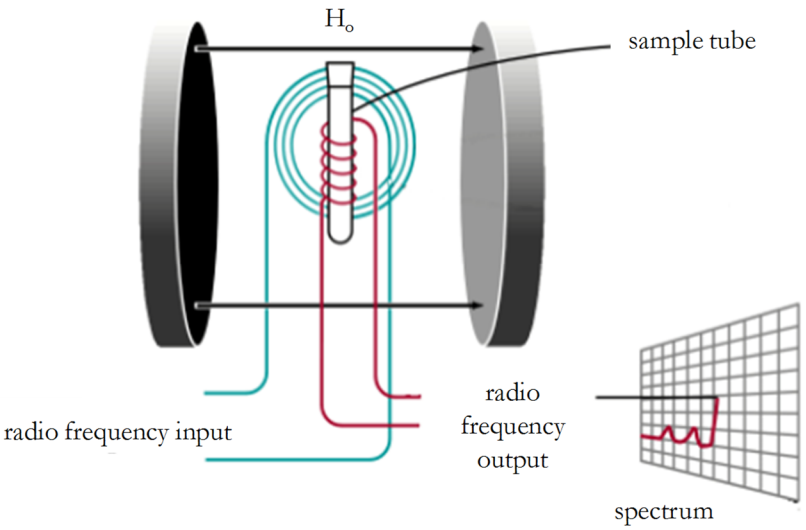

Figure 3.33 – Schematic representation of an NMR setup, the sample being placed in a magnetic field (magnetic field strength H_o) and excited by a radio frequency circuit. Adapted from [10].

3.8 Fluorescence Spectroscopy (also known as spectrofluorometry)

This technique is based on the irradiation of a sample containing fluorophores (or fluorochromes) with a beam of light at a given wavelength, and detection of the light emitted from the sample.

Photons absorbed by the fluorophore molecules cause transition of the electron energy level from the so-called ground state to an excited electronic state, for a finite time (typically a few nanoseconds). Further collision with other molecules leads to lower vibrational states, within the excited state. Emission of light occurs when the electrons transition back to the ground state (Figure 3.34). This emission normally occurs at lower energy wavelengths due to energy dissipation during the excited-state lifetime.

Each fluorophore has its most efficient energy absorption at a specific wavelength and a corresponding wavelength where the energy is re-emitted, and these values constitute the excitation and emission spectra, characteristic of each fluorophore. The Stokes Shift, difference between the excitation and emission wavelengths, is characteristic of each fluorophore as well as the intensity at which it emits light.

The instrumentation for this technique (Figure 3.35) consists of a light source, a sample holder, a detector, beam filters or monochromators that allow selection of both the excited and emitted wavelengths and bandwidths, and a shutter to reduce photodecomposition of the sample by minimizing the period of time that the sample is exposed to light.

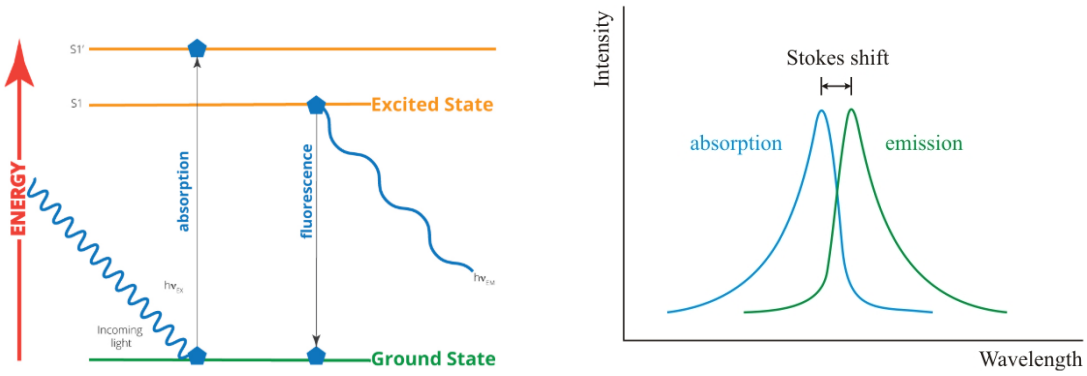

Figure 3.34 – Left: Schematic representation of fluorescence phenomenon, showing photon absorption causing transition of electrons of the molecule in the ground state to an excited state followed by relaxation to the lowest energy state within the excited state; finally, a photon is emitted when the electrons transits back to the ground state. **Right:** Diagram showing Stroke's shift in absorption and emission spectra. Adapted from [11].

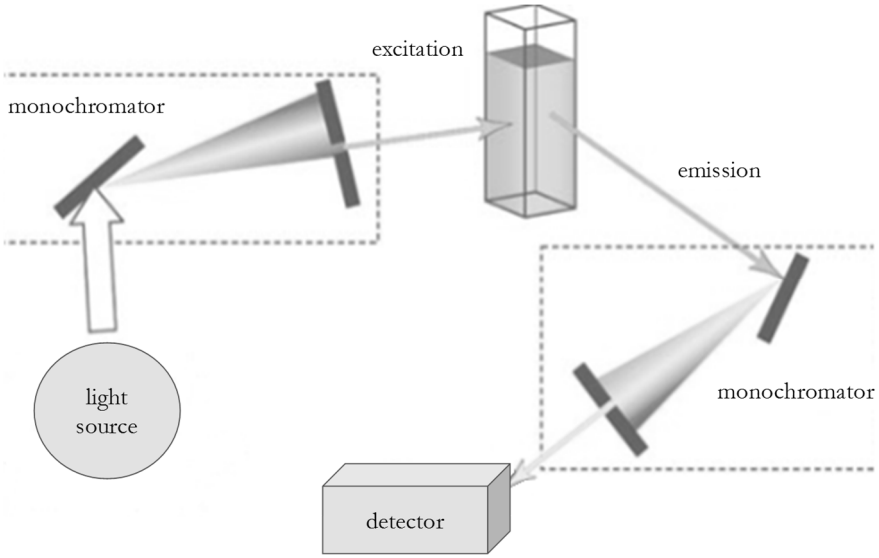

Figure 3.35 – Schematic representation of fluorometer main components.

Photobleaching and quenching are phenomena that influence fluorescence. Quenching refers to the decrease of fluorescence intensity commonly as a result of molecular interactions. For example, molecular oxygen quenches almost all known fluorophores.[12] Photobleaching refers to the irreversible chemical alteration of the fluorophores leading to the loss of its ability to fluoresce. This can be minimized by reducing the time at which the fluorophore is in an excited state.[13]

Solvent polarity, temperature and pH of the solution might influence the fluorescence intensity and therefore these parameters should be controlled for the fluorescence measurements.

When performing multicolour experiments - where two or more fluorophores are present - spectral overlap (or fluorescence spillover) must be evaluated. Fluorescence spillover occurs when signal from one fluorophore interferes with signals from other fluorophores (Figure 3.36). Areas of spectral spillover for varying emission filters can be quantified and

compensation might have to be applied to generate meaningful data. Another two key factors that should be considered as they may offset the results, are the extinction coefficient (EC), a measurement of the absorption of light by a molecular species at a given wavelength, and the relative concentration of the molecular targets.

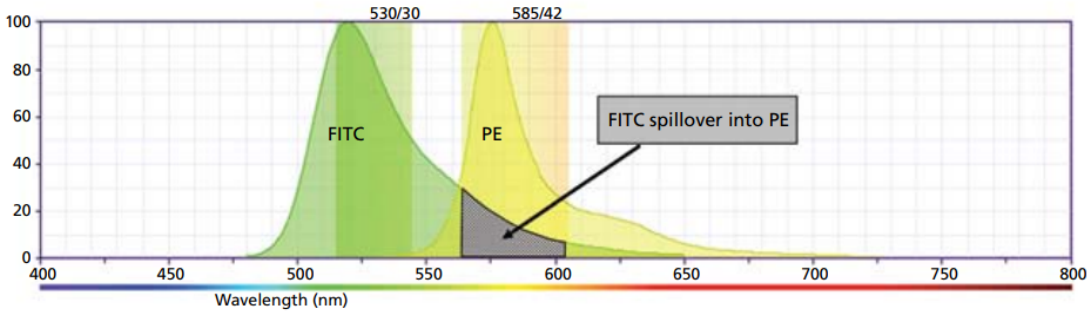

Figure 3.36 – Example of fluorescence spillover, showing emission spectra for two different fluorescent molecules, FITC and PE, and a portion of FITC signal being measured in the PE detector (585/42 bandpass). Adapted from [14].

3.9 Optical microscopy

Optical or light microscopy is the most traditional form of microscopy, consisting of the use of visibly light and a single or multiple lens to magnify the sample. A diaphragm and a condenser lens allow the control of focus and amount of light reaching the sample. Inverted microscopes have the objectives located below the sample stage, in contrast to upright microscopes where the objectives are placed above.

Phase contrast microscopy is a contrast-enhancing optical microscopy technique widely used in biological and medical research. This technique replaced brightfield microscopy for investigating specimens (such as cells, tissues and organisms) which are transparent and uncoloured under brightfield illumination and therefore had to be stained for observation.

By incorporating phase contrast optical accessories (such as specialised phase objectives and phase condensers) (Figure 3.37), a difference in brightness between the specimen and the background is provided and images with high contrast and rich detail can be achieved.

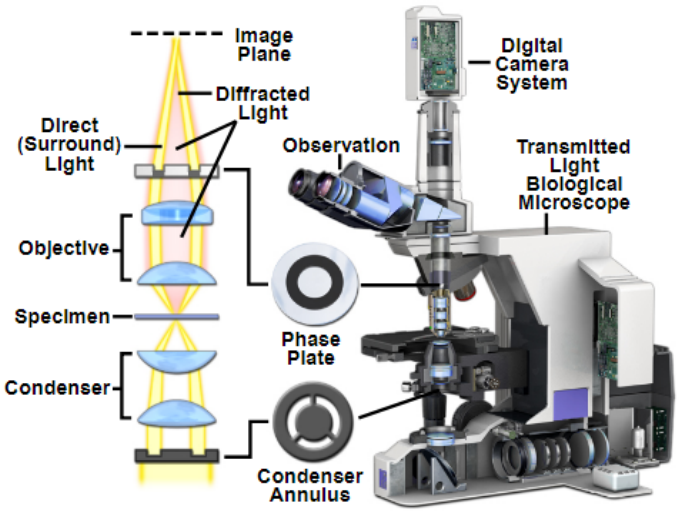

Figure 3.37 - Main components of an upright phase contrast microscope. Adapted from [15].

3.10 Transmission Electron Microscopy (TEM)

Transmission electron microscopy operates on similar principles to optical microscopy except that electrons are used instead of light and electromagnetic lenses instead of glass lenses, with greater resolution being achieved. A beam of electrons is directed at a very thin sample (requirement for transmitted electrons) in a vacuum environment. Electrons are transmitted through the sample and the image is projected in a fluorescent screen or a CCD camera. Magnification of the samples by more than 50 million times is possible with this technique. [16]

3.11 Scanning Electron Microscopy (SEM)

Scanning Electron Microscopy (SEM) (Figure 3.38) produces images by detecting secondary electrons that are emitted from a surface, due to a primary electron beam directed at the sample through applying a voltage between a conductive sample and a filament. This occurs in a vacuum environment. The electron beam, which can be controlled by changing the current that passes through the electromagnetic lenses, is scanned across the surface of the sample in a raster or line by line pattern, with detectors building up an image by mapping the detected signals by beam positioning. The SEM is a high-resolution instrument capable of interacting with a few nanometers to several microns of the sample surface, depending on beam parameters and sample type.[16]

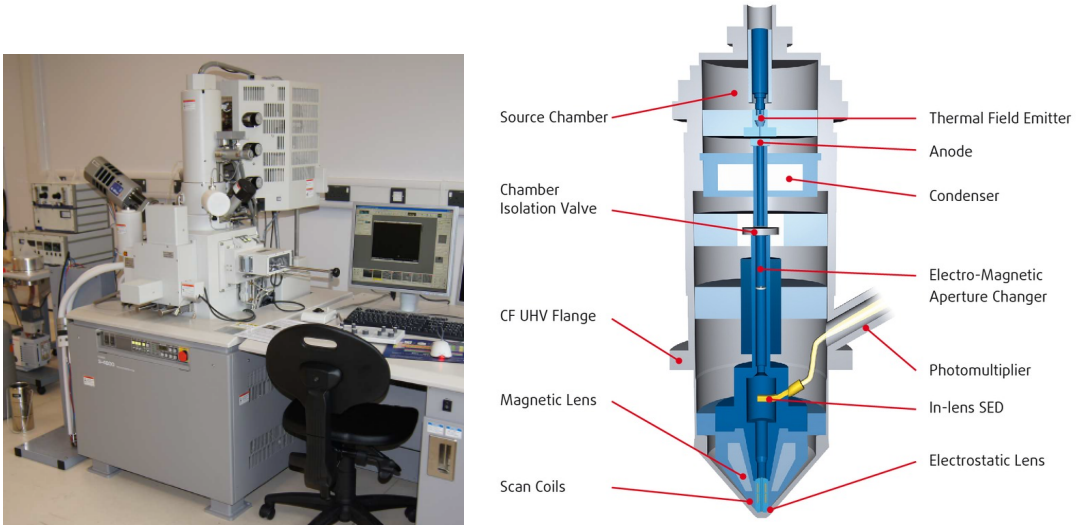

Figure 3.38 – Left: Photo of Hitachi S-4800 SEM system coupled to an EDX detector. Right: Diagram of a typical SEM column with an electron gun located at the top of the column, the electrons passing through a combination of lens and apertures to produce a focused beam; a photomultiplier is used for electron detection. Adapted from [17].

Both TEM and SEM use a beam of electrons, electromagnetic/electrostatic lens and electron apertures to create images. TEM has a resolution greater than SEM but sample preparation for TEM is more complex. Because SEM imaging relies on electron interactions at the surface, rather than transmission, it is able to image bulk samples and has a much greater depth of view, producing images that are a good representation of the 3D structure of a sample while TEM is limited to the production of 2D images.

3.12 Atomic Force Microscopy (AFM)

Sample surfaces are characterised by AFM through their interaction with the sharp tip of a probing cantilever. The movement of this highly flexible cantilever is precisely controlled by a piezo scanner. The cantilever scans over the surface line by line, and its vertical deflection is measured by the reflection of the laser beam focused on its back, which is then detected by a photosensitive detector (Figure 3.39). The deflection, and consequently the force applied by the cantilever onto the sample is measured and regulated by adjusting the vertical position of the cantilever using a feedback loop, allowing the reproduction of the topography of the sample with picometer resolution.[16]

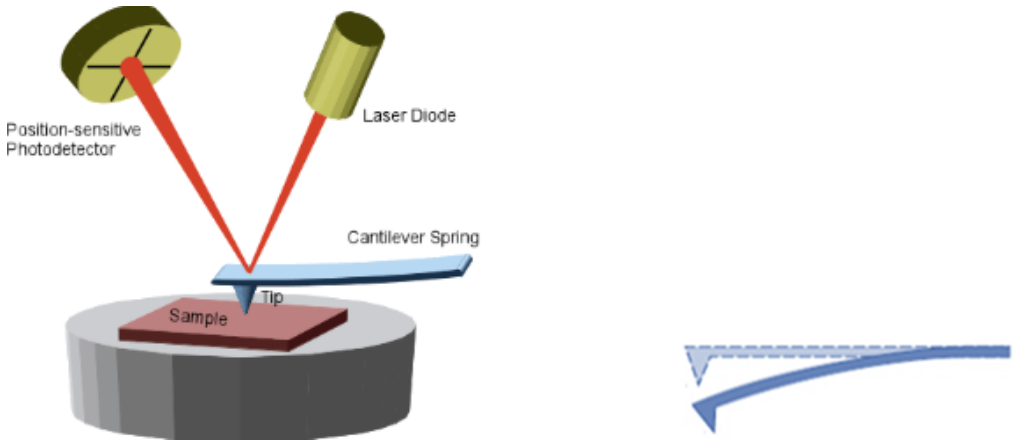

Figure 3.39 – Schematic representation of AFM main components and deflection of the cantilever as a result of its interaction with the sample. Adapted from [18].

A variety of operating modes can be used (Figure 3.40). In contact mode the tip scans in close contact with the surface and vertical deflection (force) is used as the set point. The magnitude of the force applied by the probe to the the surface can potentially cause sample damage and movement of relatively loosely attached objects. In tapping mode, a vertically oscillating tip alternately contacts with the surface and then is lifted off the surface, reducing lateral forces on the tip. In non-contact mode, an oscillating tip scans the surface without touching it, the cantilever's resonant frequency providing an indirect measure of the sample topography.

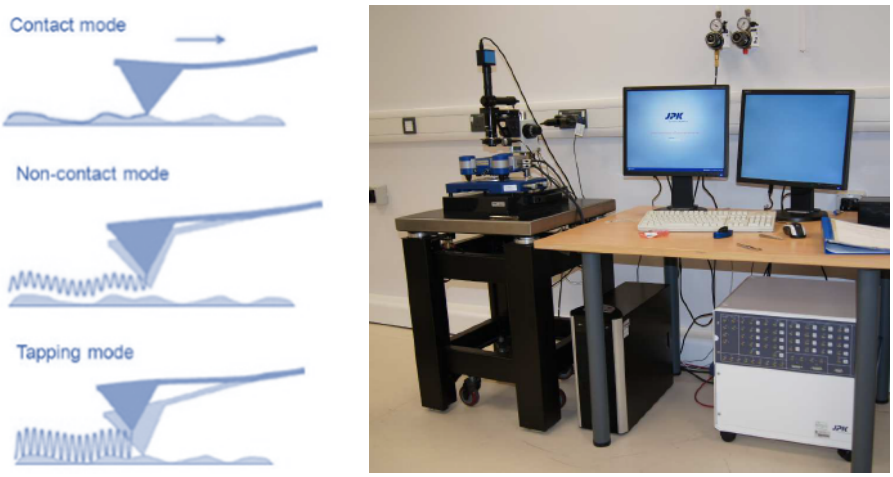

Figure 3.40 – Left: Schematic representation of AFM different operation modes. Adapted from [19]. Right: Photo of JPK NanoWizard II AFM.

AFM can be used for investigation of the roughness of a surface. Common roughness parameters are the roughness average (Ra) and the root mean squared roughness (RMS or Rq). An example of a line-profile, representing the height values as a function of the evaluation length, is shown in Figure 3.41. To evaluate the roughness of a surface, the line is extended to an area, arithmetic mean height (Sa) and root mean squared height (Sq)

representing the average of the absolute values of z (x,y) and the root mean squared of z(x,y) in the measured area, respectively (Figure 3.42).

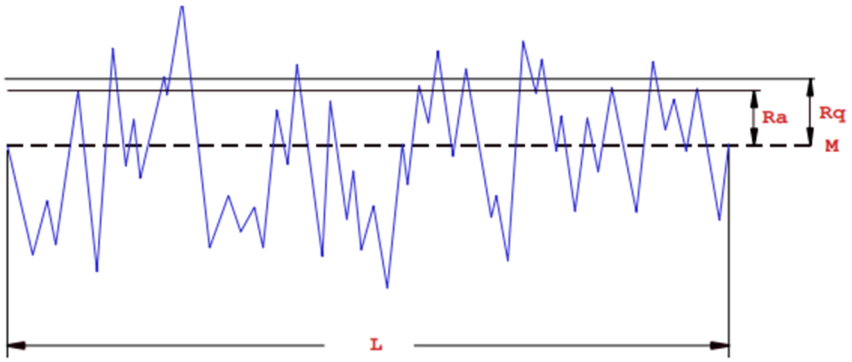

Figure 3.41 – Line profile showing Ra and Rq roughness for the evaluation length L, M representing the mean line.

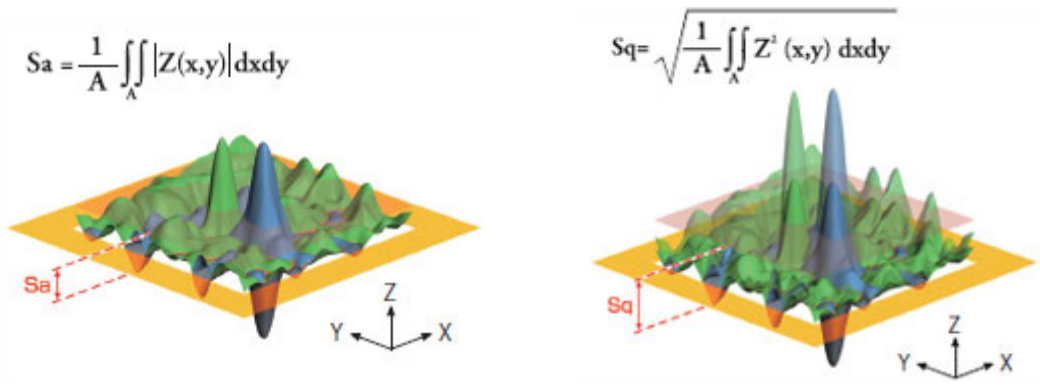

Figure 3.42 – 3D area roughness parameters Sa and Sq, expansions from 2D roughness parameters Ra and Rq, with the mean plane represented in yellow. Adapted from [20].

3.13 Physical Vapor Deposition (PVD) by Sputtering

Physical vapor deposition (PVD) of thin films by sputtering consists of using bombardment of ions to remove atoms or molecules from a target material, which then diffuse to the substrate (such as a silicon wafer) where condensation occurs, leading to the formation of a film with controlled and uniform thickness[21]. This process occurs in a

vacuum chamber. A plasma is generated by ionizing the sputtering gas, commonly an inert gas such as argon. A negative bias is applied to the target material, with the substrate grounded (Figure 3.43). The pressure is controlled in a way that is high enough for collisions to occur but not so high as to prevent the electrons gaining enough energy between collisions to ionize the atoms. Different types of sputtering power sources can be used to ionize the gas, including direct current (DC) and Radio Frequency (RF) for insulating target materials. The deposition rate is proportional to the sputtering rate which depends mostly on the type of target atoms and on incident ions energy and angle of incidence. The sample holder is usually rotated during the deposition process in order to obtain a uniform coating.

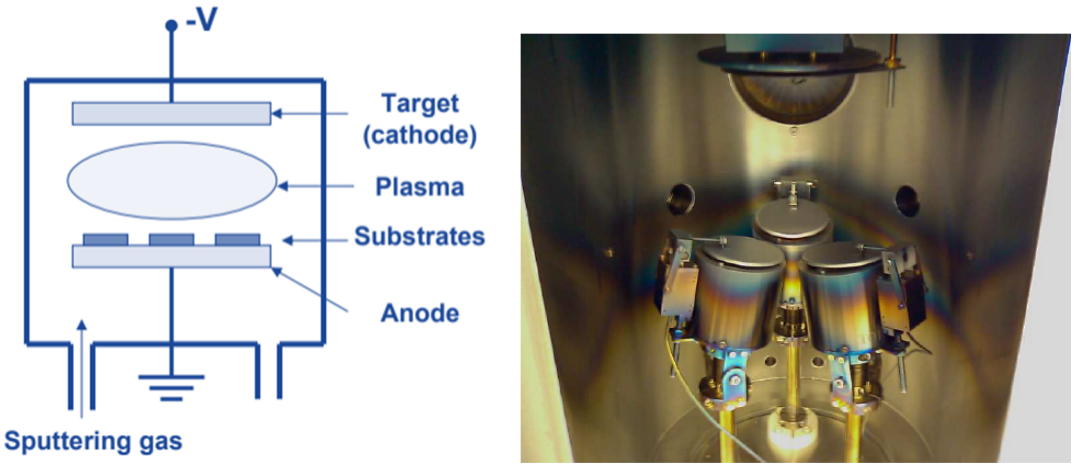

Figure 3.43 - Left: Schematic representation of a sputtering PVD setup. Right: Photo of the Lesker PVD 75 deposition chamber, showing the three magnetron sources.

3.14 List of References

1. Yuan, Y.; Lee, T. R., Contact Angle and Wetting Properties. In *Surface Science Techniques*, Springer-Verlag, Ed. 2013; Vol. 51, pp 3-34.

2. Surface free energy - theory and calculations. In *Theory Note 4*, Attension Biolin

Scientific.

3. Tompkins, H. G., *A user's guide to ellipsometry*. Academic Press: 2013.

4. Stojilovic, N., Why Can't We See Hydrogen in X-ray Photoelectron Spectroscopy? *Journal of Chemical Education* **2012,** *89* (10), 1331-1332.

5. Cushman, C.; Chatterjee, S.; Major, G.; Smith, N.; Roberts, A.; Linford, M., Trends in advanced XPS instrumentation. *Vacuum Technology and Coating* **2016**.

6. Riviére, J.; Myhra, S., XPS and UPS, AES and ISS. In *Handbook of surface and interface analysis: methods for problem-solving*, CRC Press.

7. Smith, G., Evaluation of a simple correction for thr hydrocarbon contamination layer in quantitative surface analysis by XPS. *Journal of Electron Spectroscopy and Related Phenomena* **2005,** *148* (1), 21-28.

8. Johansson, L.; Campbell, J., Reproducible XPS on biopolymers: cellulose studies. *Surface and Interface Analysis* **2004,** *36* (8), 1018-1022.

9. Homola, J., *Surface Plasmon Resonance Based Sensors*. Springer-Verlag Berlin Heidelberg: 2006.

10. Hunt, I. http://www.chem.ucalgary.ca/courses/351/Carey5th/Ch13/ch13-nmr-1b.html (accessed 08/2018).

11. Nieman, T.; Skoog, D.; Holler, F., *Principles of Instrumental Analysis*. 5th edition ed.; Brooks Cole: 1997.

12. Quenching of Fluorescence. In *Principles of Fluorescence Spectroscopy*, Lakowicz, J., Ed. Springer: Boston, 2006; pp 277-300.

13. Diaspro, A.; Chirico, G.; Usai, C.; Ramoino, P.; Dobrucki, J., Photobleaching. In *Handbook of Biological Confocal Microscopy*, Pawley, J. B., Ed. Springer Science+Business Media: New York, 2006.

14. An Introduction to Compensation for Multicolor Assays on Digital Flow Cytometers. *BD biosciences technical bulletin* **2009**.

15. Nikon https://www.microscopyu.com/techniques/phase-contrast/introduction-to-phase-contrast-microscopy (accessed 09/2018).

16. Leng, Y., *Materials Characterization - Introduction to Microscopic and Spectroscopic Methods*. John Wiley & Sons: 2013.

17. ScientaOmicron https://www.scientaomicron.com/en/products/uhv-nanoprobe/instrument-concept (accessed 09/2018).

18. Helm, C. https://physik.uni-greifswald.de/en/soft-matter-and-biophysics-prof-

christiane-helm/methods/afm-atomic-force-microscope/ (accessed 09/2018).

19. Baselt, D. The tip-sample interaction in atomic force microscopy and its implications for biological applications. California Institute of Technology, 1993.

20. Olympus https://www.olympus-ims.com/en/knowledge/metrology/roughness/3d_parameter/ (accessed 08/2018).

21. Mattox, D., *Handbook of Physical Vapor Deposition (PVD) Processing* Elsevier 2010.

4 Development of an electrically switchable surface

This chapter describes studies conducted on an ON-OFF type electrically switchable smart system, which exhibits the ability to expose and conceal progesterone on demand. Contact angle, ellipsometry, XPS and eSPR were the techniques selected to characterise the system and demonstrate its specificity by looking at complementary control systems. This smart system can be described as a sensing platform that is able to, on demand, selectively capture progesterone antibody in solution. Whilst being developed to be integrated in a biomedical device for assessment of sperm quality and fertilizing potential, the application of this system can be widely extended as this approach can be applied to other antigen-antibody systems. Preliminary studies on the development of an alternative and novel switchable system, OFF-ON type, are also described in this chapter, mainly consisting of strategic planning and XPS characterisation of different SAMs formed on gold.

Part of the work described in this chapter was recently published in a scientific journal:

Gomes, B. S.; Cantini, E.; Tommasone, S.; Gibson, J. S.; Wang, X.; Zhu, Q.; Ma, J.; McGettrick, J. D.; Watson, T. M.; Preece, J. A.; Kirkman-Brown, J. C.; Publicover, S. J.; Mendes, P. M., On-Demand Electrical Switching of Antibody–Antigen Binding on Surfaces. *ACS Applied Bio Materials* **2018.**

4.1 Introduction

This section starts with a brief introduction to biosensing platforms based on antibody-antigen interactions, followed by introducing stimuli responsive surfaces as the foundation for the development of novel tools for assisted reproductive technologies (ART), namely for sperm cell selection for Intracytoplasmic sperm injection (ICSI). Finally, this section includes a summary of preliminary studies performed towards developing a sensing platform that allows for controlled and specific capture of antibodies on surfaces, which

constitutes the foundation of the studies reported in this chapter, and points out the demand for further studies.

4.1.1 Biosensing platforms based on antibody-antigen binding interactions

According to IUPAC (International Union of Pure and Applied Chemistry), biosensors are a subset of chemical sensors that make use of, or detect, biologically relevant molecules or biological entities. Antibodies, antibody fragments, protein receptors, tissues, organelles, whole cells, nuclei acids or enzymes, can be used as biological recognising elements. Antibody-antigen binding interactions are at the heart of many biosensing platforms[1-3]. The incorporation of an antigen or antibody on surfaces and detection of their binding partner in solution has been developed into numerous clinical, non-clinical and research applications. In particular, the quantitative detection of antibodies is critical in the monitoring of antibodies production in cell culture, many bioanalytical assays and surveillance of a broad range of diseases, including autoimmune diseases, infectious diseases and allergies[4-5]. Furthermore, detection of anti-drug antibodies, which can be elicited *in vivo* to a therapeutic antigen, forms the core of the evaluation of drug immunogenicity[6]. While a wide variety of sensitive antibody detection strategies have been developed[7-9], a limitation in the inability to exert on-demand control over the sensing of target antibodies still exists. On-demand specific capture of antibodies on surfaces provides the opportunity for detection only when required, allowing the development of high-performance sensors. Such sensors could be applied, for instance, in the near real-time, long-term monitoring of biological processes in cell culture systems or in diagnostic devices for disease detection and surveillance on-demand[10-11].

Surfaces with temporal control attributes are the focus of many recent efforts, where materials exhibit the ability to modulate their properties in response to diverse external stimuli, such as electric, optical, thermal and chemical[12-14]. Surfaces have been created that are able to control bacterial adhesion *via* modulation of non-specific interactions[15-16]. Furthermore, different stimuli have been employed to control protein[17-18] and cell adhesion[19-21] on surfaces. For instance, a new class of electrically-responsive surfaces has been developed, based on the response of a charged molecular switching unit on the structure of a mixed self-assembled monolayer (SAM) to control the binding activity of a surface-tethered biotin to neutravidin in solution[17, 22-23] and surface-tethered arginylglycylaspartic acid **(**RGD) to macrophage cells[21]. These studies were based on the switching units being located in close proximity to the binding site and the binding sites being highly flexible. It has not yet been shown that electrically-responsive surfaces can be developed to control antigen-antibody interactions, in which the presence of structurally rigid binding sites and the requirement for a linker segment to promote high affinity binding represent key features to consider in the rational design of high-performing and efficient switchable sensors.

4.1.2 Stimuli-responsive surfaces as the foundation for the development of novel tools for assisted reproductive technologies (ART)

Infertility is a disease and represents a global reproductive health problem, estimated to affect as many as 186 million people worldwide[24]. Sperm dysfunction is the single most common cause of male infertility and there are currently no drugs available on the market to alleviate this condition[25]. The only option for treatment is ART, which includes fertility treatments that handle eggs and sperm, in vitro fertilization (IVF) and ICSI being the most

common types of ART. These two methods differ in the way fertilisation is achieved. ICSI (Figure 4.44) is a procedure that entails the injection of a single sperm directly into the cytoplasm of an egg, while IVF promotes the mixing of eggs and sperm in a petri dish, allowing the sperm to fertilise the egg *via* standard insemination. More than 500 000 ART cycles per year are undertaken in the EU and more than 2% of live births are achieved *via* ART[26]. However, these treatments are expensive, highly invasive, technically demanding, complex, and stressful for the patient[27]. The current live birth rate from ICSI averages around 30%. One reason for the low number is the quality of the sperm. Since ICSI has been developed, there has been little progress in obtaining a robust, clinically significant, cost effective tool for determining selection of the best sperm cell[28]. Currently, the most commonly used technique for sperm selection for ICSI is visual morphological assessment[29]. The WHO (World Health Organization) laboratory manual for the examination and processing of human sperm provides standard methods for the examination of human semen. Briefly, it recommends initial microscopic investigations, consisting of looking for sperm aggregation, mucus strand formation, the presence of cells other than spermatozoa and isolated sperm heads or tails. The number of sperm cells and non-sperm cells, the motility and viability of the sperm cells are then accessed. Finally, the cells are stained and examined. A method is recommended for normal/abnormal classification, which entails, for example, the shape and smoothness of the sperm head, the presence of vacuoles and the dimensions of the main components of the cell. The presence of head, neck, midpiece, and tail defects is investigated as well as the presence of excess residual cytoplasm. These methods do not screen for sperm developmental, nuclear and cytoplasmatic competence. In fact, chromossomal aberrations have been detected in sperm cells classified as normal after morphological assessment[30]. Despite the fact that many aspects of sperm cell biology and its surface dynamics are known, a lot of crucial

information is still lacking[31-33], thus preventing the development of novel generation sperm handling tools.

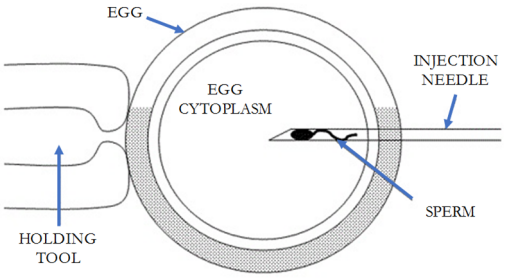

Figure 4.44 – Schematic representation of the ICSI procedure, where a single sperm is injected directly into the cytoplasm of an egg using a fine needle. Adapted from [34].

It is well known that progesterone, an ovarian steroid hormone, plays a crucial role as a sperm function modulator, even though the complex mechanisms involved are not yet completely understood[33]. Progesterone released by the oocyte-cumulus complex is responsible for the increase of intracellular calcium $[Ca^{2+}]_i$, by activating the CatSper - cationic channel of the sperm flagellum [35-36] (Figure 4.45). In turn, the influx of Ca^{2+} triggers a change in the flagellar activity of the cell[37]. The key importance of $[Ca^{2+}]_i$ signalling in the regulation of sperm function is well established[38]. Most essential sperm functions are controlled by changes in $[Ca^{2+}]_i$ and lesions in CatSper, and damaged human sperm function is linked to the two[39]. The mechanism by which progesterone regulates sperm activation has been recently proposed: upon progesterone stimulation, endocannabinoids - endogenous inhibitors of CatSper - are hydrolysed by the serine hydrolase ABHD2, leading to opening of the CatSper channel[40]. ABHD2 therefore acts as a progesterone receptor, with it being activated once bound to progesterone.

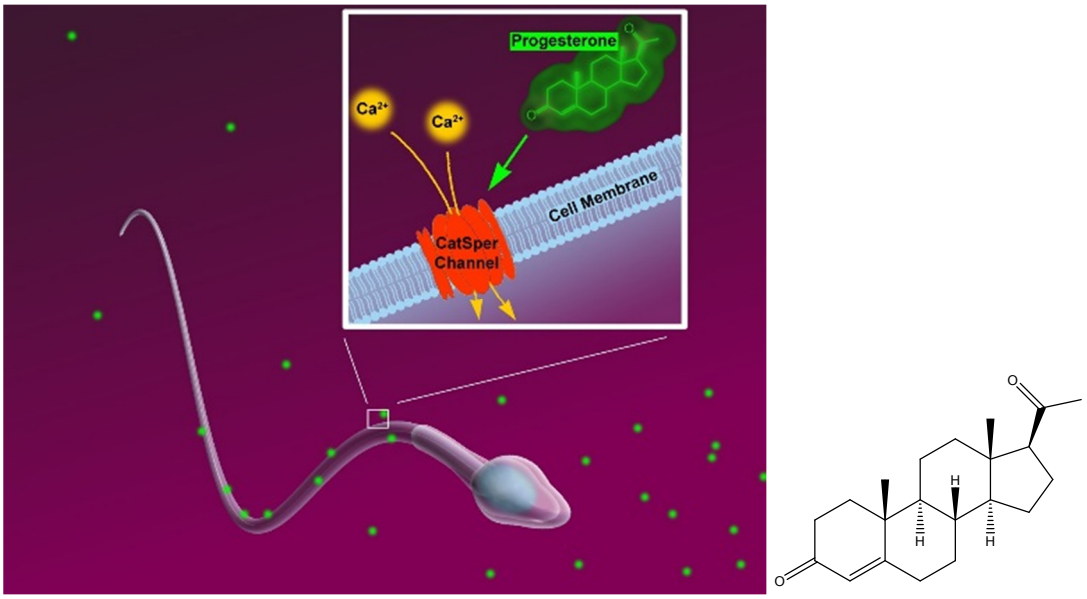

Figure 4.45 – Left: Schematic representation of the CatSper channel on the sperm cell, with calcium intake being induced by exposure to progesterone. Adapted from [41]. Right: Chemical structure of progesterone.

Sperm response to progesterone (and subsequent $[Ca^{2+}]_i$ signalling) is a good marker of sperm quality[42-44]. Ca^{2+} influx and resulting motility responses induced by progesterone can be used as a diagnostic test of sperm quality and functional competence. When exposed to progesterone, high quality sperm cells initiate rapid calcium intake and generate a burst of motility, causing reorientation or spinning of the cell. Current techniques to assess such responses are, however, cumbersome and subjective[45]. Being able to assess Ca^{2+} responses and flagellar activity in a large number of cells before and during brief, reversible, exposure to progesterone may be a novel, simple, rapid and potentially cheap high-throughput assessment of sperm quality and fertilizing potential. This system could be integrated into use with simple light-microscopy of cell motility to enable selection of good quality sperm cells – those where Ca^{2+} signalling is expressed and functional - for assisted reproductive technology uses, particularly for ICSI.

Preferable, an alternative to the use of a perfused progesterone solution or its addition to a dish for interaction with cells, should be used - a system that offers simplicity of use and feasibility to standardise, without the need for progesterone solution removal or its reapplication, which would make the process more difficult and slow. The fluid movement caused by the injection of a progesterone solution could also induce a false positive response of the cells. With this proviso in mind, the development of a smart switchable surface that can control, on demand, the exposure of sperm agonists, such as progesterone, was initiated.

4.1.3 Preliminary studies on the development of an electrically switchable surface able to expose and conceal progesterone

Preliminary studies were conducted by a previous PhD student (Eleonora Cantini) on the development of an electrically switchable surface able to expose and conceal progesterone as a function of surface potential[46]. To demonstrate the switching capability of this surface, its interaction with progesterone-antibody was investigated. This work will now be briefly described, in order to put in context the work presented in this chapter.

This system is based on the conformational switch of positively charged oligolysine peptides that are tethered to a conductive substrate, with progesterone (the bioactive molecule) being attached to the opposite end of the peptide. It is a ON-OFF system, where progesterone is initially exposed, switching to a concealed mode when a negative potential is applied to the surface. A representation of this system is shown in Figure 4.46. The stimuli-responsive surface is created on a gold sensor chip and comprises of a mixed SAM with two components: an oligopeptide (progesterone-C7-4KC) and a hexaethylene glycol-terminated thiol (C11EG6). The oligopeptide contains a terminal cysteine for attachment to the gold surface, four lysine residues as the electrically responsive switching unit, an alkyl

linker that separates the switching unit from the progesterone/antibody binding site while also holding the antigen above the surface for optimal antibody recognition, and the rigid progesterone antigen binding unit. The C11EG6 moieties on the mixed SAM have a triple function, namely (i) preventing non-specific binding, (ii) assisting in spacing out the oligopeptides to enable conformational changes to occur, and (iii) promoting accessibility of the antibody towards the surface-tethered progesterone such that binding can be maximised in the ON state. Since surface-tethered lysine residues, which exhibit protonated amino side chains at physiological pH, can adopt two distinct conformations, namely linear and folded, under a positive and negative potential, respectively,[22-23] it was reasoned that such conformational modulation could be potentially applied to provide precise temporal control over the activity and steric accessibility of the progesterone antigen to the antibody.

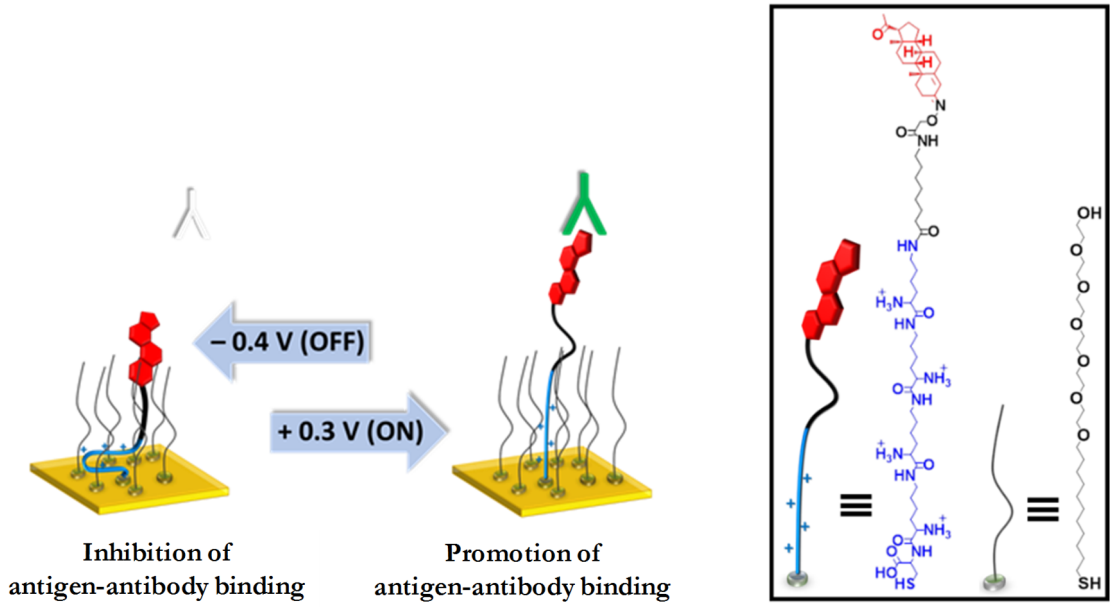

Figure 4.46 - Schematic of the dynamic progesterone-C7-4KC oligopeptide SAM harnessed for temporal control of antibody binding. The electrically responsive SAM conceals the rigid progesterone unit under a negative potential (–0.4 V), inhibiting antibody binding, via folding of the peptide residues pulling progesterone into the surface of the SAM. Conversely, a positive potential (+0.3 V) promotes antigen activity and consequently allows high antibody binding capacity, via

unfolding of the peptide residues, releasing the progesterone unit from the surface of the SAM. Inset: chemical structures of the progesterone-C7-4KC oligopeptide (left) and oligo(ethylene glycol) thiol (C11EG6) (right) used for mixed SAM formation.

This work reported a new molecular design that harnesses a surface-based conformational switching mechanism[22-23] to introduce a sensing platform that allows for efficient and specific capture of antibodies on surfaces only when desired. The on-demand sensing of antibodies is based on an electrical stimulus that offers several attractive features to be integrated with sensing platforms since it provides fast response times, allows for easy creation of multiple individually addressable switchable regions on the same surface, and uses low applied voltage and electrical field strengths that are biocompatible[47]. Herein, the smart surfaces are integrated with a surface plasmon resonance (SPR) sensing platform, allowing label-free and real-time detection. Progesterone, being a low molecular weight antigen, is characterized by a rigid core chemical structure, which is also present in many steroid hormones and many drug antigens where the steroid skeleton is combined with structural elements possessing appropriate biological activities.[48-49] An IgG anti-progesterone antibody, progesterone-3 anti-mouse monoclonal antibody (anti-Pg MAb), was selected and employed as the target for on-demand sensing.

The progesterone-C7-4KC:C11EG6 mixed SAM was characterised by CA, ellipsometry and XPS, which confirmed the presence of both components. This mixed SAM was formed from the incubation of gold surfaces in solutions of 0.98 : 0.02 C11EG6 : progesterone-C7-4KC, selected based on previous studies[17, 23].

Following the characterisation of the mixed SAM, attention was turned to the investigation of its antibody binding capability and ability to switch progesterone antigen activity on-demand. Antibody binding to the switchable SAMs was investigated using electrochemical

SPR (eSPR), which allowed monitoring of surface binding while an electrical potential was applied to the surface using a three-electrode electrochemical cell and a potentiostat. In this system, the gold surfaces act as the working electrode, a Pt wire as the counter electrode, and an Ag/AgCl electrode as the reference electrode. Monitoring of surface binding was initiated by establishing a baseline using phosphate buffer saline (PBS) solution while no electrical potential (open circuit (OC) conditions), negative (–0.4 V) or positive (+0.3 V) potential was applied. Subsequently, the antibody for progesterone - anti-Pg MAb - diluted in degassed PBS was flowed over the surface, after which the surface was rinsed with continuous flow of PBS to remove any unbound antibody.

The recorded sensorgrams for the progesterone-C7-4KC:C11EG6 mixed SAM at different electrical potential conditions (OC (no applied potential), −0.4 V and +0.3 V) are illustrated in Figure 4.47. Table 4.1 summarises the final binding capacity (BC) at the three electrically different states, as well as the switching efficiency (SE) for the mixed SAM. The BC is defined as the difference in the SPR response units between the beginning of the antibody injection and the end of washing with PBS. The SE was calculated as the percentage difference between the binding capacity when a positive potential was applied (BC_{ON}) and the binding capacity when a negative potential was applied (BC_{OFF}), divided by BC_{ON}:

$$\boldsymbol{SE = \frac{BC_{ON} - BC_{OFF}}{BC_{ON}} \times 100}$$

Equation 4.4

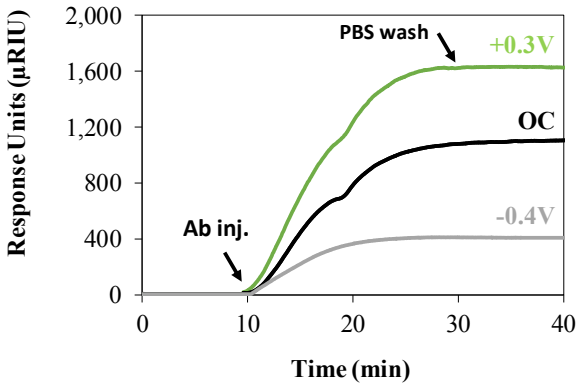

Figure 4.47 – SPR sensorgrams for the binding of anti-Pg MAb to the progesterone-C7-4KC:C11EG6 mixed SAM, in PBS, under OC (no applied potential), ON (+0.3 V) and OFF (−0.4 V) conditions. Adapted from [46].

Table 4.1 – Binding capacity under OC (no applied potential), OFF (−0.4 V) and ON (+0.3 V) conditions, expressed in Response Units (RU), and switching efficiency of the progesterone-C7-4KC:C11EG6 mixed SAM. The values are the average of three samples, with the errors reported as standard deviation.

Binding Capacity, BC (RU)			**Switching Efficiency, SE (%)**
−0.4 V	**OC**	**+0.3 V**	
478 ± 39	1,195 ± 39	1,744 ± 90	73 ± 3

The progesterone-C7-4KC:C11EG6 mixed SAM shows high antibody binding with immobilization capacity of at least 1.2 ng/mm^2 in OC conditions and 1.7 ng/mm^2 for an applied potential of +0.3 V (1,000 RU = 1 ng/mm^2).

While good accessibility occurs in OC conditions, the presence of +0.3 V induces further increase in binding capacity that can be explained by the adopted unfolded and extended

conformation of the oligolysines under a positive electrical potential.[22-23] The results suggest that in a fully extended state, the progesterone moieties are largely free from steric interactions from the surface, and thus, are entirely exposed for antibody binding. In OC conditions, the progesterone-C7-4KC is more flexible and adopts multiple conformations that can be partially buried by the C11EG6 chains. When a negative potential is applied the oligolysines collapse to a folded conformation, pulling the progesterone head partially into the C11EG6 chains and concealing it from the subphase, resulting in decreased binding capacity.

A switching efficiency above 70% was achieved for this system. The switching efficiency is highly dependent on the ability of concealing the progesterone moiety under a negative potential and there is a substantial reduction of the binding capacity, from ~1700 RU to ~500 RU with a change in electrical potential.

4.1.4 Demand for further studies

Further investigations of the system described above are the aim of this chapter, in order to proceed with the development of a biomedical device for high quality sperm cell assessment and also to facilitate the general application of this approach to other antigen-antibody systems. For instance, the response of the system to a different range of potentials applied to the surface will be explored and additional control experiments run, to demonstrate the specificity of this system. These studies are crucial for drawing conclusions about this new sensing platform.

In addition, a new approach for a switchable surface is proposed which has an OFF-ON switching where the bioactive molecule is initially hidden and a negative potential is applied when the exposure of the biomolecule is demanded (Figure 4.48). This will guarantee a

better control of the surface, in comparison with the ON-OFF system mentioned above. When using these devices for studies with cells, progesterone will not be exposed before the stimulus is applied. Moreover, the stimulus is not required during cell attachment procedure.

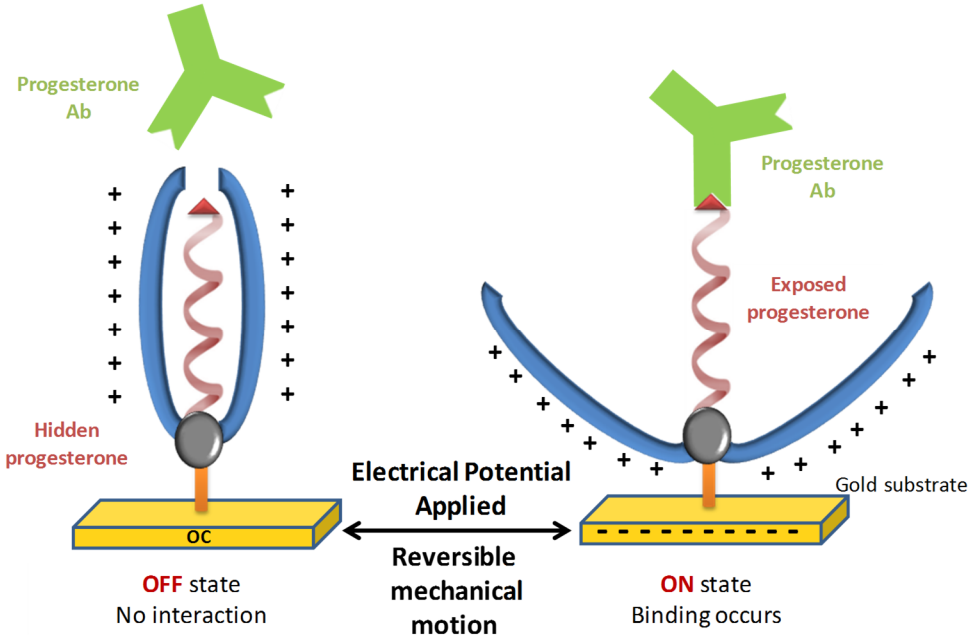

Figure 4.48 – Schematic representation of a switchable surface where double-arm molecules are employed as cages to the bioactive molecules (progesterone in this case), concealing (inactive state) or exposing (active state) the functional regions. Upon application of a negative potential, the positively charged double-arm molecular system will experience an attractive force to the surface, leading to a mechanical motion that will expose the bioactive molecule and promote binding to an antigen (progesterone antibody).

4.2 Aim and Objectives

The aim of the work described in this chapter is therefore to proceed with the development of an electrically switchable surface, following preliminary studies. In addition, a new approach for a switchable surface will be outlined.

The following objectives were outlined:

1. Additional surface characterisation and optimisation of the progesterone-C7-4KC:C11EG6 mixed SAM.
2. Electrochemical SPR studies using a different range of potentials applied to the surface, comparing to the ones previously applied, to understand the effect of the electrical potential on the switching efficiency of the progesterone-C7-4KC:C11EG6 mixed SAM.
3. Formation and characterisation of 5KC:C11EG6 mixed SAM, a surface in which no progesterone is present, to investigate the specificity of the progesterone-C7-4KC:C11EG6 mixed SAM.
4. Formation and characterisation of progesterone-C11-SH:EG3SH mixed SAM, a surface in which no peptide is present, to investigate whether the switching occurs due to the presence of the peptide.
5. Preliminary studies on the development of an alternative switchable surface, OFF-ON type of switching - SAM formation and characterisation.

4.3 Results and Discussion

4.3.1 Additional optimisation of progesterone-C7-4KC:C11EG6 mixed SAM and surface characterisation

In order to continue the studies with the progesterone-C7-4KC:C11EG6 mixed SAM (described in 4.1.3), additional optimisation of the SAM formation was performed as well as additional characterisation.

The XPS analysis of the mixed SAM previously revealed a high percentage of unbound sulfur[46]. The introduction of an ultrasonic bath step to the rinsing process was therefore investigated, aiming to reduce the amount of unbound sulfur. The high-resolution scans of the S 2p regions are shown in Figure 4.49. From the fitting of the S 2p regions and area integration, the percentage of unbound sulfur was calculated and is shown in Table 4.2. A reduction from 39.2 % ± 1.2 of unbound sulfur to 20.7 % ± 0.4 was observed. Bound thiolate is known to have a S $2p_{3/2}$ binding energy of 161.9 eV[50]; the second doublet corresponds to sulfur not bound to the gold, being present at a higher energy (S $2p_{3/2}$ at 163.5 eV).

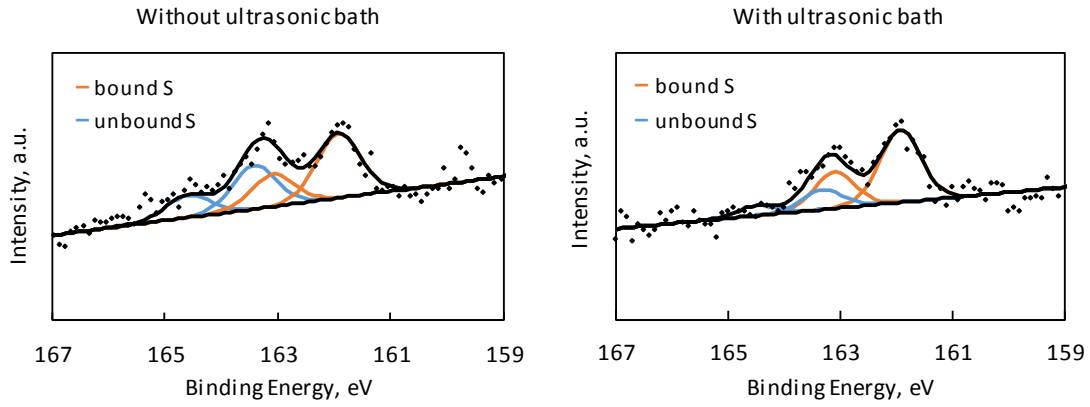

Figure 4.49 - XPS high resolution scans of S 2p region with fitted component peaks, showing bound and unbound sulfur in the progesterone-C7-4KC:C11EG6 mixed SAM, without (left) and with (right) ultrasonic bath in the rinsing step of SAM formation.

Table 4.2 – Percentage of bound and unbound sulfur calculated from XPS high resolution scans of S 2p region for the progesterone-C7-4KC:C11EG6 mixed SAM. The values are the average of three samples, with the errors reported as standard deviation.

	bound S 2p %	**unbound S 2p %**
Previously measured (without ultrasonic bath)	63.2 ± 0.7	36.8 ± 0.7
Without ultrasonic bath	60.8 ± 1.2	39.2 ± 1.2
With ultrasonic bath	79.3 ± 0.4	20.7 ± 0.4

From the XPS data, the surface fraction of each component of the mixed SAM was calculated (Table 4.3). From integrating the area of the S 2p and N 1s peaks and taking into consideration that the oligopeptide contains 11 N atoms and 1 S atom and the C11EG6 contains no N atoms and only 1 S atom, the number of C11EG6 per oligopeptide on the surface was calculated using Equation 4.5. The mole fraction was then calculated, being the ratio of each component to the total number of moles of both components.

$$\text{No. of molecules of C11EG6} = \left(11 \times \frac{Area_{S\,2p}}{Area_{N\,1s}}\right) - 1$$

Equation 4.5

The calculated value is comparable, within the error, to the solution mole fractions used to prepare the progesterone-C7-4KC:C11EG6 mixed SAM.

Table 4.3 – Mole fractions of each component of the progesterone-C7-4KC:C11EG6 mixed SAM, in solution and on the surface, calculated from the XPS data. The values are the average of three samples, with the errors reported as standard deviation.

	mole fraction progesterone-C7-4KC	**mole fraction C11EG6**
in solution	0.02	0.98
on the surface	0.03 ± 0.01	0.97 ± 0.01

This variation of the rinsing process didn't change the switching efficiency of the surface, as tested by SPR, with a switching efficiency of 73 % obtained when injecting progesterone antibody under positive and negative potentials, the same as obtained previously[46].

Ellipsometry measurements were made before and after applying positive and negative potentials to the progesterone-C7-4KC:C11EG6 mixed SAM. Making use of a three-electrode electrochemical cell connected to a potentiostat, the potential was applied for 30 min in PBS, then the surfaces were rinsed with water and dried under a stream of argon. The control experiment consisted of immersing the sample in PBS for 30 min without any potential being applied, then rinsed with water and dried. Results are shown in Figure 4.50.

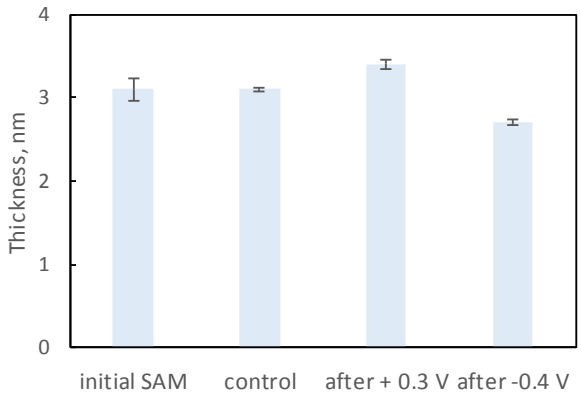

Figure 4.50 – Film thickness measured by ellipsometry before and after applying positive (+0.3 V) and negative (-0.4 V) potentials for 30 min to the gold surface functionalised with the progesterone-C7-4KC:C11EG6 mixed SAM. No potential was applied to the control surface, being immersed in PBS for 30 minutes. The values are the average of three samples, with the errors reported as standard deviation.

The measured film thickness is larger after a positive potential has been applied (3.40 nm ± 0.05) and smaller after a negative potential has been applied (2.70 nm ± 0.04), compared to the initial measured SAM thickness (3.10 nm ± 0.14). These results corroborate the assumption that progesterone is in closer proximity to the ethylene glycol matrix when a negative potential is applied to the surface, which is accordance with the eSPR results.

4.3.2 Different ranges of potentials applied for the switching of progesterone-C7-4KC:C11EG6 mixed SAM

SPR experiments were previously run using a maximum negative electrical potential of –0.4 V and a maximum positive potential of +0.3 V in order to prevent any undesirable loss of monolayer stability, based on previous potential and time-dependent electrochemical stability experiments conducted on peptide-based SAMs[17]. In order to understand the

effect of the electrical potential on the switching efficiency, eSPR experiments were conducted using less negative (–0.2 V) and positive (+0.2 V) potentials. As illustrated in Table 4.4, the switching efficiencies, as determined using Equation 4.4, were shown to decrease if such potentials are used as ON or OFF conditions. Thus, higher switching efficiencies are achieved by using high electrical potentials within the range of electrochemical stability of the SAM. It is likely that at high positive or negative potentials there is a stronger repulsion or attraction between the positively charged oligolysine SAMs and the positively or negatively polarized surface, respectively. While for the higher applied potentials, the conformation of the oligolysines changes from a fully extended conformation (at positive potential) to a folded conformation (at negative potential), the change in configuration is not so noticeable for less negative and positive applied potentials.

Table 4.4 - Switching efficiencies of the progesterone-C7-4KC:C11EG6 mixed SAM when different combinations of positive or negative potentials are used. The values are the average of three samples, with the errors reported as standard deviation.

ON Potential (V)	OFF Potential (V)	Switching Efficiency, SE (%)
+0.2	–0.2	4 ± 1
+0.2	–0.4	46 ± 8
+0.3	–0.2	38 ± 7

4.3.3 Investigation of the specificity of the system by testing the switching of different SAMs

In order to demonstrate that electrical potential control over antibody binding occurs due to conformational changes of the oligopeptide that lead to the concealment or exposure of the progesterone antigen, two different type of control SAMs were prepared and analysed. The first control was a 5KC:C11EG6 mixed SAM (Figure 4.51), a surface in which no progesterone is present, to address the question whether antibody binding occurs due to the presence of an electrical potential that attracts or repels the anti-Pg MAb.

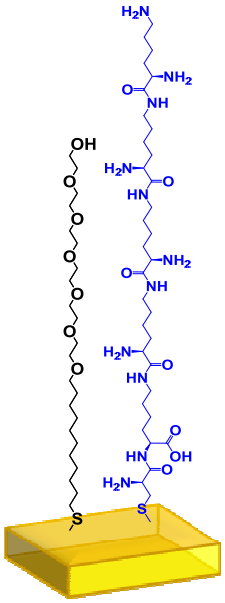

5KC:C11EG6 mixed SAM

Figure 4.51 - Chemical structures of the components used for the formation of the 5KC:C11EG6 mixed SAM on a gold substrate. The molecular structure shown on the left (black) is the C11EG6.

The 5KC:C11EG6 mixed SAM was prepared by immersion of a gold substrate into a solution of 0.98 : 0.02 C11EG6:5KC and characterized by contact angle and ellipsometry as shown in Table 4.5. As expected, the contact angle data shows the presence of a

hydrophilic surface, with similar thickness to that of the progesterone-C7-4KC:C11EG6 mixed SAM (3.0 ± 0.1 nm vs 3.1 ± 0.4 nm).

Following Cassie's law (Equation 4.6), the mole fraction of each component in the mixed SAM (q1 and q2) was calculated from the advancing contact angle values of each pure SAM (θ1 and θ2) and of the mixed SAM (θ12).

$$\cos \theta_{12} = q_1 \cos \theta_1 + q_2 \cos \theta_2$$

Equation 4.6

Table 4.5 - Advancing water contact angle and ellipsometric thickness values for the control 5KC:C11EG6 mixed SAM on gold surface. The values are the average of three samples, with the errors reported as standard deviation.

SAM	Mole fraction of C11EG6 in solution	Mole fraction of C11EG6 on the surface (from Cassie's law)	Contact Angle (°)	Thickness (nm)	
				Measured	Theor.
5KC	0	-	74 ± 5	3.3 ± 0.4	4.3
5KC:C11EG6	0.98	0.93 ± 0.04	44 ± 1	3.0 ± 0.1	-
C11EG6	1	-	41 ± 2	2.4 ± 0.1	2.9

The ratio of 5KC:C11EG6 on the surface is comparable to the one obtained for progesterone-C7-4KC:C11EG6 (0.93 ± 0.04 molar fraction of C11EG6 vs 0.97 ± 0.01

molar fraction of C11EG6, respectively). These values are also similar, within the error, to the mole fractions in solution used for the SAM formation (0.98).

XPS analysis was performed to confirm the chemical composition of the mixed SAM. High resolution scans were obtained for the key elements and are shown in Figure 4.52. From the integration of the elemental peak areas, relative atomic percentages for each element were calculated and are shown in

Table 4.6, as well as the relative component percentage for each element. The results obtained are in accordance with the theoretical values, based on the stoichiometry of the molecules, constituting further evidence for the formation of the 5KC:C11EG6 mixed SAM. From integrating the area of the S 2p and N 1s peaks and taking into consideration that the 5KC oligopeptide contains 11 N atoms and 1 S atom and the C11EG6 contains no N atoms and only 1 S atom, the number of C11EG6 per oligopeptide on the surface was calculated using Equation 4.5. The mole fraction was then calculated, being the ratio of each component to the total number of moles of both components. An average mole fraction of 0.03 ± 0.01 for 5KC and 0.97 ± 0.01 for C11EG6 was obtained for the mixed SAM. These values are in agreement with those obtained using the Cassie's equation. The three components fitted in the C 1s high resolution scan are assigned to C-H/C-C, C-O/C-N/C-S and C=O bonds[51], at binding energies of 284.8 eV, 286.6 eV and 288.2 eV, respectively. The two components fitted in the O 1s high resolution scan, at binding energies of 531.3 eV and 533.1 eV, are assigned to C=O and C-O bonds[51-53]. Unbound sulfur was detected on the surface and quantified as 33.1 %, in relation to bound sulfur. This is slightly higher than the unbound sulfur amount present in the progesterone-C7-4KC:C11EG6 mixed SAM (20.7 %).

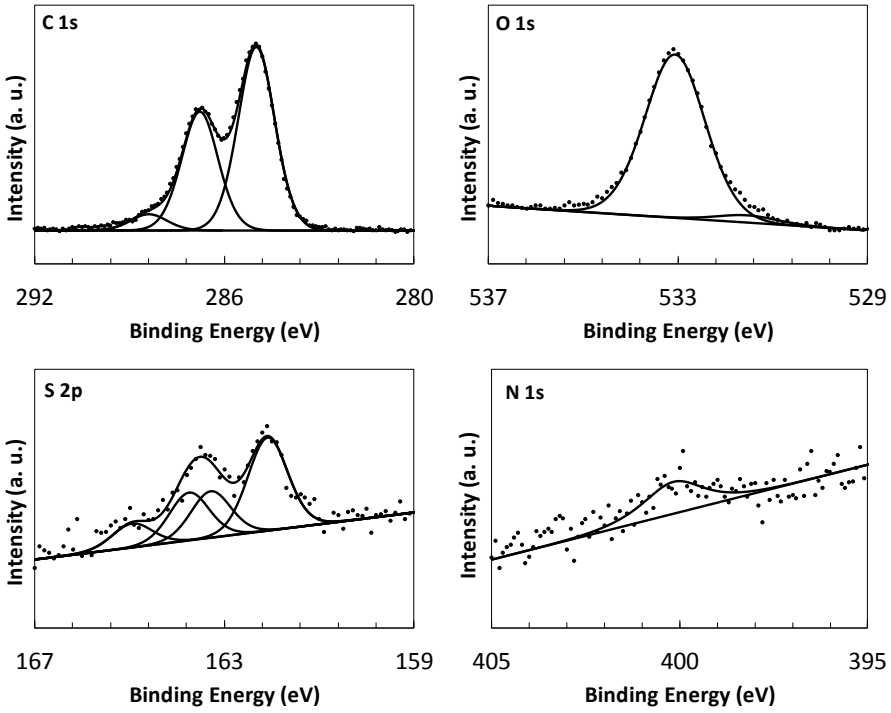

Figure 4.52 - XPS spectra of the C 1s, O 1s, S 2p and N 1s regions for the 5KC:C11EG6 mixed SAM.

Table 4.6 - Relative atomic percentages and relative component percentages for the 5KC: C11EG6 mixed SAM calculated from XPS spectra. The values are the average of three samples, with the errors reported as standard deviation.

	Relative Atomic Percentages		**Components**	**Relative Component Percentages**	
	Measured	**Theor.**		**Measured**	**Theor.**
O	16.5 ± 4.2	22.2	O-C	92.2 ± 1.2	97.8
			O=C	7.8 ± 1.2	2.2
C	78.4 ± 4.3	73.7	C-C	59.8 ± 5.4	39.4
			C-S, C-N and C-O	34.9 ± 5.5	59.9
			C=O	5.3 ± 0.1	0.7
S	3.9 ± 0.3	3.2	S-Au	66.9 ± 2.4	-
			S-H	33.1 ± 2.4	-
N	1.2 ± 0.1	1.0	-	-	-

The recorded sensorgrams for the 5KC:C11EG6 mixed SAM at three different electrical potential conditions (OC, −0.4 V and +0.3 V) are illustrated in Figure 4.53. The sensorgrams for the progesterone-C7-4KC:C11EG6 mixed SAM at different electrical potential conditions (OC, −0.4 V and +0.3 V), previously shown in Figure 4.47, were added to this Figure for comparison purposes. In contrast to different binding affinities of the antibody for progesterone-C7-4KC:C11EG6 mixed SAM at different electrical potentials, the amount of antibody that adsorbed non-specifically to the 5KC:C11EG6 mixed SAM under OC, −0.4 V and +0.3 V was very limited. The limited detected binding is likely to be a result of double layer effects. It is well known that at the electrode-solution interface, the value of the electrical potential differs from that in the bulk solution. This is due to the arrangement of positive and negative charges and solvent molecules at a small distance from the electrode surface. An electrical double layer is formed in this region, which is mainly influenced by the applied electrical potential and the electrolyte (in this case PBS) concentration.

These results demonstrate that the electrical potential has no direct effect on attracting or repelling the antibody to or from the surface.

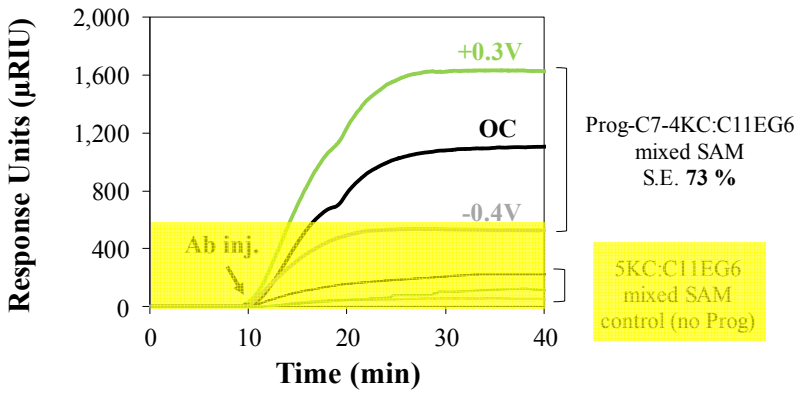

Figure 4.53 – SPR sensorgrams for the binding of anti-Pg MAb to the control 5KC:C11EG6 mixed SAM (no progesterone), in PBS, under OC (no applied potential), ON (+0.3 V) and OFF

(−0.4 V) conditions (highlighted in yellow); SPR sensorgrams for the binding of anti-Pg MAb to the progesterone-C7-4KC:C11EG6 mixed SAM are also included, for comparison purpose.

Another control mixed SAM was designed, prepared and characterised to demonstrate that modulation of antibody binding was due to the conformational changes of the progesterone oligopeptide on the surface induced by an electrical potential. The control mixed SAM was prepared with a non-switchable progesterone thiol (progesterone-C11-SH) and a tri(ethylene glycol) thiol (EG3SH), as shown in Figure 4.54.

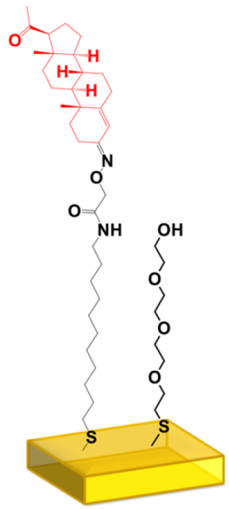

Progesterone-C11-SH:EG3SH
mixed SAM

Figure 4.54 - Chemical structures of the components used for the formation of the progesterone-C11-SH:EG3SH mixed SAM.

The progesterone-C11-SH compound was synthesised in collaboration with Dr. Stefano Tommasone by EDC/HOBt coupling of progesterone 3-(O-carboxymethyl)oxime and 11-amino-1-undecanethiol hydrochloride and isolated after column chromatography purification.

The progesterone-C11-SH:EG3SH mixed SAM was prepared by immersion of gold substrates into solutions of 0.98 : 0.02 EG3SH : progesterone-C11-SH and characterized by contact angle and ellipsometry as shown in Table 4.7. The advancing contact angle value obtained for the mixed SAM was between the contact angle values obtained for the pure SAMs of each component. From applying Cassie's law, a mole fraction of 0.91 ± 0.08 for EG3SH in the progesterone-C11-SH:EG3SH mixed SAM was calculated. The experimental thickness value obtained for the progesterone-C11-SH:EG3SH mixed SAM is also situated between the theoretical molecular length of both molecules, constituting another indication of the presence of a binary monolayer.

Table 4.7 - Advancing water contact angle and ellipsometric thickness values for the control progesterone-C11-SH:EG3SH mixed SAM on gold surfaces. The values are the average of three samples, with the errors reported as standard deviation.

SAM	Mole fraction of EG3SH		Contact Angle	Thickness (nm)	
	in solution	on the surface (from Cassie's law)	(°)	Measured	Theor
prog-C11-SH	0	-	73 ± 2	2.2 ± 0.1	2.8
prog-C11-SH:EG3SH	0.98	0.91 ± 0.08	37 ± 1	1.9 ± 0.4	-
EG3SH	1	-	32 ± 2	0.7 ± 0.1	1.4

As for the previous SAMs, XPS analysis was performed (Figure 4.55) to confirm the chemical composition of the formed mixed SAM. Table 4.8 shows the relative atomic percentages and relative component percentages for the progesterone-C11-SH:EG3SH mixed SAM. From integrating the area of the S 2p and N 1s peaks and taking into consideration that the progesterone-C11-SH molecule contains 2 atoms of N and 1 atom of S and the EG3SH molecule contains no N atoms and only 1 S atom, an average mole

fraction in the mixed SAM of 0.13 ± 0.02 for progesterone-C11-SH and 0.87 ± 0.02 for EG3SH was obtained. These results illustrate comparable surface fractions, within the error, to those indicated by the contact angle data. However, the surface mole fraction of EG3SH calculated from XPS data is significantly lower than the one used in solution (0.98), indicating preferential attachment of the progesterone-C11-SH component to the gold surface. The preferential adsorption of a longer chain component has been observed before with mixed SAMs and can be attributed to an overall thermodynamic control of the adsorption process[54].

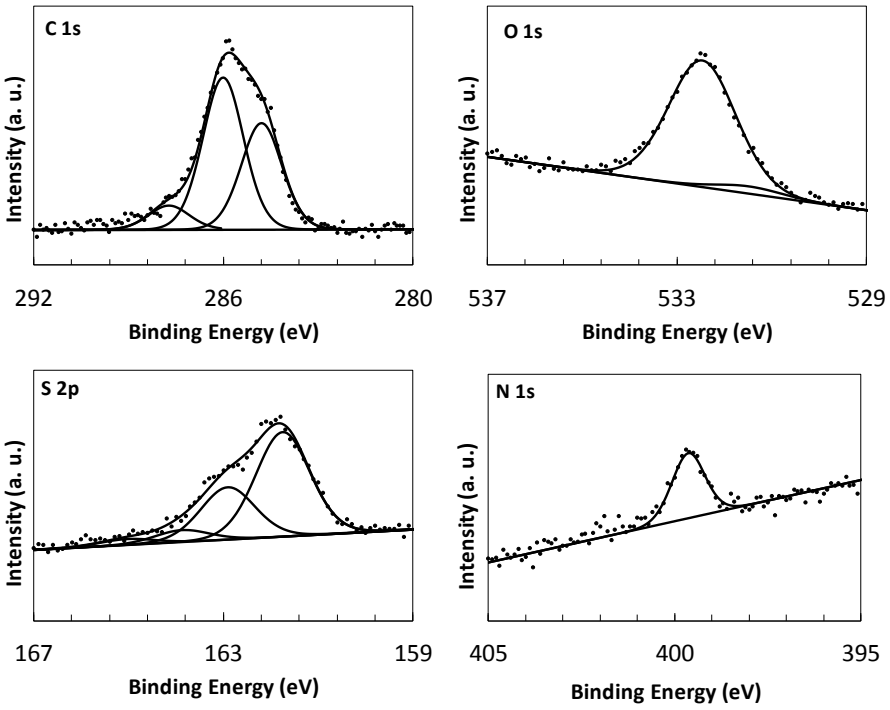

Figure 4.55 - XPS spectra of the C 1s, O 1s, S 2p and N 1s regions for the progesterone-C11-SH:EG3SH mixed SAM.

Table 4.8 - Relative atomic percentages and relative component percentages for the progesterone-C11-SH:EG3SH mixed SAM calculated from XPS spectra. The values are the average of three samples, with the errors reported as standard deviation.

	Relative Atomic Percentages		**Components**	**Relative Component Percentages**	
	Measured	**Theor.**		**Measured**	**Theor.**
O	20.1 ± 0.9	23.7	O-C	92.9 ± 1.3	93.2
			O=C	7.1 ± 1.3	6.8
C	60.0 ± 0.5	68.5	C-C	39.9 ± 2.4	30.7
			C-S, C-N and C-O	52.6 ± 1.9	67.0
			C=O	7.5 ± 0.8	2.4
S	15.7 ± 0.9	6.2	S-Au	90.5 ± 1.8	-
			S-H	9.5 ± 1.8	-
N	4.2 ± 0.4	1.6	-	-	-

The recorded sensorgrams for the progesterone-C11-SH:EG3SH mixed SAM at different electrical potential conditions (OC, −0.4 V and +0.3 V) are illustrated in

Figure 4.56. While the progesterone antibody binds to this surface, there is no significant effect when different electrical potential conditions are applied, the calculated switching efficiency being 18 ± 5 %. This result is in another indication that the switching is due to the oligolysine conformational changes. Sensorgrams were also acquired for EG3SH SAMs on gold to investigate the occurrence of non-specific binding, shown in the same Figure.

No significant difference was observed when applying the three different potential conditions on this surface, with minimal binding of progesterone antibody being detected.

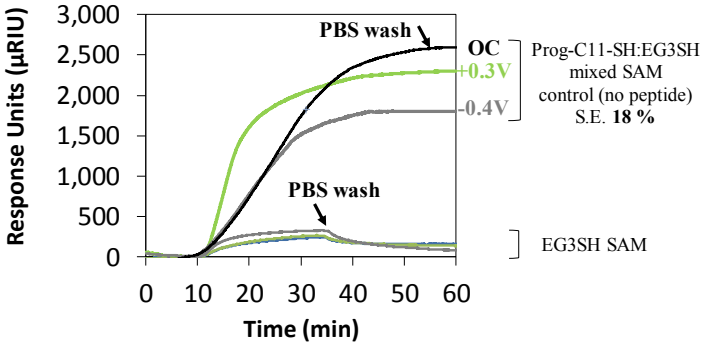

Figure 4.56 – SPR sensorgrams for the binding of anti-Pg MAb to the control progesterone-C11-SH:EG3SH mixed SAM (no peptide) and to the EG3SH SAM, in PBS, under OC (no potential), ON (+0.3 V), and OFF (−0.4 V) conditions.

These control experiments provide valuable evidence that antibody binding is controlled by the exposure of the progesterone moiety, which in turn is controlled by the oligolysine conformational changes induced by the application of an electrical potential.

Based on previous studies[22-23], the binding activity inhibition is interpreted as being the result of the progesterone being in close proximity to the ethylene glycol matrix, hindering molecular recognition. It is of significance to highlight that despite the presence of a heptyl linker between the oligolysine switching unit and the antigen binding site, the electrically-triggered conformational changes in the oligolysine are able to distort the progesterone into a conformation that lacks affinity for the antibody. In addition, the findings revealed that the conformational rigidity of the progesterone moiety does not affect the ability of the oligolysine chains to induce conformational changes that either promote or inhibit progesterone-antibody interactions. The findings suggest that the oligolysine conformational changes upon application of an electrical potential can be propagated over a span of at least 2.6 nm (i.e. the length of the heptyl linker-progesterone units).

4.3.4 Preliminary studies on the development of an OFF-ON switchable surface

The path for a new type of switchable surface has been sketched in Figure 4.14, based on a peptide consisting of two identical side chains, or branched arms, which will expose or hide the central branch incorporating a biomolecule of interest. Upon application of a negative potential, the positively charged double-arm molecular systems will experience an attractive force to the surface, leading to a mechanical motion that will expose the biomolecule, in this case represented by biotin. Biotin was chosen for these proof-of-concept studies, due to the well-known strong and rapid non-covalent interaction with avidin protein (Ka = 10^{15} M^{-1}) and its deglycosylated version, neutravidin[55]. Neutravidin protein was selected over avidin since it exhibits lower non-specific binding due to its lower isoelectric point (6.3), while retaining a high biotin-binding affinity[55].

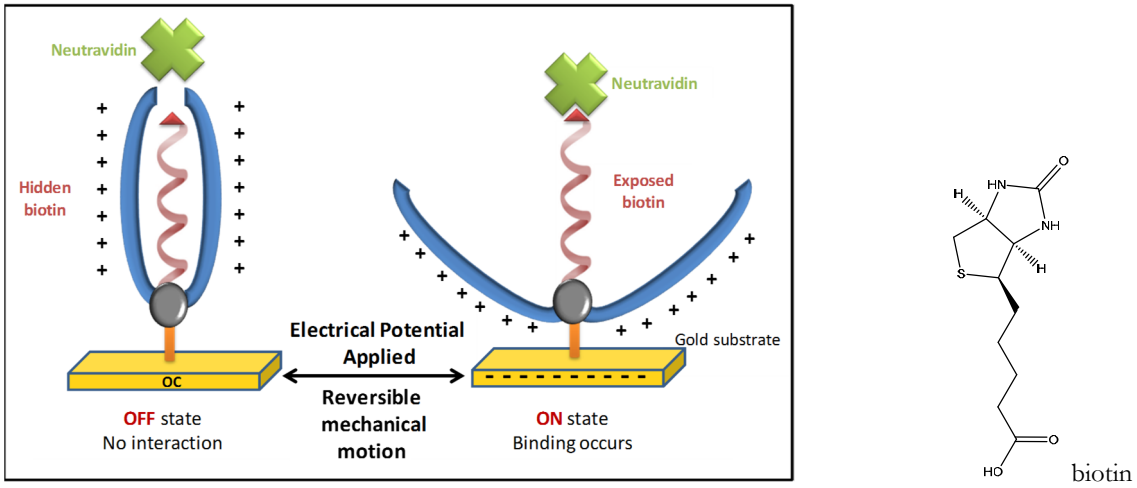

Figure 4.57 – Left: Smart switchable surface, where double-arm molecules are employed as cages to the biomolecules (for example biotin), concealing (inactive state) or exposing (active state) biomolecule functional regions. Upon application of a negative potential, the positively charged double-arm molecular systems will experience an attractive force to the surface, leading to a mechanical motion that will expose the biomolecule. Right: molecular structure of biotin.

Peptide Protein Research Ltd has been collaborating with our research group on the synthesis of the peptide derived double-arm molecules. However, the synthesis has thus far proved challenging and the hunt for a suitable route is still ongoing. The chemical structure of the proposed switchable surface is shown in Figure 4.58. The double-arm molecular system consists of aspartic acid oligopeptides attached to a core structure that incorporates an azide group. The purpose of the azide group is to allow further attachment of a biomolecule of interest (for example biotin or progesterone) *via* copper-catalysed azide-alkyne cycloaddition[56] (click chemistry). A biotin molecule attached to the double-armed peptide is shown in Figure 4.59. Click chemistry (Figure 4.60) is among a wide variety of strategies, covalent and noncovalent, that have been applied for SAM surface modification. It provides selective and efficient chemical modification with low by-product formation and easy surface characterisation[57]. The short chain thiol incorporated in the mixed SAM, 2-mercaptoethanol (2MET), prevents non-specific binding on gold and assists in spacing out the peptide to enable conformational changes to occur, i.e., the mechanical motion of the oligopeptide arms.

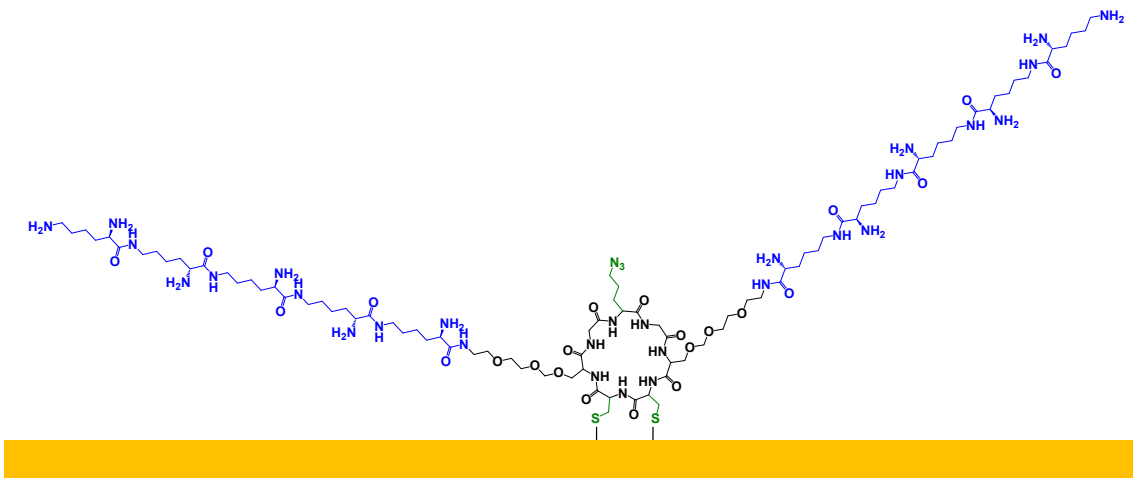

Figure 4.58 - Chemical structure of the switchable molecule mixed SAM on gold, incorporating two components: i) the aspartic acid oligopeptides ("arms") attached to the core cyclic peptide exhibiting an azide group; ii) the spacer, 2MET.

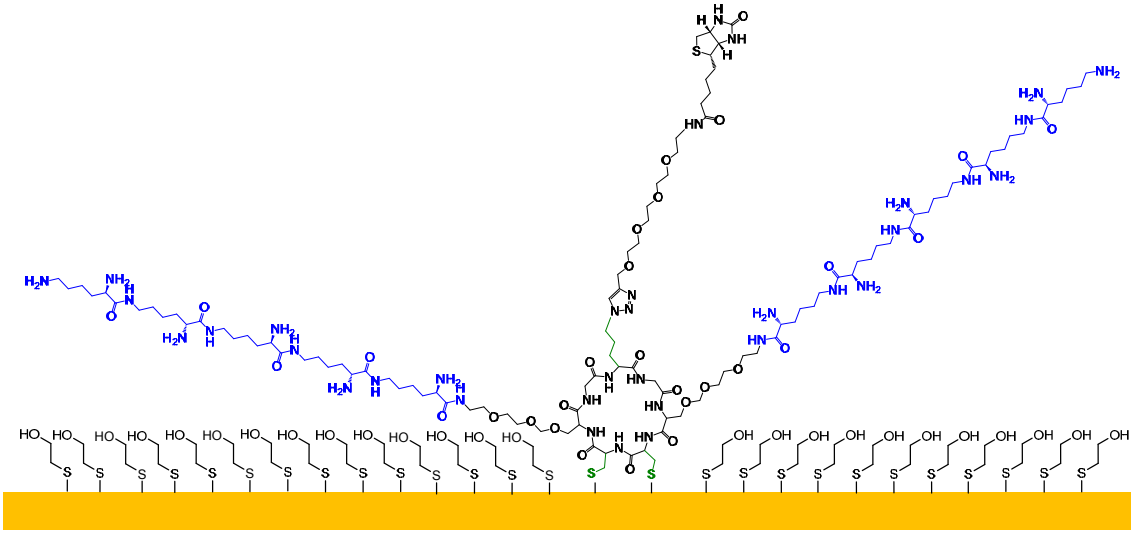

Figure 4.59 - Chemical structure of the switchable molecule mixed SAM on gold after attachment of biotin via click chemistry.

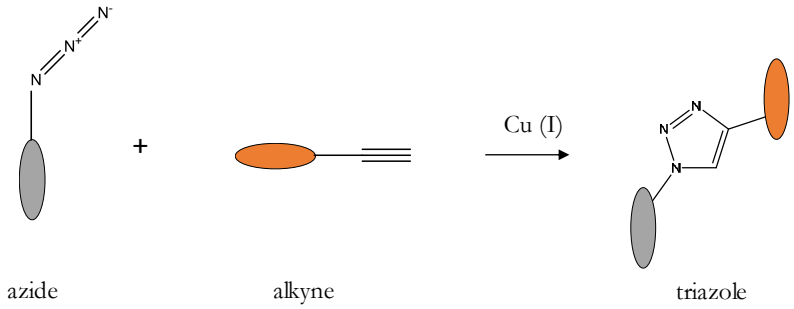

Figure 4.60 - Schematic representation of the copper-catalysed azide-alkyne cycloaddition (click chemistry) reaction.

The core structure of the switchable peptide (cyclic structure shown in Figure 4.61a), was successfully synthesised by Peptide Protein Research Ltd. A SAM of this component was formed on a gold substrate and characterised by contact angle, ellipsometry and XPS. The attachment of a biotin-alkyne molecule (Figure 4.61d) to the cyclic-peptide:2MET mixed SAM was also tested, aiming for a surface with similar structure to the one shown in Figure 4.61c.

For the SAM formation, clean gold surfaces were incubated for 24 h in freshly prepared aqueous solutions of the cyclic peptide and then rinsed with ultrapure water and dried under a stream of argon.

Ellipsometry measurements resulted in a calculated thickness of 0.95 nm ± 0.07, which is in accordance with the theoretical thickness calculated from ChemDraw: 1.12 nm. The measured contact angle for this surface was 52 ° ± 2, which is in accordance with values reported in the literature for an azide terminated SAM[58].

The characterisation of this surface *via* XPS also demonstrated the presence of the azide group, which has a very characteristic signature as a result of three different chemical environments of the nitrogen atoms. High resolution scans for the key elements are shown in Figure 4.62. In this case, not only azide groups but other nitrogen species are present in the SAM (see chemical structure in Figure 4.61a) and therefore the area of the three components fitted to the N 1s area is not the same for each component, as it would be if only azide groups were present. The relative atomic percentages and relative component percentages calculated from the XPS data are shown in Table 4.9. The cyclic peptide molecule has 10 atoms of N and 2 atoms of S, giving a theoretical N/S ratio of 5. The calculated ratio N/S for the SAM (8.7 ± 0.8) is higher than the theoretical one. This fact might be related to possible inaccuracy of the relative sensitivity factors used when normalizing the XPS data. In addition, there may be some signal attenuation for sulfur as it is bound to the gold surface and covered by the peptide and terminal azide groups. The presence of the C-O component is assigned to contamination from exposure to air.

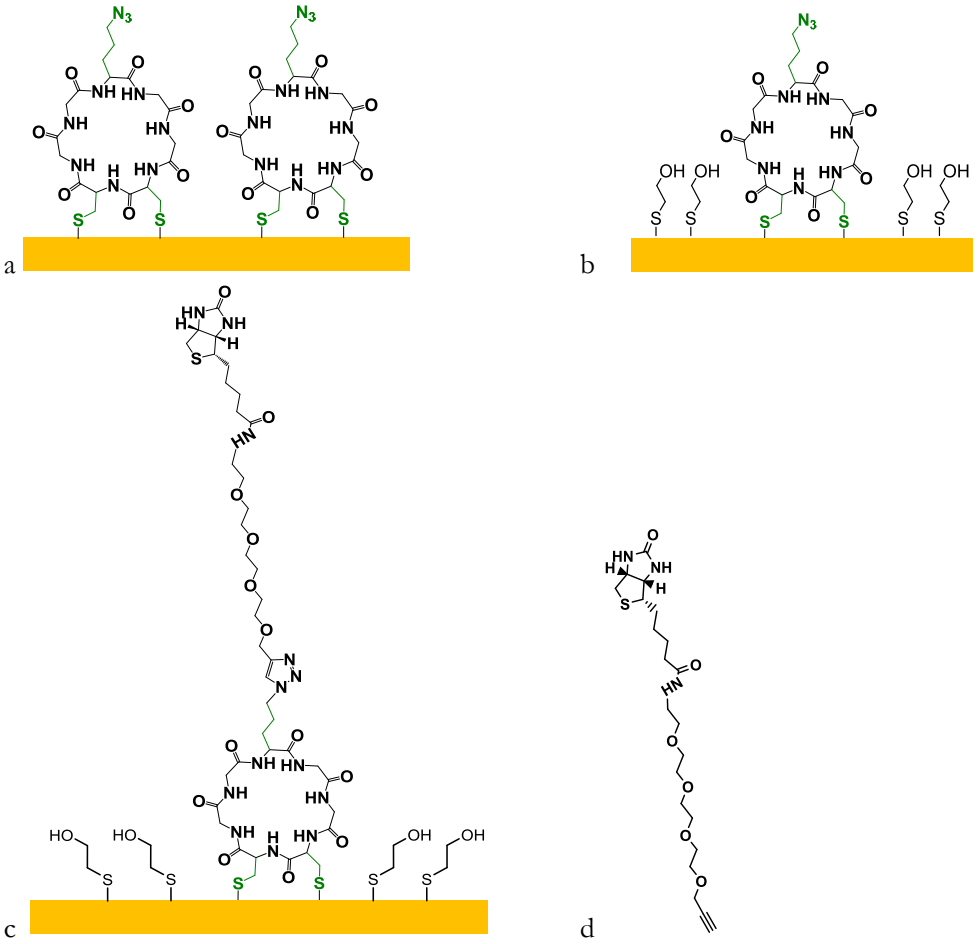

Figure 4.61 – Chemical structure of a) the cyclic peptide SAM on gold with an azide terminal group; b) the cyclic peptide : 2MET mixed SAM on gold; c) the cyclic peptide : 2MET mixed SAM on gold after attachment of the biotin molecule; d) biotin-PEG4-alkyne molecule used for click chemistry reaction with the azide group of the cyclic peptide molecule.

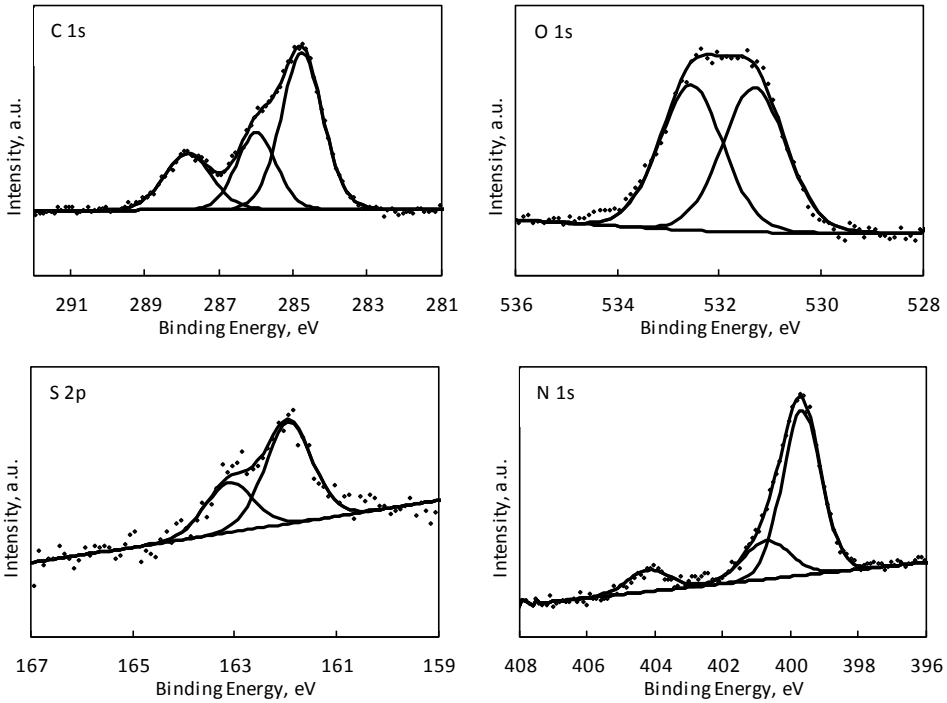

Figure 4.62 – XPS spectra of the C 1s, O 1s, S 2p and N 1s regions for the cyclic peptide SAM.

Table 4.9 - Relative atomic percentages and relative component percentages for the cyclic peptide SAM calculated from XPS spectra. The values are the average of three samples, with the errors reported as standard deviation.

	Relative Atomic Percentages		Components	Relative Component Percentages	
	Measured	**Theor.**		**Measured**	**Theor.**
O	19.5 ± 0.7	18.4	O-C	50.0 ± 0	0
			O=C	50.0 ± 0	100
C	63.6 ± 1.0	50.0	C-C	56.0 ± 3.0	10.5
			C-S, C-N and C-O	22.9 ± 2.5	52.6
			C=O	21.1± 0.6	36.8
S	1.7 ± 0.2	5.3	S-Au	100	100
N	15.1 ± 0.2	26.3	N^-, N-C	69.6 ± 2.7	80
			N	10.1 ± 0.9	10
			N+	20.3 ± 1.8	10

A mixed SAM formed by the cyclic peptide and the spacer molecule, 2MET, was then tested for the attachment of a biotin molecule, biotin-PEG4-alkyne, *via* click chemistry conjugation. For mixed SAM formation, gold substrates were incubated in solutions of 0.98 : 0.02 2MET : cyclic peptide (Figure 4.61b). Detailed information about the click chemistry protocol can be found in the experimental chapter. Briefly, the reaction was

undertaken for 3 h, at room temperature with stirring, in 1:2 water:DMSO solution, in the presence of $CuSO_4$, tris[(1-benzyl-1H-1,2,3-triazol-4-yl)methyl]amine (TBTA) and sodium ascorbate. After the reaction, the surface was copiously rinsed with DMSO and then ultrapure water, and finally dried under a stream of argon.

The success of the reaction was investigated by XPS, by analysing the surface before and after the reaction. Results, shown in Figure 4.63 and Table 4.10, confirm the presence of the cyclic peptide in the mixed SAM (before the click reaction), as the key elements C, O, N and S were detected. As expected, there is a reduction of N/S, as well as a reduction of the C=O component, in comparison with the pure cyclic peptide SAM, since 2MET is not composed of either N or C=O. Calculated N/S ratio for the mixed SAM is 2.5 ± 0.5, in contrast with 8.7 ± 0.8 for the pure cyclic peptide SAM. The ratio of cyclic peptide and 2MET on the surface can be estimated from the C=O component. Assuming that the C-O/C=O components considered as air contamination from the XPS data of the cyclic peptide SAM is similar to that of the mixed SAM, then this amount can be subtracted from the mixed SAM, to give 70 % of C-O (from 2MET) and 30 % of C=O (from the cyclic peptide). Each molecule of cyclic peptide has seven C=O, while each molecule of 2MET has only one C-O so the mole fraction of cyclic peptide to 2MET would be 0.06. This estimated value doesn't take into consideration signal attenuation effects and is slightly bigger than the one used in solution (0.02), which might be an indication of preferential binding of this component during the mixed SAM formation. The preferential adsorption of a longer chain component has been observed before with mixed SAMs and can be attributed to an overall thermodynamic control of the adsorption process.[54]

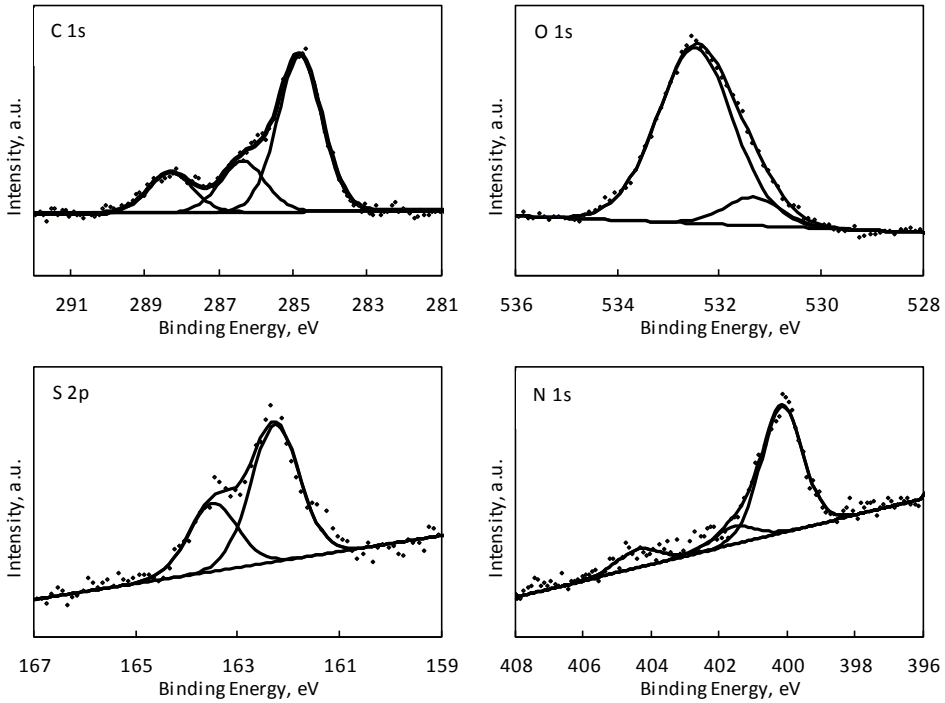

Figure 4.63 – XPS spectra of the C 1s, O 1s, S 2p and N 1s regions for the cyclic-peptide:2MET mixed SAM.

Table 4.10 - Relative atomic percentages and relative component percentages for the cyclic-peptide:2MET mixed SAM calculated from XPS spectra. The values are the average of three samples, with the errors reported as standard deviation.

	Relative Atomic Percentages	**Components**	**Relative Component Percentages**
O	28.6 ± 0.8	O-C	87.0 ± 1.6
		O=C	13.0 ± 1.6
C	60.3 ± 2.3	C-C	66.4 ± 5.1
		C-S, C-N and C-O	17.9 ± 3.0
		C=O	15.7 ± 2.4
S	3.1 ± 0.3	S-Au	100
N	8.0 ± 2.1	N^-, N-C	80.4 ± 2.6
		N	9.7 ± 1.9
		N^+	9.8 ± 0.9

After the click reaction, the N/S ratio is expected to increase, as the attached biotin molecule would add 3 N atoms and 1 S atom to the overall structure. Results are shown in Figure 4.64 and Table 4.11. The change in N/S, from 2.5 ± 0.5 to 2.9 ± 0.1, is not significant within the error. However, there is a change detected in the chemical environment of N and S, which is in accordance with the conversion of the azide group into a triazole group and the presence of a S species that is not bound to gold. A slight increase in the C-O component relative percentage is also noticed, changing from 17.9 % ± 3.0 to 22.7 % ± 0.7. All together these results indicate attachment of the biotin molecule to the surface. The relative percentage of the new nitrogen component present on the surface after the click reaction at lower binding energy is 12.6 % ± 2.4. This could be considered as

the percentage of triazole groups and provides an estimate of the click reaction yield. Once again, this value does not take into account signal attenuation effects.

This study demonstrates the feasibility of using a cyclic peptide molecule with an azide group for the creation of a mixed SAM on gold and further functionalisation of this surface with a molecule of interest containing an alkyne group using click chemistry. Further development of this system into a switchable surface is dependent on the successful synthesis of the double arms molecule, which would allow eSPR studies on the exposure of the switchable surface to neutravidin in solution to be undertaken.

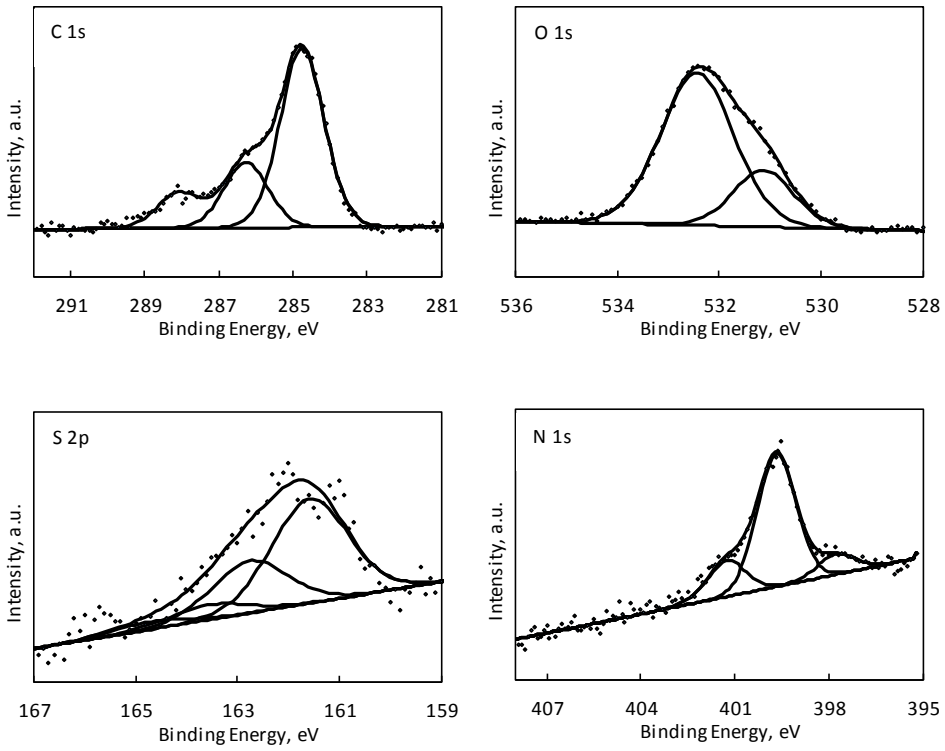

Figure 4.64 - XPS spectra of the C 1s, O 1s, S 2p and N 1s regions for the cyclic-peptide:2MET mixed SAM after click chemistry conjugation with biotin-alkyne.

Table 4.11 - Relative atomic percentages and relative component percentages for the cyclic-peptide:2MET mixed SAM after click chemistry reaction with biotin-alkyne molecule, calculated from XPS spectra. The values are the average of three samples, with the errors reported as standard deviation.

	Relative Atomic Percentages	**Components**	**Relative Component Percentages**
	Measured		**Measured**
O	26.2 ± 1.1	O-C	76.7 ± 1.6
		O=C	23.3 ± 1.6
C	61.3 ± 0.9	C-C	64.2 ± 0.2
		C-S, C-N and C-O	22.7 ± 0.7
		C=O	13.1 ± 0.5
S	3.2 ±0.2	S-Au	88.9 ± 2.2
		S-C	11.1 ± 2.2
N	9.4 ± 1.2	N1	12.6 ± 2.4
		N2	69.3 ± 1.6
		N3	18.0 ± 3.6

4.4 Conclusions

The control studies undertaken were of major importance to trace conclusions about the switchable system based on the progesterone-C7-4KC:C11EG6 mixed SAM, an ON-OFF type of switching. Ellipsometry measurements after the electrical switch corroborate the assumption that when a negative potential is applied to the surface, progesterone is in closer proximity to the spacer matrix. Different ranges of applied potentials provided a better understanding of the effect of the electrical potential on the switching efficiency of

the system, a decrease in switching efficiency being observed when lower potentials were used as ON or OFF conditions. Investigations on a surface with no progesterone demonstrated the specificity of the system and by examining the switching potential of a surface where no peptide was present, it was demonstrated that the switching only occurs in the presence of the peptide. The design principles and strategies for achieving high switching efficiencies described herein can be adapted, in future studies, to other highly relevant antigen-antibody systems. Electrical switching can be easily applied and regulated, making it an excellent remote trigger to biosensing applications. While so far antibody-antigen interactions have always been evaluated in static conditions, this work paves the way towards the development of on-demand antibody biosensors for a wide range of medical, biotechnological and pharmaceutical applications.

The preliminary studies on an alternative switchable surface, this time an OFF-ON type of switching, demonstrated the viability of using a cyclic peptide to create a mixed SAM on gold and the simple attachment of a biomolecule of interest to the surface *via* click chemistry.

4.5 List of References

1. Casalini, S.; Dumitru, A. C.; Leonardi, F.; Bortolotti, C. A.; Herruzo, E. T.; Campana, A.; de Oliveira, R. F.; Cramer, T.; Garcia, R.; Biscarini, F., Multiscale Sensing of Antibody - Antigen Interactions by Organic Transistors and Single-Molecule Force Spectroscopy. *ACS Nano* **2015,** *9* (5), 5051-62.
2. Marquette, C. A.; Blum, L. J., State of the art and recent advances in immunoanalytical systems. *Biosens. Bioelectron.* **2006,** *21* (8), 1424-1433.
3. Wen, W.; Yan, X.; Zhu, C. Z.; Du, D.; Lin, Y. H., Recent Advances in Electrochemical Immunosensors. *Anal. Chem.* **2017,** *89* (1), 138-156.
4. Tian, L.; Heyduk, T., Antigen Peptide-Based Immunosensors for Rapid Detection

of Antibodies and Antigens. *Anal. Chem.* **2009,** *81* (13), 5218-5225.

5. Vallee-Belisle, A.; Ricci, F.; Uzawa, T.; Xia, F.; Plaxco, K. W., Bioelectrochemical Switches for the Quantitative Detection of Antibodies Directly in Whole Blood. *J. Am. Chem. Soc.* **2012,** *134* (37), 15197-15200.

6. Gunn, G. R.; Sealey, D. C. F.; Jamali, F.; Meibohm, B.; Ghosh, S.; Shankar, G., From the bench to clinical practice: understanding the challenges and uncertainties in immunogenicity testing for biopharmaceuticals. *Clin. Exp. Immunol.* **2016,** *184* (2), 137-146.

7. de Moraes, A. C. M.; Kubota, L. T., Recent Trends in Field-Effect Transistors-Based Immunosensors. *Chemosensors* **2016,** *4* (4), 26.

8. Tang, D. P.; Cui, Y. L.; Chen, G. A., Nanoparticle-based immunoassays in the biomedical field. *Analyst* **2013,** *138* (4), 981-990.

9. Tarn, M. D.; Pamme, N., Microfluidic platforms for performing surface-based clinical assays. *Expert Rev. Mol. Diagn.* **2011,** *11* (7), 711-720.

10. Gomes, B. S.; Simoes, B.; Mendes, P. M., The increasing dynamic, functional complexity of bio-interface materials. *Nat. Rev. Chem.* **2018,** *2* (3), 15.

11. Gomes, B. S.; Mendes, P. M., Stimuli-Responsive Nanostructured Surfaces for Biomedical Applications. In *Functional Organic and Hybrid Nanostructured Materials*, Li, Q., Ed. 2018.

12. Cantini, E.; Wang, X. Y.; Koelsch, P.; Preece, J. A.; Ma, J.; Mendes, P. M., Electrically Responsive Surfaces: Experimental and Theoretical Investigations. *Acc. Chem. Res.* **2016,** *49* (6), 1223-1231.

13. Mendes, P. M., Stimuli-responsive surfaces for bio-applications. *Chem Soc Rev* **2008,** *37*, 2512-2529.

14. Mendes, P. M., Cellular nanotechnology: making biological interfaces smarter. *Chemical Society Reviews* **2013,** *42* (24), 9207-9218.

15. Pranzetti, A.; Mieszkin, S.; Iqbal, P.; Rawson, F. J.; Callow, M. E.; Callow, J. A.; Koelsch, P.; Preece, J. A.; Mendes, P. M., An Electrically Reversible Switchable Surface to Control and Study Early Bacterial Adhesion Dynamics in Real-Time. *Adv. Mater.* **2013,** *25* (15), 2181-2185.

16. Xiong, X. H.; Wu, Z. Q.; Yu, Q.; Xue, L. L.; Du, J.; Chen, H., Reversible Bacterial Adhesion on Mixed Poly(dimethylaminoethyl methacrylate)/Poly(acrylamidophenyl boronic acid) Brush Surfaces. *Langmuir* **2015,** *31* (44), 12054-12060.

17. Yeung, C. L.; Iqbal, P.; Allan, M.; Lashkor, M.; Preece, J. A.; Mendes, P. M., Tuning

Specific Biomolecular Interactions Using Electro-Switchable Oligopeptide Surfaces. *Adv. Funct. Mater.* **2010,** *20*, 2657-2663.

18. Yu, Q.; Shivapooja, P.; Johnson, L. M.; Tizazu, G.; Leggett, G. J.; Lopez, G. P., Nanopatterned polymer brushes as switchable bioactive interfaces. *Nanoscale* **2013,** *5*, 3632-3637.

19. Gong, Y.; Li, C.; Yang, J.; Wang, H.; Zhuo, R.; Zhang, X., Photoresponsive "Smart Template" via Host Guest Interaction for Reversible Cell Adhesion. *Macromolecules* **2011,** *44*, 7499-7502.

20. Desseaux, S.; Klok, H., Temperature-Controlled Masking/Unmasking of Cell-Adhesive Cues with Poly(ethylene glycol) Methacrylate Based Brushes. *Biomacromolecules* **2014,** *15*, 3859-3865.

21. Lashkor, M.; Rawson, F. J.; Stephenson-Brown, A.; Preece, J. A.; Mendes, P. M., Electrically-Driven Modulation of Surface-Grafted RGD Peptides for Manipulation of Cell Adhesion. *Chem. Commun.* **2014,** *50* (98), 15589-15592.

22. Pranzetti, A.; Davis, M.; Yeung, C. L.; Preece, J. A.; Koelsch, P.; Mendes, P. M., Direct Observation of Reversible Biomolecule Switching Controlled By Electrical Stimulus. *Adv. Mat. Interfaces* **2014,** *1* (5), 1400026.

23. Yeung, C. L.; Wang, X.; Lashkor, M.; Cantini, E.; Rawson, F. J.; Iqbal, P.; Preece, J. A.; Ma, J.; Mendes, P. M., Modulation of Biointeractions by Electrically Switchable Oligopeptide Surfaces: Structural Requirements and Mechanism. *Adv. Mat. Interfaces* **2014,** *1* (2), 1300085.

24. Inhorn, M. C.; Patrizio, P., Infertility around the globe: new thinking on gender, reproductive technologies and global movements in the 21st century. *Hum Reprod Update* **2015,** *21* (4), 411-26.

25. Barratt, C. L.; Mansell, S.; Beaton, C.; Tardif, S.; Oxenham, S. K., Diagnostic tools in male infertility-the question of sperm dysfunction. *Asian J Androl* **2011,** *13* (1), 53-8.

26. Calhaz-Jorge, C.; De Geyter, C.; Kupka, M. S.; de Mouzon, J.; Erb, K.; Mocanu, E.; Motrenko, T.; Scaravelli, G.; Wyns, C.; Goossens, V., Assisted reproductive technology in Europe, 2013: results generated from European registers by ESHRE. *Hum Reprod* **2017,** *32* (10), 1957-1973.

27. Teoh, P. J.; Maheshwari, A., Low-cost in vitro fertilization: current insights. *Internationl Journal of Womens Health* **2014,** *6*, 817-27.

28. Sanchez, V.; Wistuba, J.; Mallidis, C., Semen analysis: update on clinical value,

current needs and future perspectives. *Reproduction* **2013,** *146* (6), R249-58.

29. Chaichian, S.; Tamannaie, Z.; Rohani, H.; Ahmadi, M.; Nasr, M.; Pazouki, A.; Mehdizadehkashi, A., Relationship between sperm parameters and intracytoplasmic sperm injection outcome. *Middle East Fertility Society Journal* **2015,** *20* (4), 251-254.

30. Worrilow, K. C.; Eid, S.; Woodhouse, D.; Perloe, M.; Smith, S.; Witmyer, J.; Ivani, K.; Khoury, C.; Ball, G. D.; Elliot, T.; Lieberman, J., Use of hyaluronan in the selection of sperm for intracytoplasmic sperm injection (ICSI): significant improvement in clinical outcomes--multicenter, double-blinded and randomized controlled trial. *Hum Reprod* **2013,** *28* (2), 306-14.

31. Gadella, B. M.; Luna, C., Cell biology and functional dynamics of the mammalian sperm surface. *Theriogenology* **2014,** *81* (1), 74-84.

32. Perez-Cerezales, S.; Lopez-Cardona, A. P.; Gutierrez-Adan, A., Progesterone effects on mouse sperm kinetics in conditions of viscosity. *Reproduction* **2016,** *151* (5), 501-7.

33. Lopez-Torres, A. S.; Chirinos, M., Modulation of Human Sperm Capacitation by Progesterone, Estradiol, and Luteinizing Hormone. *Reproductive Sciences* **2017,** *24* (2), 193-201.

34. http://www.sims.ie/treatments/intracytoplasmic-sperm-injection-icsi.1040.html (accessed 01.06.2018).

35. Lishko, P. V.; Botchkina, I. L.; Kirichok, Y., Progesterone activates the principal Ca2+ channel of human sperm. *Nature* **2011,** *471* (7338), 387-91.

36. Strunker, T.; Goodwin, N.; Brenker, C.; Kashikar, N. D.; Weyand, I.; Seifert, R.; Kaupp, U. B., The CatSper channel mediates progesterone-induced Ca2+ influx in human sperm. *Nature* **2011,** *471* (7338), 382-6.

37. Kaupp, U. B.; Kashikar, N. D.; Weyand, I., Mechanisms of sperm chemotaxis. *Annu Rev Physiol* **2008,** *70*, 93-117.

38. Correia, J.; Michelangeli, F.; Publicover, S., Regulation and roles of Ca2+ stores in human sperm. *Reproduction* **2015,** *150* (2), R65-76.

39. Smith, J. F.; Syritsyna, O.; Fellous, M.; Serres, C.; Mannowetz, N.; Kirichok, Y.; Lishko, P. V., Disruption of the principal, progesterone-activated sperm Ca2+ channel in a CatSper2-deficient infertile patient. *Proc Natl Acad Sci U S A* **2013,** *110* (17), 6823-8.

40. Miller, M. R.; Mannowetz, N.; Iavarone, A. T.; Safavi, R.; Gracheva, E. O.; Smith, J. F.; Hill, R. Z.; Bautista, D. M.; Kirichok, Y.; Lishko, P. V., Unconventional endocannabinoid signaling governs sperm activation via the sex hormone progesterone. *Science* **2016,** *352*

(6285), 555-9.

41. Caesar https://www.mpg.de/1225277/sperm_female_hormone (accessed 01.06.2018).

42. Lishko, P.; Kirichok, Y.; Ren, D.; Navarro, B.; Chung, J.; Clapham, D., The control of male fertility by spermatozoan ion channels. *Annu Rev Physiol* **2012,** *74*, 453-75.

43. Munire, M.; Shimizu, Y.; Sacata, Y.; Minaguchi, R.; Aso, T., Impaired hyperactivation of human sperm in patients with infertility. *Journal of medical and dental sciences* **2004,** *51*, 99-104.

44. Sumigama, S.; Mansell, S.; Miller, M.; Lishko, P.; Cherr, G.; Meyers, S.; Tollner, T., Progesterone Accelerates the Completion of Sperm Capacitation and Activates CatSper Channel in Spermatozoa from the Rhesus Macaque. *Biology of reproduction* **2015,** *93* (6), 1-11.

45. Giojalas, L. C.; Iribarren, P.; Molina, R.; Rovasio, R. A.; Estofan, D., Determination of human sperm calcium uptake mediated by progesterone may be useful for evaluating unexplained sterility. *Fertil Steril* **2004,** *82* (3), 738-40.

46. Cantini, E. Switchable Surfaces for Biomedical Applications. doctoral dissertation, University of Birmingham, 2017.

47. Parthasarathy, P.; Mendes, P. M.; Schopf, E.; Preece, J. A.; Stoddart, J. F.; Chen, Y., Spatially Controlled Assembly of Nanomaterials at the Nanoscale. *J. Nanosci. Nanotechnol.* **2009,** *9* (1), 650-654.

48. Krieg, R.; Jortzik, E.; Goetz, A. A.; Blandin, S.; Wittlin, S.; Elhabiri, M.; Rahbari, M.; Nuryyeva, S.; Voigt, K.; Dahse, H. M.; Brakhage, A.; Beckmann, S.; Quack, T.; Grevelding, C. G.; Pinkerton, A. B.; Schonecker, B.; Burrows, J.; Davioud-Charvet, E.; Rahlfs, S.; Becker, K., Arylmethylamino steroids as antiparasitic agents. *Nat. Commun.* **2017,** *8*, 12.

49. Bansal, R.; Acharya, P. C., Man-Made Cytotoxic Steroids: Exemplary Agents for Cancer Therapy. *Chem. Rev.* **2014,** *114* (14), 6986-7005.

50. Castner, D. G., X-ray Photoelectron Spectroscopy Sulfur 2p Study of Organic Thiol and Disulfide Binding Interactions with Gold Surfaces. *Langmuir* **1996,** *12*, 5083-6.

51. Beamson, G.; Briggs, D., *High resolution XPS of organic polymers, the scienta ESCA300 database*. Wiley: Chichester, 1992.

52. Wu, M.; Feng, Q.; Sun, X.; Wang, H.; Gielen, G.; Wu, W., Rice (Oryza sativa L) plantation affects the stability of biochar in paddy soil. *Scientific Reports* **2015,** *5*, 10001.

53. Ahmed, M.; Byrne, J.; McLaughlin, J.; Ahmed, W., Study of Human Serum Albumin

Adsorption and Conformational Change on DLC and Silicon Doped DLC Using XPS and FTIR Spectroscopy. *Journal of Biomaterials and Nanobiotechnology* **2013,** *04* (02), 194-203.

54. Laibinis, P.; Nuzzo, R.; Whitesides, G., Structure of monolayers formed by coadsorption of two n-alkanethiols of different chain lengths on gold and its relation to wetting. *Journal of Physical Chemistry* **1992,** *96* (12), 5097-5105.

55. ThermoScientific, Avidin-Biotin Technical Handbook. **2009**.

56. Rostovtsev, V.; Green, L.; Fokin, V.; Sharpless, K., A Stepwise Huisgen Cycloaddition ProcessCopper(i)-Catalyzed Regioselective Ligationof Azides and Terminal Alkynes. *Angewandte Chemie International Edition* **2002,** *41* (14), 2596-99.

57. Nicosia, C.; Huskens, J., Reactive self-assembled monolayers: from surface functionalization to gradient formation. *Mater. Horiz.* **2014,** *1* (1), 32-45.

58. Zheng, S.; Yang, Q.; Mi, B., Novel antifouling surface with improved hemocompatibility by immobilization of polyzwitterions onto silicon via click chemistry. *Applied Surface Science* **2016,** *363*, 619-26.

5 Design and fabrication of a micropatterned device and its orthogonal functionalisation for studies with sperm cells

This chapter describes the design and fabrication, by means of standard photolithography techniques, of a micropatterned device composed of gold and glass. This device will be used for future studies with cells. AFM, SEM and EDX were used for characterisation of the fabricated device. In addition to microfabrication, a method for chemical functionalisation of the fabricated device was also investigated. Contact angle, ellipsometry and XPS were used for the characterisation of each functionalisation step of gold and glass. Optical microscopy was used to demonstrate cell attachment.

5.1 Introduction

Due to its relevance in the work described in this chapter, a brief introduction to photolithography techniques and orthogonal functionalisation will now be given.

Photolithography techniques are popular in the semiconductor industry as a top down approach for the fabrication of integrated circuits [1-2]. These techniques allow the fabrication of features down to the micron size range and involve coating a metal substrate with a layer of photosensitive polymer, called photoresist (Figure 5.65a). When exposing the sample to light through a photomask (typically made of a transparent substrate such as quartz and an opaque material such as chrome oxide), light only reaches some regions of the photoresist and a photochemical reaction occurs in these exposed regions. Depending on which type of photoresist is used, this photochemical reaction will either increase or decrease the dissolution rate of this polymer in a developer solution. If a positive photoresist is used, the

exposed regions will be easily dissolved in the development step, while the unexposed regions remain intact. If a negative photoresist is used, only the unexposed regions will dissolve during the development process (Figure 5.65b). After immersion of the sample in developer solution and creation of a pattern of photoresist on the surface, a dry or wet etching process follows. This step involves transferring the image formed on the surface into a layer underneath the resist. The metal layer will only etch in the uncovered regions, remaining intact in the regions covered with photoresist, therefore allowing the creation of a patterned metal surface. The final step of this process is the complete removal of the photoresist. [3-4]

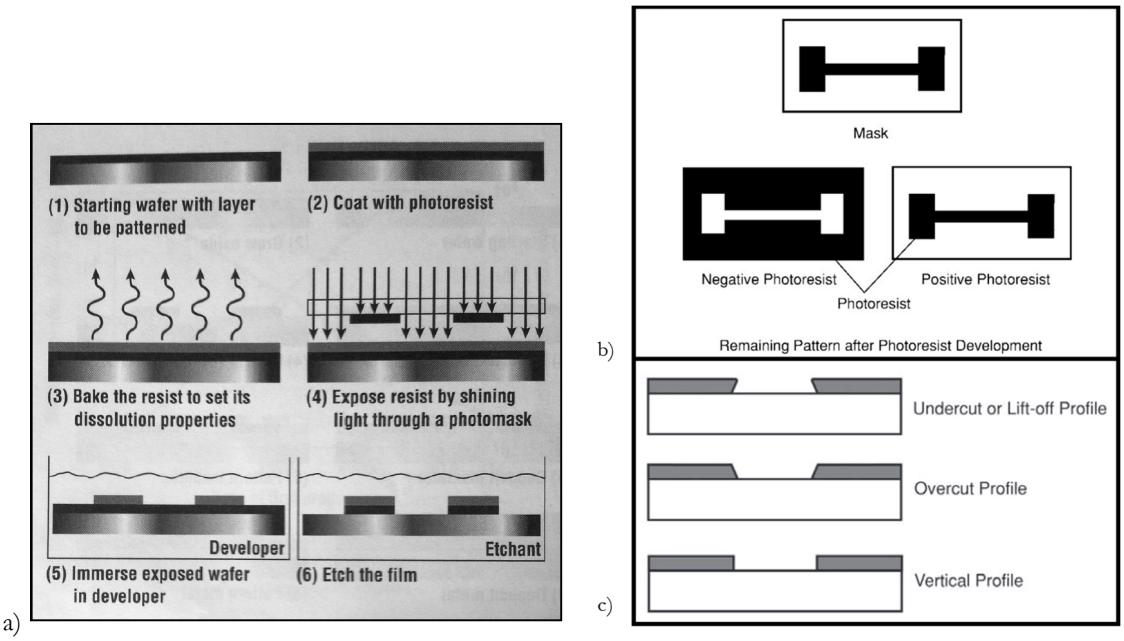

Figure 5.65 a) Optical lithography process steps for pattern creation. Adapted from [3]. b) Differentiation between the patterns remaining after photoresist development when using a negative and a positive photoresist. Adapted from [5]. c) Different types of photoresist profiles

A lift-off procedure can be used as an alternative to the etching process described above. With this procedure, a metal coating is applied after the formation of photoresist patterns and therefore the removal of the photoresist is accompanied by the removal of the metal

deposited thereon. A lift-off procedure is commonly selected for the fabrication of gold structures due to poor adhesion of the resist[6] and difficulties associated with etching this metal[5]. Different photoresist profiles can be obtained in photolithography, as shown in Figure 5.65 c. For a lift-off process, an undercut profile is desirable to prevent metal coating the sidewalls of the photoresist and to facilitate photoresist removal. If a continuous film of metal is created, then access to the photoresist is blocked and it can't be removed, preventing the fabrication of the desired features.

Micropatterned surfaces have a multitude of applications and are not confined to conductive materials. They have been extensively used by the scientific community in the development of biosensors and in applications which involve the study of cells (Figure 5.66).

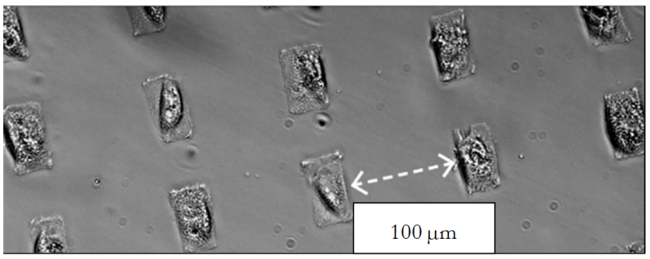

Figure 5.66 Fibroblast cells plated on fibronectin micropatterns. Adapted from [7].

For many applications, these micropatterned surfaces must be functionalised after fabrication. Several methods have been published regarding orthogonal functionalisation, i.e. selective chemical functionalisation of polymaterial substrates (Figure 5.67).

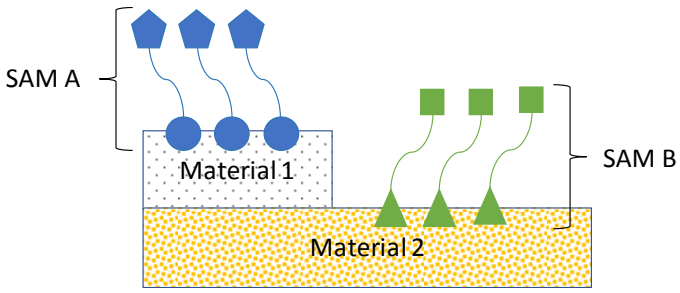

Figure 5.67 Scheme representing orthogonal functionalisation of a micropatterned surface, where self-assembled monolayer A is created on material 1 and self-assembled monolayer B is created on material 2.

Functionalisation of gold and glass surfaces has received particular attention, taking advantage of the well-known selective gold-thiol and glass-silane interactions. A handful of reports detailing such practices is summarised in Table 5.12. These functionalisation procedures vary from selective immobilization of polystyrene particles into glass holes[8], to immobilization of two different proteins onto gold nanosquares[9] or one on each side of a chip[10], and cell adhesion to well defined sites which consist of different proteins that constitute the extracellular matrix, such as RGD[11] and fibronectin[12]. The protocols for orthogonal functionalisation vary from single-step to multi-step, with concentrations of each component in solution ranging from 0.25 mM [12] to 135 mM [10]. No reports on the selective immobilization of sperm motile cells on glass combined with the creation of a mixed SAM on gold could be found in the literature. This novel approach is proposed in this work.

Table 5.12 Literature reports on the orthogonal functionalisation of gold and glass surfaces.

Substrates	Components	Functionalisation steps	Techniques	Ref.
Au Si	(CH2)11-NH-C(O)-biotin thiol 1H,1H,2H,2H-perfluorodecane thiol tricloro(1H,1H,2H,2H-perfluoroocyl) silane 2-[methoxy(polyethyleneoxy) propyl] trimethoxysilane	**Single step** 48h incubation in thiol/silane dry DCM solution; DCM rinse, water rinse; N_2 dry	XPS, TOF-SIMS, AFM	9
Au poly Si	mercapto undecanoate-NHS 11-(triethoxysilyl undecanal)	**Multi step** 3h incubation in thiol ethanolic sol.; overnight incubation with TR-WGA; 3h incubation in silane ethanolic sol.; overnight incubation in F-ConA	SEM, EDX, fluorescence	10
Au mesh glass holes	3-mercapto-1-propanol N-trimethoxy silylpropyl-N,N,N-trimethyl ammonium chloride	**Multi step** 1h incubation with aq. solution of silane; rinse; 2h incubation with ethanolic solution of thiol; rinse; dry at 90°C for 1h	AFM, confocal microscopy	8
Au glass	1-hexadecanethiol 2-methoxy(polyethyleneoxy)-propyltrimethoxysilane	**Single step** 72h incubation in thiol and silane; rinse; bake at 100°C for 1h	XPS, AFM	13 11
Au nps glass	cRGD-thiol poly(ethylene glycol)	**Multistep** PEGylation – immersion in PEG and TEA in dry toluene, at 80°C overnight; rinse and N_2 dry; click chemistry; 2h incubation with aq. sol of peptide-thiol; rinse	fluorescence, QCM, XPS	12

5.2 Aim and objectives

Along with the development of a switchable surface for exposure and concealment of progesterone, described in chapter 4, and before proceeding with sperm cell studies, a device where cells can be attached and exposed to the developed switchable surface is required. Design and fabrication of this device was the aim of the work described in this chapter, as well as the investigation of a method for chemical functionalisation of the device. Gold and glass were the materials chosen as the main components of a micropatterned device where the glass surface is functionalised for single sperm cell attachment and the gold surface is functionalised with an electrically switchable surface for interaction with sperm cell tails (Figure 5.68).

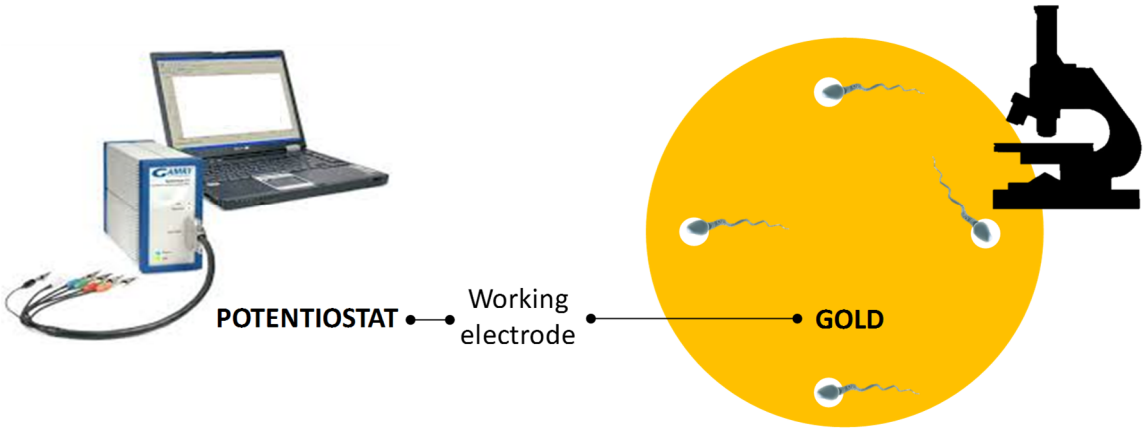

Figure 5.68 Schematic representation of the device to be developed for studies with sperm cells, incorporating the switchable surface described in chapter 4.

The main objectives for the work described are:

1. Design, fabrication and characterisation of a device for studies with sperm cells.
    a. Designing the micropatterned device - choice of materials and features.
    b. Fabricating the device by means of standard lithography techniques.

c. Characterisation of the fabricated device by AFM, SEM and EDX.

2. Development of a method for orthogonal functionalisation of the fabricated device.
    a. Selection of a strategy for the chemical functionalisation of gold and glass.
    b. Functionalisation of glass and gold surfaces for sperm cell attachment and interaction.
    c. Surface characterisation by means of contact angle, ellipsometry and XPS.
    d. Test cell attachment by means of optical microscopy.

5.3 Results and Discussion

5.3.1 Design, fabrication, and characterisation of a micropatterned device for studies with sperm cells

5.3.1.1 Designing the micropatterned device - choice of materials and features

Materials choice

Borosilicate glass is a cheap, transparent, and commonly used material in imaging optics and cell studies. In addition, the functionalisation of glass with silanes is well described in the literature[14]. Microscope glass slides were used as substrate for the micropatterned device. Table 5.13 gives approximate percentage values of the chemical composition of microscope slides.

To allow the controlled change of electrical potential when connected to a potentiostat, the substrate for the switchable surface had to be conductive. Gold was chosen due to its well-known stability and easy formation of SAMs from thiols on gold surfaces[16]. The more

transparent this surface is, the easier it is to visualise the sperm cells using optical microscopy. Therefore a very thin layer of gold is desired.

Table 5.13 Chemical composition of microscope slides. Adapted from [15].

Components	Approximate composition (%)
Silicon dioxide (SiO_2)	72.20
Sodium oxide (Na_2O)	14.30
Potassium oxide (K_2O)	1.20
Calcium oxide (CaO)	6.47
Magnesium oxide (MgO)	4.30
Aluminium oxide (Al_2O_3)	1.20
Iron oxide (Fe_2O_3)	0.03
Sulfur oxide (SO_3)	0.30

Features choice

Aiming to visualise the response of each single cell, a circular area slightly bigger than the average size of a normal sperm head (3-5 μm x 2-3 μm [17]) (Figure 5.69) was chosen for the immobilisation of the cells *via* their heads. Each sperm cell should be attached in a way that prevents physical contact between cells. At the same time, the number of observed cells in the microscope field of view should be maximized.

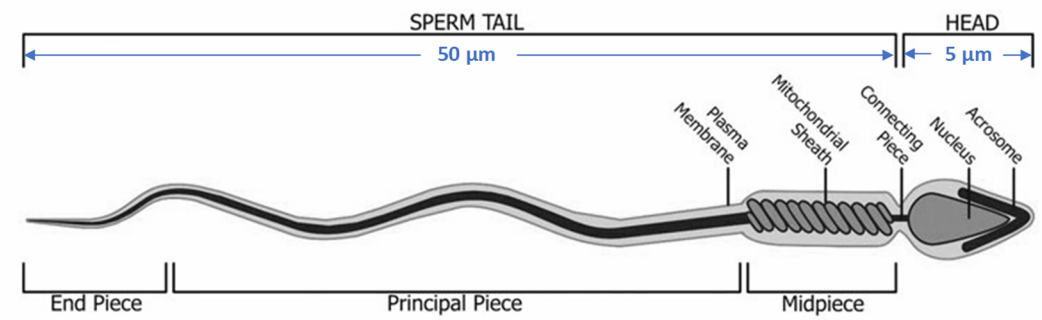

Figure 5.69 Schematic representation of a human sperm cell with dimensions of the head, midpiece and tail.

As the sperm cell flagellum (tail plus midpiece) has a length of approximately 50 µm, a 150 µm pitch was set between circular glass areas to avoid sperm cell interactions whilst maximising the number of observed cells in the microscope field of view (Figure 5.70). The sperm cell tail will interact with the functionalised gold surface, while its head will remain attached to the functionalised glass circle. Each device will allow the immobilisation of a group of cells, whose behaviour will then be analysed individually upon exposure to the progesterone peptide. The glass circles are surrounded by gold, where the switchable surface, with electrically tuneable properties, will be formed.

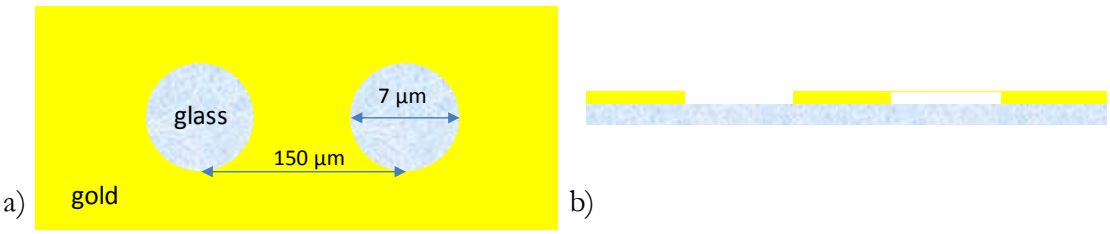

Figure 5.70 Schematic representation of a micropattern to be created on glass microscope slides (not to scale) a) top view and b) front view.

5.3.1.2 Fabrication and characterisation of a micropatterned device

A device consisting of a glass microscope slide covered with a gold micropattern (7 μm diameter glass circles with 150 μm pitch) was fabricated using standard lithography techniques. The protocol is described in detail in the methods chapter. Briefly, it consisted of cleaning the microscope slides, spin coat them with photoresist and expose them to UV light through a photomask. After immersing the slides in a developer solution, a pattern of photoresist was created on the glass surface, consisting of circles of photoresist (7 μm diameter circles). This surface was then covered with a thin gold layer (50 nm) using physical vapour deposition by sputtering, followed by a lift off process, i.e. removal of gold from the areas covered with photoresist during photoresist removal. Optimisation of the fabrication process consisted of testing different exposure doses and developing times. A thick layer of photoresist was used in order to promote an undercut resist profile.

To demonstrate that the intended micropattern was successfully fabricated, the device was characterised by AFM, SEM and EDX. SEM, along with an incorporated EDX system, was used to verify the diameter of the glass circles and to confirm the surface elemental composition. The pattern in Figure 5.71shows a representative image from three analysed samples. As expected, the diameter of the glass circles was measured as 7 μm ± 0.5 (Figure 5.72). The minimum distance between circles was also confirmed to be 150 μm. The EDX spectrum below (Figure 5.73) confirms the presence of gold and the main glass components (Si, O, Ca, Na, Mg).

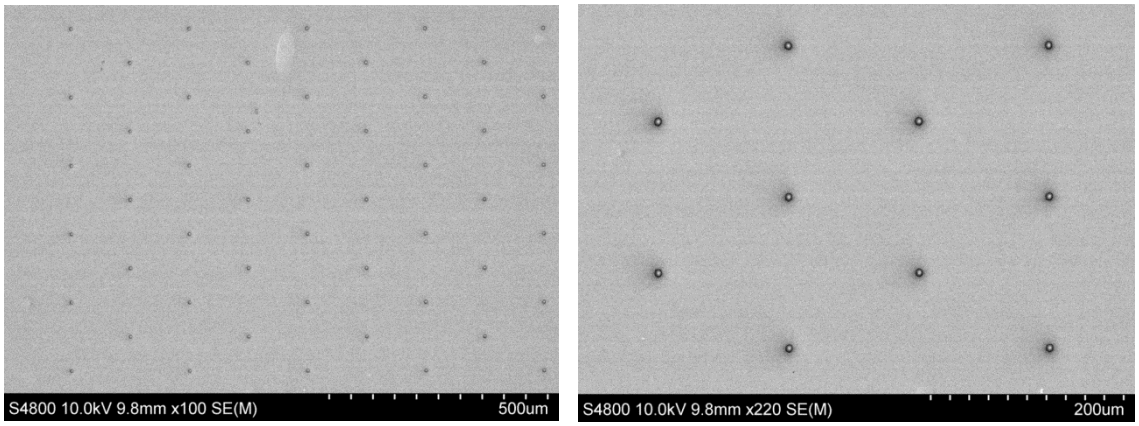

Figure 5.71 SEM images of the fabricated device, showing the glass circles pattern where single sperm cells will be attached.

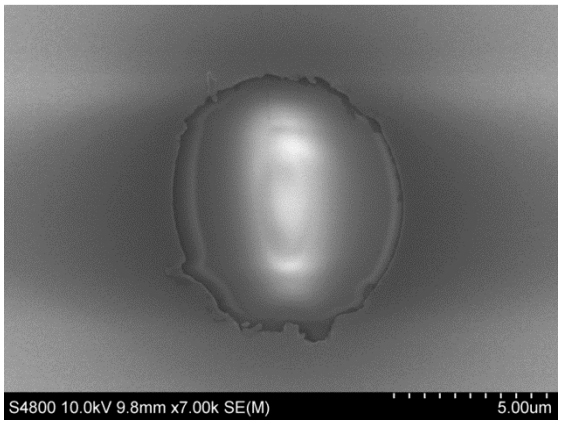

Figure 5.72 Zoomed in SEM image of the fabricated device, showing one of the glass circles where a single sperm cell will be attached.

The bright area shown in the centre of the glass circle, in Figure 5.72, is due to charging effects. Some defects are visible at the periphery of the circle, which are likely to be a result of re-deposition of lifted metal on the substrate during the lift off process. This can be reduced by optimising the lift-off media, using a photoresist with a higher undercut or by using a bi-layer lift-off process, where a better lift-off profile is created using two different types of resist on top of one another[18].

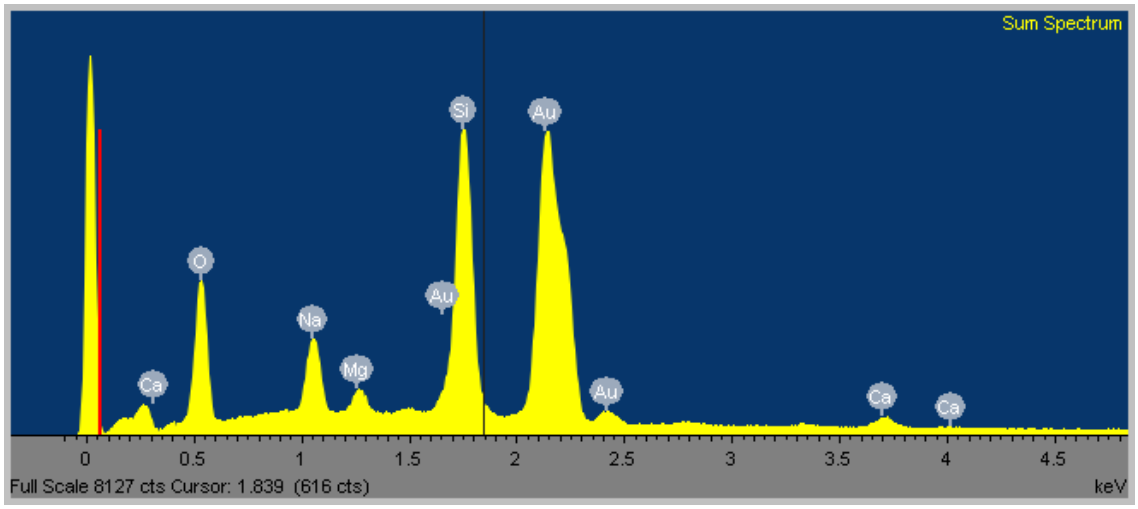

Figure 5.73 EDX spectrum of the fabricated device showing the presence of gold and main components of glass.

AFM was used to determine the roughness of the fabricated device, since it can influence the quality of SAMs [19] created on these surfaces. The technique selected for gold film deposition has an influence on the structure and initial adhesion of the film. The quality of a gold film formed by sputtering in a physical vapor deposition chamber is mainly dependent on the experimental parameters used for the deposition process, such as deposition rate and pressure. Sputtering was used instead of evaporation merely due to equipment availability. In fact, for a lift-off process, evaporation of gold is recommended over sputtering as the evaporation process is less isotropic, resulting in uncoated resist sidewalls and thus providing an easier lift-off.[6] Therefore, in addition to the suggestions discussed above for the improvement of the lift-off process, the use of evaporated gold films is recommended. The aforementioned defects are also visible on Figure 5.74b and confirms the location of residues on the surface.

Values for roughness are shown in Table 5.14 and were calculated based on the images shown below (Figure 5.74b), which are representative of three analysed samples. The root mean square roughness (Sq) of 1.12 ± 0.15 nm obtained for gold is close to the average value of 1.2 nm routinely observed with most gold deposition techniques (sputtering, evaporation and electroplating)[20]. The achieved value is also comparable to the roughness of gold substrates used in ellipsometry, contact angle and XPS experiments described in this dissertation, which have an Sq of < 2.5nm. The measured roughness is similar for both gold and glass.

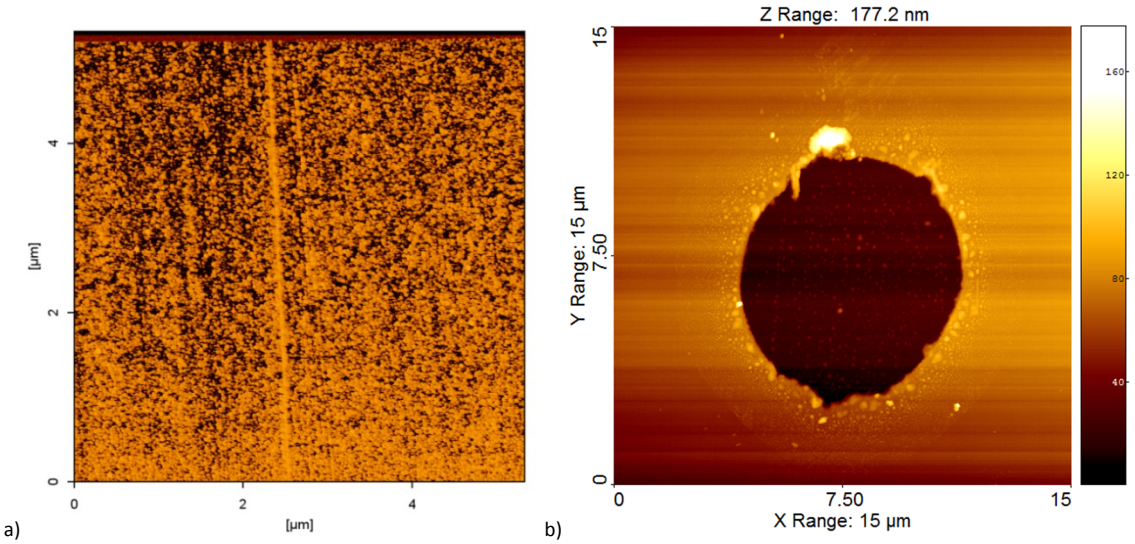

Figure 5.74 AFM images of the fabricated device showing a) an area of sputtered gold on glass; b) a glass circle surrounded by gold.

Table 5.14 Roughness measurements for fabricated devices. The values are the average of three samples, with the errors reported as standard deviation.

Roughness	Gold	Glass
Sa (average roughness)	0.78 ± 0.07 nm	1.08 ± 0.07 nm
Sq (root mean square roughness)	1.12 ± 0.15 nm	1.88 ± 0.13 nm

In conclusion, the micropattern devices were successfully fabricated by using standard photolithography techniques and characterised by means of AFM, SEM and EDX.

5.3.2 Development of a method for the orthogonal functionalisation of the micropatterned device for studies with sperm cells.

5.3.2.1 Strategy for the chemical functionalisation of gold and glass

Poly-d-lysine (PDL) is a positively charged peptide commonly used in cell research due to its cytophilic properties[21], including for the attachment of human sperm cells to glass surfaces[22]. This was therefore deemed a suitable component for the proposed application. The molecular structure of PDL is shown in Figure 5.75.

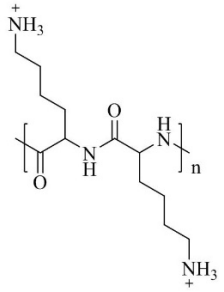

Figure 5.75 Molecular structure of PDL.

When developing a strategy for the orthogonal functionalisation of the device, particular attention was given to two studies reported by the Wheeler's group, which placed PDL layers on glass and silicon dioxide surfaces. The first study reported the use of a photoresist to create a pattern of PDL on a silicon dioxide surface[23]. The physisorbed PDL layer is said to remain on the silicon dioxide surface after sonication in acetone, and only removed from areas previously covered with photoresist. The second study reported a method for the covalent attachment of PDL on glass, using (3-glycidyloxypropyl)trimethoxy silane (or 3GPS) as a crosslinker. The functionalised surfaces were characterised by XPS and contact angle[24]. Bearing in mind that silanes also adsorb onto gold[25], a combination of the two methods was chosen for the proposed system (Figure 5.76).

The orthogonal functionalisation strategy consisted of:

-protection of gold with a layer of photoresist;

-functionalisation of glass with covalently bound PDL, *via* silanization, for cell attachment;

-removal of the photoresist layer;

-functionalisation of gold with a thiol.

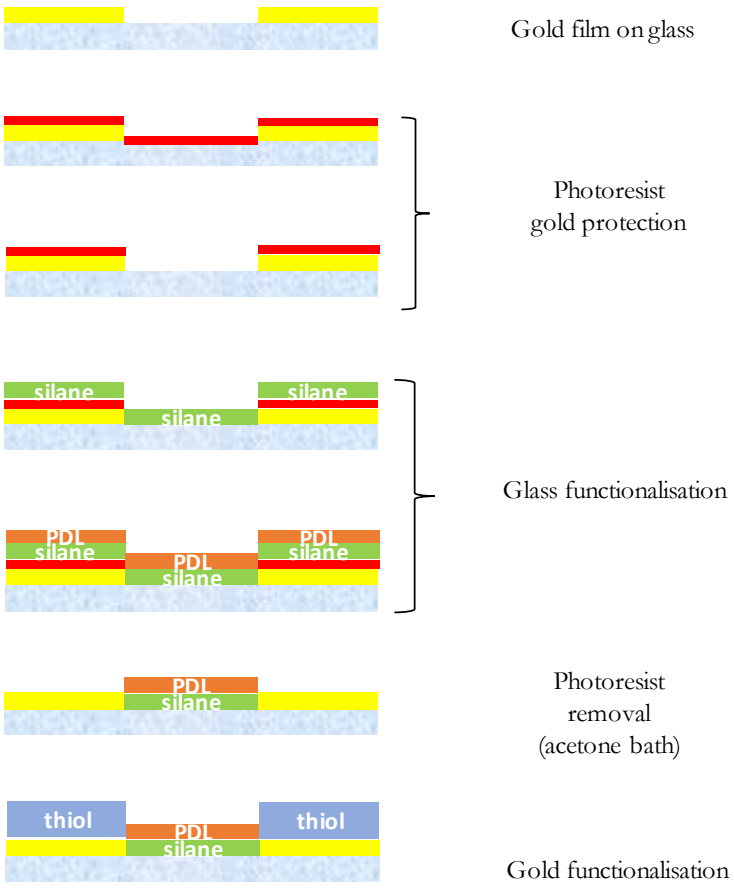

Figure 5.76 Strategy selected for the orthogonal functionalisation of the micropatterned device.

The novelty of this approach is the use of a photoresist protection layer for the orthogonal functionalisation of gold and glass, enabling micropatterning of motile sperm cells and their controlled exposure to a mixed SAM on gold with electrically switchable properties.

For the activation of glass before silane functionalisation, several methods are commonly used: immersion in piranha solution, UV-ozone (UVO) exposure, oxygen plasma, or immersion in concentrated NaOH or KOH solution. However, it must be taken into consideration that these conditions will be applied to the photoresist layer on gold and most of these methods will etch the photoresist layer. A thick layer of photoresist is therefore needed, to withstand the activation process.

Several questions were to be investigated with respect to the chosen functionalisation strategy. Would the photoresist layer withstand the conditions used for glass functionalisation? Would the PDL layer withstand the conditions used for photoresist removal as well as the conditions used for gold functionalisation? With these questions in mind, the following steps were followed. Starting with the formation of a PDL layer covalently attached to a glass surface *via* silane functionalisation, this layer was then tested for cell attachment. Once verified that the functionalisation of glass affected the gold surface, the gold surface was protected with a layer of photoresist prior to silane functionalisation. After silane functionalisation, the protective layer was removed from the gold surface *via* an acetone wash, a step previously described in the literature to not affect the PDL layers on glass. The final step of the orthogonal functionalisation process was to functionalise the gold surface with a thiol based SAM. For this step to be successful, the PDL layer on glass must be impervious to thiol SAM formation, and the gold surface has to be cleaned prior to thiol SAM formation. XPS, ellipsometry and contact angle techniques were selected for surface characterisation, and optical microscopy was utilised to test cell attachment.

To simplify the analysis of XPS and ellipsometry data, glass was replaced by silicon in these experiments. Analysing changes to the glass surface by every element in its composition would prove time consuming by XPS and glass transparency makes ellipsometry measurements inadequate. The results were assumed to be similar for these two materials, glass and silicon, as both contain SiO_2 for silane functionalisation. Cell attachment studies were performed on glass, as transparency is needed.

It is well known that the structure, thickness, wettability, reactivity and stability of silane films are affected by preparation conditions. Temperature, solvent, surface water content

and time of reaction are critical parameters[14, 26]. The silane chosen for this work was 3GPS, and was used as a crosslinker for PDL. The chemical structures of PDL and 3GPS attached to glass or Si are represented in Figure 5.77.

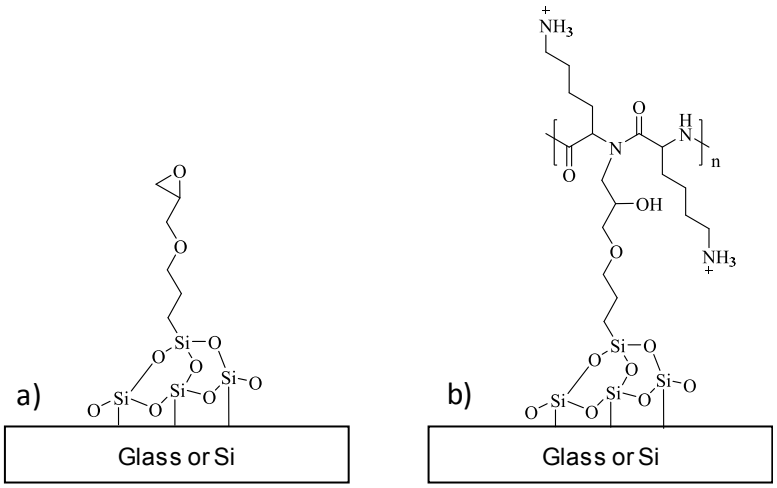

Figure 5.77 Chemical structures involved in the functionalisation of glass (or silicon) substrates for cell attachment. a) glass or Si-SiO_2 substrate functionalised with the silane 3GPS; b) glass or Si-SiO_2-3GPS functionalised with PDL.

C11EG6 was the only thiol used for gold functionalisation. This thiol is one of the components of the mixed SAM system constituting the ON-OFF switchable surface. The choice of using this component only was made due to the high cost of using the other component (progesterone peptide thiol) and in the interest of simplifying the XPS studies. Future work should include the use of the whole system. The C11EG6 thiol is referred to as "thiol" in the subsequent subchapters.

5.3.2.2 Covalent attachment of a PDL layer to a glass surface for cell attachment

Following the protocol reported by Nam et al.[24], plain silicon and microscope slides were functionalised with PDL via silanization with 3GPS. Briefly, the procedure consisted of 10

minutes UVO exposure, followed by submersion of the slides in a freshly prepared solution of 3GPS in toluene for 20 min. Afterwards, the slides were rinsed with toluene, dried under argon and incubated at 120°C for 30 min, and covered with freshly prepared PDL for 60 min. Finally, the slides were rinsed with water and dried under argon.

The surfaces were characterised at each functionalisation step by contact angle, ellipsometry and XPS.

Contact angle and ellipsometry results are shown below (Table 5.15). Presented values correspond to the mean calculated for at least 3 different samples, with 3 points being measured per sample. The errors presented correspond to the standard deviation.

Table 5.15 Static water contact angle and thickness (measured by ellipsometry) of 3GPS and 3GPS-PDL films formed on glass and silicon. The values are the average of three samples, with the errors reported as standard deviation.

Surface	Measured thickness (nm)	Theor. Thickness (nm)		Measured contact angle (°)	Literature contact angle (°)
		ChemDraw	Literature		
Si-SiO_2	-	-	-	≤ 10	<5 [27], [0 – 90]* [28]
Si-SiO_2-3GPS	0.82 ± 0.15	0.90	0.8 [12]	37± 4	[42-57] [24, 27, 29-30]
Si-SiO_2-3GPS-PDL	1.18 ± 0.32	1.44	-	60 ± 1	[26-70] [24, 31-32]
Glass	-	-	-	≤ 10	<5 [24]
Glass-3GPS	-	-	-	42 ± 4	30 [24]
Glass-3GPS-PDL	-	-	-	60 ± 3	22 [24]

* related to the thickness of the oxide layer.

As expected, both 3GPS and PDL layers are hydrophilic surfaces, with measured water contact angles lower than 90°. The hydrophilic properties of these surfaces are due to the presence of hydrophilic functional groups such as the epoxy group of the silane and the amino group of PDL. Contact angle values for these films are similar for both substrates (glass and silicon) indicating the creation of similar films. The values measured for 3GPS on Si (37° ± 4) are close to the values reported in the literature (varying from 42° [27] to 57° [30]). The values measured for the PDL film (60° ± 1°) are also in accordance with the wide range of values reported in the literature (from 26° [24] to 70° [32]).

Reported water contact angle values for clean silicon with a native oxide layer, vary from 0° to 90° depending on the thickness of the oxide layer. The contact angles of silicon surfaces appear to decrease with increasing oxide layer thicknesses, with the lowest values being associated with 4 nm thick oxide layers and the highest value being associated with an oxide layer thinner than 1 nm[28]. The measured value is presented as lower than 10° as the instrument does not provide an accurate measurement below this value. The proximity to the lower range of water contact angles indicates the presence of an oxide layer close to 4 nm thick.

Thickness values obtained by ellipsometry for 3GPS (0.82 ± 0.15 nm) and 3GPS-PDL (1.18 ± 0.32 nm) on Si are also in accordance with values reported in the literature[12, 23] and with the theoretical thickness estimated on ChemDraw. Results for contact angle and ellipsometry are summarized in Figure 5.78.

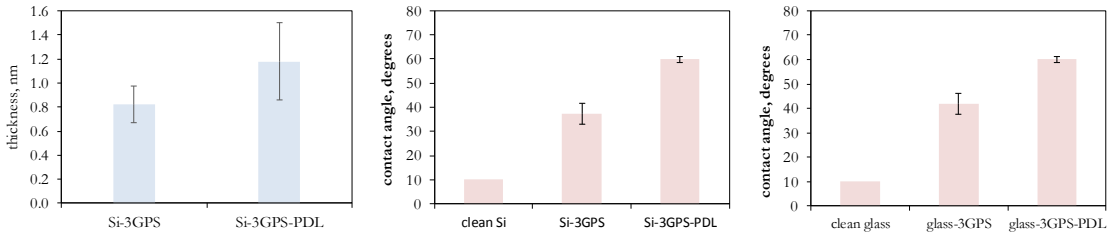

Figure 5.78 Thicknesses measured by ellipsometry (blue plot) and static water contact angle for 3GPS and 3GPS-PDL films formed on glass and on silicon. The values are the average of three samples, with the errors reported as standard deviation.

XPS high resolution scans were acquired for the key chemical elements that constitute the 3GPS-PDL layer: Si, N, O and C. As a control, clean Si surfaces were also analysed (Figure 5.79). Relative atomic percentages, calculated from the high resolution scans, are shown in Figure 5.80 and Table 5.16.

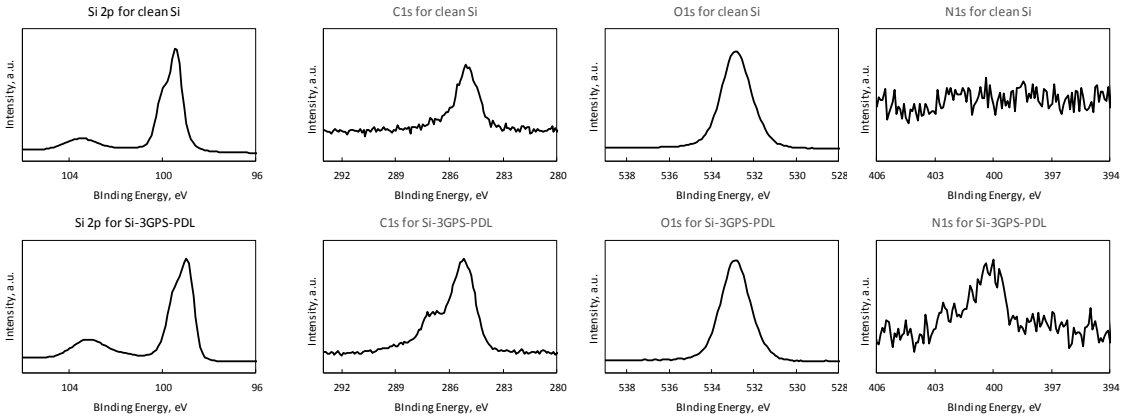

Figure 5.79 High resolution XPS scans for the key elements (Si, C, O and N) present on clean Si and on Si-3GPS-PDL surfaces.

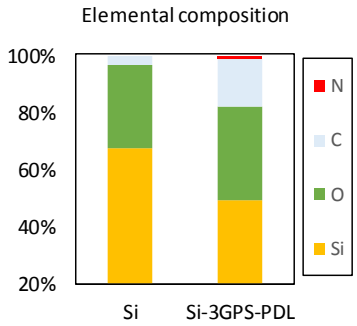

Figure 5.80 Relative atomic percentage of the clean Si surface and the 3GPS-PDL film on Si, calculated from regions of high resolution XPS spectra.

Table 5.16 Relative atomic percentages of key elements present on clean Si and on 3GPS-PDL film on Si calculated from regions of high resolution XPS spectra. The values are the average of three samples, with the errors reported as standard deviation.

	Relative elemental composition (atomic %)			
Surface	C 1s	O 1s	Si 2p	N 1s
Si	3 ± 0.3	29 ± 0.1	68 ± 0.2	0
Si-3GPS-PDL	17 ± 0.5	33 ± 1	49 ± 2	1 ± 0.2

The adsorption of atmospheric hydrocarbons as a result of the exposure of samples to a typical laboratory environment is well known. The presence of an adventitious carbon peak on supposedly clean surfaces is ubiquitous and its intensity is related to the degree of contamination[33]. The presence of carbon in the "clean" Si surface was therefore anticipated. The C1s spectrum for both clean Si and 3GPS-PDL reacted surfaces can be deconvoluted into 3 peaks, corresponding to C-C and C-H bonds (at 284.8 eV), C-O and C-N bonds (at 286.6 eV) and C=O (at 288.5 eV) bonds (Figure 5.81). As a result of the

functionalisation of Si, there is an increase in the component fraction of C-O, C-N and C=O, compared to the Si surface covered with hydrocarbon contamination.

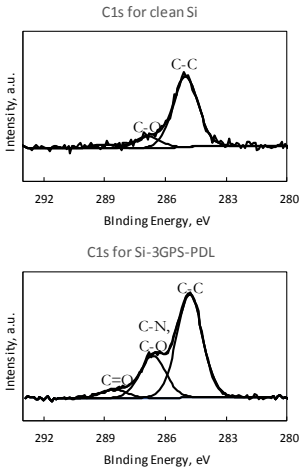

Figure 5.81 High resolution XPS scans of C1s with fitted component peaks for a) clean Si and b) Si-3GPS-PDL.

The oxygen contamination on clean Si is also common from exposure of samples to the atmosphere and was therefore expected.

Regarding the Si 2p spectrum, the first Si $2p_{3/2}$, at 99.4 eV, can be assigned to the Si element. The secondary peak is assigned to SiO_2, which is likely to be overlapped with signals derived from oxygen contamination and other species such as Si-OH.

As expected, the Si-3GPS-PDL samples show less silicon and more carbon, compared to clean silicon. The depth of sample analysed by XPS is around 10 nm and therefore when very thin films like this one (1.18 nm) are analysed, there is still a large contribution from the substrate material (in this case, silicon). Nitrogen is present in the 3GPS-PDL reacted samples, confirming the attachment of PDL. The ratio of nitrogen to carbon calculated from high resolution XPS spectra data is 0.04 ± 0.01. This value is lower than expected

from the stoichiometric composition (2 Ns for 11 Cs, giving N/C as 0.18). Several factors might contribute to this result, namely: a) the fraction of carbon that comes from contamination as a result of air exposure, would lead to a lower N/C ratio; b) the incomplete reaction of PDL to the 3GPS film; c) lack of accuracy of the relative sensitivity factors applied for the normalisation of the XPS data.

Further investigations could provide more information about the PDL layer, for example, angle resolved XPS measurements could be performed to confirm the position of nitrogen in the film. It is expected that higher incubation times with PDL, would lead to the formation of films with higher percentages of nitrogen, which would in turn have an effect on the number of sperm cells attached. For the aim of this work, it is not a requirement to have a large number of cells attached to the surface.

5.3.2.3 Attachment of sperm cells to PDL functionalised surfaces

After creation of the PDL layer covalently attached to the glass surface, cell attachment to the surface was tested using a flow cell system combined with an inverted microscope (Figure 5.82).

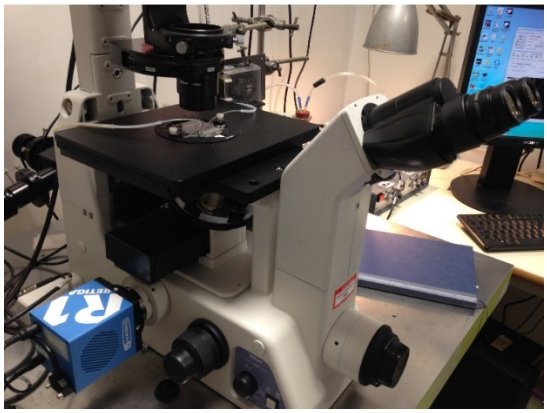

Figure 5.82 Experimental setup with a flowcell system. After incubation with sperm cells, the chamber was washed with buffer at a low flowrate to remove lose cells, leaving behind sperm cells that were attached to the functionalised surface. The surface was then ready for imaging.

As shown in Figure 5.83, sperm cells were successfully attached to the 3GPS-PDL functionalised glass, previously characterised by contact angle. A control experiment was performed using a standard PDL layer physiosorbed onto glass, without 3GPS silane as a crosslinker, resulting in a similar number of cells attached.

a) 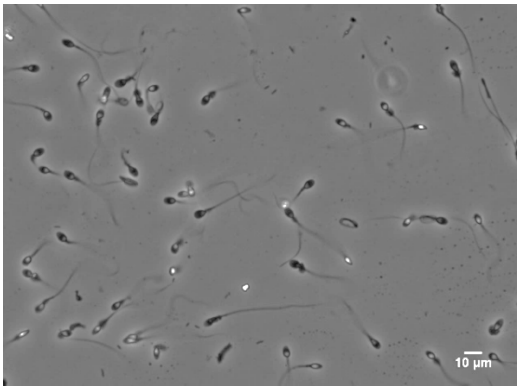

b) 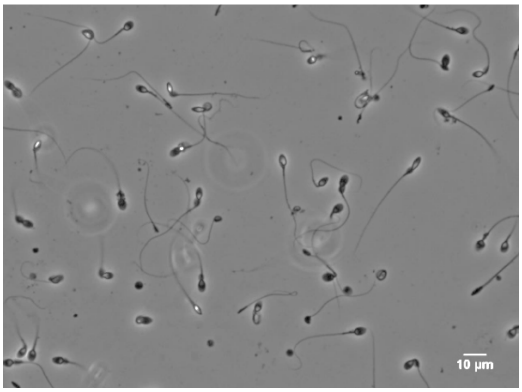

Figure 5.83 Optical microscope image for cell attachment on a) glass-3GPS-PDL and on b) standard PDL on glass (control).

5.3.2.4 Investigating gold surface changes under the conditions used for glass functionalisation

Adsorption of silanes onto gold has been reported in the literature [25]. In order to investigate gold surface changes under the conditions used for glass functionalisation, clean gold surfaces were treated as described in the previous subchapter for the formation of the 3GPS-PDL layer, and surface characterisation was performed. Contact angle and ellipsometry measurements, summarised in Table 5.17, showed a change in the surface

properties in comparison to clean gold surfaces. The contact angle increased and ellipsometry measurements indicated the presence of a thin film on the gold surface.

Table 5.17 Thickness (measured by ellipsometry) and static water contact angle values of gold surfaces before and after exposure to the conditions used for the functionalisation of glass. The values are the average of three samples, with the errors reported as standard deviation.

Surface	Thickness (nm)	Contact angle (°)
Au (UVO 10 min)	-	77
Au-silane	0.90 ± 0.16	95 ± 0.4

The presence of nitrogen and silicon on the gold surface was verified by XPS. The survey scan for these samples is shown in Figure 5.84. These results confirm change to the gold surface during glass functionalisation process. Therefore, it is vital that the gold surface is protected during this process. The protection of gold with a photoresist layer is investigated in the next subchapter.

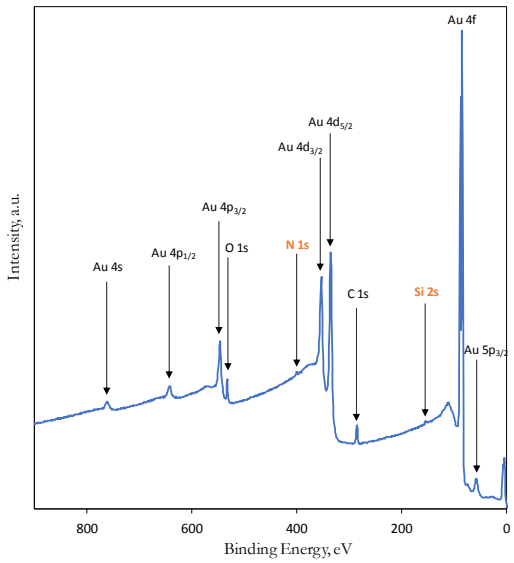

Figure 5.84 XPS survey scan of the gold surface after treatment following the 3GPS-PDL functionalisation protocol, highlighting the presence of nitrogen and silicon, from PDL and 3GPS, respectively.

5.3.2.5 Testing the photoresist removal via acetone washing process on gold

A gold sample was covered with a thick layer of photoresist (PR) and exposed to the glass/silicon functionalisation protocol. Photoresist-3GPS-PDL layer removal from the gold surface by acetone wash was then verified by means of XPS. High resolution scans were acquired for the key elements and are shown in Figure 5.85.

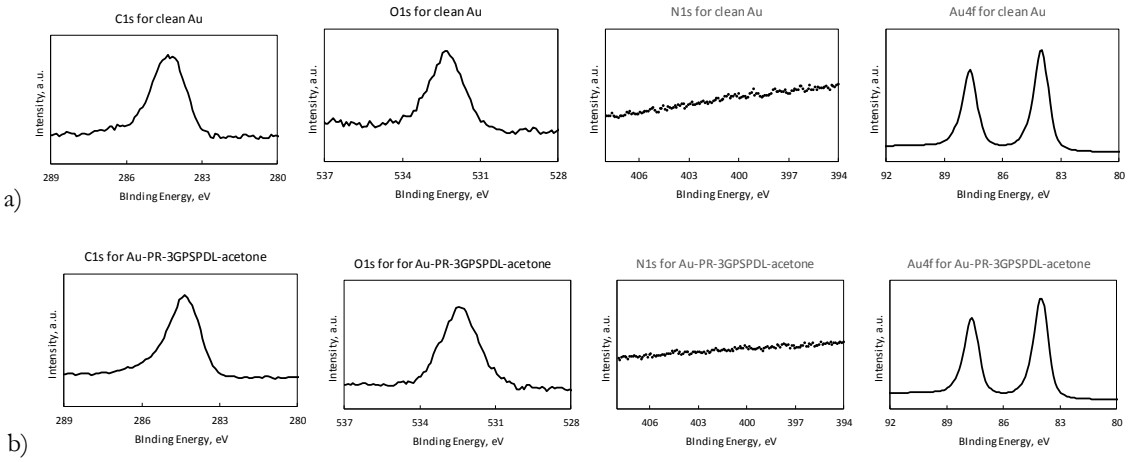

Figure 5.85 High resolution XPS scans for a) clean Au and b) Au surface after photoresist protection, 3GPS-PDL functionalisation and acetone wash for photoresist removal.

Nitrogen is not present on the surface after rinsing with acetone for 2 minutes, indicating the absence of PDL on the surface. The high resolution XPS scans show no obvious difference between the clean gold sample and the gold sample after photoresist removal, with only carbon and oxygen contamination being present. Despite the similarity in the shape of the peaks from the high resolution scans, there is a significant difference in the carbon content when quantifying the relative atomic percentages for the key elements, accompanied by an attenuation of the gold signal (Table 5.18 and Figure 5.86).

This amount of carbon on the surface might originate from a residual amount of photoresist present on the surface. However, this was not detected on the optical microscope.

Table 5.18 Relative atomic percentages of key elements present on clean Au surfaces and on PR-3GPS-PDL reacted Au surfaces after acetone washing, calculated from high resolution XPS spectra. The values are the average of three samples, with the errors reported as standard deviation.

	Relative elemental composition (atomic %)		
Surface	C 1s	O 1s	Au 4f
Clean Au	32 ± 0.8	11 ± 0.4	57 ± 0.4
Au-PR-3GPS-PDL after acetone wash	50 ± 2	15 ± 0.2	35 ± 3

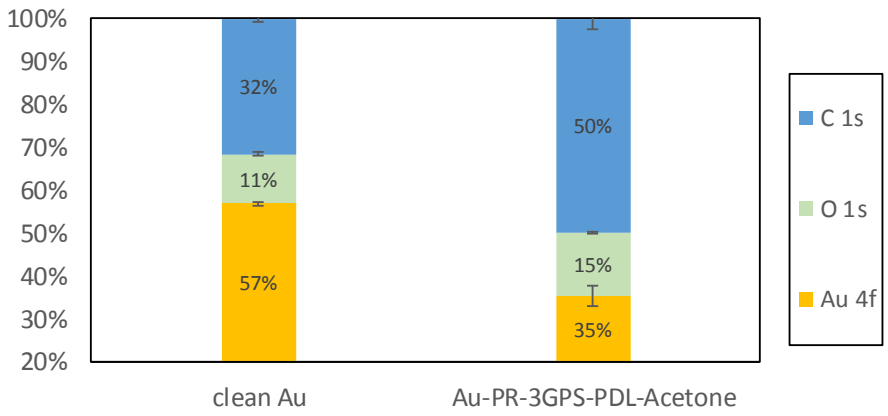

Figure 5.86 Relative atomic percentage of clean Au surfaces and PR-3GPS-PDL reacted Au surfaces after acetone washing, calculated from regions of high resolution XPS spectra. The values are the average of three samples, with the errors reported as standard deviation.

5.3.2.6 Investigating the functionalisation of clean and photoresist treated gold surfaces with thiol SAMs

Ellipsometry, contact angle, and XPS techniques were utilised to analyse thiol SAM formation on clean gold surfaces and thiol SAM formation on gold surfaces which had undergone the photoresist-3GPS-PDL removal process (termed 'treated Au' and 'Au'). The thickness values for thiol SAMs created on clean gold were slightly lower than that of thiol SAMs created on treated gold surfaces (Table 5.19). The contact angle values are also different (38° ± 2° vs 61° ± 3°).

Table 5.19 Static water contact angle and thickness (measured by ellipsometry) of the thiol SAM formed on clean gold (Au-thiol) and on PR-3GPS-PDL film on gold after acetone wash (treated Au-thiol). The values are the average of three samples, with the errors reported as standard deviation.

Surface	Measured thickness (nm)	Measured contact angle (°)
Au-thiol	1.72 ± 0.08	38 ± 2
Treated Au-thiol	1.98 ± 0.11	61 ± 3

High resolution XPS scans of these surfaces are shown in Figure 5.87 and calculated relative atomic percentages are shown in Table 5.20.

Only sulfur, carbon, oxygen and gold were detected, as expected, for the thiol films. In particular, the presence of sulfur, confirms the presence of the thiol attached to the gold surface. However, the C1s scan for the thiol SAM formed on clean Au shows a higher amount of C-O bonds, compared to the thiol SAM formed on gold previously covered

with photoresist. Also, the relative atomic percentage of carbon is higher with the latter (Table 5.20), which is in accordance with the higher percentage of carbon observed for the Au-PR-3GPS-PDL surfaces after acetone washing (Table 5.18).

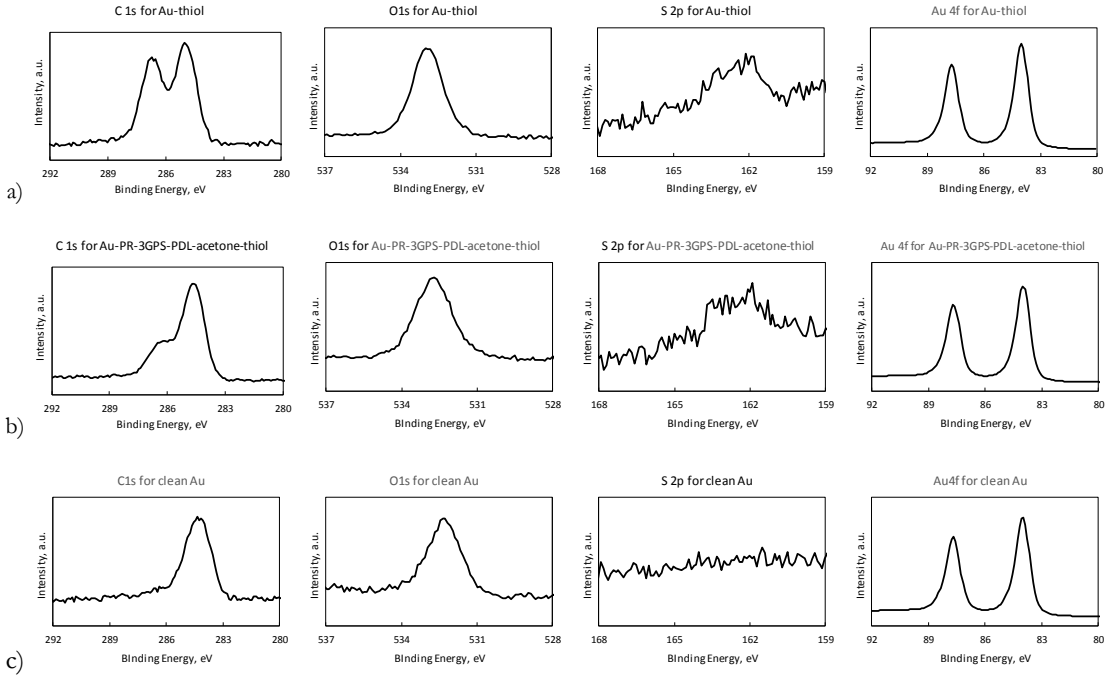

Figure 5.87 High resolution XPS scans of a) Au-thiol, b) treated Au-thiol and c) clean Au.

Table 5.20 Relative atomic percentages of key elements present on clean Au surfaces, on treated Au-thiol surfaces, and on Au-thiol surfaces, calculated from high resolution XPS spectra. The values are the average of three samples, with the errors reported as standard deviation.

	Relative elemental composition (atomic %)			
Surface	C 1s	O 1s	Au 4f	S 2p
Clean Au	32 ± 1	11 ± 0.4	57 ± 0.4	0
Treated Au-thiol	64 ± 4 (C-O: 26 ± 1)	17 ± 1	18 ± 4	1 ± 0.3 (bound: 64 ± 3)
Au-thiol	49 ± 2 (C-O: 47 ± 2)	18 ± 0.3	32 ± 2	1 ± 0.1 (bound: 71 ± 9)

Regarding the S 2p region, the average value for the amount of bound sulfur is slightly higher for the thiol SAM formed on clean Au, compared to the treated gold surface, but this difference is not significant considering the associated standard deviation values. The low relative atomic percentage of sulfur is expected due to the attenuation of signal caused by the overlying chain. Deconvoluted peaks for C1s and S2p regions are shown in Figure 5.88.

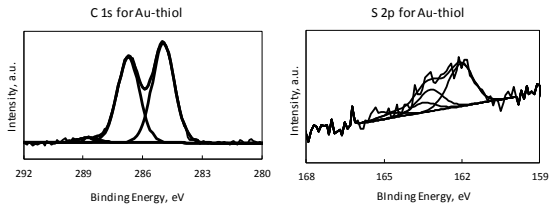

Figure 5.88 High resolution XPS scans of C1s and S 2p with fitted component peaks for Au-thiol and treated-Au thiol surfaces.

Considering the results for the characterisation of the thiol film on gold, one can say that the films formed on both clean gold and treated gold surfaces are different. However, as the thiol is present on the surface, and depending on the application, this difference might not be an issue. Further optimisation of the photoresist removal process could be performed to eliminate these differences. A few tests were performed regarding the rinsing step with acetone by increasing the rinsing duration (1h), adding sonication (*via* an ultrasonic bath) and heating the solution (40°C) but no improvement was observed in terms of the contact angle values of the resulting thiol film. A different option to be tried could be to reduce the temperature used in the heating step of the silanization process as high temperature (≥110°C) can lead to a high degree of photoresist crosslinking, becoming more rigid and making it difficult to dissolve and remove from the surface. However, one must guarantee that toluene from the 3GPS solution is completely evaporated from the surface. Two key factors in SAM formation are the incubation time and the concentration of the thiol solutions used. Therefore, future work could involve optimising these conditions in order to improve the quality of the formed SAM.

Further investigation on the functionalised gold surfaces will have to be performed when moving from the single component thiol film to the double thiol components switchable system. In addition to XPS studies, SPR studies where a progesterone antibody binds to the progesterone peptide, will provide a more detailed characterisation of the surface.

5.3.2.7 Testing the effect of acetone washing process and thiol incubation on the functionalised silicon surfaces

The 3GPS-PDL layer on Si was unaffected by acetone washing or by incubation with thiol as shown below in Figure 5.89, Table 5.21, and Figure 5.90. The high resolution scans are very similar before and after acetone washing and also before and after incubation with thiol.

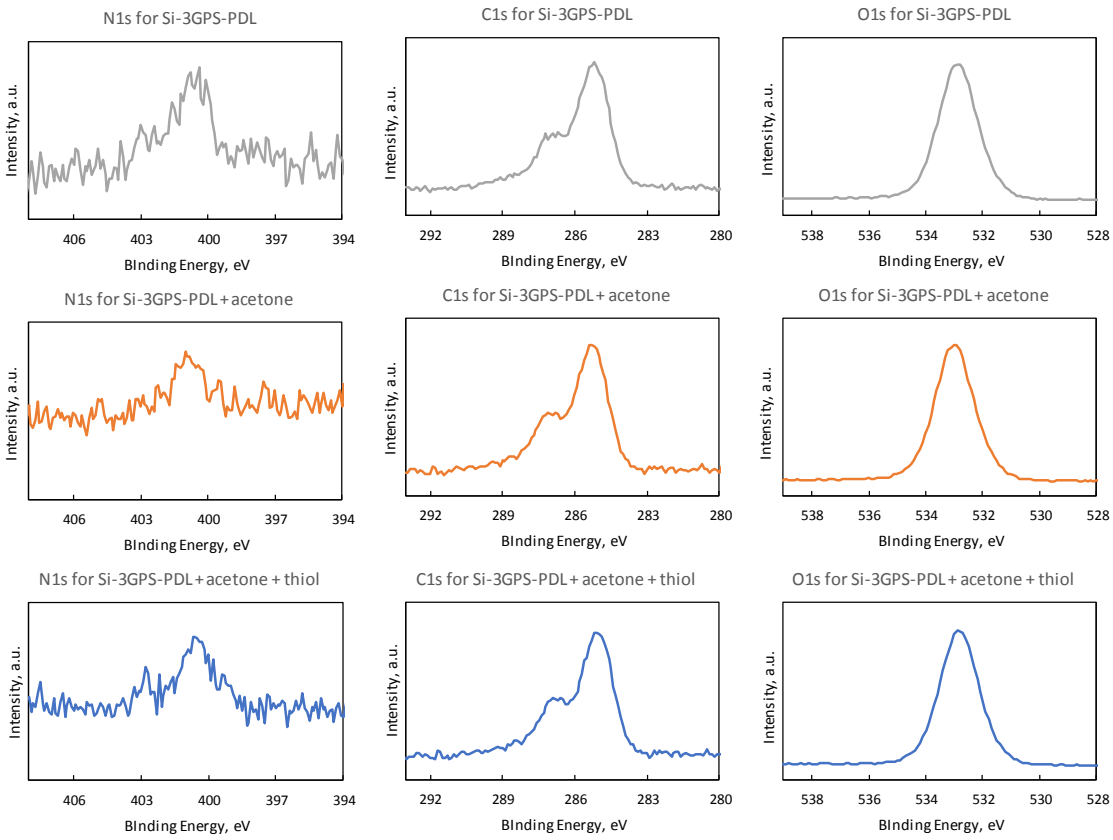

Figure 5.89 High Resolution XPS scans for the key elements (C, O and N) of a) Si-3GPS-PDL surfaces and subsequent b) acetone wash and c) incubation with the thiol.

Table 5.21 Relative atomic percentages of key elements present on 3GPS-PDL film on Si, on 3-GPS-PDL after acetone rinse, and on 3-GPS-PDL film on Si after acetone rinse and incubation with thiol, calculated from regions of high resolution XPS spectra. The values are the average of three samples, with the errors reported as standard deviation.

	Relative elemental composition (atomic %)			
Surface	C 1s	O 1s	Si 2p	N 1s
Si-3GPS-PDL	17 ± 1	33 ± 1	49 ± 1	1 ± 0.1
Si-3GPS-PDL + acetone wash	18 ± 1	34 ± 2	48 ± 1	1 ± 0.1
Si-3GPS-PDL + acetone wash + thiol	18 ± 2	35 ± 2	46 ± 3	1 ± 0.5

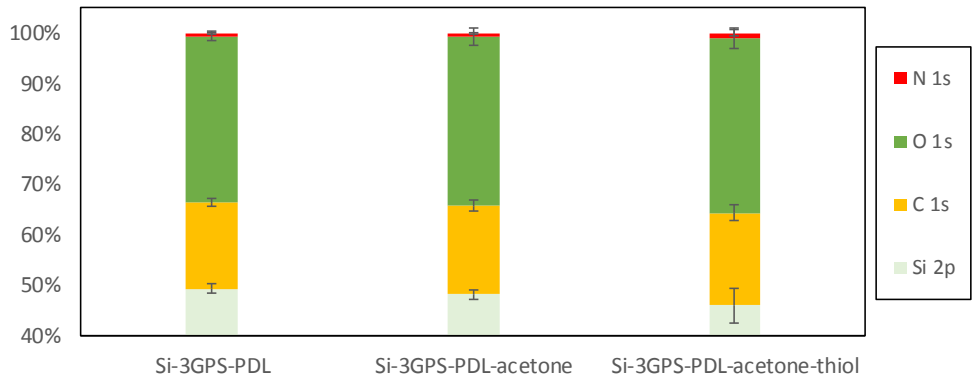

Figure 5.90 Relative atomic percentages of key elements present on 3GPS-PDL film on Si, on 3GPS-PDL film on Si after acetone rinse and 3GPS-PDL film on Si after acetone rinse and incubation with thiol, calculated from regions of high resolution XPS spectra. The values are the average of three samples, with the errors reported as standard deviation.

Presence of sulfur was also investigated on the Si-3GPS-PDL surface after incubation in thiol solution. For this purpose, a high resolution scan for S 2s region (Figure 5.91) was used instead of S 2p region, as this region is overlapped by a fundamental Si 2s plasmon[34]. No sulfur peak was detected in that region, indicating that the thiol was not present on the surface, at least not in a concentration detectable by XPS. For comparison, a S 2s region scan is shown for the thiol SAM on gold, where a small peak is present.

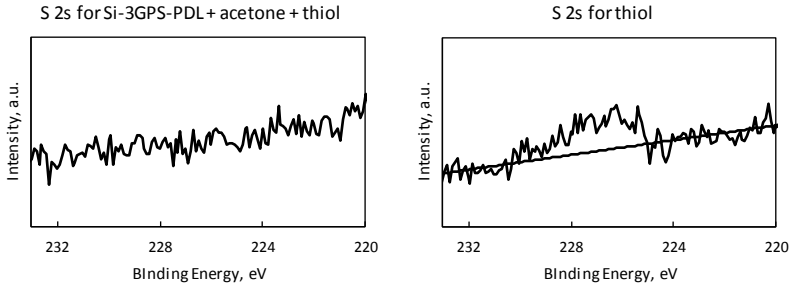

Figure 5.91 High resolution XPS scans for S 2s regions of a) Si-3GPS-PDL surface followed by acetone wash and incubation with the thiol; b) thiol SAM on Au.

Complementary to the XPS results, contact angle and thickness values shown in Table 5.22, also indicate that the 3-GPS-PDL film on Si was not affected by acetone washing or incubation with thiol solution.

Table 5.22 Static water contact angle and thickness (measured by ellipsometry) of 3GPS-PDL films formed on silicon followed by acetone washing and incubation with thiol. The values are the average of three samples, with the errors reported as standard deviation.

Surface	Measured thickness (nm)	Measured contact angle (°)
Si-3GPS-PDL + acetone washing	1.00 ± 0.01	48 ± 5
Si-3GPS-PDL + acetone washing + thiol	0.99 ± 0.02	52 ± 5

Finally, sperm cell attachment tests were performed on the 3GPS-PDL layers after acetone washing and incubation with thiol. As seen in Figure 5.92, the surface kept its ability for cell attachment.

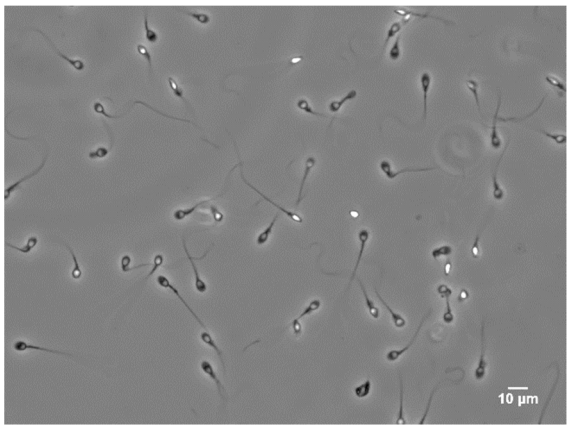

Figure 5.92 Optical microscope image of cell attachment onto glass substrate with 3GPS-PDL layers after acetone washing and incubation with C11EG6 thiol.

5.4 Conclusions and Future Work

A micropatterned device was successfully fabricated for future studies with cells. A method was developed for the orthogonal functionalisation of the micropatterned device, based on the protection of the gold surface with a photoresist film prior to the functionalisation of glass, and removal of this protective layer before functionalisation of gold with a thiol SAM. The strategy followed for orthogonal functionalisation of gold and glass proved to be successful, as demonstrated by surface characterisation techniques such as ellipsometry, contact angle, XPS, and optical microscopy. On one hand, the photoresist layer on gold survived the conditions used for the formation of the silane-PDL layer on glass. On the other hand, the silane-PDL layer on glass survived the photoresist removal from gold process and further functionalisation with thiol, remaining effective for cell attachment. This novel approach for functionalisation of gold and glass allowed the patterning of sperm cells with simultaneous exposure to a functionalised gold surface. Combined with a switchable surface formed on gold, these studies provide a novel tool for cell biology applications.

After having developed the method for the orthogonal functionalisation of the fabricated device, one additional step needs to be added to the microfabrication process, which consists of covering the gold regions with photoresist. This can be done by standard photolithography. Briefly, the fabricated device is spin coated with photoresist and exposed to light, under the same micropatterned mask that was used for the fabrication process. After immersion in developer solution, the photoresist will only remain on the gold regions, being removed from the glass circles. The devices will then be ready for functionalisation.

The following investigations could be performed in continuation of the studies described in this chapter:

(i) Optimisation of the fabrication process in order to obtain defect free devices.

(ii) Testing the developed orthogonal functionalisation method to functionalise the gold surface with the mixed components of the switchable surface described in chapter 4, rather than a single component as described in this chapter, and confirm the chemical composition of the formed surface by using surface characterisation techniques.

(iii) Testing the fabricated device for micropatterning of cells.

5.5 List of References

1. Sreenivasan, S., Nanoimprint lithography steppers for volume fabrication of leading-edge semiconductor integrated circuits. *Nature Microsystems & Nanoengineering* **2017,** *3* (17075).

2. Moreau, W., *Semiconductor Lithography Principles, Practices, and Materials*. Springer US: 1988.

3. Campbell, S., *Fabrication engineering at the micro- and nanoscale, 4th edition*. Oxford University Press: 2013.

4. Brydson, R.; Hammond, C., Generic Methodologies for Nanotechnology: Classification and Fabrication. In *Nanoscale Science and Technology*, Kelsall, R.; Hamley, I.; Geoghegan, M., Eds. John Wiley & Sons: 2005.

5. Zaouk, R.; Park, B.; Madou, M., Introduction to microfabrication techniques. *Methods in Molecular Biology* **2006,** *321*.

6. MicroChemicals, Basics of microstructuring Lift-Off. *MicroChem Technical Notes*.

7. Nanoscale labs, Micropatterning. (accessed 26.04.2018, from http://www.nanoscalelabs.com/micropatterning.html).

8. Stelling, C.; Mark, A.; Papastavrou, G.; Retsch, M., Showing particles their place: deterministic colloid immobilization by gold nanomeshes. *Nanoscale* **2016,** *8* (30), 14556-64.

9. Palazon, F.; Leonard, D.; Le Mogne, T.; Zuttion, F.; Chevalier, C.; Phaner-Goutorbe,

M.; Souteyrand, E.; Chevolot, Y.; Cloarec, J., Orthogonal chemical functionalization of patterned gold on silica surfaces. *Beilstein Journal of Nanotechnology* **2015,** *6*, 2272-7.

10. Durán, S.; Duch, M.; Patiño, T.; Torres, A.; Penon, O.; Gómez-Martínez, R.; Barrios, L.; Esteve, J.; Nogués, C.; Pérez-García, L.; Plaza, J., Technological development of intracellular polysilicon–chromium–gold chips for orthogonal chemical functionalization. *Sensors and Actuators B: Chemical* **2015,** *209*, 212-224.

11. Slater, J.; Frey, W., Nanopatterning of fibronectin and the influence of integrin clustering on endothelial cell spreading and proliferation. *Journal of Biomedical Materials Research Part A* **2008,** *87* (1), 176-95.

12. Schenk, F.; Boehm, H.; Spatz, J.; Wegner, S., Dual-functionalized nanostructured biointerfaces by click chemistry. *Langmuir* **2014,** *30* (23), 6897-905.

13. Park, S., Fabrication and characterization of nanopatterns for selective cell adhesion. *Journal of the Korean Physical Society* **2015,** *67* (4), 706-712.

14. Dugas, V.; Demesma, C.; Chevolot, Y.; Souteyrand, E., *Use of organosilanes in biosensors*. Nova Science Publishers: New York, 2010.

15. Agar Scientific Technical data. (accessed 26.04.2018, from http://www.agarscientific.com/microscope-slides.html).

16. Love, J.; Estroff, L.; Kriebel, J.; Nuzzo, R.; Whitesides, G., Self-assembled monolayers of thiolates on metals as a form of nanotechnology. *Chemical reviews* **2005,** *105* (4).

17. Eliasson, R., Standards for investigation of human semen.pdf. *Andrologie* **1971,** *3* (2), 49-64.

18. Golden, J.; Miller, H.; Nawrocki, D.; Ross, J., Optimization of bi-layer lift-off resist process. *MicroChem Technical Notes* **2005**.

19. Tabor, R.; Morfa, A.; Grieser, F.; Chan, D.; Dagastine, R., Effect of gold oxide in measurements of colloidal force. *Langmuir* **2011,** *27* (10), 6026-30.

20. Knarr, R.; Quon, R., Direct Force Measurements at the Smooth Gold/Mica Interface. *Langmuir* **1998,** *14*, 6414-6418.

21. McKeehan, W.; Ham, R., Stimulation of clonal growth of normal fibroblasts with substrata coated with basic polymers. *The Journal of Cell Biology* **1976,** *71*, 727-734.

22. Nash, K.; Lefievre, L.; Peralta-Arias, R.; Morris, J.; Morales-Garcia, A.; Connolly, T.; Costello, S.; Kirkman-Brown, J.; Publicover, S., Techniques for imaging Ca2+ signaling in human sperm. *Journal of Visualized Experiments* **2010,** (40).

23. Corey, J.; Brunette, A.; Chen, M.; Weyhenmeyer, J.; Brewer, G.; Wheeler, B., Differentiated B104 neuroblastoma cells are a high-resolution assay for micropatterned substrates. *Journal of Neuroscience Methods* **1997,** (75), 91-97.

24. Nam, Y.; Branch, D.; Wheeler, B., Epoxy-silane linking of biomolecules is simple and effective for patterning neuronal cultures. *Biosensors and Bioelectronics* **2006,** *22* (5), 589-97.

25. Spencer, M.; Nyberg, G., Adsorption of silane and methylsilane on gold surfaces. *Surface Science* **2004,** *573* (2), 151-168.

26. Kim, J., Formation, structure, and reactivity of amino-terminated organic films on silicon substrates. In *Interfaces and interphases in analytical chemistry*, American Chemical Society: 2011.

27. Luzinov, I.; Julthongpiput, D.; Liebmann-Vinson, A.; Cregger, T.; Foster, M.; Tsukruk, V., Epoxy terminated self assembled monolayers: molecular glues for polymer layers. *Langmuir* **2000,** *16* (2), 504-516.

28. Williams, R.; Goodman, A., Wetting of thin layers of SiO2by water. *Applied Physics Letters* **1974,** *25* (10), 531-532.

29. Funk, C.; Dietrich, P.; Gross, T.; Min, H.; Unger, W.; Weigel, W., Epoxy-functionalized surfaces for microarray applications: surface chemical analysis and fluorescence labeling of surface species. *Surface and Interface Analysis* **2012,** *44* (8), 890-894.

30. Shin, D.; Lee, K.; Jang, K.; Kim, J.; Chung, W.; Kim, Y.; Lee, Y., Protein patterning by maskless photolithography on hydrophilic polymer-grafted surface. *Biosensors and Bioelectronics* **2003,** *19* (5), 485-494.

31. Ai, H.; Lvov, Y.; Mills, D.; Jennings, M.; Alexander, J.; Jones, S., Coating and Selective Deposition of Nanofilm on Silicone Rubber for Cell Adhesion and Growth. *Cell Biochemistry and Biophysics* **2003,** *38*.

32. Cantini, E. Switchable Surfaces for Biomedical Applications. University of Birmingham, 2017.

33. Smith, G., Evaluation of a simple correction for the hydrocarbon contamination layer in quantitative surface analysis by XPS. *Journal of Electron Spectroscopy and Related Phenomena* **2005,** *148* (1), 21-28.

34. Mélinon, P.; Kéghélian, P.; Prével, B.; Perez, A.; Guiraud, G.; LeBrusq, J.; Lermé, J.; Pellarin, M.; Broyer, M., Nanostructured silicon films obtained by neutral cluster depositions. *The Journal of Chemical Physics* **1997,** *107* (23), 10278-10287.

6 Development of a Method for the Functionalisation of Fluorescent Spheres with a Low Density of Progesterone Oligopeptide

This chapter describes a method for the covalent bi-functionalisation of polystyrene fluorescent spheres. These spheres, presenting on their surface a low density of thiolated progesterone oligopeptide and a low molecular weight polyethylene glycol as a spacer, will be the basis for further studies with sperm cells and their response to the functionalised particles in terms of Ca^{2+} signalling. XPS and fluorometry were the main techniques used for the characterisation of the functionalised fluospheres. Several challenges were found along the functionalisation process, which are discussed in this chapter.

6.1 Introduction

The functionalisation of nanoparticles with biomolecules has received abundant attention in the last few decades[1] with particular focus on biomedical applications such as diagnosis, through biosensors[2-3] and molecular imaging enhancing[3-5], and therapeutics, through targeted drug delivery[6-7]. In comparison to the functionalisation of flat surfaces, the functionalisation of particles brings an additional major challenge, which is maintaining colloidal stability, i.e. controlling the aggregation and sedimentation of the particles.

Fluorescently labelled polystyrene particles (fluospheres) are commercially available in a wide range of sizes and surface chemistries and have been explored for the aforementioned applications. The toxicity of polystyrene has been extensively studied and this material is considered inert and biocompatible. However, nanoparticle toxicology is distinct from the toxicology of the corresponding bulk material, due to the increased reactivity of the nanoparticles as a result of the large surface to volume ratio. The evaluation of the

toxicology of functionalised nanoparticles requires investigation of nanoparticle-cell interactions.[8]

Several studies have investigated the interaction of nanoparticles (predominantly gold[9-11] but also silver[12-13], silica[14], zinc oxide[15], iron oxide[16], and europium[17]) with sperm cells (human[9-10], mice[12-13, 15-16], boar[14] and bovine[17-18] spermatozoa). The main focus was on the effect of the nanoparticles on cell viability and motility. According to those studies, some particles did not seem to affect the cells[14, 17-18] while others had negative effects on cells[9, 12, 15-16], mainly in terms of decreased motility, frequently in a dose-dependent manner[10]. Braydich-Stolle et al.[12] called attention to the important fact that it is not only the nanoparticles that might influence cells, but also the cellular environment which might have an effect on the physicochemical properties of the nanoparticles and this aspect should therefore be considered in biocompatibility studies.

Progesterone-C7-4KC oligopeptide and a hexaethylene glycol-terminated thiol (C11EG6) (Figure 6.93) were the main components used for the development of an electrically switchable surface, as described in chapter 4. This surface was created for interaction with sperm cells, where exposure to progesterone is controlled by the electrical potential applied to the surface. The interaction of progesterone-C7-4KC oligopeptide with sperm cells had not been investigated before and a better understanding of how the cells will respond to this oligopeptide is crucial. It is expected that the cells will react to the exposure of the progesterone peptide in the same way as they would react to the exposure of progesterone molecules in solution, but this has not been tested yet. Steric hindrance might have an effect on the interaction of the sperm cells with a planar functionalised surface. For this reason, studies will be conducted with a solution of fluospheres functionalised with a low density of the oligopeptide. The choice of promoting the interaction of cells with

functionalised particles in solution, in comparison to the use of a planar functionalised surface, aims to reduce steric hindrance effects and allow more chance of contact of the progesterone peptide with the cell receptors. Future work will entail fluorescence imaging of labelled sperm cells interacting with the progesterone-fluospheres, and collecting information on Ca^{2+} signalling (see detailed information on this subject in chapter 4). Before that, a functionalisation method must be developed for the covalent attachment of the progesterone peptide to the fluospheres, and full characterisation of the functionalised fluospheres must be performed. Following the same strategy as for the developed switchable surface, the oligopeptide molecules will be spaced at the surface of the fluospheres to prevent nonspecific adsorption, and to allow full access of the progesterone present for binding interactions. In addition, it is vital that no unreacted reagents or secondary products are left in the solution, even in very small amounts (picomolar concentrations), since these could interact with the sperm cells and distort the results produced.

6.2 Aim and objectives

The aim of the work described in this chapter was to develop a method for bi-functionalisation of fluorescent spheres with a low density of progesterone oligopeptide.

Objectives:

1. Design a functionalisation method for the fluospheres *via* a covalent approach.
2. Characterisation of commercially supplied amine-terminated fluospheres by TEM, DLS, NMR and XPS.
3. Functionalisation of amine-terminated fluospheres with a maleimide crosslinker and characterisation by NMR and XPS.

4. Functionalisation of maleimide-terminated fluospheres with C11EG6 and progesterone oligopeptide (Figure 6.96). Characterisation of the resulting products by DLS, XPS and fluorescence microscopy (using a labelled progesterone antibody).
5. Optimisation of the labelling of sperm cells for fluorescence imaging.

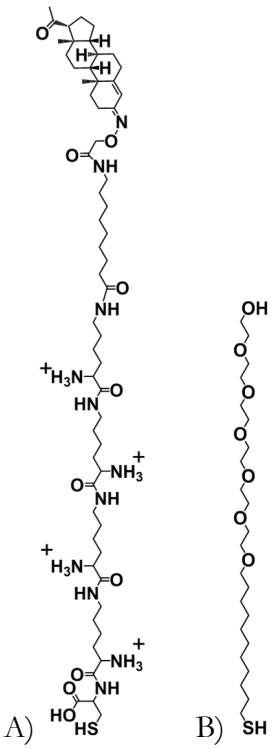

Figure 6.93 – Chemical structure of A) the progesterone-C7-4KC oligopeptide and B) the spacer hexaethylene glycol thiol (C11EG6), main components of the electrically switchable surface as described in chapter 4.

6.3 Results and Discussion

6.3.1 Designing the functionalisation of fluospheres with an oligopeptide – covalent approach

Amine-terminated dye-encapsulated polystyrene spheres were selected as a starting point for these studies. The dye trapped within the polystyrene is not exposed to the external environment of the spheres, and therefore is protected from oxygen exposure, presenting minimal photobleaching. The particles should be no bigger than the size of the sperm cell (55 μm x 3 μm) and should be visible under an optical microscope, and thus 200 nm diameter spheres were chosen. The strategy followed for the functionalisation of the particles was to make use of a heterobifunctional cross-linker with N-hydroxysuccinimide (NHS) ester and maleimide groups. The spheres exhibit a functional group density of 2.39 x 10^6 NH_2 groups per particle. The pKa of the amine-fluospheres ranged from 10 to 11 and thus the particles were positively charged at physiological pH.

The colour of the dye incorporated in the fluospheres was selected based on the calcium indicator fluorescent dye used for sperm cells labelling, and also the specification of the instrument available to perform the fluorescence imaging experiments, namely the beam filters. Two different calcium dyes were tested, with the results presented in section 6.3.6.

Maleimide functionalised particles were formed from the well-known reaction of primary amines with NHS esters (Figure 6.94). Then, the simple and selective reaction of maleimides with thiols[3, 19](Figure 6.95) was applied to covalently attach the thiolated oligopeptide to the particles.

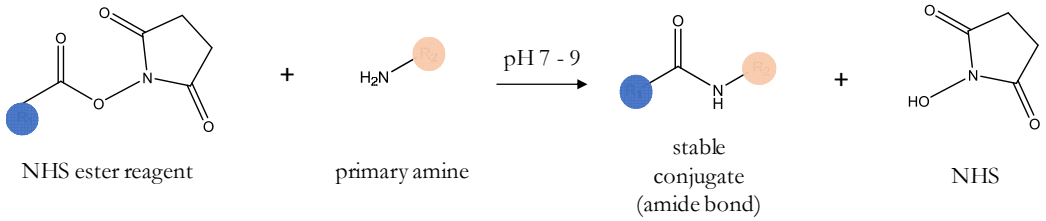

Figure 6.94 - Reaction scheme of a N-hydroxysuccinimide (NHS) ester reagent with a primary amine, forming a stable amide bond.

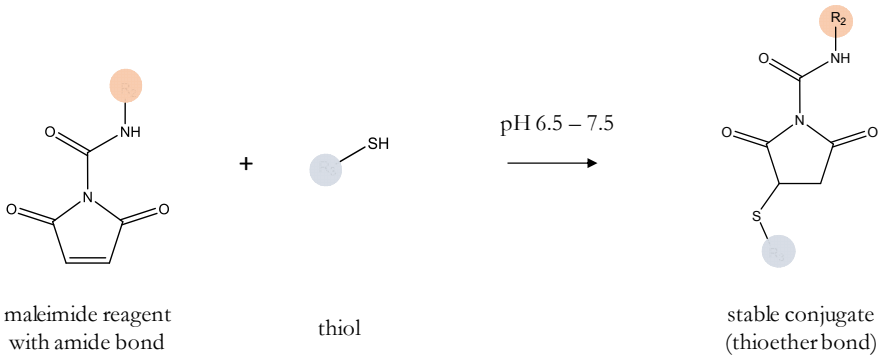

Figure 6.95 - Reaction scheme of a maleimide reagent with a thiol, forming a stable thioether bond.

A schematic representation of the functionalisation strategy is shown in Figure 6.96.

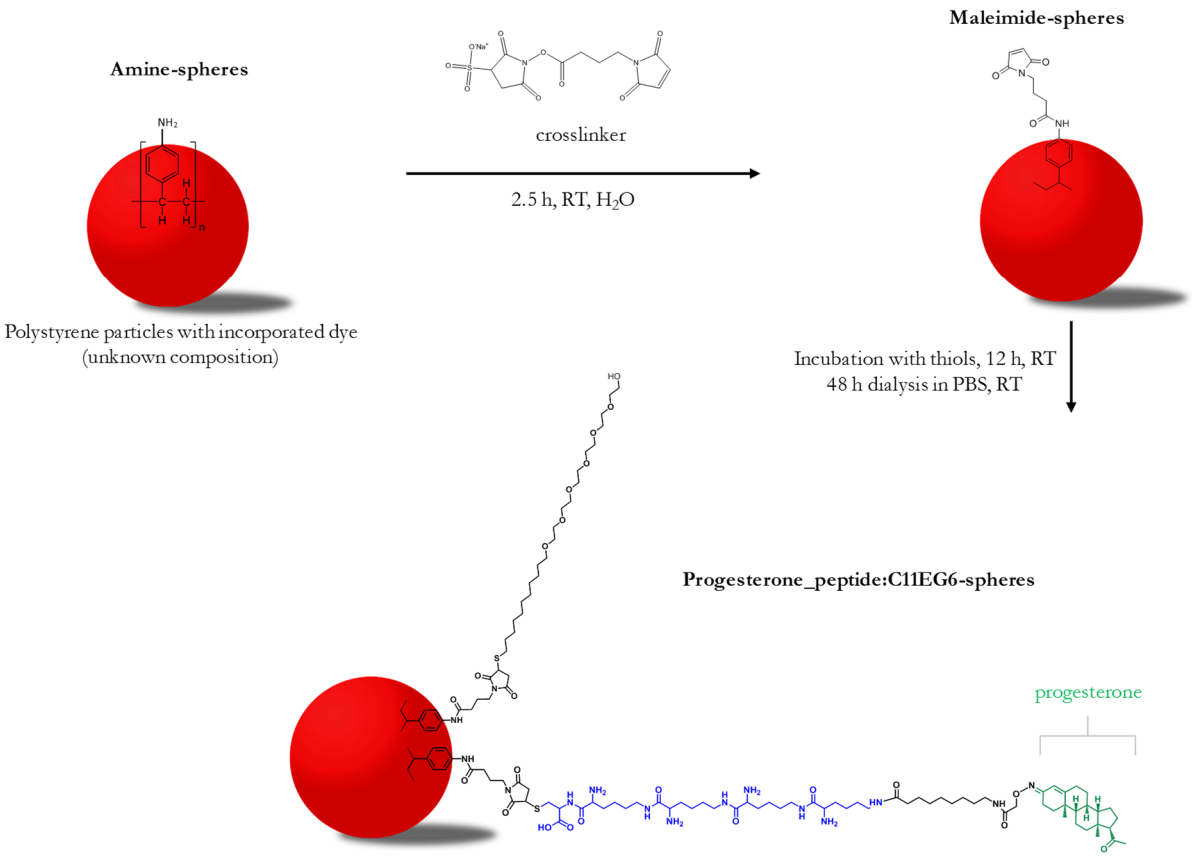

Figure 6.96 - Schematic representation of the functionalisation strategy for amine-terminated fluospheres.

Two distinct NHS esters were initially tested, N-α-maleimidoacet-oxysuccinimide ester (AMAS) and N-(γ-Maleimidobutyryloxy) sulfosuccinimide ester (sulfo-GBMS) (Figure 6.97). The latter was selected over the former as AMAS was found to be insoluble in the reaction solvent (water) and would require the use of an organic solvent such as DMSO or DMF. The use of DMSO would demand an extra step in the functionalisation to remove this solvent. The presence of DMSO would make the spheres characterisation process more complex, particularly with XPS analysis, and could potentially interfere with the studies with cells.

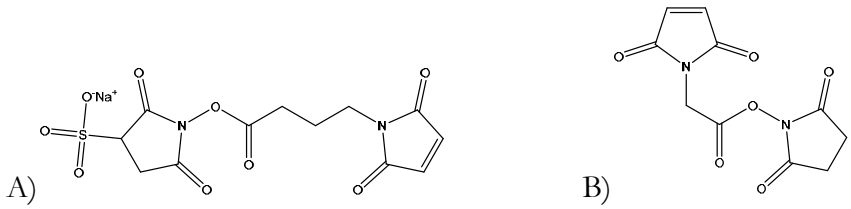

Figure 6.97 - Molecular structure of A) N-(γ-Maleimidobutyryloxy) sulfosuccinimide ester (sulfo-GBMS), a water-soluble amine-to-sulfhydryl crosslinker, containing NHS-ester and maleimide reactive groups at opposite ends of a 7.3 Å spacer arm; B) N-α-maleimidoacet-oxysuccinimide ester (AMAS), a water-insoluble amine-to-sulfhydryl crosslinker, containing NHS-ester and maleimide reactive groups at opposite ends of a 4.4 Å spacer arm.

Polyethylene glycol (PEG) has been widely used in drug and gene delivery systems as a coating for loaded nanoparticles in order to improve their stability and resistance to protein adsorption[20-22]. With this work, PEG was used as a spacer and not as a base for the formation of a homogeneous corona which is commonly performed with PEG of much higher molecular weights (≥ 2 kDa)[21]. The use of thiolated PEGs as spacers on gold nanoparticles (with 14 nm diameter) was explored by Sanz et al.[23] to promote loading of RNA onto the surface of the particles. In the study, the particles were first functionalised with a low density of two types of thiolated PEGs containing different terminal functional groups (carboxyl and azide). These functional groups were then used for further coupling reactions. The low density of PEG allowed further binding of thiolated oligonucleotides onto the non-saturated surface of the gold nanoparticles.

A few studies are reported in the literature on the functionalisation of amine-terminated polystyrene fluospheres. For example, a study by Chan et al.[24] described the functionalisation of amine terminated polystyrene fluospheres with thiolated antibodies, making use of a heterobifunctional PEG linker with maleimide functional groups. DLS and radiolabelling techniques were employed for the characterisation of the functionalised

particles, with observed increase of particles diameter after antibody attachment and an average conjugation efficiency of 10%. Non-specific binding was also investigated making use of non-thiolated antibodies, with an observed conjugation 30% lower than the one observed for the thiolated antibodies, demonstrating a high amount of non-specific binding.

6.3.2 Characterisation of pristine amine-terminated fluospheres

TEM was used to verify the size of the commercially supplied amine-terminated fluospheres. Size distribution of the particles was calculated based on the acquired TEM images shown in Figure 6.98. The average diameter of the counted particles was 178 nm ± 10 nm. This value is close to the size stated by the supplier: 200 nm ± 20 nm.

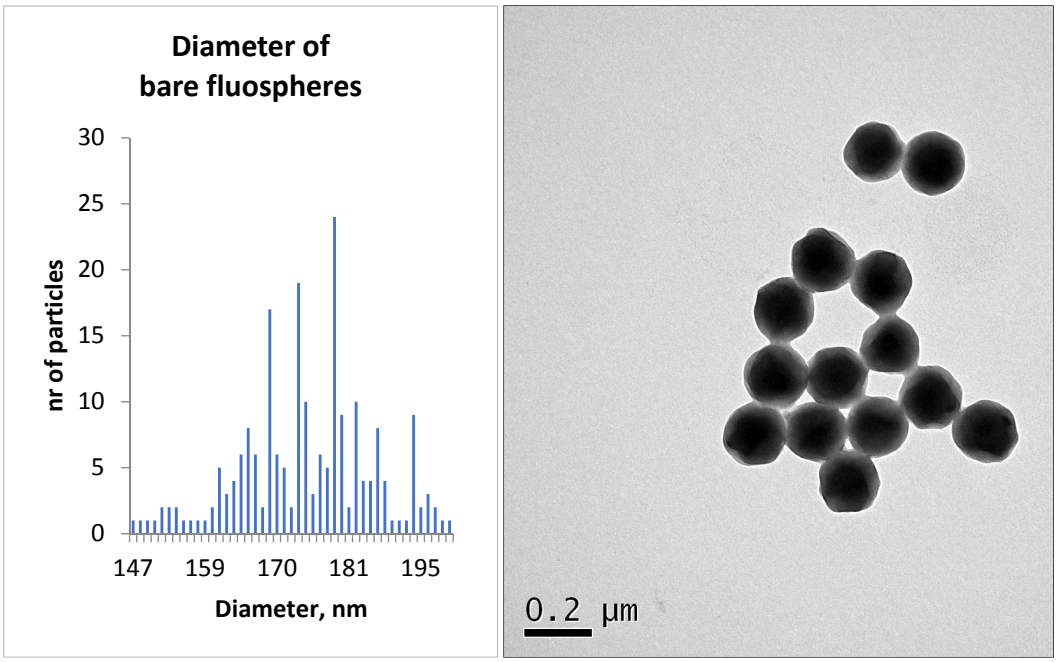

Figure 6.98 – Left: Histogram of data calculated from TEM images, based on a total of 209 particles. Right: TEM image of pristine amine-terminated fluospheres.

NMR, DLS and XPS data were also acquired for the amine-terminated spheres and are shown in the following sections.

Amine-terminated fluospheres were supplied in a solution containing sodium azide as an anti-microbial agent. The first step of the functionalisation process was to remove this compound from the solution in order to avoid competitive reactions with reagents used for functionalisation. Centrifugal filter units with a pore size of 100 nm were used for this purpose (Figure 6.99).

Figure 6.99 - Centrifugal filter units used for fluospheres filtration, where an incorporated cellulose membrane allows precise molecular weights cut-offs.

6.3.3 Characterisation of maleimide-spheres by NMR and DLS

The first reaction entailed the exposure of the amine functionalised particles to a 10-fold molar excess of the crosslinker for 2.5 h at pH 7.5, to form stable amide bonds with the maleimide groups. Unreacted reagent and by-products were removed by centrifugal filtration. The maleimide functionalised particles were then ready for incubation with thiols.

^{1}H NMR was used to investigate the functionalisation of the particles with the maleimide crosslinker. Figure 6.100 shows the ^{1}H NMR spectra of both starting materials and product (pristine fluospheres, AMAS crosslinking reagent and functionalised fluospheres) in $CDCl_3$. The proton of the alkene in the maleimide unit is visible at 6.8 ppm[25] in the spectrum of

the pure AMAS reagent (spectrum B) as well as that of the functionalised fluospheres (spectrum C), and is absent in the pristine fluospheres spectrum (spectrum A) as expected. The signal assigned to the CH_2 group of the maleimide, at 4.25 ppm, is also present in spectra B and C, although slightly shifted in spectrum C comparing to B, due to a different chemical environment. In addition, the CH_2 signal of the succinimide is observed in spectrum B, at 2.80 ppm, but not in spectrum C, as expected.

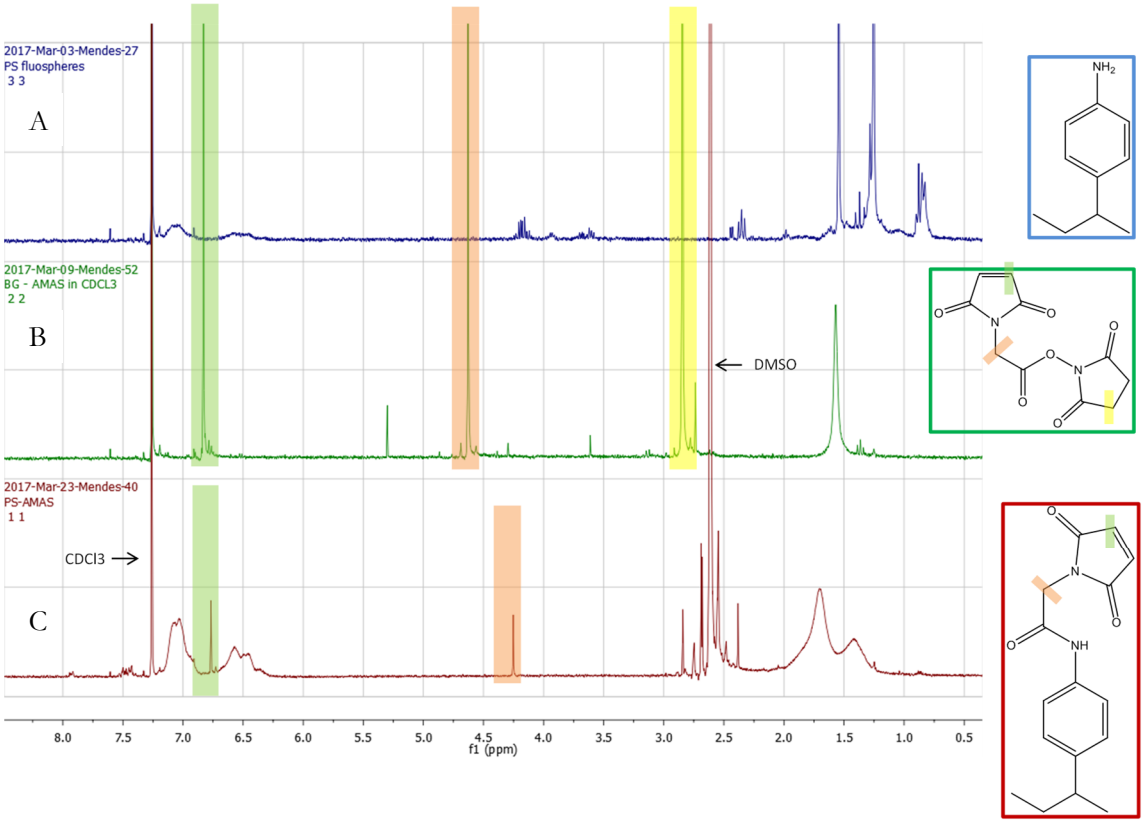

Figure 6.100 - ^1H NMR 300 MHz spectra in $CDCl_3$ of A) amine-terminated fluospheres, as purchased; B) AMAS crosslinking reagent solution; C) maleimide-terminated fluospheres, with the maleimide proton appearing at 6.8 ppm.

The following step was to incubate the maleimide-terminated fluospheres with thiols, to form stable thioether bonds. The molar ratio of progesterone peptide and C11EG6 in solution was 1:15, the molar concentration of C11EG6 being equivalent to the molar

concentration of spheres. These were incubated overnight at room temperature. For purification, a dialysis membrane with a molecular weight cut-off of 1 000 kDa, corresponding to a membrane pore size of 100 nm, was used. Dialysis was used instead of centrifugal filter units in order to prevent aggregation of the functionalised particles[26].

The functionalisation of the spheres was expected to induce changes in their physiochemical properties, such as their hydrodynamic diameter. The hydrodynamic diameter of the amine-spheres, the C11EG6-spheres and the progesterone_peptide:C11EG6-spheres was measured by DLS. Measurements were performed at 20 °C and pH 7.0, and the spheres were suspended in PBS 1x. Ten measurements of 30 s duration were recorded for each sample. Results are shown in Table 6.23. The increase in particle diameter after incubation with thiols is an indication of successful functionalisation of the particles surface. However, the increase is higher than expected, bearing in mind the chain length of C11EG6 (3.6 nm) and of the progesterone peptide (6 nm), while the value measured for the amine-spheres is close to the one measured by TEM. The measured hydrodynamic diameter (245 nm for the C11EG-spheres and 342 nm for the progesterone_peptide:C11EG6-spheres) is not large enough to be considered as a result of the agglomeration of two spheres, which would be at least 380 nm. This indicates the presence of non-organized multilayers as a result of weak interactions such as hydrogen bonding between hydroxyl, amine and thiol groups. The presence of these weak interactions could possibly be decreased or eliminated by improving the purification method. It is also observed that after functionalisation, the solution of spheres became more polydisperse, with a broader distribution of sizes detected by DLS, as indicated by the polydispersity index (PDI). The PDI observed for the progesterone_peptide:C11EG6-spheres was ten times higher than the one observed for the amine-spheres.

Table 6.23 – Average particle diameter and polydispersity index (PDI) measured by DLS for amine-spheres, C11EG6-spheres and progesterone_peptide:C11EG6-spheres.

	PDI	Particle diameter, nm
Amine-spheres	0.1	190
C11EG6-spheres	0.5	255
Progesterone_peptide:C11EG6-spheres	1.0	342

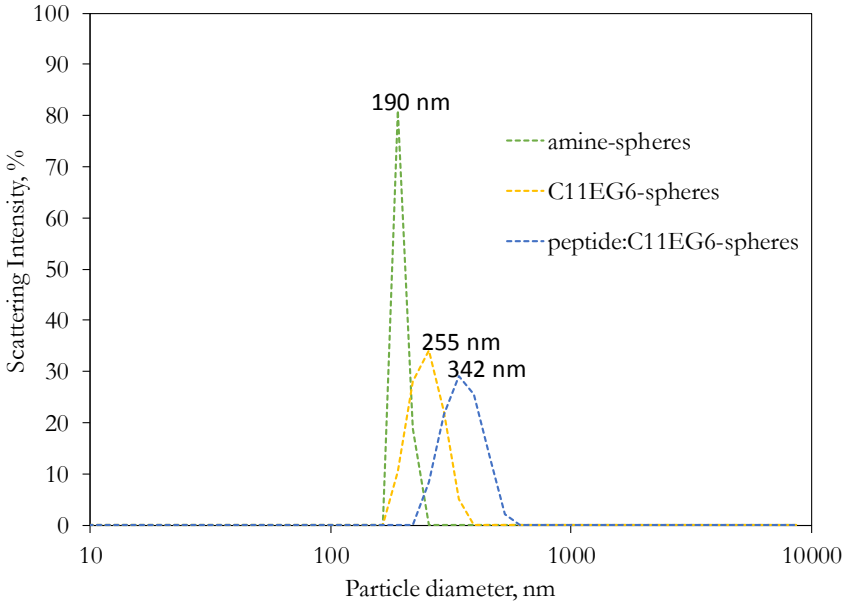

Figure 6.101 – Particle diameter distribution profile of amine-spheres, C11EG6-spheres and progesterone_peptide:C11EG6-spheres.

6.3.4 Characterisation of functionalised fluospheres by XPS

For XPS studies, four different samples were prepared, at different functionalisation stages:

A) amine-spheres, after sodium azide removal and resuspension in water.

B) maleimide-spheres suspended in water;

C) progesterone_peptide:C11EG6-spheres in PBS;

D) C11EG6-spheres in PBS.

Figure 6.102 shows the chemical structures and stoichiometry of the samples, as well as possible unreacted groups still present on the fluospheres after each functionalisation step.

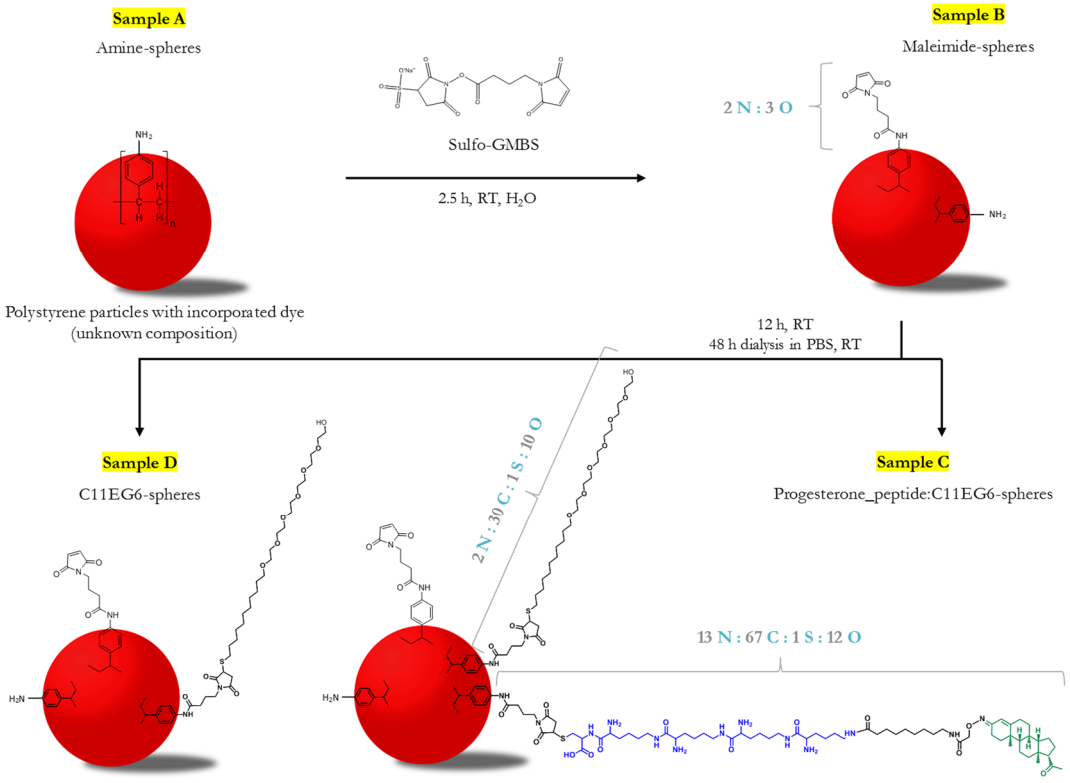

Figure 6.102 – Schematic representation of functionalised fluospheres, including chemical structures, stoichiometry, reaction conditions and possible unreacted groups.

The samples were prepared for XPS analysis by placing 4 x 50 µL drops (in the same location) of each aqueous suspension on the substrate (Au on Si wafer), and leaving the solutions to dry at room temperature.

Due to differential charging occurring during data acquisition (more detailed information about the occurrence of charging during XPS measurements can be found in sub-chapter 3.3), there is not enough data for standard deviation calculation. The spectra where charging occurred were not taken into consideration. The data shown represents an average of two measurements. An example of scans with visible charging is shown in Figure 6.103, where O 1s and C 1s regions show distorted and broader peaks in comparison to non-charged scans.

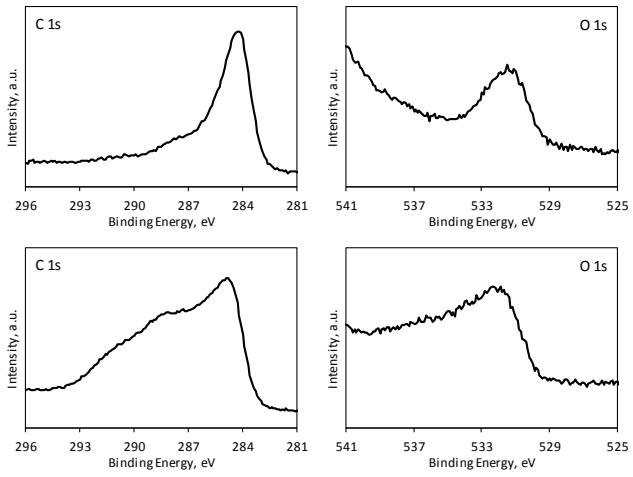

Figure 6.103 - High resolution XPS scans for C 1s (LEFT) and O 1s (RIGHT) regions of sample B (maleimide-spheres), showing the occurrence of charged (BOTTOM) compared to non-charged (TOP)scans.

Fitted high resolution XPS scans for the key elements (C, O, S and N) are shown in Figure 6.104 and calculated ratios, based on the integration of the elemental peak areas further corrected for the respective elemental RSF, are shown in Table 6.24. Nitrogen and sulfur were key elements for the calculation of relative ratios of the different molecules on the functionalised spheres.

The presence of carbon and nitrogen was expected for all samples as these elements are present in their chemical structures (Figure 6.102). Oxygen is only a component of samples B to D, its presence in sample A being a result of air contamination and water.

The presence of sulfur was only expected in samples C and D, which contain thiol based SAMs. This was observed, with no sulfur detected in samples A and B.

The three components fitted in the C 1s region are assigned to C-C and C-H bonds, at 284.8 eV, C-O and C-N bonds at 286.7 eV, and C=O bonds at 288.4 eV. For the O 1s region, two components can be fitted and are assigned to C-O and C=O bonds, at 531.8 eV and 533.5 eV, respectively. The oxygen peak is very broad. This might be a result of contributions from water (overlapping with the peak assigned to C=O bonds) and from oxidised sulfur.

For samples C and D, sodium is also detected in O 1s region. The Na KLL peak is normally observed at 536 eV. Sodium is one of the components in PBS - the buffer used in samples C and D. The nitrogen peak at 399.7 eV is assigned to NH_2 groups. The peaks for sulfur in the S 2p region are of very low intensity and thus no peak deconvolution was performed for these. Two different environments were detected for this element, the first S $2p_{3/2}$ peak positioned at 162.9 eV representing bound sulfur and an oxidised environment being assigned to the S $2p_{3/2}$ peak positioned at 168.7 eV. The sulfur at the lower binding energy is assigned to the thioether bond formed when the thiol reacts with the maleimide group. The presence of an oxidised form of sulfur is an indication of the presence of unbound thiol, which is likely to be a result of an inefficient purification step where unbound material is still present after the filtration step.

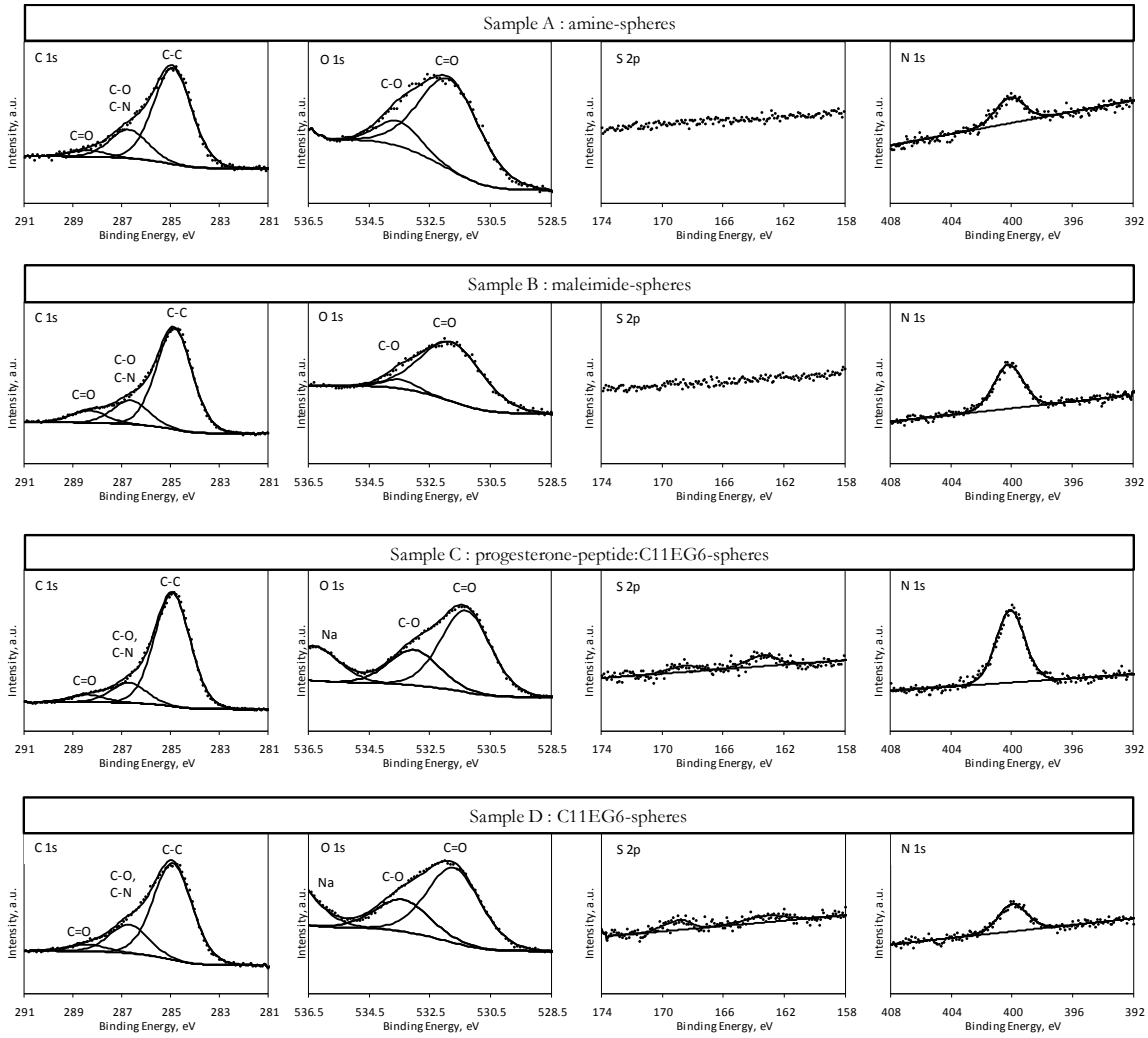

Figure 6.104 - High resolution XPS scans for the C 1s, O 1s, S 2p and N 1s regions of samples A - D, with Na KLL peaks observed in the O 1s regions of samples C and D.

Table 6.24 – Ratios of the corrected fitted areas of samples A - D for the key elements C, O, N, and S. Values are an average of two measurements.

	C/N		N/S		O/N	
	measured	theoretical	measured	theoretical	measured	theoretical
A	7.8	-	-	-	10.6	0
B	7.1	-	-	-	1.1	1.5
C	7.2	-	5.1	-	3.2	-
D	9.4	-	2.7	2.0	5.3	5.0

From the comparison of data from samples B and D, the efficiency of the functionalisation of the maleimide spheres with the spacer molecule (hexaethylene glycol thiol C11EG6) was estimated. From the comparison of samples C and D, the relative quantity of progesterone peptide present in sample C was calculated. The results are shown and discussed below.

Oxygen contamination on sample A is high, due to water and/or organic contamination. Assuming the amount of oxygen on samples A and B is high and constant, masking the expected increase of O (3 atoms of O for every 2 atoms of N) as a result of functionalisation with the maleimide group, then an increase in N/O from sample A to sample B would be expected and this was observed – the ratio of O to N decreases from 10.6 to 1.1.

Comparing samples B and D, the quantity of nitrogen should remain constant as the hexaethylene glycol thiol molecule does not contain any nitrogen. The quantity of O should increase, as the thiol introduces 7 additional atoms of O. An increase in O/N was observed, indicating that functionalisation was successful. The increase in O is higher than

expected (5.1 vs 3.3), indicating oxygen contamination or decreased signal from N due to this element being covered by the hexaethylene glycol chains.

The N/S ratio for sample D is slightly higher than expected (2.7 vs 2.0). This might be an indication of incomplete functionalisation with the thiols. It might also be the case that the signal from S is not as high as expected due to this element being covered by the hexaethylene glycol chains. An additional factor that must be considered is the lack of accuracy of the relative sensitivity factors used for normalization of the data. If the two last factors are disregarded, then one can estimate that 74% of the groups were functionalised with the thiol (Figure 6.105 - left), with the remaining 26% corresponding to amine and maleimide unreacted groups.

Comparing N/S for samples C and D, the estimated value for the relative percentage of progesterone peptide, in relation to C11EG6 is 16%. This value is close to the one obtained when considering N/O instead of N/S : 14.5%. The calculated relative percentages of the different components in sample C are as follows: 12 % progesterone peptide, 62 % C11EG6 spacer and 26% amine/maleimide unreacted groups (Figure 6.105 – right).

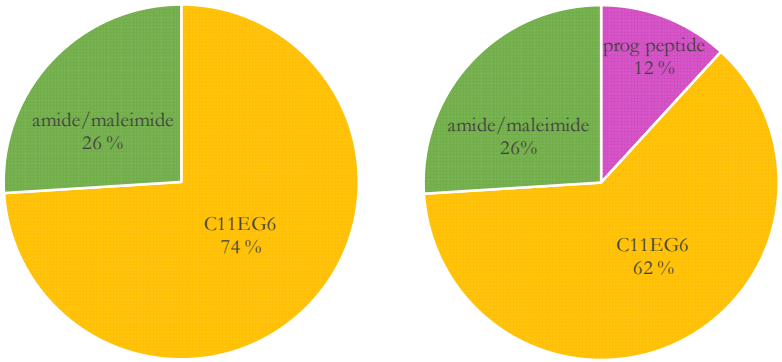

Figure 6.105 – Relative percentages of different components (amine and maleimide unreacted groups, C11EG6 spacer, and progesterone peptide) for C11EG6-spheres (LEFT) and progesterone_peptide:C11EG6-spheres (RIGHT), calculated from XPS data.

6.3.5 Characterisation of functionalised fluospheres by spectrofluorometry

In addition to XPS analysis, spectrofluorometry studies were conducted to confirm functionalisation of the fluospheres with the progesterone peptide, by observing the binding of a labelled progesterone antibody to the functionalised particles (Figure 6.106).

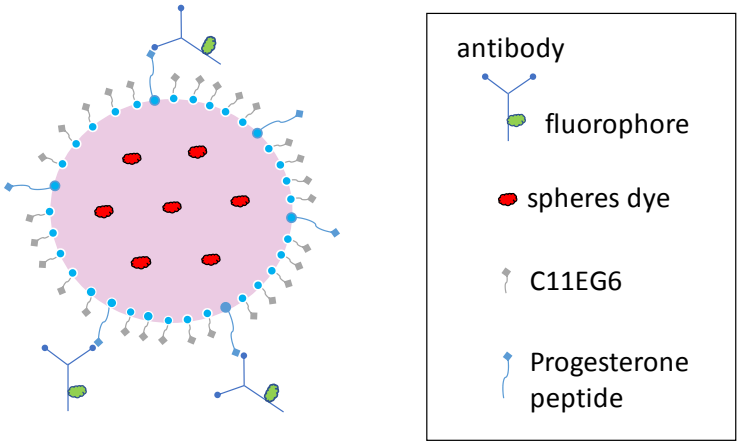

Figure 6.106 – Schematic representation of a labelled antibody binding to the progesterone-functionalised particles.

For this purpose, an IgG monoclonal progesterone antibody was labelled with Alexa Fluor 488 dye (Figure 6.107 - left), a green fluorophore with maximum absorption at 495 nm, low self-quenching properties and high fluorescence quantum yield. The dye contained tetrafluorophenyl (TFP) ester reactive groups, which react with primary amines of proteins to form stable dye-protein conjugates (Figure 6.108). NH_2 groups are abundant on the antibody surface (Figure 6.107 - right) and are therefore common targets for the attachment of fluorophores. However, the activity of the antibody might be affected by the

labelling process if the attachment occurs within the antibody binding site, so the density of labelling must be optimised.

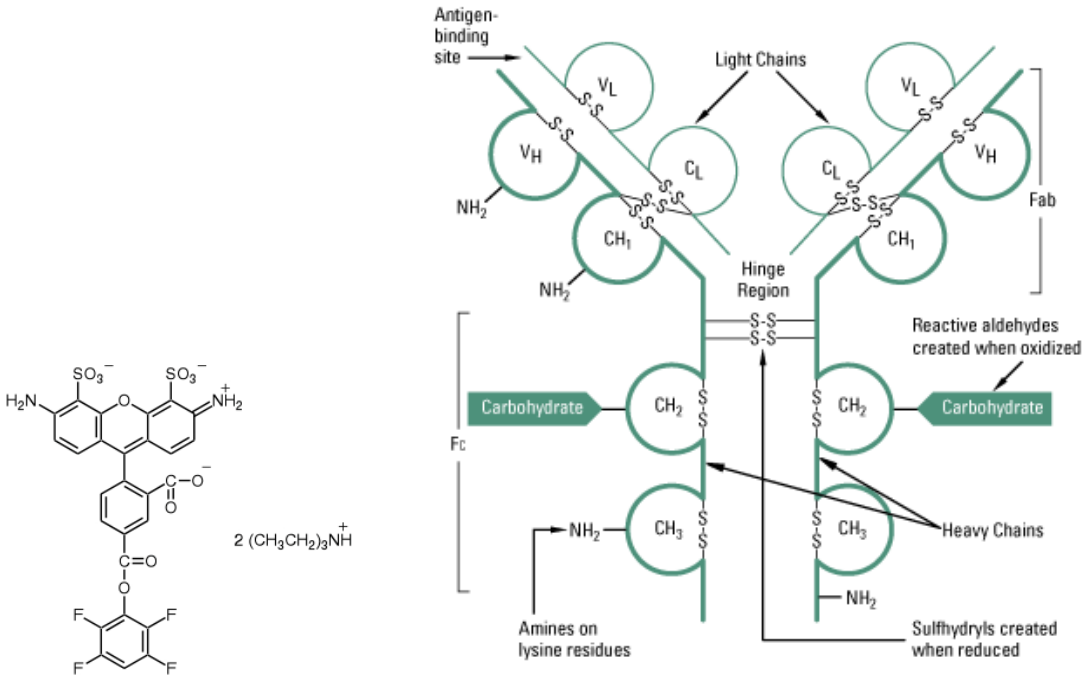

Figure 6.107 – LEFT: Molecular structure of the Alexa Fluor 488 dye. RIGHT: Schematic representation of antibody structure.[27]

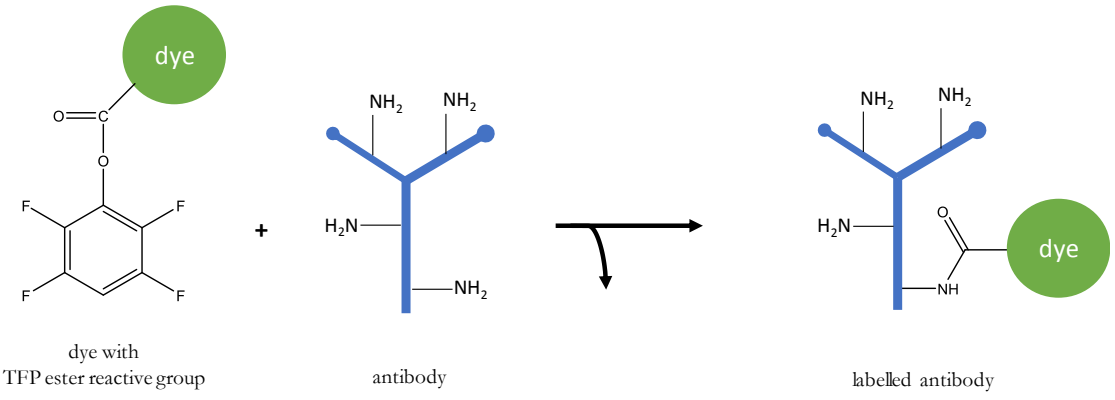

Figure 6.108 – Antibody labelling with dye containing TFP ester reactive group.

The antibody dye was chosen in accordance to the fluorescence spectra of the fluorospheres, to avoid overlapping of dye emissions. Figure 6.109 shows excitation and emission spectra for the red amine-fluospheres and for the green dye used for antibody labelling.

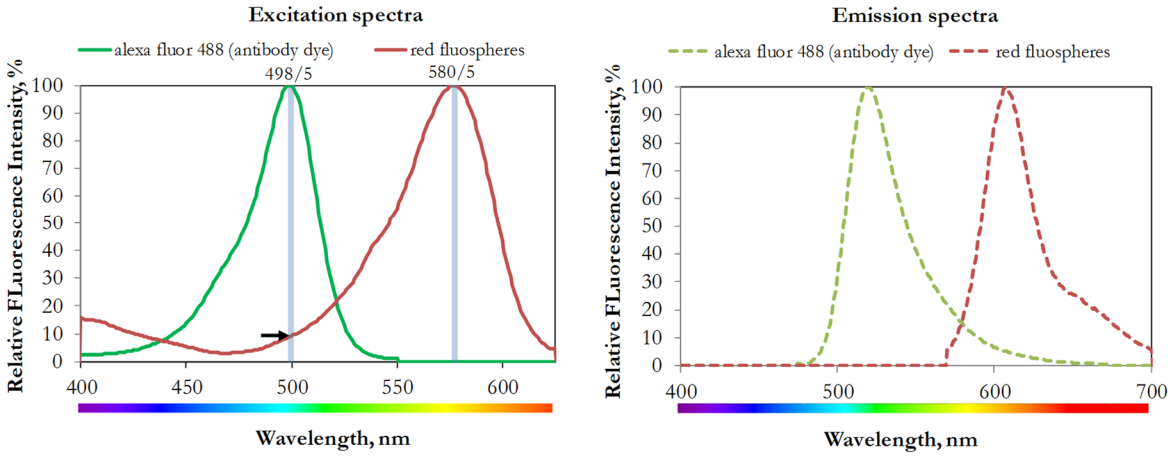

Figure 6.109 – LEFT: Overlay of excitation spectra for Alexa Fluor 488 dye (used for progesterone antibody labelling) and the red amine-fluospheres. Excitation wavelengths / slit bandwidths are also displayed on the plot. The overlapping region for the 498 excitation wavelength is highlighted with an arrow, corresponding to a max of approx. 9% of intensity for the red fluospheres. RIGHT: Overlay of emission spectra for Alexafluor488 dye (used for progesterone antibody labelling) and the red amine-fluospheres.

As shown in Figure 6.109, excitation with 580 nm wavelength, slit bandwidth of 5 nm, provides maximum excitation of the red fluospheres and does not overlap with the excitation range of the labelled antibody, meaning that no signal will be detected from the antibody when this excitation wavelength is used. The plot also indicates that an excitation of 498 nm, slit bandwidth of 5 nm, will provide relatively inefficient excitation of the labelled antibody, with an observed maximum of 9%. Maximum emission is expected for the labelled antibody at 521 nm, while the fluospheres will have a maximium emission

intensity at 608 nm. Measuring the emission for an excitation of 580 nm will provide the value for the fluospheres intensity that can then be subtracted (9% of it) from the emission at 498 nm, the rest corresponding to the antibody emission. Alternatively, measuring the emission of the fluospheres without antibody will provide the contribution coming from the fluospheres, without the interference of the antibody.

The molar extinction coefficient (EC) for Alexa Fluor 488 is 73 000 cm^{-1} M^{-1}. The extinction coefficient for the red fluorospheres however, is unknown and therefore it is not possible to compare them. For the range where there is overlap of the two species, a higher relative percentage of one of the fluorescent molecules will offset the intensity. However, this does not prevent the aim of this fluorescence study, which is to confirm the presence of the antibody on the functionalised fluospheres.

Alexa Fluor™ 488 Antibody Labelling Kit was used, and the protocol mainly consisted of incubating the antibody with the dye for 1 h at room temperature, followed by purification with a resin column. To test wether the antibody's potential to bind to the analyte was affected by the labelling process, SPR experiments were run, injecting each antibody (labelled and non-labelled) to a progesterone-C8-4KC:C11EG6 mixed SAM on gold (further details on this mixed SAM can be found in chapter 4). Results are shown in Figure 6.110. No significant difference was observed in the SPR response for the binding of labelled antibody compared to the non-labelled antibody, indicating that the labelling process did not affect the binding capacity of the antibody.

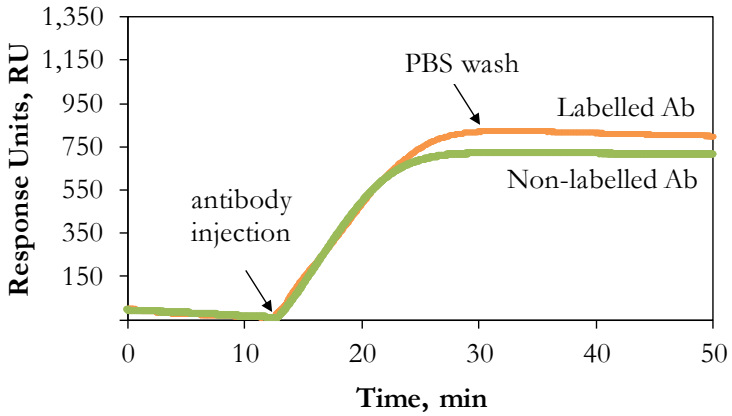

Figure 6.110 – SPR sensorgram for the binding of the anti-progesterone antibody to the progesterone-C8-4KC : C11EG6 mixed SAM.

Progesterone_peptide:C11EG6-fluospheres were incubated with the labelled antibody (final concentration in solution 100 nM) for 120 min or 20 min and then purified with centrifuge filters, to remove unbound antibody. Centrifuge filter units were used over dialysis membranes, as dialysis membranes for micro size volumes of antibody solutions were unavailable. After filtration, the fluospheres were resuspended in buffer (PBS) and fluorescence measurements were taken.

The same procedure was followed for the C11EG6-spheres, run as a control experiment, where less binding should occur. The binding of progesterone antibody to a C11EG6 SAM on gold was first investigated by SPR, shown in Figure 6.111. The observed non-specific binding was approximately 25% of the SPR response obtained for the progesterone-C8-4KC : C11EG6 mixed SAM.

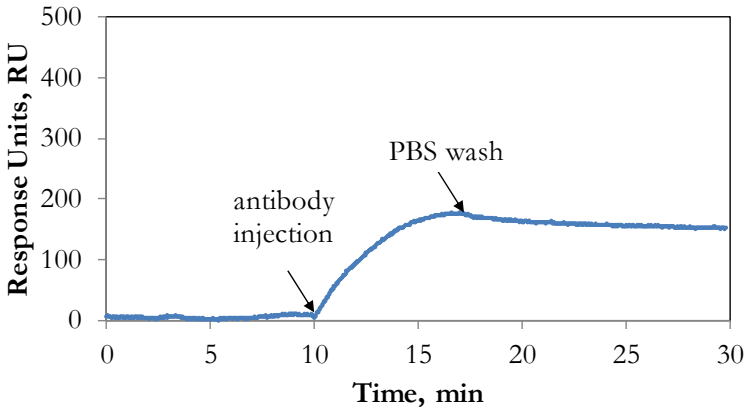

Figure 6.111 – SPR sensorgram for the binding of anti-progesterone antibody to the C11EG6 SAM on gold.

To reduce non-specific binding, the antibody incubation time was reduced from 120 min to 20 min. Comparison between these two incubation times is shown in Figure 6.112, which presents the fluorescence emission spectra for the C11EG6-spheres after incubation with the labelled antibody for different times. A reduction in maximum intensity of 37% was observed and therefore this was the incubation time selected for further studies with the peptide:C11EG6-spheres.

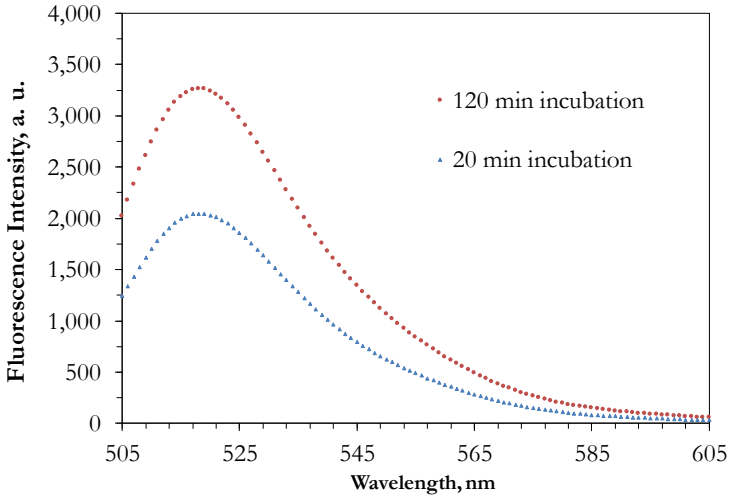

Figure 6.112 - Fluorescence emission spectra for excitation at 494 nm (5 nm bandwidth slit) for C11EG6-spheres after 120 min and after 20 min incubation with labelled antibody.

Emission spectra acquired for the progesterone_peptide:C11EG6-spheres and the C11EG6-spheres before and after incubation with labelled antibody are shown in Figure 6.113. Both progesterone_peptide:C11EG6-spheres and C11EGG6-spheres exhibit similar fluorescence intensity before incubation with the antibody, indicating a similar concentration of spheres. After incubation with the antibody, both functionalised spheres showed an increase in fluorescence intensity. The progesterone_peptide:C11EG6-spheres, however, displayed a significantly higher intensity (29% increase), compared to the C11EG6 spheres, indicating that a higher amount of labelled antibody was bound to these particles. These results, together with the XPS results, are a strong indication of the successful attachment of the progesterone peptide to the particles. However, non-specific binding is high. Non-specific antibody binding has been previously shown with a C11EG6 SAM on flat gold surfaces (Figure 6.111). In this case the surface is likely to be much more organized and compacted, with a higher surface coverage of the substrate (gold) compared to that of the functionalised particles. The antibody might also be interacting with unreacted amine and maleimide groups on the surface of the spheres. Another possibility is an inefficient washing method, meaning unbound antibody may still be present in solution. Non-specific binding could potentially be limited by either using a lower concentration of antibody or by improving the washing method. Curiously, a similar difference in terms of specific binding and non-specific binding was observed in the study by Chan et al.[24].

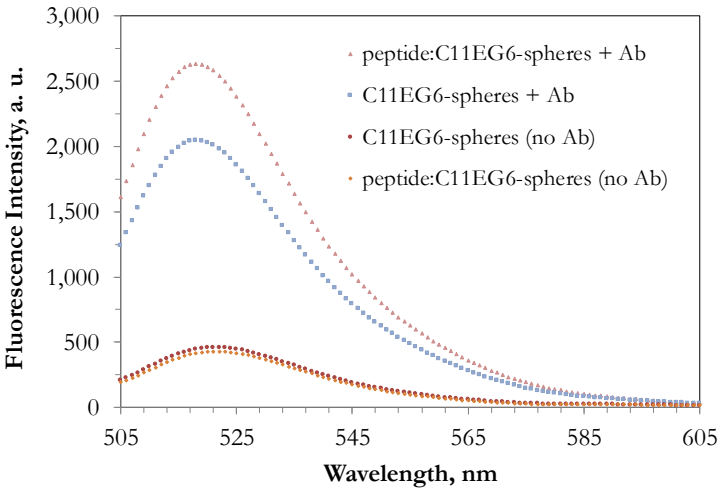

Figure 6.113 – Fluorescence emission spectra for excitation at 494 nm (5 nm bandwidth slit) of progesterone_peptide:C11EG6-spheres after 20 min incubation with the labelled antibody. Control experiments, also shown in this plot, consisted of measuring emission spectra for C11EG6-spheres (no progesterone peptide) incubated with the antibody in the same conditions, and measuring emission spectra for progesterone_peptide:C11EG6-spheres and for C11EG6-spheres without incubation with the antibody.

6.3.6 Optimisation of sperm cell labelling process for fluorescence imaging

For fluorescence imaging studies, sperm cells will need to be labelled with a calcium indicator fluorescent dye which exhibits an increase in fluorescence upon Ca^{2+}binding. The indicator must provide sensitive detection of Ca^{2+} transients with fluorescence intensities largely dependent on the concentration of Ca^{2+}.

When calcium channels in the sperm cells open, as a response to the exposure of progesterone, an increase in fluorescence intensity will be noticed, caused by the increase of calcium inside the cell which then binds to the calcium dye. Two different dyes were tested: Oregon green and Fluo-4 (Figure 6.114). Due to the presence of acetoxymethyl (AM) esters, these dyes are loaded into the sperm cells by simple addition of the dyes to the

extracellular medium, and are diffused across the the cell membrane due to their hydrophobicity. DMSO and pluronic-F127 are commonly used solvents for dissolving AM-linked Ca^{2+} dyes before addition to aqueous solutions.[28]

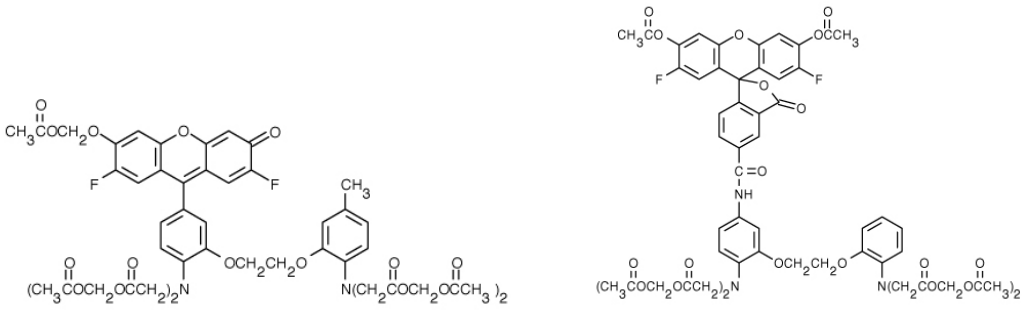

Figure 6.114 – Chemical structures of calcium indicator fluorescent dyes Fluo-4 (LEFT) and Oregon Green (RIGHT).

The fluorescence intensity was measured in order to select the most suitable dye and results are shown in Table 6.25. Fluo-4 showed the highest intensity/background for the instrument used and therefore was selected for future work with sperm cells. Figure 6.115 shows microscopic images acquired of sperm cells labelled with Fluo-4.

Table 6.25 - Fluorescence intensity of labelled cells after background normalization. The values are the average of three samples, with the errors reported as standard deviation.

Dye	Fluo-4	Oregon Green
Average fluorescence intensity of cells (normalized background), a. u.	16 297 ± 2 788	8 125 ± 1 168

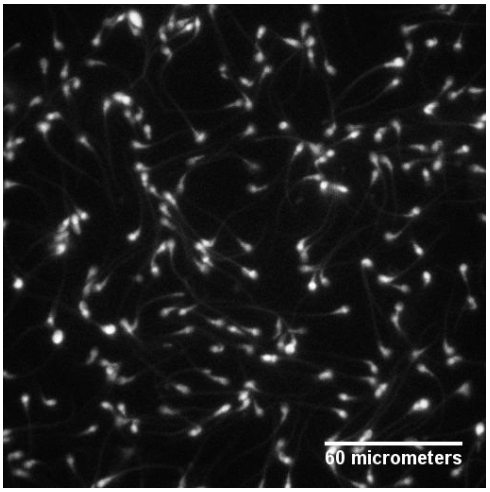

Figure 6.115 - Fluorescence microscopy image of sperm cells labelled with fluo-4, immobilised on a glass slide coated with PDL.

6.4 Conclusions and Future Work

A few challenges were found when developing a method for bi-functionalisation of amine-terminated fluospheres with a low density of progesterone. Further investigations are required before proceeding with studies on sperm cells response to the progesterone oligopeptide on the spheres.

XPS studies provided valuable information about the average chemical composition of the surface of particles and indicated that the particles were successfully functionalised, first with maleimide groups and then with two thiolated components - hexaethylene glycol and progesterone oligopeptide.

However, these studies also indicated that unreacted amine and maleimide groups are still present on the surface after the attachment of thiols. These groups might interact with the

cells and therefore an investigation of a way to block these unreacted groups, possibly by using a short chain polyethylene glycol thiol, must be explored.

XPS results also revealed the presence of oxidised sulfur, which is an indication of an inefficient purification process. DLS results also suggested inefficient purification. This step therefore also requires improvement.

In addition to the information obtained by XPS and in order to validate those results, quantitative information about the extent of surface functionalisation and surface coverage could be ascertained using a different technique. The use of an Ellman's assay has been reported for a similar purpose[23], where after incubation with the thiols, the solution was centrifuged and free thiolated chains in the supernatant were quantified spectrophotometrically. However this method might overestimate the surface coverage if molecules are non-specifically bound to the surface. Size exclusion chromatography, gas or liquid chromatography, gels and colorimetric approaches could also be used for quantitative information of surface coverage[20].

When investigating the interaction of a labelled progesterone antibody with the functionalised particles by spectrofluorometry, the highest increase in fluorescence was achieved for the particles functionalised with the progesterone peptide, once again indicating the presence of progesterone on the surface of the spheres. However, a high level of non-specific binding was shown. Improving the washing method after incubation with the antibody and using a decreased concentration of antibody is likely to decrease the observed non-specific binding interactions. Spectrophotometry could also be used to quantify the amount of unbound antibody and therefore indirectly provide quantitative information about antibody bound to the spheres surface.

Zeta potential measurements could provide information on the colloidal stability of the spheres and visible changes should be detected when comparing different stages of functionalization.

The amount of progesterone loading can potentially be varied by changing the concentrations of peptide incubated with the spheres.

Future work should also include the confirmation of the absence of unreacted reagents and secondary products after each functionalisation step. This can be performed *via* analytical techniques such as liquid or gas chromatography. The final purification method should be improved until the unwanted compounds are no longer detectable in solution, in order to ensure that the response from the sperm cells is only due to the interaction with the functionalised fluospheres.

6.5 List of References

1. Oh, J.; Park, D.; Joo, J.; Lee, J., Recent advances in chemical functionalization of nanoparticles with biomolecules for analytical applications. *Analytical and Bioanalytical Chemistry* 2015, *407* (29), 8627-45.
2. Rick, J.; Tsai, M.; Hwang, B., Biosensors Incorporating Bimetallic Nanoparticles. *Nanomaterials* 2015, *6* (1).
3. Murcia, M.; Naumann, C., Biofunctionalization of Fluorescent Nanoparticles. In *Nanotechnologies for the Life Sciences*, Wiley-VCH 2007.
4. Thiruppathi, R.; Mishra, S.; Ganapathy, M.; Padmanabhan, P.; Gulyas, B., Nanoparticle Functionalization and Its Potentials for Molecular Imaging. *Advanced Science* 2017, *4* (1600279).
5. Kim, J.; Lee, N.; Hyeon, T., Recent development of nanoparticles for molecular imaging. *Philosophical transactions of the royal society A* 2017, *375* (2107).
6. Kumar, B.; Jalodia, K.; Kumar, P.; Gautam, H., Recent advances in nanoparticle-

mediated drug delivery. *Journal of Drug Delivery Science and Technology* 2017, *41*, 260-68.

7. Bahrami, B.; Hojjat-Farsangi, M.; Mohammadi, H.; Anvari, E.; Ghalamfarsa, G.; Yousefi, M.; Jadidi-Niaragh, F., Nanoparticles and targeted drug delivery in cancer therapy. *Immunology Letters* 2017, *190*, 64-83.

8. Loos, C.; Syrovets, T.; Musyanovych, A.; Mailander, V.; Landfester, K.; Nienhaus, G.; Simmet, T., Functionalized polystyrene nanoparticles as a platform for studying bio-nano interactions. *Beilstein J Nanotechnol* 2014, *5*, 2403-12.

9. Wiwanitkit, V.; Sereemaspun, A.; Rojanathanes, R., Effect of gold nanoparticles on spermatozoa: the first world report. *Fertility and Sterility* 2009, *91* (1), 7-8.

10. Moretti, E.; Terzuoli, G.; Renieri, T.; Iacoponi, F.; Castellini, C.; Giordano, C.; Collodel, G., In vitro effect of gold and silver nanoparticles on human spermatozoa. *Andrologia* 2013, *45* (6), 392-6.

11. Taylor, U.; Barchanski, A.; Petersen, S.; Kues, W. A.; Baulain, U.; Gamrad, L.; Sajti, L.; Barcikowski, S.; Rath, D., Gold nanoparticles interfere with sperm functionality by membrane adsorption without penetration. *Nanotoxicology* 2014, *8* (1), 118-27.

12. Braydich-Stolle, L.; Lucas, B.; Schrand, A.; Murdock, R.; Lee, T.; Schlager, J.; Hussain, S.; Hofmann, M., Silver nanoparticles disrupt GDNF/Fyn kinase signaling in spermatogonial stem cells. *Toxicological Sciences* 2010, *116* (2), 577-89.

13. Yoisungnern, T.; Choi, Y.; Han, J.; Kang, M.; Das, J.; Gurunathan, S.; Kwon, D.; Cho, S.; Park, C.; Chang, W.; Chang, B.; Parnpai, R.; Kim, J., Internalization of silver nanoparticles into mouse spermatozoa results in poor fertilization and compromised embryo development. *Scientific Reports* 2015, *5*, 11170.

14. Barkalina, N.; Jones, C.; Kashir, J.; Coote, S.; Huang, X.; Morrison, R.; Townley, H.; Coward, K., Effects of mesoporous silica nanoparticles upon the function of mammalian sperm in vitro. *Nanomedicine* 2014, *10* (4), 859-70.

15. Abbasalipourkabir, R.; Moradi, H.; Zarei, S.; Asadi, S.; Salehzadeh, A.; Ghafourikhosroshahi, A.; Mortazavi, M.; Ziamajidi, N., Toxicity of zinc oxide nanoparticles on adult male Wistar rats. *Food and Chemical Toxicology* 2015, *84*, 154-60.

16. Nasri, S.; Rezai-Zarchi, S.; Kerishchi, P.; Sadeghi, S., The Effect of Iron Oxide Nanoparticles on Sperm Numbers and Mobility in Male Mice. *Zahedan Journal of Research in Medical Sciences* 2015, *17* (10).

17. Makhluf, S.; Arnon, R.; Patra, C.; Mukhopadhyay, D.; Gedanken, A.; Mukherjee, P.; Breitbart, H., Labeling of Sperm Cells via the Spontaneous Penetration of Eu3+ Ions as

Nanoparticles Complexed with PVA or PVP. *Journal of Physical Chemistry C* 2008, *112* (33).

18. Makhluf, S.; Qasem, R.; Sara Rubinstein; Gedanken, A.; Breitbart, H., Loading magnetic nanoparticles into sperm cells does not affect their functionality. *Langmuir* 2006, *22*, 9480-82.

19. Houseman, B.; Gawalt, E.; Mrksich, M., Maleimide-Functionalized Self-Assembled Monolayers for the Preparation of Peptide and Carbohydrate Biochips. *Langmuir* 2003, *19*, 1522-31.

20. Jokerst, J.; Lobovkina, T.; Zare, R.; Gambhir, S., Nanoparticle PEGylation for imaging and therapy. *Nanomedicine* 2011, *6* (4), 715-28.

21. Suk, J.; Xu, Q.; Kim, N.; Hanes, J.; Ensign, L., PEGylation as a strategy for improving nanoparticle-based drug and gene delivery. *Advanced Drug Delivery Reviews* 2016, *99*, 28-51.

22. Sun, C.; Du, K.; Fang, C.; Bhattarai, N.; Lee, D.; Ellenbogen, R.; Veiseh, O.; Ratner, B.; Zhang, M.; Kievit, F.; Stephen, Z., PEG-mediated synthesis of highly dispersive multifunctional superparamagneitc nanoparticles: their physicochemical properties and function in vivo. *ACS nano* 2010, *4* (4).

23. Sanz , V.; Conde, J.; Hernandez, Y.; Baptista, P.; Ibarra, M.; Fuente, J., Effect of PEG biofunctional spacers and TAT peptide on dsRNA loading on gold nanoparticles. *Journal of Nanoparticle Research* 2012, *14* (917).

24. Chan, L.; Wang, Y.; Lin, L.; Upton, M.; Hwang, J.; Pun, S., Synthesis and characterization of anti-EGFR fluorescent nanoparticles for optical molecular imaging. *Bioconjugate Chemistry* 2013, *24* (2), 167-75.

25. Ramesh, S.; Sivasamy, A.; Kim, J., Synthesis and characterization of maleimide-functionalized polystyrene-SiO2/TiO2 hybrid nanocomposites by sol-gel process. *Nanoscale Research Letters* 2012, *7* (350), 1-14.

26. Vauthier, C.; Cabane, B.; Labarre, D., How to concentrate nanoparticles and avoid aggregation? *European Journal of Pharmaceutics and Biopharmaceutics* 2008, *69* (2), 466-75.

27. thermofisher https://www.thermofisher.com/uk/en/home/life-science/antibodies/antibodies-learning-center/antibodies-resource-library/antibody-methods/antibody-labeling-immobilization-sites.html.

28. Paredes, R.; Etzler, J.; Watts, L.; Zheng, W.; Lechleiter, J., Chemical calcium indicators. *Methods* 2008, *46* (3), 143-51.

7 Experimental Procedures

7.1 Chemicals

7.1.1 Purchased and used as received

The following chemicals were purchased from Sigma Aldrich and used as received: Sulfuric acid 95-98%, hydrogen peroxide solution 30 wt. % in water , 11-(mercaptoundecyl) hexa(ethylene glycol) (C11EG6), immersion oil ref. 56822 with refractive index 1.515 (used for SPR), (3-glycidyloxypropyl)trimethoxysilane (3GPS) ≥98%, pluronic F-127, sodium dodecyl sulfate ≥98.5%, glycine ≥99%.

Progesterone-C7-4KC peptide was purchased from Peptide Protein Research Ltd (UK). The product was purified in acetonitrile and water containing 0.1% trifluoroacetic acid prior to liophilisation therefore being present as its trifluoroacetic salt. 5KC peptide was also purchased from Peptide Protein Research Ltd (UK).

Progesterone-3 IgG1 monoclonal antibody (ref. ABIN283834 - raised in mouse using progesterone-BSA linked at position 3 as the immunogen; affinity constant: $75x10^{10}$ L/M; supplied in PBS pH 7.2 with 0.05 % NaN_3) was purchased from Antibodies-online GmbH (Germany).

Calcium indicators Oregon Green™ 488 BAPTA-1 AM and Fluo-4 AM were purchased from Thermo Fischer Scientific Ltd.

N-γ-maleimidobutyryl-oxysulfosuccinimide ester (sulfo-GMBS) and N-α-maleimidoacet-oxysuccinimide ester (AMAS) were purchased from Thermo Fischer Scientific Ltd.

Modified Earle's Balanced Salt Solution (EBSS) ($CaCl_2 \cdot 2H_2O$ 1.80 mM, KCl 5.37 mM, $MgSO_4 \cdot 7H_2O$ 0.81 mM, $NaHCO_3$ 26.19 mM, $NaH_2PO_4 \cdot 2H_2O$ 1.01 mM, NaCl 116.36 mM,

D-glucose 5.55 mM, sodium pyruvate $C_3H_3O_3Na$ 2.73 mM, sodium lactate $C_3H_5O_3Na$ 41.75 mM) was purchased from Biological Industries Ltd (Israel).

Phosphate Buffered Saline (PBS) 10x pH 7.4 (KH_2PO_4 1.06 mM, NaCl 155.2 mM, $Na_2HPO_4 \cdot 7H_2O$ 3.0 mM) was purchased from Thermo Fischer Scientific Ltd and freshly diluted 10x with water.

Poly-d-lysine hydrobromide >98 % molecular weight 500 000 – 550 000 daltons was purchased from BD Biosciences.

AZ ECI 3027 photoresist and AZ726 MIF developer were bought from MicroChem (Germany).

HPLC grade solvents (ethanol, acetone, toluene and dimethylsulfoxide (DMSO)) were purchased from the local solvents store.

Whenever the use of water is mentioned in the protocols, this refers to Ultra-High Quality water.

7.1.2 Synthesis of progesterone-C11-SH

In collaboration with Dr. Stefano Tommasone, the progesterone-C11-SH compound (Figure 7.116) was synthesised by EDC/HOBt coupling of progesterone 3-(O-carboxymethyl)oxime and 11-amino-1-undecanethiol hydrochloride and isolated after column chromatography purification.

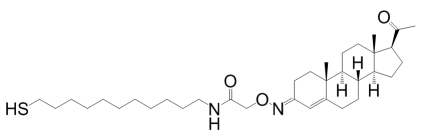

Figure 7.116 – Chemical structure of progesterone-C11-SH.

Progesterone 3-(O-carboxymethyl)oxime (15.0 mg, 0.039 mmol), N-(3-dimethylaminopropyl)-N'-ethylcarbodiimide hydrochloride (8.1 mg, 0.042 mmol) and 1-hydroxybenzotriazole hydrate (5.7 mg, 0.085 mmol) were dissolved in anhydrous dichloromethane (1.5 mL) and stirred at room temperature for 30 min. Then, a solution of 11-amino-1-undecanethiol hydrochloride (10.2 mg, 0.042 mmol) and N,N-diisopropylethylamine (15.0 μL, 0.085 mmol) in anhydrous dichloromethane (0.7 mL) was added and the reaction mixture was stirred overnight. The solution was then diluted with additional dichloromethane and washed with H_2O. The organic layer was separated, dried over $MgSO_4$ and filtered with the solvent removed under reduced pressure. The product was purified by column chromatography on silica gel (EtOAc:Hexane, 34:66) (10.1 mg; 45% yield): $[\alpha]_D^{20}$ = 85.2 (c = 1.0, in $CHCl_3$); ^{1}H NMR (400 MHz, $CDCl_3$, δ): 6.20 (t, J = 5 Hz, 1H, NH), 5.76 (d, 1 Hz, 1H, CH=C), 4.93 (s, 2H, $COCH_2O$), 3.29 (dt, J_1 = 7 Hz, J_2 = 6 Hz, 2H, CH_2NH), 3.00 (ddd, J_1 = 17 Hz, J_2 = 4 Hz, J_3 = 3 Hz, 1H, CH_2C=N'), 2.52 (t, J = 7 Hz, 2H, CH_2SH), 2.50 (overlapped, 1H), 2.40-2.10 (overlapped, 4H), 2.12 (s, 3H, CH_3CO), 2.05 (m, 1H), 1.92 (m, 1H), 1.83-1.25 (overlapped, 26H), 1.19-1.09 (m, 2H), 1.07 (s, 3H, CH_3-C19), 0.99 (m, 1H), 0.88 (m, 1H), 0.65 (s, 3H, CH_3-C18); ^{13}C NMR (100 MHz, $CDCl_3$, δ): 209.5 (C=O), 170.0 (C=O amide), 158.3, 157.1, 116.8 (*C*H=C), 110.6, 73.0 (CO*C*H_2O, 72.9, 63.8, 56.3, 54.0, 53.7, 44.1, 39.1, 38.9 (CH_2NH), 38.1, 36.3, 35.9, 34.8, 34.2, 33.2, 32.6, 32.2, 31.6 (CH_3CO), 29.6, 29.4, 29.2, 28.5, 27.0, 24.8 (CH_2SH), 23.0, 21.5, 21.3, 19.7 (CH_2C=N), 18.2, 17.9 (C19), 13.5 (C18); ESI+MS m/z (%): 573 (100) [M^+ - H], 595 (85) [M^+ - Na]; HRMS (ESI) m/z: [M + H]$^+$ calcd for $C_{34}H_{57}N_2O_3S$, 573.4090; found, 573.4092.

^{1}H and ^{13}C NMR spectra were recorded on a Bruker AVIII400 NMR spectrometer at 400 MHz and 101 MHz respectively, at room temperature. Chemical shifts are reported in ppm relative to TMS (δ 0.00) for the ^{1}H NMR and to chloroform (δ 77.0) for the ^{13}C NMR

spectroscopy. Mass spectra were recorded with Waters Xevo G2-XS Tof Time of Flight Mass Spectrometer.

7.2 Materials

7.2.1 Gold, glass and silicon substrates

SPR sensor chips, sized 1 cm x 1 x cm, consisted of a polycrystalline gold surface (50 nm) on glass substrate and were bought from Reichert Technologies - Ametek Inc (USA).

For ellipsometry, contact angle and XPS studies, gold (100 nm thickness and rms-roughness < 2,5 nm) on silicon <100> wafers precoated with titanium, bought from George Albert PVD (Germany), were cut into 1 cm x 1cm pieces using a diamond scriber. Silicon substrates <100> single side polish, 381 μm thick, were purchased from IDB Technologies Ltd (UK).

Borosilicate glass cover slips, used for cell attachment studies, 22 mm x 50 mm x 1.5 mm, were purchased from VWR international.

7.2.2 Microfabrication materials

Glass microscope slides Gerhard Menzel plain cut edges, 26 mm x 76 mm x 1-1.2 mm, from ThermoScientific, were used as substrate.

A positive glass photomask supplied by JD photo was used for the photolithography process with the features consisting of 7 μm diameter circles and 150 μm pitch.

For sputtering metal deposition, gold and chromium targets, 99.95 % pure, from Kurt J. Lesker were used.

7.2.3 Materials used for fluospheres experiments

Amine terminated fluospheres (ref. F8763), 0.2 μm, red (580/605), specific surface area 2.8 x 10^5 cm^2/g, 2.39 x 10^6 amine groups/particle, pKa 10-11, suspended in distilled water with 2 mM azide, concentration 4.5 x 10^{12} particles/mL, were purchased from Thermo Fischer Scientific Ltd.

Antibody labelling kit alexa fluor 488, green color, was purchased from Thermo Fischer Scientific Ltd.

Centrifugal Filter units Millipore Ultrafree-MC, pore size 0.1 μm, sample volume 500 uL, were purchased from Sigma Aldrich.

Dialysis devices Spectra/Por flot-a-lyzer G2, molecular weight cut-off 1000 kD, volume 10 mL, were purchased from Spectrum (USA).

A Hellma fluorescent quartz micro-cuvette with 3 windows, chamber volume of 45 μL and pathlength of 3 mm x 3 mm, was purchased from Sigma Aldrich.

7.3 Protocols

7.3.1 Flat surfaces functionalisation

7.3.1.1 Substrate cleaning

Before functionalisation, the gold/glass/silicon substrates were submerged in a strong oxidizing piranha solution (70% H_2SO_4, 30% H_2O_2) to remove organic residues. The reaction was performed under a fume hood, for 8 min, in a cold bath, followed by rinsing with copious amount of water and drying under argon. Alternatively, the substrates were cleaned by a UVO cleaner Jelight 342-220, for 10 min, positioning the samples 5 mm

below the radiation source ((low pressure Mercure vapor grid lamp with an average intensity of 28 mW/cm^2 at 254 nm), followed by sonication in ethanol for 10 min.

7.3.1.2 3GPS-PDL functionalisation of glass or silicon

After UVO clean, the substrates were soaked for 20 min in a freshly prepared, and sonicated for 5 min, solution of 1% (v/v) 3-GPS in toluene. The substrates were then rinsed with flowing toluene for 10 sec , submerged in fresh toluene and sonicated for 2 min and finally rinsed again with toluene flow for 10 sec followed by drying under argon. The following step consisted of placing the substrates in a vacuum oven at 120 °C for 30 min and then waiting for them to reach room temperature before applying a drop (300 µL) of freshly prepared PDL (0.1 mg/mL in PBS 0.5x). Finally, the substrates were rinsed with water flow for 10 sec, submerged in fresh water and sonicated for 2 min, and finally rinsed again with water flow for 10 sec followed by drying under argon.

7.3.1.3 3GPS-PDL functionalisation on glass or on Si followed by incubation with C11EG6 thiol

The glass or silicon slides functionalised with 3GPS-PDL were incubated overnight, at room temperature, with a 0.1 mM ethanolic solution of C11EG6 and then rinsed with flowing ethanol for 10 sec, submerged in fresh ethanol and sonicated for 2 min, rinsed again with ethanol flow for 10 sec followed by drying under argon.

7.3.1.4 Functionalisation of gold protected with photoresist

Gold on silicon substrates were spin coated with photo resist AZ6612 at 3000 rpm for 45 sec (estimated thickness 1.39 μm), followed by baking in a hot plate for 100 sec at 110 °C. These slides were exposed to the same functionalisation protocol described above (3.3.1.2) for 3GPS-PDL functionalisation of glass or silicon. The slides were then rinsed with flowing acetone for 10 sec, submerged in fresh acetone and sonicated for 2 min, rinsed again with acetone flow for 10 sec followed by flowing ethanol and drying under argon. For functionalisation with C11EG6 thiol, the procedure described below (4.3.1.6) for "C11EG6 SAM on gold" was followed.

7.3.1.5 Progesterone-C8-4KC/C11EG6 mixed SAM on gold

Freshly cleaned gold substrates were incubated overnight, at room temperature, in a freshly prepared mixed solution of progesterone-C8-4KC (molar fraction 0.025) and C11EG6 (molar fraction 0.975, 0.1 mM) in ethanol. The substrates were then rinsed with flowing ethanol for 10 sec, submerged in fresh ethanol and sonicated for 2 min and rinsed again with flowing ethanol for 10 sec, followed by drying under argon.

7.3.1.6 C11EG6 SAM on gold

Freshly cleaned gold substrates were incubated overnight, at room temperature, in a freshly prepared 0.1 mM ethanolic solution of C11EG6. The substrates were then rinsed with flowing ethanol for 10 sec, submerged in fresh ethanol and sonicated for 2 min and rinsed again with flowing ethanol for 10 sec, followed by drying under argon.

7.3.1.7 Progesterone-C11-SH/EG3SH mixed SAM on gold

Freshly cleaned gold substrates were incubated overnight, at room temperature, in a freshly prepared mixed solution of progesterone-C11-SH (molar fraction 0.025) and EG3SH (molar fraction 0.975, 0.1 mM) in ethanol. The substrates were then rinsed with flowing ethanol for 10 sec, submerged in fresh ethanol and sonicated for 2 min and rinsed again with flowing ethanol for 10 sec, followed by drying under argon.

7.3.1.8 5KC/C11EG6 mixed SAM on gold

Freshly cleaned gold substrates were incubated overnight, at room temperature, in a freshly prepared mixed solution of 5KC (molar fraction 0.025) and C11EG6 (molar fraction 0.975, 0.1 mM) in ethanol. The substrates were then rinsed with flowing ethanol for 10 sec, submerged in fresh ethanol and sonicated for 2 min and rinsed again with flowing ethanol for 10 sec, followed by drying under argon.

7.3.2 Fluospheres functionalisation

Step 1 - Sodium azide removal

The fluospheres solution (concentration of 4.5 x 10^{12} spheres/mL), as bought, was sonicated for 30 min before each use. 45 uL of the stock solution were diluted in 500 μL of water. This solution was then filtrated using a centrifugal filter (Figure 7.117) at 10 000 rcf for 15 min and resuspended in 4.5 mL of water (concentration of 4.5 x 10^{10} spheres/mL).

Figure 7.117 - Centrifugal filter units showing filtered red fluospheres.

Step 2 – Functionalisation with sulfo-GMBS

A solution of sulfo-GMBS with concentration of 147.25 μg/mL or 1.88 μmol/mL was freshly prepared by diluting 2.5 mg in 500 μL of water and sonicating for 10 min. Since the sulfo-GMBS is moisture sensitive, the vial was first allowed to equilibrate to room temperature before opening and the needed amount of reagent was immediately dissolved and used.

4.5 mL of fluospheres prepared in step 1 were incubated with the 500 μL solution of sulfo-GMBS (10-fold-molar) for 2.5 h at room temperature, the vial being gently inverted every 15 min.

The excess of crosslinker was removed by using centrifugal filter units at 10 000 rcf for 15 min, followed by resuspension in 5 mL of water and sonication for 10 min.

Step 3 – Functionalisation with progesterone-C8-4KC and C11EG6

Peptide solutions were always freshly prepared just prior to use. The progesterone peptide was removed from the freezer and allowed to equilibrate to room temperature before opening the container.

0.5 mg of progesterone peptide were first diluted in 100 μL ethanol and then in 900 μL of water. The solution was sonicated for 10 min. 1 mM solution of C11EG6 was prepared by diluting 5 μL in 100 μL of ethanol and then in 9.9 mL of water.

200 uL of the prepared peptide solution were added to 5 mL of sulfo-GMBS spheres and sonicated for 5 min. 30 min later, 2 mL of 1 mM solution of C11EG6 and 2.8 mL of water were then added and the 10 mL mixture was incubated overnight, at room temperature and placed on the moving plate selected to a gentle rotation. The final concentration of progesterone peptide in solution was 13.5 μM, the final concentration of C11EG6 being 200 μM.

This solution was then dialysed against PBS for removal of unreacted thiols.

For functionalisation with C11EG6 only, the procedure was similar to the one described above except that 5 mL of sulfo-GMBS spheres were incubated overnight with 5 mL of 1mM solution of C11EG6 and no peptide solution was added.

Step 4 - Dialysis

For the dialysis membrane preparation, the device was filled with 10% ethanol, capped and submerged in the same solution for 10 min. The solution was then aspired out and the device was flushed thoroughly with water and then soaked in the same solution for 20 min. The water was then aspirated out and the remaining drops were shaken out. The membrane was ready to use immediately, not allowing it to dry out.

The solution to be dialysed was loaded into the dialysis device, which was then placed floating (using the floatation ring) in the dialysis container (1 L glass cylinder), previously filled up with PBS 1x and a stir bar (Figure 7.118). This system was placed on a magnetic

stirring plate and the stirring was adjusted to form a gentle rotating current, avoiding strong vortex. The solution was dialysed at room temperature for 24h with 4 complete buffer changes. After this period, the solution was aspirated out of the membrane with a pipette and the membrane was discarded.

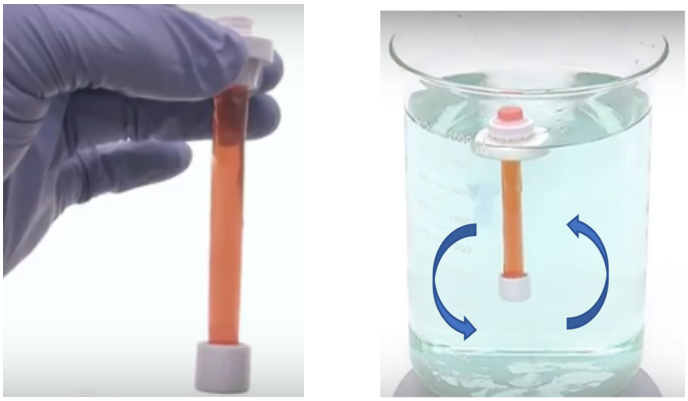

Figure 7.118 – Photo of dialysis membrane close up and placed inside dialysis beaker with stirring. Adapted from [1].

7.3.3 Cell attachment and labelling

Cells preparation

Sperm cells from anonymous donors were prepared according to the procedure used by Publicover and co-workers[2], with slight variations described as follows. Semen samples were stored at room temperature for no more than 30 min. Cells were isolated from the seminal plasma by swim up into supplemented Earle's balanced salt solution (sEBSS) with 0.3% (w/v) fatty acid free BSA. 700 µL of sEBSS was pipetted into each of a series of 5 ml test tubes and gently underlayered (slow release of the cells to avoid air bubbles) with 300 µL of semen. After incubation for 1 hour (37 °C; 6% CO_2) the top 0.7 mL was gently

removed from each test tube, transferred to loosely-capped tubes and kept incubated (37 °C; 6% CO_2).

Cells labelling

Oregon Green BAPTA1-AM (OGB) or Fluo-4-AM dyes were used for labelling sperm cells. The dyes were prepared by adding 20 μL of Pluronic acid F-127 (surfactant used to facilitate the solubilization of water-insoluble dyes) in DMSO (100 mg Pluronic acid in 0.5 mL DMSO) to 50 μg aliquot of OGB or Fluo-4-AM. 1.2 uL of the prepared dye solution was added to the cells (for a 5 μM final concentration of dye), being incubated (37 °C; 6% CO_2) for 40 min before imaging.

Cells counting

Sperm cells were counted in a Computer Assisted Sperm Analysis (CASA) system from Hamilton Thorne equipped with Human Motility Software. 10 μL of cells were loaded into a neubauer chambers for the cell counting.

7.3.4 Antibody labelling

Antibody labelling kit alexa fluor 488 was used for the labelling of progesterone antibody. 100 uL of 1 mg/mL solution of antibody were prepared by dilution in PBS and 10 uL sodium bicarbonate 1 M were added before transferring the solution to the reactive dye vial. The vial was gently inverted for a few minutes and then incubated for 1 h at room temperature, with gentle inversions every 15 min. In the meantime, the purification resine column was prepared by settling a volume bed of 1.5 mL; buffer was allowed to elute and

then discarded, the column being now ready for the labelled antibody purification. The reacted solution was placed on the spin column and allowed to adsorb into the resin bed for 1 minute. The column (Figure 7.119) was then attached to the collection tube and placed in a swinging bucket rotor Centrifuge Eppendorf 5804r for 5 min at 1100 x g. After centrifugation, the collection tube contained the labelled antibody in PBS.

Figure 7.119 – Photo of resin purification column loaded with green labelled antibody.

7.3.5 Binding of labelled antibody to the functionalised spheres

5 μL of labelled antibody 2.1 μM were diluted in 45 μL of PBS and 5 μL of functionalised fluospheres were also diluted in 45 μL of PBS. These volumes were mixed together and incubated for 20 min at room temperature in a moving plate. The mixture was then filtrated using the centrifugal filter units at 10 000 rcf for 15 min and resuspended in 100 μL of PBS.

The same protocol was followed for the functionalised spheres but without adding labelled antibody, only adding 50 μL of PBS. This solution was then filtrated and resuspended in

the same way and used as a control for the spectrofluorometry studies as it would have the same concentration of spheres as the solution exposed to the antibody.

7.3.6 Fabrication of a micropatterned device

Device fabrication was performed in a cleanroom environment (class 100 and 1000 cleanroom facilities) to minimize contaminations. A lift-off approach was used for the fabrication process, illustrated below (Figure 7.120).

The glass slides were cleaned in Piranha solution as described above.

Photolithography

After cleaning, the slides were placed in a hot plate at 250 °C for 20 min, cooled down to room temperature and then placed in a Laurell WS-650 Spin Coater. The following conditions were selected for spin coating the positive tone photoresist AZ ECI 3027 onto the slides: acceleration ramp of 1000 rpm, rotation of 4000 rpm for 45 sec. After spin coating, the slides were soft-baked at 100 °C for 5 min. Mask alignment and UV exposure were performed with a Suss Microtec MA8 Gen3 Mask Aligner. An exposure dose of 150 mJ/cm^2 (measured at a wavelength of 365 nm), using soft contact mode, was found to give the best results. A post-exposure bake at 100 °C for 1 min was performed. The slides were then cooled down slowly to room temperature, developed for 1 min 45 sec using developer AZ726 MIF, rinsed thoroughly with water and dried with argon.

Sputtering

Samples were loaded into a Kurt Lesker PVD75 Sputter Coater and pumped down to a base pressure of $<10^{-5}$ Torr. Chromium deposition rate of 1 Å/s was achieved when the following conditions were applied: argon flow of 30 sccm, providing a pressure of 1.5 mTorr, power setpoint of 50 W DC and 10 rpm for the rotation speed of the sample holder. A 50 nm layer of gold was sputtered directly after chromium deposition without breaking vacuum. A deposition rate of 1.4 Å/s was achieved when the following conditions were applied: argon flow of 30 sccm, providing a pressure of 1.5 mTorr, power setpoint of 30 W and 5 rpm for the rotation speed of the sample holder.

For each batch, an additional sample of silicon was loaded on the PVD Sputter Coater, together with the glass slides, to get a SEM cross section image and confirm the gold layer thickness.

Lift-off

For the lift off, the slides were submerged in DMSO at 80 ºC (no agitation) for 2 hours and then left submerged in the same solution overnight at room temperature, following a 1 min ultra-sonic bath. The slides were then rinsed thoroughly with water and dried with argon. After that, the slides were rinsed with acetone making use of a cotton swab. Slides were then rinsed with isopropanol and dried with argon.

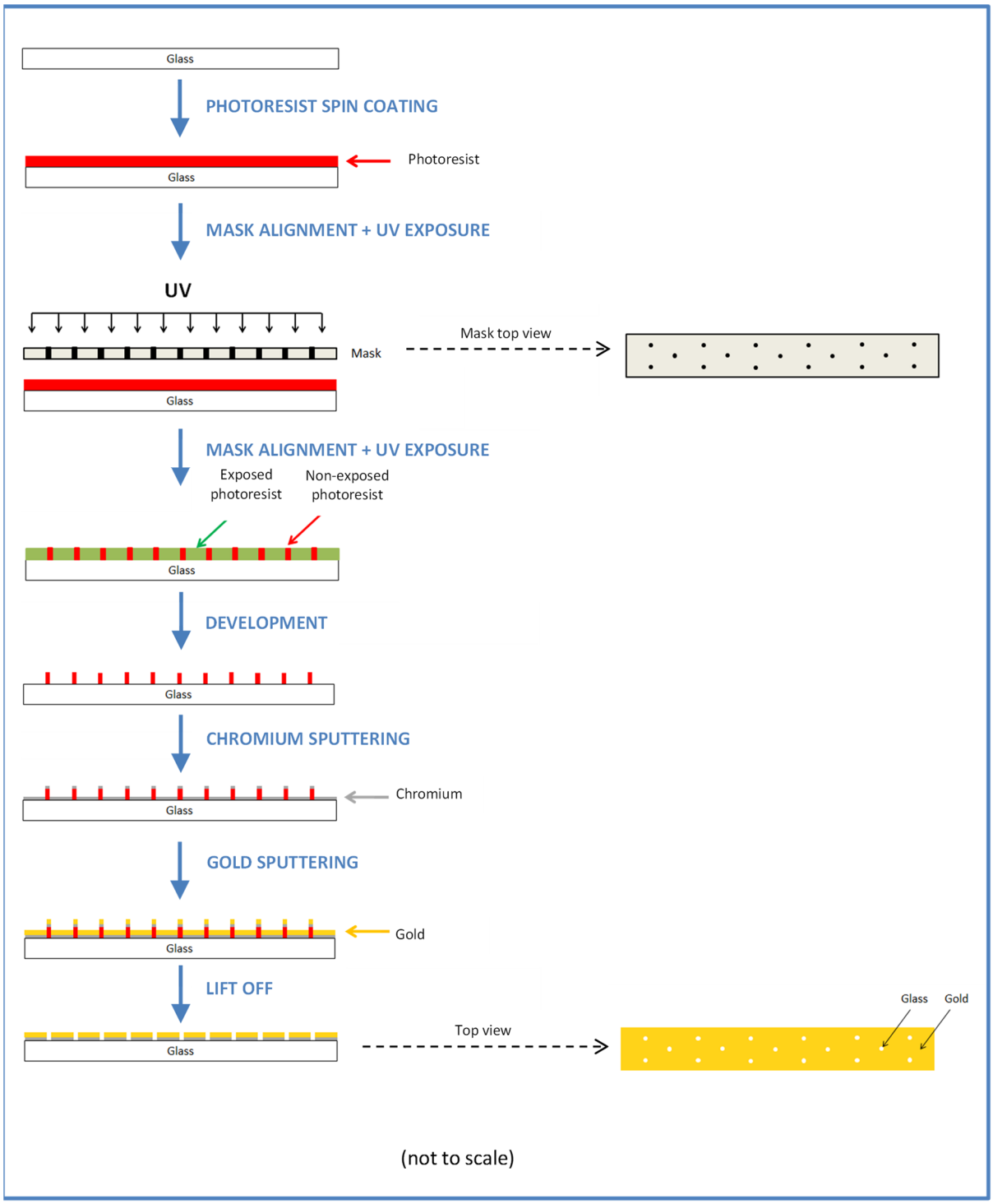

Figure 7.120 – Simplified scheme of the device fabrication process.

7.3.7 Characterisation

7.3.7.1 Contact angle

The instrument used for contact angle measurements was an Attension Theta optical tensiometer from Biolin Scientific. Before use, the instrument was calibrated for the chosen camera zoom and the syringe was filled with water ensuring there were no bubbles in the needle or tube. Drop size was set to 5 uL. The contact angle was calculated by OneAttension software. Three drops per sample were measured, being placed in random positions of the surface, the samples being prepared in triplicate. The values presented are therefore an average of 9 measurements (triplicate samples, 3 measurements per sample) and the error bars represent the standard deviation within the measurements.

7.3.7.2 Ellipsometry

Ellipsometry measurements were performed using a Jobin-Yvon UVISEL ellipsometer from Horiba Scientific. The angle of incidence between the analyser and the polariser was fixed at 70° and the selected wavelength range was 250-800 nm with 5 nm increments. DeltaPsi 2 software (version 2.6.8.239) was used to fit the data through mathematical modelling. Delta and Psi were measured for the clean substrate, just before SAM formation, and then again for the film-covered surface. The model used for fitting the data consisted of a substrate base layer of gold or silicon (data from measurements for clean substrate) and a Cauchy transparent layer on top, with fixed optical properties and an initial value for the refractive index of the film being set to 1.45 (valid for organic SAMs). A multi-guess iterative calculation procedure was set with an initial film thickness value based on reported values for each SAM. When thickness values could not be found from literature, thickness values were estimated using ChemBio3D Ultra (version 14.0.0.117,

CambridgeSoft). After drawing the SAM molecule, the full length was measured from the atom binding to the gold surface (sulfur atom for SAMs formed from thiols) to the end functional group of the molecule. The goodness of fit to data was evaluated by the χ^2 value calculated by the software, the lowest value corresponding to the best fitting. Samples were prepared in triplicate and three measurements were performed for each sample by randomly selecting 3 different areas of the sample. The values presented are therefore an average of 9 measurements (triplicate samples, 3 measurements per sample), the error bars representing the standard deviation within the measurements.

7.3.7.3 Surface Plasmon Resonance / Electrochemical SPR

A SR7000DC SPR instrument with simultaneous two-channel measurements from Reichert (USA) was used. The standard Reichert flow cell is made of Teflon and incorporates 2 channels as shown in Figure 7.121.

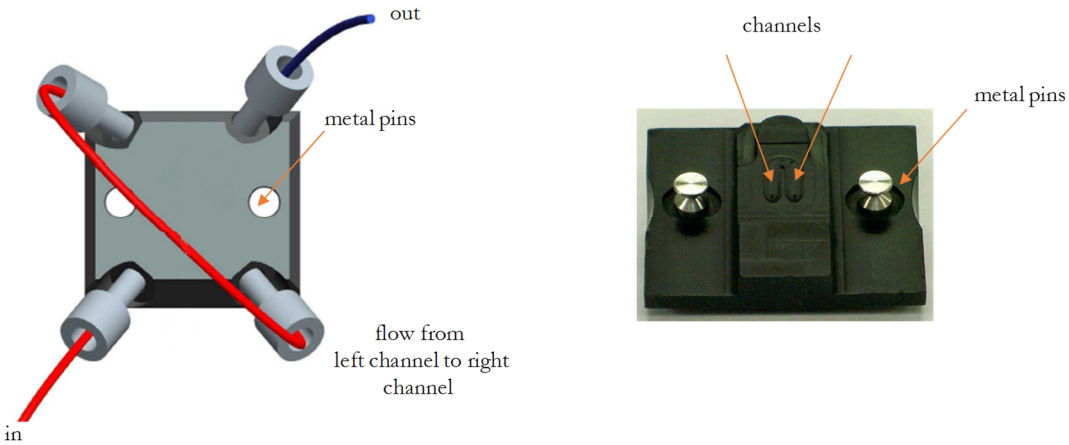

Figure 7.121 – Left: top view of SPR microfluidic flow cell with 2 fluidic channels plumbed in series; right: photo of SPR flow cell turned upside down, showing the two channels and the metal pins used for positioning the cell. Adapted from Reichert SR7500DC System user guide REV-E.

For the electrochemical SPR experiments, an electrochemical flow cell (Figure 7.122) from Reichert was used, with a total volume of 32 µL, connected to a Gamry G300 potentiostat, an Ag/AgCl reference electrode and a platinum counter electrode. The area of the fluidic channel, which corresponds to the surface area of the working electrode (gold), was 10.5 mm^2. The counter electrode had a surface area of 22.8 mm^2 and the reference electrode had a surface area of 32.2 mm^2. The potentiostat was warmed up for 30 min before use.

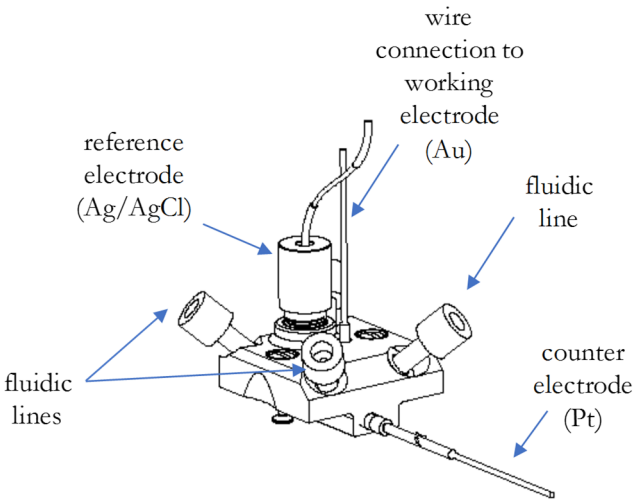

Figure 7.122 – Electrochemical flow cell. Adapted from Reichert electrochemical flow cell user guide v3.

Before use, the SPR instrument was cleaned with 0.5% sodium dodecyl sulfate (SDS), 50 mM glycine pH 9.5 and water. The buffer, PBS 1x, was prepared daily, being filtered (0.2 µm filter), degassed and purged with argon for 30 min. The fluidic system was flushed with buffer before the experiments. The flow cell was cleaned by sonication in detergent solution and rinsed with water. The injection solutions were also freshly prepared. This instrument was permanently ON, hence no need to warm up before use. A drop of matching refractive index oil was placed on the prism surface every time a new sensor slide

was loaded, so that the sensor slide is optically coupled to the prism surface. The experiments were performed at 25° C. Functionalised sensor slides were run in triplicate for the SPR studies.

7.3.7.4 XPS

XPS measurements were acquired using the following instruments, depending on the availability: a) a Thermo Scientific K-Alpha system or b) a Kratos Axis Supra system, both with a monochromatic Al kα (photon energy of 1486.68 eV) source. The samples were clipped onto the stainless steel sample holder with copper clips. The analysis chamber was under a pressure of ~7.5 x 10^{-9} Torr and data was collected from large areas (700 μm x 300 μm) of the samples surface, the take-off angle being 90^{o} to the surface plane. Survey scans were run with a pass energy of 200 eV and 0.4 eV energy step. High resolution scans were acquired using a lower pass energy (40 eV and 0.1 eV energy step). Each spectrum is a result of at least 5 scans. The charge neutraliser system was only used for the fluospheres samples. Fitting of XPS peaks was performed using CasaXPS (2.3.18dev1.1.p) processing software. The binding energy scale calibration was based on the position of the Au 4f7/2 peak at 84 eV. U 2 Tougaard background was selected and a Gaussian/Lorentzian GL(30) lineshape was applied. Relative sensitivity factors used for quantification were selected in accordance to the instrument used. The C 1s spectra were fitted by setting all the peaks to an equal full width at half maximum (FWHM) and each S doublet was constrained to have a peak separation of 1.16 eV, a 2:1 area ratio ($2p_{3/2}$: $2p_{1/2}$) and identical FWHM.

7.3.7.5 Spectrofluorometry

The instrument used for spectrofluorometry was a Jasco FP-8500 with integrated temperature controller to maintain the temperature of the sample constant. Jasco Spectra Manager software was used for instrument control and data acquisition. Every set of experiments was run in the same day to avoid variable conditions of the instrument (the excitation lamp and the photomultiplier tube being the main potential sources of variability). The temperature was set to 20 °C, emission mode was on with 5 nm slit for both emission and excitation, scan speed 500 nm/min, wavelength range 450-700 nm and sensitivity set to high. Measurements were run for each sample at excitation of 494 nm and then at excitation of 580 nm. The micro-cuvette was washed with HPLC ethanol and water between samples.

7.3.7.6 DLS

DLS measurements were performed in a Malvern Zetasizer Nano with Malvern 7.11 software. Temperature was set to 20°C. Standard disposable polystyrene cuvettes (10 x 10 x 45) mm^3 were used. Samples were ultrasonicated for 20 min before measurements. Measurement angle was set to automatic, equilibration time was set to 2 min and number of repeats was set to 5 runs per sample. Material (polystyrene) and solvent (water) were defined in the software. The output data consisted of the mean hydrodynamic radius, size distribution and polydispersity index.

7.3.7.7 SEM and EDX

SEM was performed with a Hitachi FE-SEM S-4800 Scanning Electron Microscope coupled to an Oxford Instruments X-Max EDX detector, with an acceleration voltage of 10 kV.

7.3.7.8 TEM

For TEM, a Jeol 2100 200 kB fitted with a Lab6 filament was used. Operating voltage was 80 keV. The particles were dispersed on a carbon coated copper TEM grid and allowed to dry overnight. Image J 1.48v software was used for obtaining the values of the particles diameter.

7.3.7.9 NMR

^{1}H NMR spectra were acquired at 300 MHz using a Bruker AV III 300. For sample preparation, 240 μL of the fluospheres stock solution were filtrated and dried under vacuum, followed by resuspension in $CDCl_3$ (without TMS).

7.3.7.10 AFM

For AFM, a JPK Nanowizard II was used with a Bruker NCHV tip (42 N/m, 320 kHz, 8nm nominal tip radius) in tapping mode. Images were levelled using a linear fit to each scan line. The average roughness and root mean square (RMS) roughness of gold and glass surfaces on the fabricated devices were obtained using SPIP software (Image Metrology), based on 3 points measurements.

7.3.7.11 Cells imaging

The system used for investigation of live cells attachment to the functionalised surfaces consisted of an inverted Nikon Eclipse TE300 microscope equipped with a Retiga R1 CCD camera Qimaging (Figure 7.123). The microscope room was at constant controlled temperature, set to 25 °C. The polycarbonate flow chambers were previously washed with liquid soap and dried. Vacuum grease was applied (with the help of a thin paint brush) to promote sealing when the functionalised slide and the cover slip were attached to the chamber. After incubating 200 µL of cells in the flow chamber attached to the functionalised surface for 20 min at 37 °C, the chamber was mounted onto the microscope stage (Figure 7.124), and connected to a perfusion system (consisting of a peristaltic and a vacuum pump). A flow of 1 mL/min of EBSS with BSA was set for 20 min in order to wash away the non-attached cells from the chamber before imaging. A 40 x objective was used for capturing the images in phase contrast mode, 10 ms exposure.

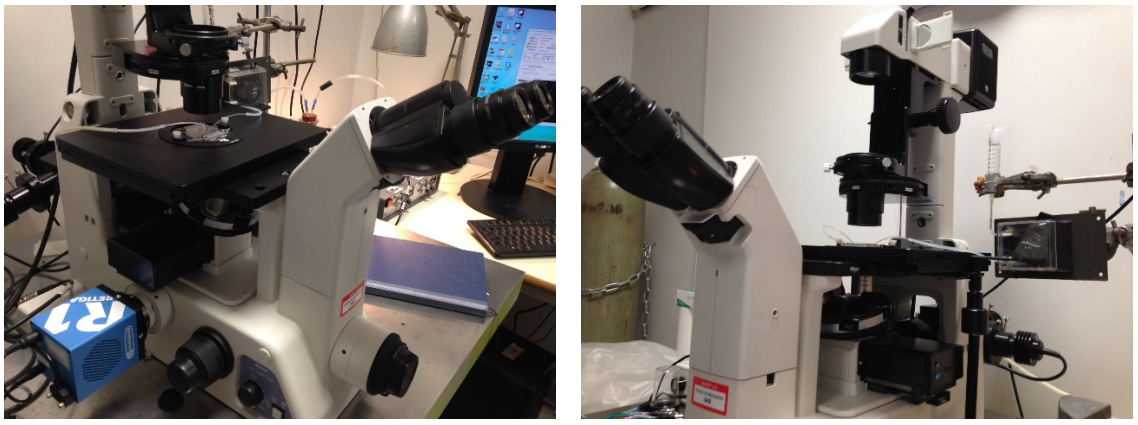

Figure 7.123 – Photos of Nikon Eclipse TE300 microscope equipped with a Retiga R1 CCD camera, showing the flow chamber loaded onto the microscope stage and connected to a perfusion system.

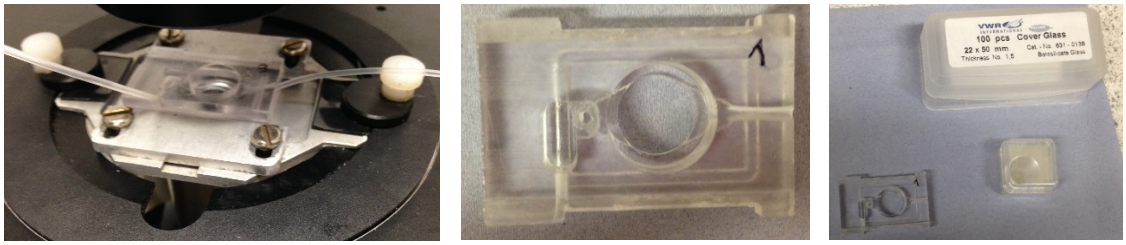

Figure 7.124 – Let: Photo of flow chamber connected to a perfusion system, loaded onto the microscope stage; middle: close-up photo of flow chamber, with inlet flow on the right side and outlet flow on the bottom left; Right: photo of rectangular cover slips that were functionalised for cell attachment and circular cover slips for chamber sealing.

7.4 List of References

1. Spectrum Labs. http://spectrumlabs.com/dialysis/FloatALyzer.html (accessed August 2018).

2. Nash, K.; Lefievre, L.; Peralta-Arias, R.; Morris, J.; Morales-Garcia, A.; Connolly, T.; Costello, S.; Kirkman-Brown, J. C.; Publicover, S. J., Techniques for imaging Ca2+ signaling in human sperm. *Journal of Visualized Experiments* **2010,** (40), 1-4.

8 Conclusions and Future Work

The work described herein entails a diversity of studies which, combined, pave the way for the development of new tools for assisted reproductive technologies, based on electrically switchable surfaces. This work is fundamental to the next stage of studies, involving cells, providing a novel platform for the controlled exposure of progesterone to a group of cells dispersed on a micropatterned surface and whose response in terms of calcium signalling can be followed. Using advanced surface analysis techniques, such as XPS and eSPR, in addition to standard techniques in the biosciences field, such as spectrofluorometry, a variety of surfaces were characterised. The strategies described can be applied to the development of a variety of systems incorporating other biomolecules of interest for a wide range of medical, biotechnological and pharmaceutical applications. Electrical switching can be easily applied and regulated, making it an excellent remote trigger for biosensing applications.

A summary of the findings and conclusions outlined from the work described in chapters 4, 5 and 6 is presented below, as well as suggestions for further investigations.

Investigations on an ON-OFF switchable system based on a progesterone-C7-4KC:C11EG6 mixed SAM, described in **Chapter 4**, provided a better understanding on how this sensing platform can selectively, and on demand, capture progesterone antibody in solution.

Firstly, the mixed SAM formation was optimised by reducing the amount of unbound sulfur present on the surface and the mole fractions of each component on the surface were calculated from XPS data. These results showed a similar fraction on the surface to the one used in the solution where the gold substrates were incubated for the mixed SAM formation. Ellipsometry measurements corroborated the assumption that when a negative

potential is applied to the gold surface, progesterone is in closer proximity to the spacer (C11EG6) matrix, as the thickness of the film was lower after the negative potential was applied and higher after the positive potential was applied. The system responded differently when a different range of potentials was applied as ON and OFF conditions, with an observed decrease in the switching efficiency for – 0.2 V and 0.2 V in comparison to -0.3 V and +0.4 V. A surface was created where an oligopeptide without progesterone was present, in order to demonstrate the specificity of the system. After demonstrating the successful functionalisation of the surface, eSPR studies were undertaken. These studies revealed a much lower antibody binding capacity, with a limited amount of antibody non-specifically adsorbed to the mixed SAM, compared to the different binding affinities of the antibody for progesterone-C7-4KC:C11EG6 mixed SAM at different electrical potentials. These results demonstrate that the antibody is not attracted to, or from, the surface directly as a result of the applied electrical potential. Lastly, another control mixed SAM was designed, prepared and characterised, where no peptide was present. eSPR studies were then conducted, revealing that the amount of antibody binding to this surface was not affected by the different electrical potentials applied to the surface. These studies demonstrate that the switching only occurs in the presence of the peptide and is due to the conformational changes of the progesterone oligopeptide on the surface induced by an electrical potential.

Whilst being developed to be integrated in a biomedical device for assessment of sperm quality and fertilizing potential, the application of this system can be widely extended. This approach can be applied to other antigen-antibody systems as, so far, antibody-antigen interactions have always been evaluated in static conditions and on-demand antibody biosensors are highly desirable in medical, biotechnological and pharmaceutical fields.

Preliminary studies of the development of an alternative and novel switchable system, OFF-ON type, demonstrated the viability of using a cyclic peptide to create a mixed SAM on gold and the simple attachment of a biomolecule of interest to the surface *via* click chemistry. Further development of this system into a switchable surface is dependent on the successful synthesis of a "double arms" molecule, which would allow eSPR studies and the investigation and optimisation of its switching ability, following a similar strategy to the outlined for the progesterone-C7-4KC:C11EG6 mixed SAM.

The design and fabrication of a micropatterned device, composed of gold and glass, aimed to be used for studies with cells, was described in **Chapter 5**. A method for the chemical functionalisation of the fabricated device was also investigated. A novel approach is used for the patterning of sperm cells, where these are dispersed on a micropatterned device, with each individual cell being attached through its head to a glass hole surrounded by a gold surface, and the cell tail being in contact with the functionalised gold surface.

The micropatterned device was successful fabricated by means of standard photolithography techniques. Characterisation by SEM and AFM revealed that the desired pattern was formed, the surfaces presenting low roughness as desired for further functionalisation with SAMs. Some defects were, however, detected on the surface, which are a result of the lift off process. These can be eliminated by optimisation of the fabrication process.

Ellipsometry, contact angle, XPS and optical microscopy results demonstrated the efficacy of the method developed for the functionalisation of gold and glass. The photoresist layer survived the conditions used for the formation of the silane-PDL layer on glass. The silane-PDL layer on glass survived the photoresist layer removal from gold and further functionalisation with thiol, remaining effective for cell attachment. The functionalisation

of gold was only tested for a SAM, using C11EG6, rather than for a mixed SAM. The next step should be testing the method for the formation of a mixed SAM on gold, using the components of the switchable surface described in Chapter 4, including surface characterisation using the strategy described along Chapter 5. The developed method could then be tested on the fabricated micropattern devices, including cell attachment, since the studies regarding cell attachment were so far undertaken only on single glass substrates.

The development of a method for functionalisation of fluorescent spheres with a low density of progesterone oligopeptide, for further studies with sperm cells, was described in **Chapter 6**. A few challenges were found with this process and further investigations will be required before proceeding with the studies with cells.

XPS studies provided valuable information about the average chemical composition of the particles' surfaces and indicated that the particles were successfully functionalised, first with maleimide groups and then with the two thiolated components: hexaethylene glycol and progesterone oligopeptide.

However, these studies also indicated that unreacted amine and maleimide groups are still present on the surface of the particles after the attachment of thiols. These groups might interact with the cells and therefore a way to block these unreacted groups, possibly by using a short chain polyethylene glycol thiol, must be explored.

XPS results also revealed the presence of oxidised sulfur, which is an indication of an inefficient purification process and therefore this step needs to be improved. DLS results also indicate the need for improving this step.

In addition to the information achieved by XPS and in order to validate those results, quantitative information about the extent of surface functionalisation and surface coverage

could be ascertained by using a different technique such as size exclusion chromatography, gas or liquid chromatography, gels and colorimetric approaches.

When investigating the interaction of a labelled progesterone antibody with the functionalised particles by spectrofluorometry, the highest increase in fluorescence was achieved for the particles functionalised with the progesterone peptide, once again indicating the presence of progesterone on the surface of the spheres. However, a high level of non-specific binding was shown. Improving the washing method after incubation with the antibody and using a decreased concentration of antibody is likely to decrease the observed non-specific binding. Spectrophotometry could also be used to quantify the amount of unbound antibody and therefore indirectly provide quantitative information about antibody bound to the spheres surface.

Zeta potential measurements could provide information on the colloidal stability of the spheres and visible changes should be detected when comparing different stages of functionalization.

The amount of progesterone loading can potentially be varied by changing the concentrations of peptide incubated with the spheres.

Future work should also include the confirmation, via an analytical technique, such as liquid or gas chromatography, that no unreacted reagents or secondary products are left in the final solution where the functionalised spheres are suspended (down to picomolar concentrations). The final purification method should be improved until these are not detected in solution, in order to ensure that the response from the cells is only due to the interaction with the functionalised fluospheres.